NOVEL CO-PRECIPITATED OXYGEN CARRIERS FOR CHEMICAL LOOPING COMBUSTION OF GASEOUS FUEL

NGOZI CHINWE EKPE, BSc (Hons), MSc

Thesis submitted to the University of Nottingham

for the degree of Doctor of Philosophy

APRIL, 2016

ABSTRACT

Carbon Capture and Storage (CCS) is one option to meet the increasing energy demand as well as reduce net CO_2 emissions to the atmosphere. Chemical Looping Combustion (CLC) is a promising CCS technology proposed to meet the challenge of mitigating the carbon dioxide (CO_2) emissions. CLC process can be based on interconnected fluidized beds, consisting of air reactor, fuel reactor and oxygen carrier (OC) which undergoes redox reactions while it circulates between the reactors. The main products are CO_2 and water, thus eliminating the need of an additional energy intensive CO_2 separation.

The feasibility of CLC depends on the oxygen carrier's (OC) ability to transfer O_2 from air reactor to fuel reactor and have sufficient oxygen capacity, high reactivity and withstand a high number of redox cycles without significant loss in performance. OCs based on transition metal oxides of Cu, Co, Fe, Mn and Ni has been explored. Nevertheless, research is focused on improving the OCs performance with the aim to overcome their various practical limitations. Mechanical mixing and impregnation which fails to provide a high degree of dispersion and high metal loading respectively are commonly used for OC synthesis. Very few works have been reported for Mn-oxide and co-precipitated oxygen carriers. The few studies on co-precipitated OCs mainly use strong base as precipitants. One drawback to this is the repetitive washing of precipitate to remove excess alkali ions and controlled loading of active components cannot be easily obtained. In this study, weak base instead of strong base was used in the synthesis of OCs. This is the first time this controlled approach has been applied to prepare oxygen carrier in CLC for manganese and iron.

This thesis is a novel research on development and detailed investigation of co-precipitated Mn-oxide and Fe-oxide OCs with ZrO_2 and combined ZrO_2–CeO_2 support. The reaction kinetics, stability and oxygen transfer capacity (OTC) of the OCs were studied by TGA up to 1173 K in H_2, CO and CH_4. Characterization of physical and chemical structures of particles was obtained by SEM-EDX, XRD, BET and pycnometer.

The result reveals that regardless of the composition of the co-precipitated oxygen carriers, there was no interaction of the metal oxides with the support material which could have altered the thermodynamics of the redox system. Furthermore, co-precipitated Mn/Zr and Fe/Zr OCs were more reactive than their counterpart prepared by impregnation and mechanical mixing. Also, changes in reactivity and OTC suggest that the synergistic effect varies with ratios of the single oxides in the bimetallic OCs. Co-precipitated Mn-rich oxygen carriers were more reactive than Fe-rich OCs. Interestingly, OCs with zirconia-ceria support exhibited activation tendency behaviour. Moreover, the use of combined zirconia-ceria for bimetallic Mn-Fe oxide reversed the characteristic progressive decrease in the performance of the OC with equimolar composition. For co-precipitated Mn-Fe Oxide oxygen carriers, zirconia content of 44 wt. % is sufficient to maintain the mechanical integrity of the particles during redox reactions compared to a zirconia content of 20 wt. %. This research has resulted in the development of highly reactive and stable oxygen carriers, which are promising for CLC. Mn/Zr OC reached full conversion in less than 48 secs and bimetallic Mn-Fe OCs reached 30% conversion in less than 43 secs in CH_4 and maintained stability in a thirty multicycle test.

The redox reaction kinetics of the most reactive oxygen carrier using CH_4, H_2, CO and air was investigated at isothermal conditions (973-1173 K) to

determine the kinetic parameters. Models of the reduction and oxidation reactions were selected by using a model fitting method. The nucleation model was the most statistically significant and suitable model for describing the reduction and oxidation behaviour of the oxygen carrier. The values of activation energy obtained for the reduction reaction in CH_4, H_2 and CO were 142.8 KJ/mol, 32.95 KJ/mol and 26.37 KJ/mol respectively. Whereas, for the oxidation reaction, the activation energy obtained using air was 28.83 KJ/mol.

In the application of co-precipitation technique for the synthesis of multicomponent materials, a heterogeneous product could be obtained from using improper preparation conditions. Results from this research have demonstrated that, the application of the well-designed co-precipitation procedure effectively produced composite materials (up to four co-precipitated mixed metal oxides) with controlled compositions and homogeneous dispersion. Furthermore, this study provides insight into the fundamental behaviours of co-precipitated manganese and iron based oxygen carriers to aid the design and optimization of future materials development.

LIST OF PUBLICATIONS

Conference Proceedings

Ekpe, N., Snape, C. E., Sun, C., Liu, H., Novel co-precipitated manganese oxide based Oxygen carriers for chemical looping combustion. International Conference on Coal Science and Technology (ICCS&T), September, 2015, Melbourne, Australia.

Ekpe, N., Snape, C. E., Sun, C., Liu, H., Development of innovative manganese oxide based oxygen carriers for chemical looping combustion. 18th Annual Energy Utility & Environment Conference (EUEC), February, 2015, San Diego, United States of America.

Proposed Journal Publications

Ekpe, N., Snape, C. E., Sun, C., Liu, H., Novel co-precipitated manganese oxide and iron oxide based oxygen carriers for chemical looping combustion' to be submitted to Energy and Fuels.

Ekpe, N., Snape, C. E., Sun, C., Liu, H., Effect of zirconia support composition on co-precipitated bimetallic Mn-Fe oxygen carriers for chemical looping combustion' to be submitted to Fuels.

Ekpe, N., Snape, C. E., Sun, C., Liu, H., 'Novel co-precipitated Mn-Fe oxide with combined zirconia-ceria support for chemical looping combustion' to be submitted to Energy and Fuels.

Ekpe, N., Snape, C. E., Sun, C. and Liu, H., 'Kinetics of redox of co-precipitated Mn_3O_4/ZrO_2 for chemical looping combustion' to be submitted to Energy and Fuels.

Presentations

Ekpe, N., Drage, T., Snape, C. E., Development of ZrO_2 – supported mixed oxides as oxygen carrier for chemical looping combustion. UK Energy Research Centre (UKERC), Energy Summer School, July, 2013. (Poster)

Ekpe, N., Snape, C. E., Sun, C., Liu, H., Innovative manganese oxide based oxygen carrier for chemical looping combustion. UK/South Korea | UKCCS Research Centre; Developing Clean Coal Technologies and Carbon Capture & Storage Workshop, February, 2015. (Poster)

Ekpe, N., Snape, C. E., Sun, C., Liu, H., Development of ZrO_2–supported mixed oxides as oxygen carrier for chemical looping combustion. Midlands Energy Graduate School Conference (MEGS), December 2013, Birmingham, UK. (Poster)

Ekpe, N., Snape, C. E., Sun, C., Liu, H. Innovative manganese oxide based oxygen carrier for chemical looping combustion. Engineering Research Showcase, University of Nottingham, May, 2015. Nottingham, UK (Poster)

Ekpe, N., Snape, C. E., Sun, C., Liu, H. Innovative manganese oxide based oxygen carrier for chemical looping combustion. Postgraduate research showcase, Energy and sustainability research division, University of Nottingham, March, 2015. Nottingham, UK (Poster).

DEDICATION

This thesis is dedicated to my God, my heavenly Father who so loved the world, that He gave His only begotten Son, that whosoever believes in Him should not perish but have everlasting life. (John 3:16)

ACKNOWLEDGEMENTS

Thanks to my Father in heaven in whom I live and move and have my being. Thank you for your love, mercy and grace to accomplish this research. Abba Father, I acknowledge you as the source of my inspiration, knowledge, understanding and wisdom. All the glory belongs to you.

Profound thanks to my supervisor, Prof. Colin E. Snape for his supervision and tremendous support. You are the best supervisor ever and indeed you are highly appreciated. Thanks to Dr Trevor Drage for the helpful support towards the successful commencement of this project.

Thanks to the staff in the Department of Chemical and Environmental Engineering for their help and support during the course of this research: Nigel Neate, Marion Bryce, Quinn Adrian, Fred Anderton, Keith Dinsdale, David Mee, Lee Stevens and others. Special thanks to Martin Roe and Vikki Archibald for the willingness to provide needed support for laboratory equipment. You are highly appreciated for all the assistance.

Many thanks to my friends and colleagues, both past and present: Maggie Wiatros-Motyka, Elmrabet Nabila, Akinyemi Ogunkeyede, Ezekiel Agunlejika, Komonibo Ebiundu and others. Thanks for your friendship and help in so many ways.

Heartfelt thanks to my family and my beloved Godswill, for your inestimable love and tremendous support throughout the course of this research. You are amazing! Remain blessed in Him.

Finally, the financial support from EPSRC for this study is highly acknowledged with gratitude.

TABLE OF CONTENTS

LIST OF FIGURES

LIST OF TABLES

LIST OF ABBREVIATIONS

Abbreviation	Meaning
$\Delta H_c^{\ominus}$	standard heat of combustion, KJ/mol
$\Delta H_o^{\ominus}$	standard heat of reaction for the oxidation, KJ/mol
$\Delta H_r^{\ominus}$	standard heat of reaction for the reduction, KJ/mol
Σv	molecular diffusion volume
δ	film thickness
$\emptyset$	Thiele modulus
ρ	density
η	effectiveness factor
μ	dynamic viscosity
A_o	pre-exponential factor
AIC	Akaike Information Criterion
AIC_C	Akaike Information Criterion with correction
BET	Brunauer−Emmett−Teller
C	BET parameter
C_{AB}	concentration at the external boundary
C_{AS}	concentration at the external particle surface
CCS	carbon capture and storage
CLC	chemical-looping combustion
D_{AB}	binary gas phase diffusivity
df	degree of freedom
d_P	particle diameter
E_a	activation energy, KJ/mol
EDX	Energy Dispersive X-ray
F	F ratio
GHG	greenhouse gases
k	reaction rate constant

K	number of free parameters
k_c	mass transfer coefficient
M	instantaneous mass of the Oxygen carrier, mg
M	molecular mass
M_{oxd}	mass of Oxygen carrier fully oxidized, mg
M_{red}	mass of Oxygen carrier fully reduced, mg
M_yO_x	oxidized form of the oxygen-carrier
M_yO_{x-1}	reduced form of the oxygen-carrier
n	kinetic exponent
N	number of data points
N_A	Molar flux
OC	oxygen carrier
ppmv	parts per million by volume
r	observed rate of reaction
r_{gas}	maximum rate of external mass transfer
R	universal gas constant, J mol^{-1} K^{-1}
R_P	particle radius
R^2	coefficient of determination
Re	Reynolds number
Ro	oxygen ratio. The maximum mass fraction of oxygen that can be transferred between the air and fuel reactor
Roc	oxygen transfer capacity
ROT	rate of mass based conversion or rate of oxygen transport
RSS	residual sum of squares
Sc	Schmidt number
SEM	Scanning Electron Microscopy
SEM-EDX	Scanning Electron Microscopy-Energy Dispersive Spectroscopy

Sh	Sherwood number
SS	sum of squares
t	reaction time, s
T	temperature (K)
U	gas free mean velocity
v	kinematic viscosity
w	mass conversion
X	fractional conversion for reduction and oxidation of the oxygen carriers
X_{oc}	fraction of active metal oxide
XRD	X-ray diffraction
y	mole fraction

1 INTRODUCTION

1.1 Background

Recent climate changes are reported to have had wide spread impact on human and natural systems (IPCC, 2007). Each of the last three decades has been successively warmer at the Earth's surface than any preceding decade since 1850. Moreover, the warming of the climate system is unequivocal, and since the 1950s, many of the observed changes are unprecedented over decades to millennia. Some of these changes are warmed atmosphere and ocean, diminished amounts of snow and ice, and rise in sea levels. These changes have been attributed to human influence on the climate system with indications that recent anthropogenic emissions of greenhouse gases (GHG) are the highest in history (IPCC, 2014).

Carbon dioxide (CO_2) is the major greenhouse gas that contributes to global warming. Climate scientists have observed that CO_2 concentrations in the atmosphere have been increasing significantly over the past century, compared to the rather steady level of the pre-industrial era (about 280 parts per million by volume, or ppmv). The 2013 concentration of CO_2 (396 ppmv) was about 40% higher than in the mid-1800s with an average growth of 2 ppmv/year in the last ten years. The increased atmospheric concentrations of CO_2 have been attributed primarily to the combustion of fossil fuels (IEA, 2014). In order to avoid most disastrous changes to the Earth's climate, the concentration of CO_2 must not exceed 450 ppm or rise more than 15% over present concentrations. Also, the average increase in atmospheric temperature would have to be limited to less than 2^oC. Consequently, a reduction in greenhouse emissions became of paramount interest internationally. As a result, in 1997, the Kyoto Protocol was

drafted in the United Nations Framework Convention on Climate Change (UNFCCC) (UN, 1998).

Some technological options, which include Carbon Capture and Storage (CCS), were proposed in order to meet the increasing energy demand as well as reduce net CO_2 emissions to the atmosphere (IPCC, 2005). International Energy Agency (IEA) analysis suggests that CCS will play a fundamental role in global least-cost efforts to limit global warming, contributing around one-fifth of required emissions reductions in 2050 (IEA, 2012). The CCS technology involves capture of concentrated CO_2 stream from industrial and energy related sources, its transportation and long-time safe storage away from the atmosphere.

The three most common technologies employed in order to obtain CO_2 in pure stream from power production units are post-combustion, oxy-fuel combustion and pre-combustion processes (IPCC, 2005; Olajire, 2010 and Leung et al., 2014). Although the above technologies can offer capture efficiency as high as 95%, the drawback associated with them is the high energy penalty needed to obtain a pure CO_2 stream (Toftegaard et al., 2010). Consequently, collaborative efforts by different groups are being made to identify and develop alternative technologies that will greatly reduce cost of CO_2 capture (Adánez et al., 2012). One such technology is Chemical Looping Combustion (CLC).

Chemical Looping Combustion is a promising CCS technology which inherently separates CO_2 from flue gases without the energy penalty associated with other CCS technologies (Adánez et al., 2012). The carbon capture approaches - post-combustion, pre-combustion and oxy-fuel - require cost-intensive steps of active gas separation (Kanniche et al.,

2010). For instance, oxy-fuel combustion utilizes large amounts of oxygen from an energy intensive air separation unit. The work required to separate oxygen from air becomes an energy penalty for the power plant to operate with sequestration (Zhang et al., 2008). Thus, resulting in high cost and the energy penalty may reach above 7% compared with a plant without CCS (Burdyny and Struchtrup, 2010). However, in CLC, fuel is combusted using a solid containing oxygen (metal oxide) rather than air. The benefit is that the products of combustion contain mainly carbon dioxide and water, thus avoiding an additional gas separation unit (Ekström et al., 2009).

The efficient operation and adoption of CLC technology depends critically on the development of robust oxygen carriers (OC). The oxygen carrier should be able to transfer oxygen from the air reactor to the fuel reactor. Also, it is expected to have sufficient oxygen capacity, high reactivity and exhibit ability to withstand a high number of reduction-oxidation cycles without significant physical degradation or loss in performance (Adánez et al., 2012).

In the last few years, more than seven hundred oxygen carriers have been tested for chemical looping combustion. The reactivity of the oxygen carriers varies considerably and is dependent on the type of oxygen carrier, preparation method and type of inert material used as support. The materials used as supports include SiO_2, TiO_2, Al_2O_3, ZrO_2, $MgAl_2O_4$, and others. Oxygen carriers based on transition metal oxides of copper, cobalt, iron, manganese and nickel oxides have been explored because of their desirable characteristics. For instance, nickel-based oxygen carriers exhibit high oxygen capacity and reactivity. Nevertheless, drawbacks include high material cost, health, safety and environmental concerns due to its toxicity

and carbon deposition (Chiu and Ku, 2012; Luo et al., 2015 and Lyngfelt, 2015). Furthermore, it can easily be deactivated by sulphur from coal and cannot completely convert fuels to carbon dioxide and water due to thermodynamic restriction (Wang et al., 2015 and Lyngfelt, 2015). Copper-based oxygen carriers exhibit high reaction rates, high oxygen transfer capacity, low cost and poses less environmental concerns compared to other oxygen carriers (de Diego et al., 2007; Cao and Pan, 2006 and Cao et al., 2006). Iron-based oxygen carriers are non-toxic, possess high melting point, better mechanical strengths, environmentally friendly and have lower cost compared to others (Adánez et al., 2012). Iron oxide exhibit good oxidizing capability and thus is able to fully convert carbonaceous fuel to carbon dioxide and water (Luo et al., 2015). Also, pure iron oxide exhibit sintering effect at high operating temperatures and rapidly loses reactivity and its oxygen-carrying capacity after the first several redox cycles (Fan and Li, 2010). Manganese-based oxygen carriers have advantages similar to iron-based oxygen carriers. Manganese oxide is considered non-toxic and it is a relatively cheap material. In addition, its oxygen carrying capacity is higher than that of Fe-based oxygen carriers. However, the issue with Manganese-based oxygen carriers is low reactivity with fuels (Nandy et al., 2016).

Against the backdrop of the limitations associated with the oxygen carriers, research is focused on the development of new oxygen carriers with enhanced performance characteristics. The key aim is to overcome their various practical limitations and be able to meet the demands and specifications for CLC for inherent carbon dioxide capture (Adánez, 2012). Furthermore, current and ongoing research is focused on oxygen carrier screening, laboratory testing and development of production techniques.

As mentioned previously, more than seven hundred oxygen carriers have been tested for chemical looping combustion. Nevertheless, very limited works have been reported on oxygen carriers directly related to co-precipitation. Also, manganese oxide has received little attention and is less studied than nickel, copper and iron based oxygen carriers (Lyngfelt, 2015).

Studies that focused on the iron and manganese system has been reported by Rydén et al. (2011), Azimi et al. (2011) and Ksepko et al. (2012). The oxygen carriers investigated were prepared by mechanical or spray drying. Ksepko et al. (2012) examined the effect of hydrogen sulphide on supported Fe/Mn oxides in a CLC process utilizing coal-derived synthesis gas. It was suggested that there is the possibility of larger amount of active components (Fe/Mn) not well dispersed in the ZrO_2 support, thus contributing to lower reaction rates. On the other hand, the studies by Rydén et al. (2011) and Azimi et al. (2011) focused almost exclusively in the context of Chemical Looping Oxygen Uncoupling (CLOU) process, where the solid fuel is burned with gaseous oxygen released by the oxygen-carrier in the fuel-reactor. Nevertheless, there was indication that the physical stability of the examined materials was low and may need an inert support to improve stability.

It has been noted that the production method for oxygen carriers directly determines their physical properties such as mechanical strength, porosity and degree of dispersion. Moreover, these can influence the oxygen carriers' reactivity, strength and stability during consecutive CLC reduction-oxidation cycles (Guo et al., 2009). Traditional methods typically used for oxygen carrier preparations are mechanical mixing and impregnation which

fails to provide high degree of dispersion and high metal loading respectively (Fan and Li, 2010).

Although, many oxygen carriers have been tested for chemical looping combustion, very limited works have been reported on oxygen carriers directly related to co-precipitation. These few studies (mainly for nickel and copper-based oxygen carriers) typically use strong base such as potassium hydroxide as precipitating agents (Imtiaz et al., 2012 and Chuang et al., 2008). One drawback is the repetitive washing of the precipitate to remove the excess alkali ions and controlled loading of the active components may not be easily obtained (Benrabaa et al., 2012). In contrast to other co-precipitation techniques used in CLC, the procedure adapted in this work utilized aqueous ammonia as the precipitating agent. This co-precipitation procedure has been previously applied for the invention of adsorbent materials for mercury capture (Snape et al., 2010). This technique allows for materials with high surface area, high degree of dispersion and controlled metal loading to be obtained.

In conclusion, iron oxide and manganese oxide would constitute low-cost, environmentally benign oxygen carrier materials in comparison to nickel oxide. Furthermore, zirconia seems to contribute to the thermal stability of these oxygen carriers during cyclic tests (Ksepko et al., 2012). Moreover, only few works have been reported for manganese oxide and co-precipitated oxygen carriers. Consequently, to bridge this knowledge gap, it became of interest to exploit the co-precipitation technique for manganese and iron based oxygen carriers for chemical looping combustion. Hence, this thesis is a novel research on the development and detailed investigation of co-precipitated manganese oxide and iron oxide

based oxygen carriers supported on zirconia and combined zirconia-ceria for chemical looping combustion.

1.2 Aims and Objectives

The aim of this study was to

- Develop and investigate the operation of novel co-precipitated reactive and stable oxygen carriers for chemical looping combustion utilizing gaseous fuel.

The specific objectives of the project are to:

- Synthesize via the co-precipitation technique oxygen carriers based on manganese oxide and iron oxide coupled with zirconia and combined zirconia-ceria as supports.
- Perform experiments to obtain measurements for different formulations of synthetic oxygen carriers in laboratory scale reactor - Thermogravimetric Analyser (TGA)
- Characterise the chemical and physical properties of the oxygen carriers using Scanning Electron Microscopy / Energy-Dispersive X-ray Spectroscopy (SEM-EDX), X-ray Diffraction (XRD), gas pycnometer, nitrogen adsorption isotherm and relate these properties to their reactivity.
- Evaluate the performance of the oxygen carriers for conditions required by large scale systems.
- Obtain kinetic parameters (for the most promising oxygen carrier) that will be of importance in the design of a chemical looping system.

1.3 Thesis Structure

This thesis is divided into nine chapters and the layout is as follows:

- Chapter 1 presents an introduction to the research project by providing an overview of the background, the rationale, aim and objectives of the study.
- Chapter 2 presents pertinent references to some of the literature on global warming, carbon capture and storage technologies, chemical looping combustion processes. Also included, is a detailed review of relevant literatures on oxygen carriers for chemical looping combustion.
- Chapter 3 highlights the description of the experimental techniques and materials employed in this study.
- Chapter 4 analyses and discusses results on monometallic oxygen carriers.
- Chapter 5 and 6 presents results and discussion on the co-precipitated bimetallic oxygen carriers supported on zirconia.
- Chapter 7 discusses results on the co-precipitated bimetallic oxygen carriers on zirconia and ceria as combined support.
- Chapter 8 is a presentation on kinetics.
- Chapter 9 presents the conclusions from this study and recommendations for future work.

2 LITERATURE REVIEW

2.1 Climate Change

It has been reported that warming of the climate system is unequivocal, and since the 1950s, many of the observed changes are unprecedented over decades to millennia. Also, since 1850, each of the last three decades has been successively warmer at the Earth's surface than any preceding decade (Figure 2.1). In the Northern Hemisphere, it is reported that 1983–2012 was likely the warmest 30-year period of the last 1400 years of the instrumental record of global surface temperature (IPCC, 2013).

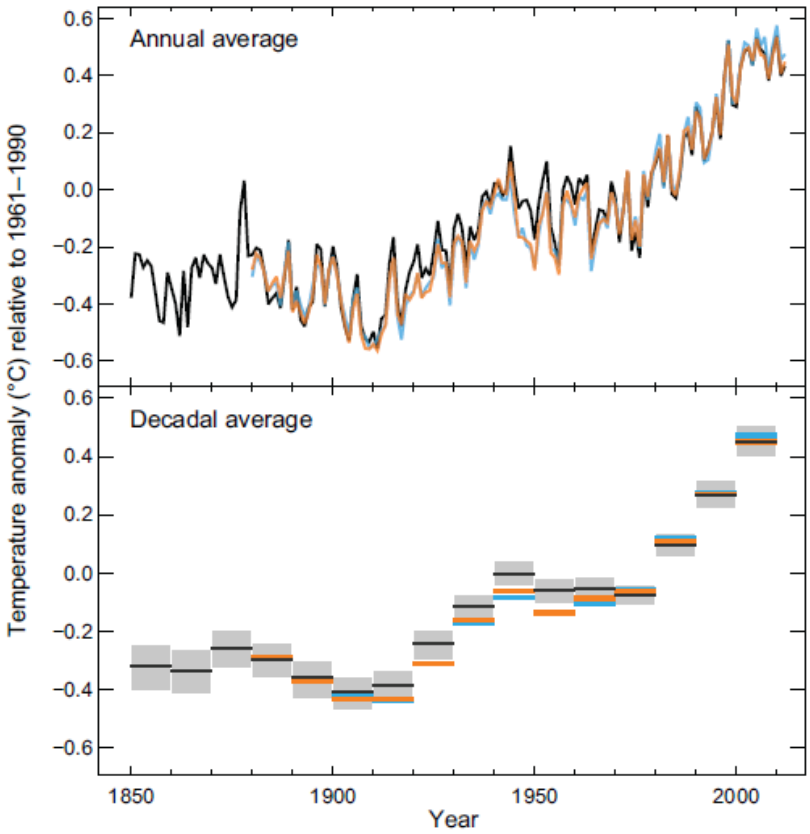

Figure 2.1: Observed globally averaged combined land and ocean surface temperature anomaly 1850–2012 (IPCC, 2013)

The Intergovernmental Panel on Climate Change (2013) reported that regional climate changes, particularly temperature increases have been observed to affect many natural systems. Reports indicate that the atmosphere and ocean have warmed, the amounts of snow and ice have diminished, sea level has risen, and the concentrations of greenhouse gases have increased. Also, over the last two decades, the Greenland and Antarctic ice sheets have been losing mass.

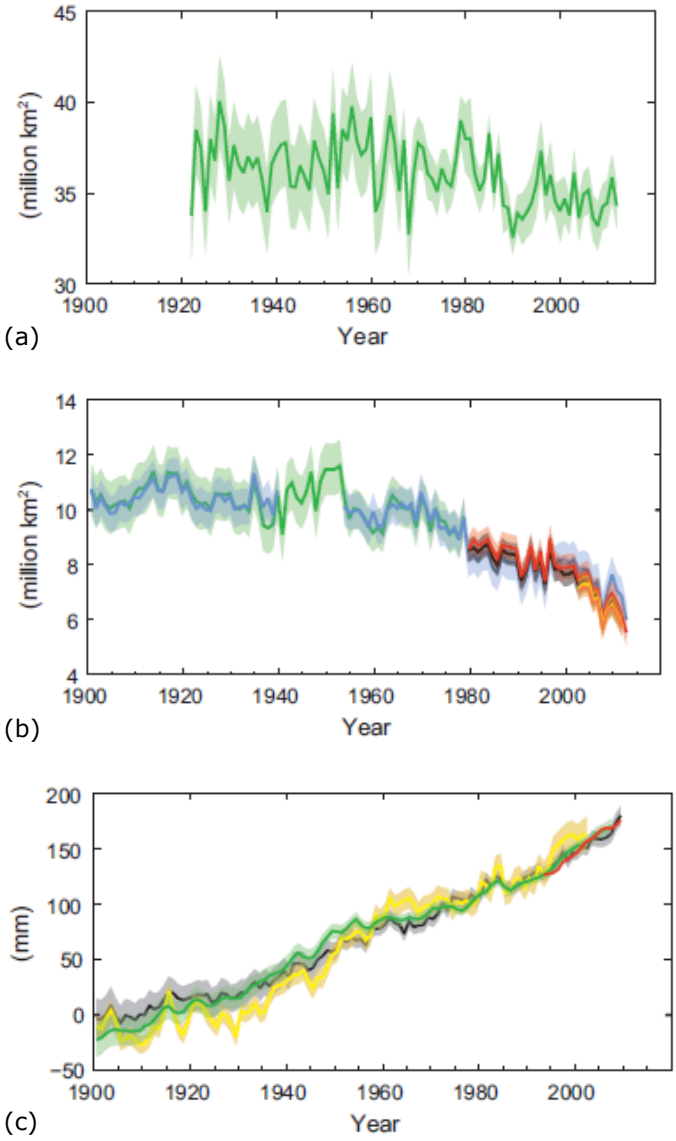

Figure 2.2 Multiple observed indicators of a changing global climate: (a) Northern Hemisphere spring snow cover. (b) Arctic summer sea ice extent. (c) Global average sea level change (IPCC, 2013).

There is continued shrinkage of glaciers, and Arctic sea ice and Northern Hemisphere spring snow cover have continued to decrease in extent. Furthermore, the rate of sea level rise since the mid-19th century has been larger than the mean rate during the previous two millennia. Over the period 1901 to 2010, global mean sea level rose by 0.19 [0.17 to 0.21] m (Figure 2.2). In addition, the most robust global changes in climate extremes are seen in measures of daily temperature and there is strong evidence that warming has led to changes in temperature extremes, including heat waves since the mid-20th century and probably increases in heavy precipitation (IPCC, 2013).

2.2 Causes of Climate Change

The above changes have been caused mainly by the increased concentration of greenhouse gases (GHG) emitted to the atmosphere. In addition, most of the observed increase in global average temperature for the past 50 years has been attributed to anthropogenic GHG concentrations. It is stated that since pre-industrial times, the global GHG emissions due to human activities have grown with an increase of 70% between 1970 and 2004. The GHG includes methane (CH_4), carbon dioxide (CO_2), nitrous oxide (N_2O), hydro-fluorocarbons (HFCs), perfluorocarbons (PFCs) and sulphur hexafluoride (SF_6). However, it has been observed that CO_2 concentration is higher in comparison to other GHG (IPCC, 2007).

The International Energy Agency (IEA) noted that among the many human activities that produce greenhouse gases, energy emissions, mostly CO_2, account for the largest share of global GHG emissions as shown in Figure 2.3. Furthermore, compared to the rather steady level of the pre-industrial era (about 280 ppmv), the global CO_2 concentrations in the atmosphere

have been increasing significantly over the past century. The global CO_2 concentration increased to 390 ppm in 2010 (Dlugokencky and Tans, 2012). In the last ten years with an average growth of 2 ppmv/year, the 2013 concentration of CO_2 (396 ppmv) was about 40% higher than in the mid-1800s (IEA, 2014).

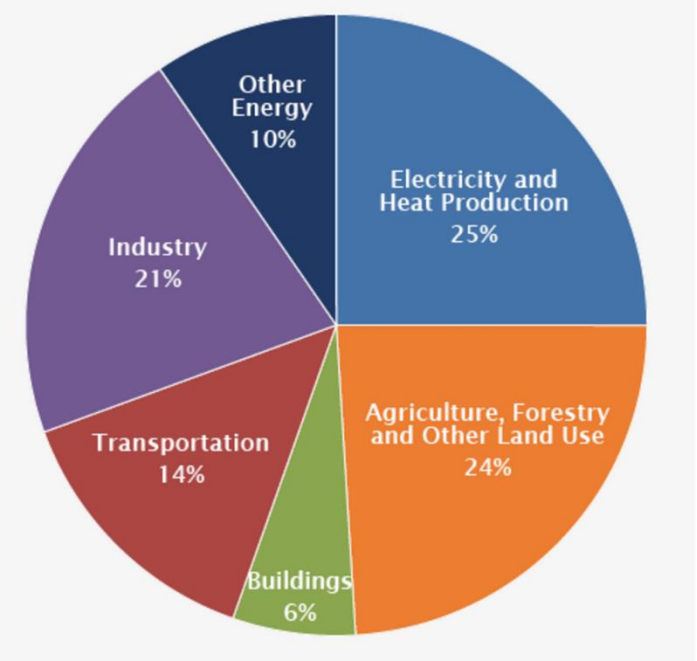

Figure 2.3: Global greenhouse gas emissions by economic sector based on global emissions from 2010 (EPA, 2016)

The increased atmospheric concentrations of CO_2 have been attributed primarily to the combustion of fossil fuels (Gitay et al., 2002). Also, IEA (2014) stated that despite the growth of non-fossil energy such as nuclear and hydropower (considered as non-emitting), the share of fossil fuels within the world energy supply is relatively unchanged over the past 41 years. Moreover, in 2012, fossil fuel still accounts for over 80% of the world energy supply. As a result of dependency on fossil fuel for energy production, the annual CO_2 emissions from fossil fuel combustion have dramatically increased from near zero to almost 32 $GtCO_2$ in 2012 as shown in Figure 2.4 (IEA, 2014).

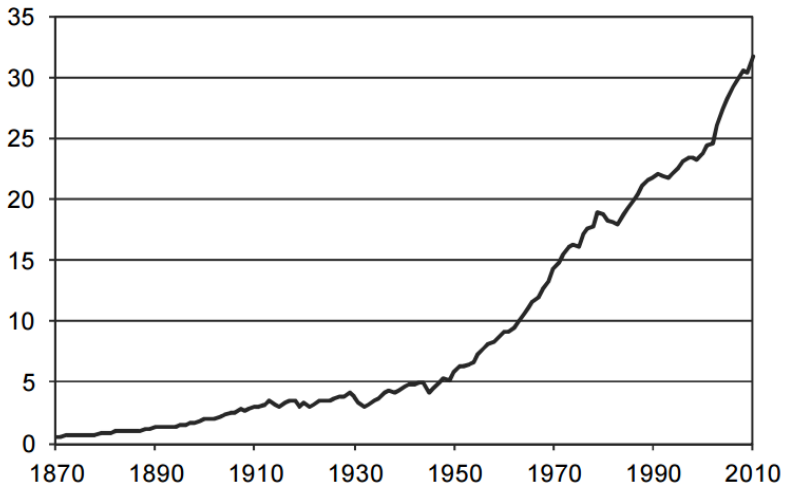

Figure 2.4: Trend in CO_2 emissions from fossil fuel combustion (IEA, 2014).

The continuous increase in CO_2 concentration in the atmosphere has rendered it the focus of attention towards solving the challenge of excessive global warming (Yamasaki, 2003). To avoid most disastrous changes to the Earth's climate, the GHG concentrations need to be stabilized and concentration of CO_2 must not exceed 450 ppm (or rise more than 15% over present concentrations). Also, the average increase in global average atmospheric temperature would have to be limited to below 2^{o}C. Consequently, a reduction in greenhouse emissions became of paramount interest internationally and in 1997, the Kyoto Protocol was drafted in the United Nations Framework Convention on Climate Change (UNFCCC), (UN, 1998). After ratification in 2005, the developed countries agreed to reduce their mean GHG emissions to 5.2% relative to 1990 levels over the period 2008-2012 (Dlugokencky and Tans, 2012). Recently, a second commitment period, which will run from 2013 to 2020 has been agreed upon by thirty-eight countries. These countries have decided to take commitments to curb domestic emissions and one option to comply with their Kyoto Protocol targets is by reducing emissions from fossil fuel combustion (IEA, 2014).

Projections of energy demand to 2035 indicate that fossil fuels (oil, coal and natural gas) account for 53% of the increase in energy demand and will continue to supply the bulk of global energy consumption (IEA, 2010). In order to meet the increasing energy demand as well as reduce net CO_2 emissions to the atmosphere, the following technological options were proposed (IPCC, 2005):

- Reduce energy consumption by increasing the efficiency of energy conversion and/or utilization.
- Reduce carbon intensity in the energy supply which comprise of switch to less carbon intensive fuels example, nuclear energy and increase the use of renewable energy sources such as biofuels, wind and solar power.
- Sequester CO_2 by enhancing biological absorption capacity in forest and soils.

From the above reports, the need for technological options to reduce CO_2 emission to the atmosphere has been necessitated by the global climate change. An overview of Carbon Capture and Storage (CCS) as one option to reduce the emission of CO_2 to the atmosphere and thereby mitigate the effect of climate change will be the focus of the following Section 2.3.

2.3 Carbon Capture and Storage (CCS)

There are unmistakable signs that the much-needed global energy transition is in progress. Nevertheless, this is not yet at a pace that leads to a lasting reversal of the trend of rising CO_2 emissions (IEA, 2015). Also, none of the above-mentioned technology options or probably their sum efforts will produce the desired low levels of CO_2 emissions. Consequently, CO_2 Capture and Storage (CCS) has become an additional option needed to

attain the desired low levels of CO_2 emissions (IPCC, 2005). International Energy Agency (IEA) analysis suggests that CCS will play a fundamental role in global, least-cost efforts to limit global warming, contributing around one-fifth of required emissions reductions by 2050 (IEA 2012).

The CCS technology involves capture of concentrated CO_2 stream from industrial and energy related sources, its transportation and long-time safe storage away from the atmosphere. An overview of the CO_2 capture is presented in Section 2.3.1.

After capture, CO_2 would be transported in high pressure pipelines or ships could be used for its long-distance transport to the storage site. On economic grounds, one alternative is to locate power stations close to electricity demand and from there transport the CO_2 to the storage site. Although, CO_2 is inert, it can pose immediate dangers to human health at concentrations of 7-10 Vol % or higher (IEA, 2001; IPPC, 2005).

In terms of CO_2 storage, this involves injection of CO_2 into the deep subsurface for permanent storage (Meyer, 2011). It is estimated that available fossil fuel resources contain carbon equivalent emissions of about 20000-25000 GTonnes of CO_2, (Golmen, 1999; Lindeberg, 2003). Consequently, due to the considerations of space, time and safety, possible storage locations for CO_2 as shown in Figure 2.5 includes deep oceans, oil fields, gas fields, deep coal beds and in aquifers.

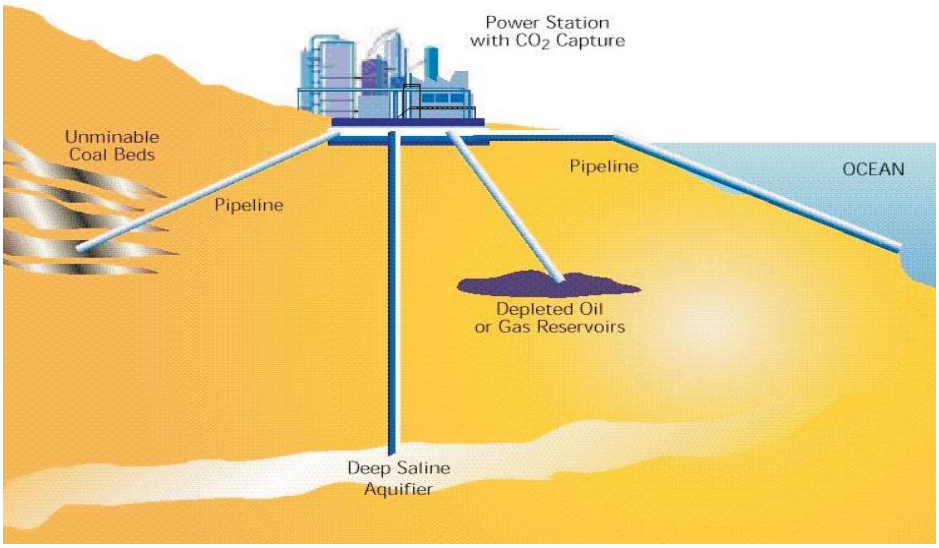

Figure 2.5: Options for storage of CO_2 (IEA, 2001).

2.3.1 Carbon Dioxide Capture Techniques

The three main technologies being developed in order to obtain CO_2 in the pure stream from power production units are post-combustion, oxy-fuel combustion and pre-combustion processes (Benson and Surles, 2006; IPCC, 2005).

In post-combustion capture, CO_2 is removed from the flue gas after combustion. The flue gas is passed through post combustion gas separation and capture technologies to separate/capture most of the CO_2. The technologies based on chemical absorption appear to be best adapted to this separation than other technologies such as adsorption, membranes and cryogenic separation (Thiruvenkatachari et al., 2009; Kanniche et al., 2010; Leung, 2014).

In the pre-combustion process, the fuel is pre-treated before combustion. The treatment relates to the gasification of coal or reforming of natural gas

to form syngas, which consist mainly of carbon monoxide and hydrogen. The syngas undergo the water-gas shift reaction with steam to yield hydrogen and CO_2. The CO_2 can then be separated using a physical absorbent (Thiruvenkatachari et al., 2009; Kanniche et al., 2010; Lee et al., 2010 and Leung, 2014).

In oxy-fuel combustion, oxygen (typically greater than 95% purity) instead of air is used for the combustion of fuel with recycling of flue gases. The use of oxygen reduces the amount of nitrogen present in the exhaust gas which affects the subsequent separation process. Furthermore, recycling the flue gas generates gas consisting mainly of sequestration-ready CO_2 and water (Leung et al., 2014; Toftegaard et al., 2010 and Wall et al., 2009)

Although these technologies illustrated in Figure 2.6 can offer capture efficiency as high as 95%, the drawback associated with them is the high energy penalty needed to obtain a pure CO_2 stream (Toftegaard et al., 2010). This gives rise to reduced energy efficiency of the processes and increase in the cost of the energy (Lyngfelt, 2001; de Visser et al., 2008; ICF, 2009; Olajire, 2010; Toftegaard et al., 2010). Consequently, collaborative efforts by different groups are being made to identify and develop alternative technologies that will greatly reduce cost of CO_2 capture (Adánez et al., 2012). Chemical looping combustion (CLC) has emerged as a promising technology to reduce the cost of CO_2 capture (Ekström et al., 2009). Further details on CLC are presented in the next section.

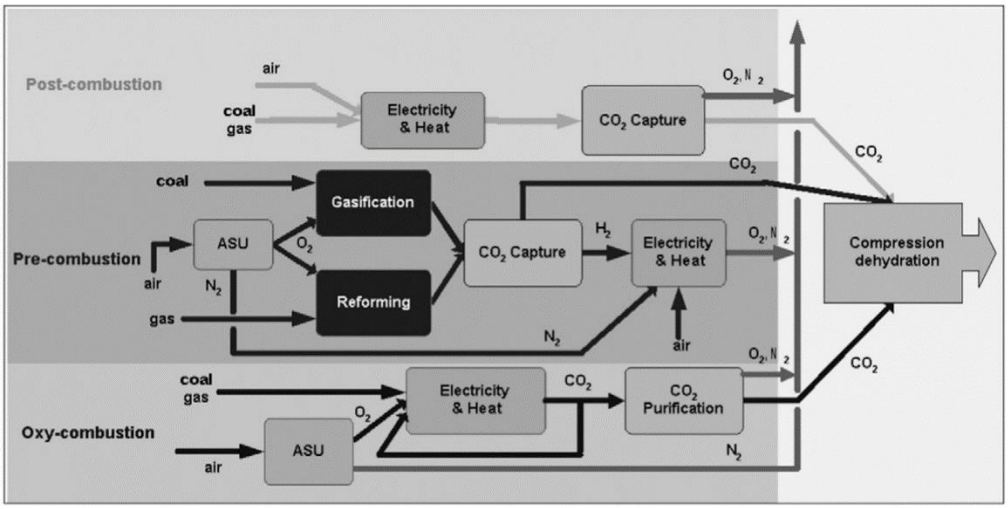

Figure 2.6: The three carbon dioxide processes (Kanniche et al., 2010)

2.4 Chemical Looping Combustion (CLC)

Chemical looping combustion (CLC) has emerged as an attractive option for carbon dioxide capture since CO_2 is inherently separated from the other flue gas. Consequently, it has significant advantage over other CO_2 capture technologies because it overcomes the energy penalty associated with other technologies for CO_2 capture and so reduces the cost of CO_2 capture. The current estimated efficiency penalty for post-combustion CCS and oxy-fuel combustion is approximately 12% and 10% respectively. The target is to reduce this efficiency penalty to about 8% by 2020. However, the efficiency losses for CLC range from 3% to 4% (Fennell, 2015). In addition, if environmental impacts are taken into consideration, CLC will be preferred to other CO_2 capture options (Petrakopoulou et al., 2011; Fan and Li, 2010).

The difference between CLC and conventional combustion is the route by which oxygen is introduced into the reaction. In conventional combustion, the fuel is in immediate contact with the oxidizing agent. However, in chemical looping combustion, the process is split into two gas-solid

reactions; oxidation of metal or (metal oxide) by air and reduction of metal oxide by fuel giving CO_2 and H_2O separate from other flue gas components. The flue gas from the air reactor consists of nitrogen and excess oxygen which are harmless. Also, given that there is no flame in the process and the relatively low reaction temperature (1073 K-1473 k), there is none or very little thermal NO_x formation (Linderholm et al., 2010; Boot-Handford et al., 2014).

The CLC process can be based on interconnected fluidized beds, consisting of an air reactor, fuel reactor and metal oxide (oxygen carrier) which undergoes redox reactions while it circulates between the reactors (Mattisson et al., 2001) as shown in Figure 2.7.

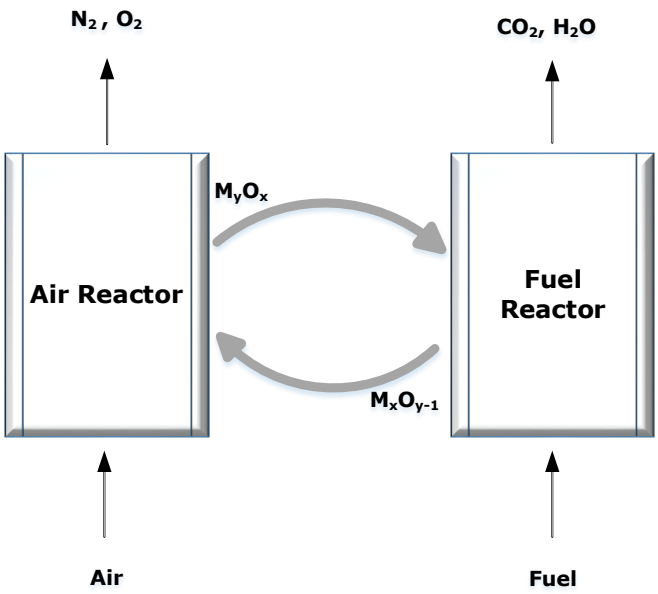

Figure 2.7: Schematic view of Chemical Looping Combustion (CLC).

The fuel typically natural gas, syngas from gasification of coal or refinery gas is oxidized by the oxygen carrier in the fuel reactor according to reaction 1. The reduced metal oxide particles are returned to the air reactor, where they are regenerated to the oxidized state by reacting with

oxygen from the air as shown in reaction 2. The flue gas from the fuel reactor contains CO_2 as shown in the net reaction 3 which can be obtained after condensation of water from the gaseous product mixture (Lyngfelt et al., 2001; Linderholm et al., 2010).

$$\text{Fuel reactor: } (2n+m)M_yO_X + C_n H_{2m} \rightarrow (2n+m)M_yO_{x-1} + mH_2O + nCO_2 \quad (1)$$

$$\text{Air reactor: } (2n+m)M_yO_{X-1} + \left(n + {}^{1}/_{2}\, m\right)O_2 \rightarrow (2n+m)M_yO_x \quad (2)$$

$$\text{Net reaction: } C_nH_{2m} + \left(n + {}^{1}/_{2}\, m\right)O_2 \rightarrow mH_2O + nCO_2 \quad (3)$$

The net reaction and heat released are identical to conventional combustion where the oxygen is in direct contact with the fuel. Reaction 1 can be either endothermic or exothermic depending on the type of fuel and the Me/MeO-pair used as an oxygen carrier while reaction 2 is exothermic. The overall CLC process, in which the metal oxide cycles between oxidized and reduced states, is exothermic (Lyngfelt et al., 2001; Jerndal et al., 2006; Linderholm et al., 2010; Siriwardane, 2016; Pröll and Hofbauer, 2011).

In summary, it is evident that the availability of suitable oxygen carrier particles is crucial to the successful application of the chemical looping process. In Section 1.1, it was noted that current and ongoing research is focused on oxygen carrier screening, laboratory investigation and development of synthesis method. Therefore, highlights on oxygen carriers for CLC application and relevant discussions on the application of chemical looping technology will be the focus of the following sections.

2.5 Applications of Chemical Looping Technology

Chemical looping is regarded as a highly versatile process scheme with the potential for application in a wide range of processes besides combustion. One of these processes is the partial oxidation process in which oxidation of the fuel is controlled to yield synthesis instead of carbon dioxide and water. Another process is the reforming reactions, where the air supplied to the oxidizer reactor is substituted by either steam or carbon dioxide in order to produce high purity hydrogen or carbon monoxide respectively (Bhavsar et al., 2014). Moreover, syngas and hydrogen are considered core chemical intermediates to produce other valuable products. The inherent product separation associated with these processes renders them more advantageous compared to the conventional counterpart processes (Luo et al., 2015). Apart from power production, one field of application of chemical looping technology is in industrial steam generation from natural gas. If the economic benefit of CO_2 capture is considered, the CLC boilers can replace the advanced technology through steam generators with basically no reduction in boiler efficiency (Lyngfelt, 2013; Pröll, 2015 and Boot-Handford et al., 2014).

Chemical looping can be applied to combustion of gaseous and solid fuels for power generation. The two main power cycles widely used in power generation are the Rankine and Brayton cycles (Figures 2.8 and 2.9). In these cycles, thermal energy is converted into mechanical energy, which is then converted to electrical energy. The gas turbine (Brayton cycle) efficiently uses high temperature gases from a combustion process, but discharges its exhaust gas at a relatively high temperature which is wasted heat/energy.

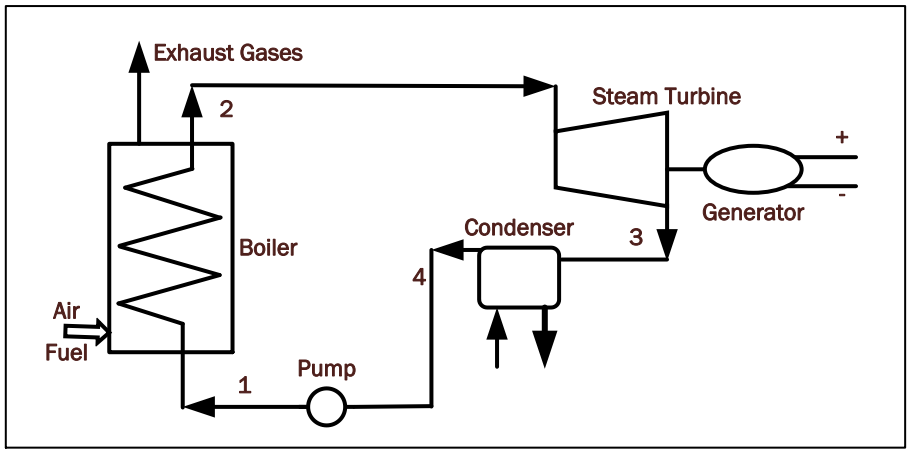

Figure 2.8: Schematic of a simple steam power plant (Ebaid and Al-hamdan, 2015).

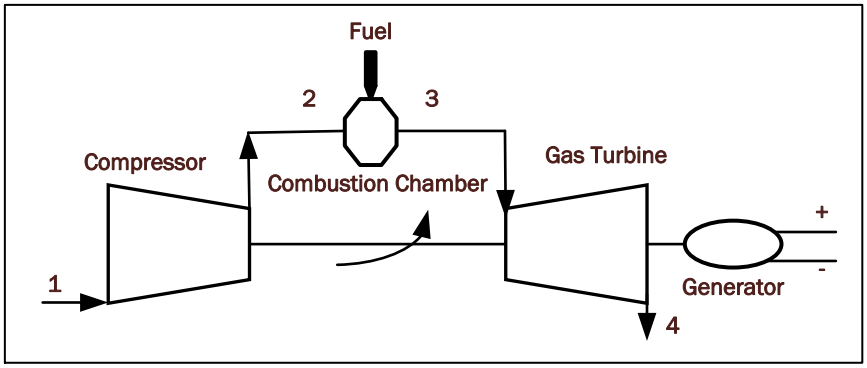

Figure 2.9: Schematic of a simple gas turbine power plant (Ebaid and Al-hamdan, 2015).

On the other hand, the steam turbine (Rankine cycle), is not able to reach the high temperature of the gas turbine due to material constraints. A combination of the two cycles (such as the Combined Cycle Gas Turbines) allows for improved overall efficiency of the power plant (Miller, 2011). Further information on these power cycles is presented in Table 2.1.

Table 2.1: The main thermodynamic cycles (Yu et al., 2015).

Power cycles	Major advantages	Major disadvantages	Thermal efficiency
Gas turbine cycle	Simple; low cost; high temperature condition	Performance affected by the fuel type	Higher than 30%
Steam cycle	Simple; high conversion efficiency	Low operating temperature	>50% when work as assisting
Combined cycle	Good performance	High cost; complex structure	Over 50%

For power production from natural gas, advanced Combined Cycle Gas Turbines (CCGT) system can reach a net efficiency of nearly 60% without CO_2 capture. Furthermore, CCGT is more efficient than a CLC system, which, unless pressurised, is limited to the steam-cycle efficiency (Boot-Handford et al., 2014). Nevertheless, Hoffmann et al. (2009) conducted a performance analysis on advanced combined cycle gas turbine plants operated by natural gas with a pre-combustion CO_2 capture system and obtained a CO_2 capture efficiency of 80%.

For a high overall efficiency of electricity production, options being considered for CO_2-ready electricity generation Include: pressurized CLC in combination with gas turbine combine cycles, and CLC for direct combustion of coal in combination with steam cycles (Pröll, 2015). The studies on the energy analysis of this form of CLC are rare. Nevertheless, if CO_2 capture is considered, this type of combustion leads to beneficial exergy efficiencies in the system (Wolf et al., 2005). Moreover, thermal efficiency as high as 52–53% in a combined cycle CLC plant operating at 1473 K in the air reactor and 13 bars has been reported by Wolf et al. (2001). This denotes 5% more efficient process than a natural gas with a

combined cycle system with advanced technology for CO_2 capture (Wolf et al., 2001).

Although more development work is needed, the application of chemical looping in power generation is highly promising. CLC technology provides a unique potential for avoiding the large costs associated with active gas separation. Furthermore, the flexibility of this process in terms of usable fuels and desired end products will continue to drive the rapid development of this technology over the near future (Linderholm and Lyngfelt, 2014 and Bhavsar et al., 2014).

2.6 Thermodynamic Considerations

2.6.1 Thermodynamics of Oxygen Carriers

In chemical-looping combustion, it is essential that solid compounds used as oxygen carriers for CLC should be able to show high conversion of the fuel to carbon dioxide and water. The redox behaviour of the oxygen carrier is largely determined by the thermochemical properties of its primary metal oxide. The oxides of Cu, Ni, Co, Fe and Mn were identified with favourable thermodynamics for CH_4, H_2 and CO conversion (Jerndal et al., 2006).

The equilibrium constant for the reduction reaction with H_2 and CO with different redox systems showed different behaviours as presented in Figure 2.10. At typical CLC conditions, CuO-Cu, Mn_3O_4-MnO and Fe_2O_3-Fe_3O_4 with equilibrium constants higher than 10^3 showed almost complete conversion to CO_2 and H_2O. Moreover, in the Fe_2O_3 reduction, Fe_3O_4 usually appears as an intermediate product and further reduction of Fe_3O_4 to FeO results in

low conversion of gas. The redox systems with an equilibrium constant of about 10^2 yield small amounts of CO and H_2. For NiO oxygen carriers, a conversion in the range 99 - 99.5% for H_2 and 98 - 99% for CO is obtained at equilibrium conditions. Furthermore, for CoO/Co system, thermodynamics is less favourable with maximum conversion of 95 - 97% for H_2 and 87 - 95% for CO. Although, full conversion could be obtained in the redox system Co_3O_4-CoO oxidation to Co_3O_4 is not favoured in air at temperatures higher than 880°C. Also, redox system $CaSO_4$-CaS has also been considered to have similar thermodynamic limitations for conversion of H_2 and CO as NiO (Adánez et al., 2012).

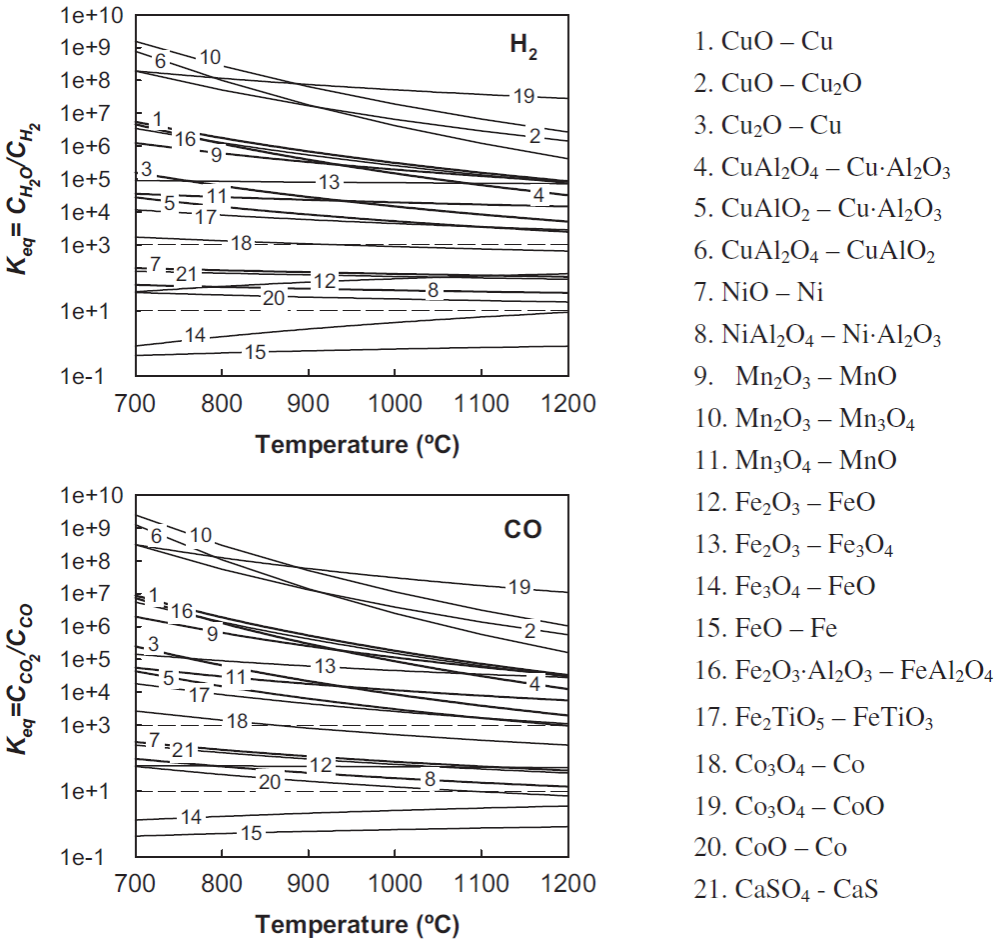

Figure 2.10: Equilibrium constant, K_{eq}, for the reduction reaction with H_2 and CO with different redox systems (Adánez et al., 2012).

In addition, the application of fuels, which contains high amount of methane in CLC could yield variable amounts of CO_2, H_2O, CO, and H_2 depending on the redox system. For temperatures of 900 to 1600 K, the gas yield of CH_4 to CO_2 for the different oxide systems is shown in Figure 2.11. The conversion of CH_4 to CO_2 is complete for redox oxide pairs Cu_2O-Cu, Mn_3O_4-MnO and Fe_2O_3-Fe_3O_4, whereas the NiO-Ni system gives somewhat lower gas yields in comparison to Cu, Mn and Fe (Mattisson and Lyngfelt, 2001).

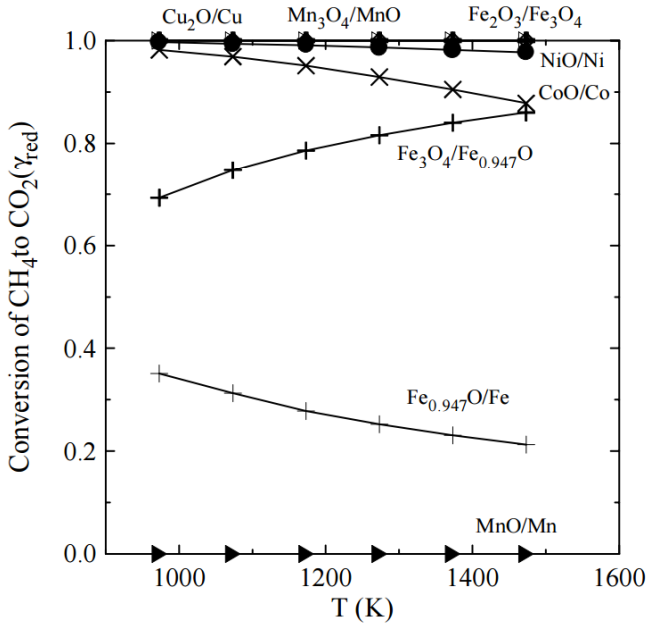

Figure 2.11: The gas yield, (γ_{red}) of CH_4 to CO_2 vs temperature for different metal oxide systems (Mattisson and Lyngfelt, 2001).

The Gibbs free energy (ΔG) variation with temperature for CO and oxygen carrier reactions calculated from HSC Chemistry was reported by Luo et al., (2015) and is illustrated in Figure 2.12. During the oxygen carrier reduction, for complete conversion of fuels to CO_2 and H_2O, the metal oxide/sulphate lines must be located at lower positions as shown in Figure 2.12. Somewhat in agreement with thermochemical information provided earlier, it was concluded that materials based on Cu-, Mn-, Co-, Fe-, and

Ni-oxides and Ca-based alkaline earth sulphates materials can be used for CLC applications.

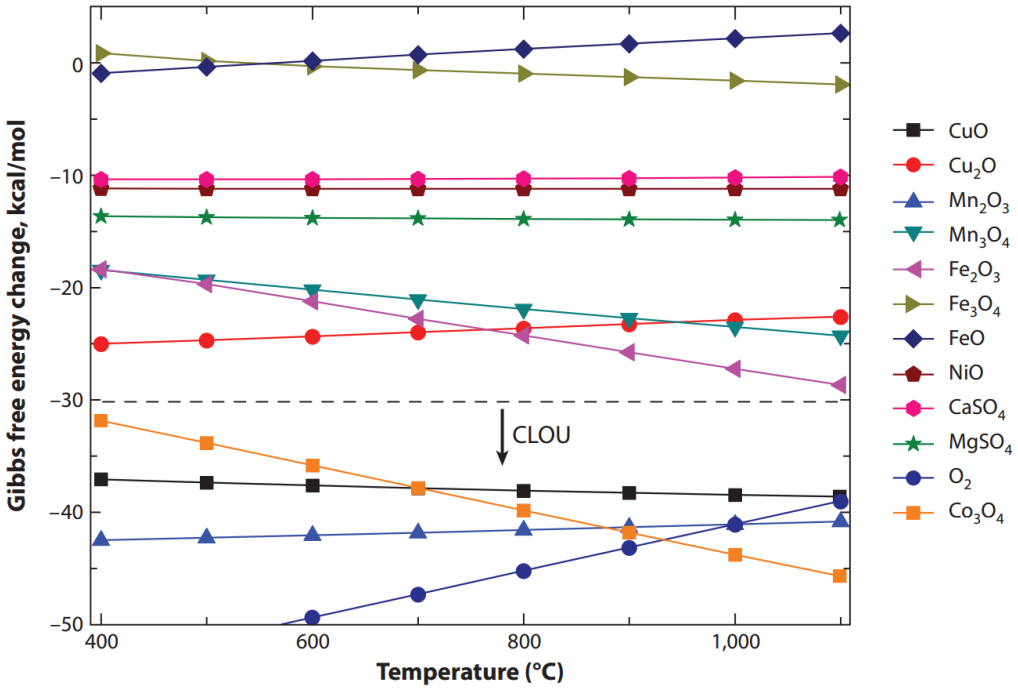

Figure 2.12: Gibbs free energy change of oxygen carrier reduction with 1 mol of CO (Luo et al., 2015).

The Chemical Looping with Oxygen Uncoupling (CLOU) process is one approach for the use of the CLC technology with solid fuel. The CLOU process is based on the use of an oxygen carrier which releases gaseous oxygen in the fuel reactor, thereby allowing the solid fuel to burn with gas-phase oxygen (Figure 2.13). Thus, the slow gasification step is avoided giving a much faster solid conversion compared to normal CLC where solid fuel reacts directly with the oxygen carrier without any release of gas phase oxygen.

Furthermore, in comparison to the normal CLC, the CLOU process operating conditions for the air-reactor is constrained due to the thermodynamic limitations of the oxygen-carrier oxidation. Thus, only

those metal oxides that have a suitable equilibrium partial pressure of gas phase oxygen at temperatures of interest for combustion has been identified as CLOU materials (Figure 2.14 and Figure 2.13).

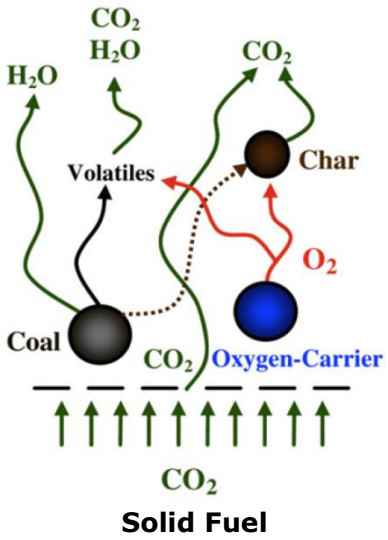

Figure 2.13: Reaction scheme for CLOU in the fuel reactor for CLOU (Adanez et al., 2012)

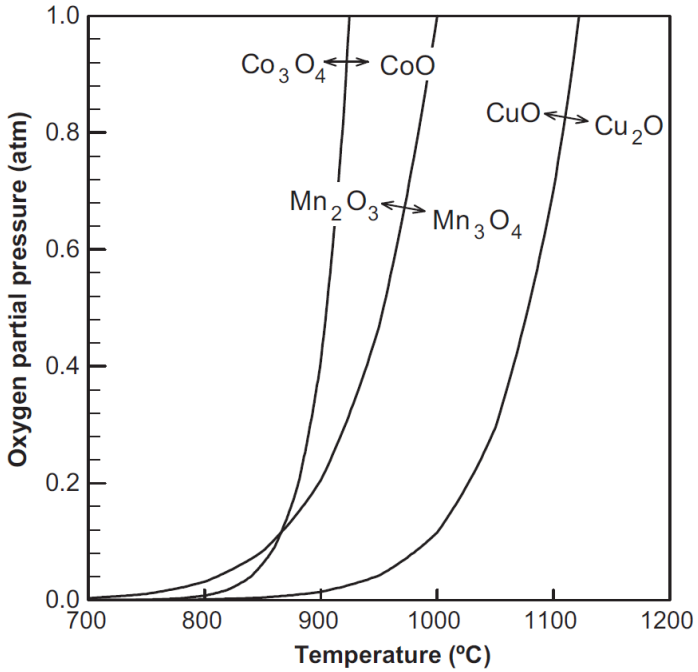

Figure 2.14: Equilibrium partial pressure of gas-phase O_2 over the metal oxide systems CuO/Cu_2O, Mn_2O_3/Mn_3O_4 and Co_3O_4/CoO as a function of temperature (Adánez, et al., 2012).

Mattisson et al. (2009) reported that these systems which include CuO-Cu_2O, Mn_2O_3-Mn_3O_4 and Co_3O_4-CoO have the capacity to release oxygen at the fuel-reactor at high temperature in the gas phase through the following reversible reactions:

$$4CuO \leftrightarrow 2Cu_2O + O_2(g) \qquad \Delta H_{850} = 263.2\ \mathrm{KJ/mol\ O_2} \qquad 3a$$

$$6Mn_2O_3 \leftrightarrow 4Mn_3O_4 + O_2(g) \qquad \Delta H_{850} = 193.9\ \mathrm{KJ/mol\ O_2} \qquad 3b$$

$$2Co_3O_4 \leftrightarrow 6CoO + O_2(g) \qquad \Delta H_{850} = 408.2\ \mathrm{KJ/mol\ O_2} \qquad 3c$$

For Cu- and Mn-based oxygen-carriers, the reactions with carbon taking place in the fuel-reactor are exothermic whereas the reaction of carbon with Co_3O_4 is endothermic. Consequently, for Cu- and Mn-based oxygen-carriers, it is possible to operate at lower temperatures in the air-reactor, which results in a significantly lower partial pressure of O_2 at equilibrium conditions at the air-reactor exit. Contrariwise, for Co_3O_4 oxygen carriers, the temperature in the air-reactor must be higher than that in the fuel-reactor and higher than the temperature required when Cu- or Mn-based oxygen-carriers are used (Adánez, et al., 2012).

A thermodynamic analysis of combined oxygen carriers for CLOU by Rydén et al. (2014) show that the ternary system Mn–Fe–O, has properties which renders it interesting for oxygen carrier applications. The binary phase diagram of the $(Mn_yFe_{1-y})O_x$ system (Figure 2.15) shows that hematite (Fe_2O_3) and bixbyite $(Mn_yFe_{1-y})_2O_3$ are favoured at lower temperature, while spinel phases $(Mn_yFe_{1-y})_3O_4$ are favoured at higher temperature. For chemical-looping with oxygen uncoupling, the reaction of interest is transition between bixbyite and spinel via the following reaction:

$$6(Mn,Fe)_2O_3 \leftrightarrow 4(Mn,Fe)_3O_4 + O_2 \qquad 3d$$

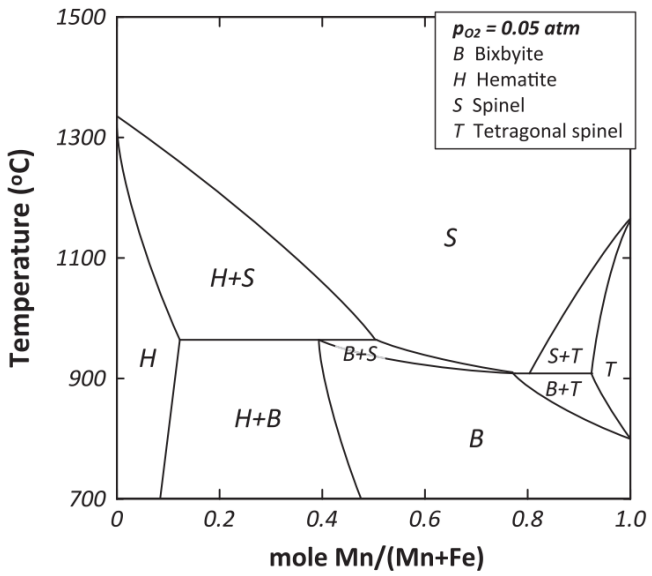

Figure 2.15: Binary phase diagram of $(Mn_yFe_{1-y})O_x$ in an atmosphere with O_2 partial pressure of 0.05 atm (Rydén et al., 2014).

There are inconsistencies in the literature with respect to thermodynamic data for combined oxides of iron and manganese (Crum et al., 2009). Nevertheless, it is interesting to report that the results obtained from the X-ray diffraction measurements confirm that the phases present in the co-precipitated combined oxides of iron and manganese developed in this work agrees quite well with the phase diagram by Rydén et al. (2014). Hence, the results reported in this study for the co-precipitated oxygen carriers of manganese and iron oxides gives an accurate content of the metal oxide products and represent the system's behaviour for chemical looping combustion.

To further aid the understanding of the metal oxide systems in this study, the physical properties of manganese oxide and iron oxide are presented in Table 2.2. Also, the values of standard heat of combustion for Mn and Fe redox systems were calculated and are presented in Section 2.6.2.

Table 2.2: Physical properties of metal oxides of iron and manganese (Source: Yaws, 2012; 2013; 2014; and Knovel, 2008).

Chemical name	Chemical formula	Molecular weight (g/mol)	Solid density (g/mL)	Melting point (°C)
Iron (II, III) oxide	Fe_3O_4	231.5	5.17	1597
Iron (III) oxide	Fe_2O_3	159.7	5.24	1538
Iron(II) oxide	FeO	71.9	5.7	1377
Manganese (II, III) oxide	Mn_3O_4	228.8	4.84	1705
Manganese (IV) oxide	MnO_2	86.94	5.08	535
Manganese (II) oxide	MnO	70.94	5.37	1840-1850
Manganese (III) oxide	Mn_2O_3	157.9	4.89	871-887

2.6.2 Heat of Combustion for Iron and Manganese Oxide Redox Systems

In this work, the combustion enthalpies for Mn_3O_4/MnO and Fe_2O_3/FeO redox pair (oxygen carriers) using hydrogen, methane and carbon as fuel have been calculated using thermodynamic data from (NIST, NIST-JANAF Thermochemical Tables) and presented in Equations 4 to 21. As previously highlighted, the net chemical reaction and heat released in the CLC process is identical to conventional combustion.

Mn_3O_4/MnO Redox System:

Reactant Gas: Hydrogen

Fuel reactor: $Mn_3O_4(s) + H_2(g) \rightarrow 3MnO(s) + H_2O(l) \quad \Delta H_r^{\ominus} = -53.5$ KJ/mol (4)

Air reactor: $^1/_2\,[6MnO(s) + O_2(g) \rightarrow 2Mn_3O_4(s)] \quad \Delta H_o^{\ominus} = {}^1/_2\,[-464.6]$

$= -232.3$ KJ /mol (5)

Net reaction: $H_2(g) + {}^1/_2\,O_2(g) \rightarrow H_2O(l) \quad \Delta H_c^{\ominus} = -285.8$ KJ/mol (6)

Reactant Gas: Methane

Fuel reactor: $4Mn_3O_4(s) + CH_4(g) \rightarrow 12MnO(s) + CO_2(g) + 2H_2O(l)$

$\Delta H_r^{\ominus} = 38.6$ KJ/mol (7)

Air reactor: $2[6MnO(s) + O_2(g) \rightarrow 2Mn_3O_4(s)] \quad \Delta H_o^{\ominus} = 2[-464.6]$

$= -929.2$ KJ/mol (8)

Net reaction: $CH_4(g) + 2O_2(g) \rightarrow CO_2(g) + 2H_2O(l) \quad \Delta H_c^{\ominus} = -890.6$ KJ/mol (9)

Reactant Fuel: Carbon

Fuel reactor: $2Mn_3O_4(s) + C(s) \rightarrow 6MnO(s) + CO_2(g) \quad \Delta H_r^{\ominus} = 70.9$ KJ/mol (10)

Air reactor: $6MnO(s) + O_2(g) \rightarrow 2Mn_3O_4(s) \quad \Delta H_o^{\ominus} = -464.6$ KJ/mol (11)

Net reaction: $C(s) + O_2(g) \rightarrow CO_2(g) \quad \Delta H_c^{\ominus} = -393.7$ KJ/mol (12)

Fe_2O_3/Fe_3O_4 Redox System:

Reactant Gas: Hydrogen

Fuel reactor: $3Fe_2O_3(s) + H_2(g) \rightarrow 2Fe_3O_4(s) + H_2O(l) \quad \Delta H_r^{\ominus} = -49.6$ KJ/mol (13)

Air reactor: $^1/_2\,[4Fe_3O_4(s) + O_2(g) \rightarrow 6Fe_2O_3(s)] \quad \Delta H_o^{\ominus} = {}^1/_2\,[-471.6]$

$= -235.8$ KJ/mol (14)

Net reaction: $H_2(g) + {}^1/_2\, O_2(g) \rightarrow H_2O(l)$ $\Delta H_c^{\ominus} = -285.4$ KJ/mol (15)

Reactant Gas: Methane

Fuel reactor: $12Fe_2O_3(s) + CH_4(g) \rightarrow 8Fe_3O_4(s) + CO_2(g) + 2H_2O(l)$

$\Delta H_r^{\ominus} = 52.9$ KJ/mol (16)

Air reactor: $2[4Fe_3O_4(s) + O_2(g) \rightarrow 6Fe_2O_3(s)]$ $\Delta H_o^{\ominus} = 2[-471.6]$

$= -943.2$ KJ/mol (17)

Net reaction: $CH_4(g) + 2O_2(g) \rightarrow CO_2(g) + 2H_2O(l)$ $\Delta H_c^{\ominus} = -890.3$ KJ/mol (18)

Reactant Fuel: Carbon

Fuel reactor: $6Fe_2O_3(s) + C(s) \rightarrow 4Fe_3O_4(s) + CO_2(g)$ $\Delta H_r^{\ominus} = 78.1$ KJ/mol (19)

Air reactor: $4Fe_3O_4(s) + O_2(g) \rightarrow 6Fe_2O_3(s)$ $\Delta H_o^{\ominus} = -471.6$ KJ/mol (20)

Net reaction: $C(s) + O_2(g) \rightarrow CO_2(g)$ $\Delta H_c^{\ominus} = -393.5$ KJ/mol (21)

Where, $\Delta H_c^{\ominus}$ is the standard heat of combustion, $\Delta H_r^{\ominus}$ and $\Delta H_o^{\ominus}$ are the standard heat of reaction for the reduction and oxidation reactions respectively at 298 K and 1 atm. The enthalpy data are balanced to one mole of reactant gases/fuel.

2.7 Oxygen Carriers

2.7.1 Properties of Oxygen Carrier Materials

In the earlier section, it is noted that Chemical looping combustion (CLC) has emerged as a promising technology to reduce the cost of CO_2 capture. Nevertheless, the feasibility of the chemical looping process depends mainly on the oxygen carrier's ability to transfer oxygen from the air

reactor to the fuel reactor over extended multicycles. Consequently, the ideal oxygen carrier is expected to be characterized by:

- High rates of oxidation and reduction considering the relationship with reactor size, solid inventory and cost associated with large reactors.
- High mechanical stability and low tendency for agglomeration.
- High fuel conversion of the fuel to carbon dioxide and water.
- Low tendency of attrition and fragmentation to minimize fines production and increase particle lifetime.
- Sufficient oxygen transport capacity is advantageous because it implies that more oxygen can be transported per unit mass of circulating material.
- High melting point to avoid agglomeration and have good fluidization.
- Resistant to impurities and no (or negligible) carbon deposition.
- Low cost, low toxicity and environmentally-friendly.

(Chandel et al., 2009; Linderholm et al., 2010; Fan, 2011; and Adánez, 2012).

From the above requirements, it has been viewed that the most critical requirements to satisfy are high reactivity and sufficient mechanical strength (Pröll and Hofbauer, 2011). Also, it is difficult for pure metals or mineral oxides to attain these key oxygen carrier properties (Adánez, 2012).

2.7.2 Oxygen Carrier Materials

Oxygen carriers are the key to the development of the chemical looping technologies. Two types of oxygen carriers proposed and investigated are

synthetic materials and natural minerals. Synthetic oxygen carriers are generally composed of single metal oxides, combined or mixed metal oxides (Wang et al, 2015). Oxygen carriers based on transition metal oxides of copper, cobalt, iron, manganese and nickel oxides have been explored because of their desirable characteristics. The oxygen carrying capacity (R_O) of the pure metal oxides is shown in Figure 2.16. The materials used as supports include SiO_2, TiO_2, Al_2O_3, $MgAl_2O_4$, bentonite, sepiolite and others.

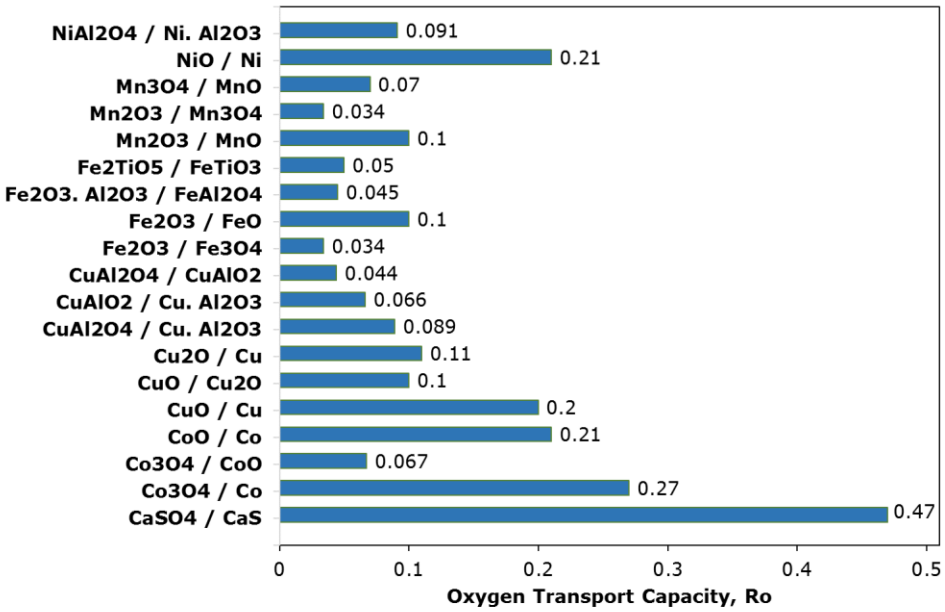

Figure 2.16: Oxygen transport capability of different redox system (Adánez et al., 2012).

Generally, the oxygen carriers investigated for CLC applications have both advantages and disadvantages. For instance, nickel-based oxygen carriers exhibit high oxygen capacity and reactivity. Nevertheless, its drawbacks include: higher material cost, carbon deposition, and health, safety and environmental concerns due its toxicity (Zafar et al., 2005; Johansson et al., 2006; Chiu and Young, 2012; Luo et al., 2015; Lyngfelt, 2015). Furthermore, nickel-based oxygen carriers can easily be deactivated by

sulphur from coal and cannot completely convert fuels to CO_2 and H_2O due to thermodynamic restriction (Wang et al., 2015; Lyngfelt, 2015). Despite the advantages of nickel oxide as oxygen carriers, high materials cost and health effects also deter the commercial use of nickel-based oxygen carriers in chemical looping processes (Luo, et al., 2015).

Copper-based oxygen carriers exhibit high reaction rates, high oxygen transfer capacity, low cost and poses less environmental concerns compared to other oxygen carriers (de Diego et al., 2007; Cao and Pan, 2006, Cao et al., 2006). All the oxygen carriers have an essentially exothermic reaction in both reactors when the fuel is H_2 or CO. However, for methane, the reaction is endothermic for other oxygen carriers except for CuO which exhibits exothermic reaction. Thus, for CuO, the particle circulation needed to maintain fuel-reactor temperature will be reduced (Lyngfelt, 2015; Cao and Pan, 2006; Chiu and Young, 2012). Nevertheless, CuO agglomerates at high temperatures due to its low melting point and the oxidation reaction rate of pure CuO rapidly decreases after a few cycles of operation (de Diego et al., 2004). Furthermore, it has the tendency to decompose at low temperatures (Jerndal et al., 2006).

Iron-based oxygen carriers are non-toxic, possess high melting point, better mechanical strength, have lower cost compared to others and are environmentally friendly (Adánez et al., 2012). Iron oxide exhibits good oxidizing capability; thus, it is able to fully convert carbonaceous fuel to CO_2 and H_2O and is less susceptible to carbon formation (Abad et al., 2007 and Garcia-Labiano et al., 2006; Luo, 2015). However, its shortcomings include lower reactivity, low fuel conversion ratio and low oxygen transport capacity. Also, pure iron oxide exhibits a sintering effect at high operating

temperatures and rapidly loses reactivity and its oxygen-carrying capacity after the first several redox cycles (Fan and Li, 2010).

Manganese-based oxygen carriers have advantages similar to iron-based oxygen carriers. This metal oxide is considered non-toxic and it is a relatively cheap material. In addition, its oxygen carrying capacity is higher than Fe-based oxygen carriers. However, the issue with manganese-based oxygen carriers is low reactivity with fuels. As mentioned previously, it is worth noting that despite the potential advantages associated with manganese oxide, it has generally received little attention and is less studied than Ni, Cu and Fe. Hence, only a few manufactured manganese materials have been used in operation (Lyngfelt, 2015).

Cobalt-based oxygen carriers offer high oxygen transport capacity and high melting point resulting to reduce sintering during chemical looping operation. However, low fuel conversion efficiency, and inherent high toxicity and environmental concerns limit their application for chemical looping technology (Chiu and Young, 2012; Adánez et al., 2012).

Metal sulphates such as $CaSO_4$ and $MgSO_4$ have been studied as oxygen carriers owing to their low cost and high oxygen transport capacity. Nevertheless, the challenge posed by these metal sulphates to CLC processes is the potential release of sulphur into the product gas stream (Luo et al., 2015).

Natural minerals, such as manganese ore, iron ore and industrial waste materials as option to solid fuels has the benefit of lower cost. However, they tend to degenerate quickly or exhibit low reactivity towards methane (Linderholm et al., 2012; Rydén et al., 2011; Leion et al., 2009).

Furthermore, ilmenite has often been studied because of its low market price, quite reactive with syngas and good fluidization behaviour renders it as one interesting option for solid fuels. Nevertheless, it was reported to have exhibited low reactivity towards methane (Lyngfelt, 2015; Azis et al., 2010; Cuadrat et al., 2012).

In addition to the advantages and disadvantages of the potential oxygen carriers discussed above, generally, the pure metal oxides do not satisfy all the desirable characteristics of an oxygen carrier and their reaction rates are reduced very rapidly after a few cycles of reduction and oxidation (de Diego et al., 2005 and Wang et al., 2015). Wide differences in reactivity with methane have been observed for the oxygen carriers and generally, reactivity is significantly higher using H_2 and CO compared to CH_4 (Johansson, Mattisson and Lyngfelt, 2006). At present, ilmenite represents a state of the art material for solid fuels, nevertheless, no real long-term operation has been accomplished (Lyngfelt, 2015).

The oxygen carriers (synthetic) discussed above for CLC application have been manufactured using different techniques. An overview of the relevant methods will be the focus of the following Section 2.7.3.

2.7.3 Oxygen Carrier Preparation

Against the backdrop of discussions in the previous section, research is still focused on the development of new oxygen carriers with enhanced performance characteristics. The aim of these studies is to find OCs, which can overcome the various practical limitations (Adánez et al., 2012; Lyngfelt, 2015). As mentioned previously, support materials are added to the primary metal oxides. Usually, the role of the support material is to

improve the primary metal oxide particle morphology, and its chemical and physical properties. Thus, the application of a production method that enhances mixing between the support material and the oxygen carrying metal oxide cannot be over emphasized. Clearly, appropriate synthesis of the particle is necessary to achieve desired particle properties (Fan and Li, 2010).

It has been noted that the synthesis method applied for the production of the oxygen carriers directly determines their physical properties such as mechanical strength, porosity and degree of dispersion. These can influence their reactivity, strength and stability during consecutive CLC redox cycles (Guo et al., 2009). Consequently, one approach to potentially improve the oxygen carrier performance is the application of a well-designed production method for oxygen carriers.

Commonly used methods for oxygen carrier production are mechanical mixing and impregnation (Fan and Li, 2010). Mechanical mixing, although inexpensive has been found to yield non-homogeneous materials giving rise to a metal oxide-rich phase and support-rich phase. For instance, it was reported that copper-based oxygen carriers produced by mechanical mixing, lost activity due to sintering of the metal rich phase. Hence, mechanical mixing was found unsuitable for metal oxides such as copper oxide which sinter at low temperatures (Diego et al., 2004). Research by Adánez et al. (2004) showed that most of the oxygen carriers produced by mechanical mixing had unacceptable reactivity and/or mechanical properties.

The impregnation (wet or dry) technique is a method which has been used for the preparation of oxygen carriers. These impregnation techniques

require tedious synthesis procedure since loading of the metal oxides on the support require repetitive process until the desired metal oxide percentage is reached. Furthermore, due to the nature of the technique, it is difficult to predict the exact amount of metal loading. Also, the metal loading obtained using dry impregnation is limited by the available pore volume of the support. In addition, the potential problem with wet impregnation is the formation of an outer shell of metal oxide, which has a weak bond with the support and tends to undergo attrition after initial cycles (Fan and Li, 2010).

The co-precipitation method has been identified as a wet chemical method which can be used to produce solid materials that are chemically homogeneous (Fan and Li, 2010). Although, more than seven hundred oxygen carriers have been tested for chemical looping combustion, very limited works have been reported on oxygen carriers directly related to co-precipitation. These few studies were mainly for nickel and copper-based oxygen carriers. Findings indicate that synthesis by co-precipitation technique could potentially yield oxygen carriers with desirable properties. For instance, Chuang et al. (2008) found that Al_2O_3-stabilized, CuO-based oxygen carrier synthesized by co-precipitation showed high redox stability over many cycles.

Thus, against the backdrop of the above findings, it became of interest to exploit the co-precipitation technique for Mn and Fe based oxygen carriers for chemical looping combustion. Nevertheless, the few studies on co-precipitated oxygen carriers reported in the literature typically use strong base such as potassium hydroxide as precipitating agent. One drawback is the repetitive washing of the precipitate to remove the excess alkali ions and controlled loading of the active components may not be easily

obtained (Imtiaz et al., 2012; Chuang et al., 2008). Moreover, materials with very low surface area are obtained when strong base is utilized as precipitating agent (Benrabaa et al., 2012).

In contrast to other co-precipitation techniques used in CLC, the procedure adapted in this work utilized aqueous ammonia (weak base) as the precipitating agent. This co-precipitation procedure has been previously applied for the invention of adsorbents materials for mercury capture (Snape et al. 2010). This technique allows for materials with high surface area, high degree of dispersion and controlled metal loadings to be obtained.

This work presents a novel research on various formulations of co-precipitated manganese oxide and iron oxide oxygen carriers supported on zirconium oxide and combined zirconia-ceria. The focus was on experimental investigations and performance evaluation of the co-precipitated oxygen carriers for Chemical Looping Combustion.

2.8 Conclusions

1. Much work has been reported for some potential oxygen carriers comprising of synthetic oxygen carriers (supported or unsupported transition metal oxides of Cu, Co, Fe, Mn and Ni) and natural minerals.
2. Despite the potential advantages, manganese based materials have generally received little attention and have been less studied than Ni, Cu and Fe.

3. Although all the proposed oxygen carriers exhibited desirable characteristics, they also have disadvantages which hinder their performance for CLC application.
4. Effort is still being focused to further improve the oxygen carrier performance with the aim to overcome their various practical limitations for CLC.
5. The preparation method has been found to have an important influence on the properties of oxygen carriers. Mechanical mixing and impregnation method is commonly used for oxygen carrier synthesis and have exhibited some shortcomings.
6. Despite the potential benefit of the co-precipitation technique to yield homogeneous material, only very few works have been reported for oxygen carriers using this preparation method.

Thus, the focus of this thesis is on the development and detailed investigation of novel co-precipitated manganese and iron oxide based materials as oxygen carriers for chemical-looping combustion using hydrogen, carbon monoxide and methane as fuel.

The following Chapter 3 provides description of the experimental techniques and methodology employed in this study.

3 MATERIALS AND METHODOLOGY

3.1 Experimental Details

The experimental work undertaken in this research comprises three main segments simplified and illustrated in Figure 3.1 and will be described in detail in Sections 3.2 – 3.3.

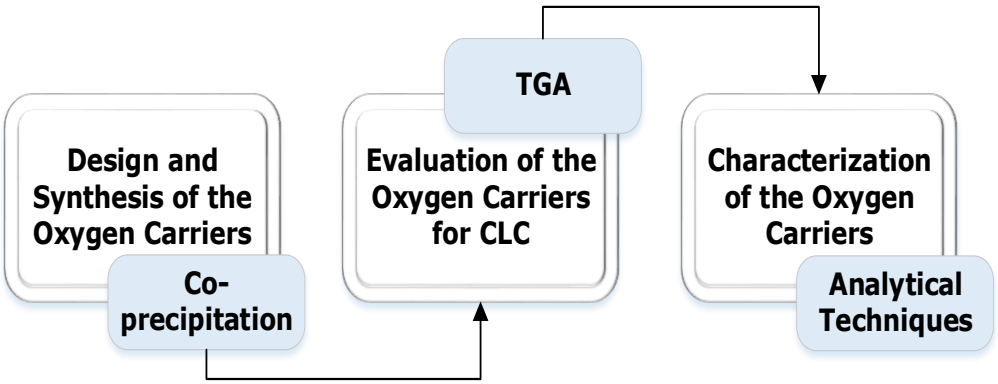

Figure 3.1: Schematic of experimental stages.

3.2 Oxygen Carriers Synthesis

The oxygen carriers studied in this work were produced by the co-precipitation technique. The synthesis flow chart for the co-precipitation process is presented in Figure 3.2. The co-precipitated manganese oxide and iron oxide oxygen carrier particles were supported on either zirconia or combined support of zirconia and ceria oxide with varied weight percent compositions.

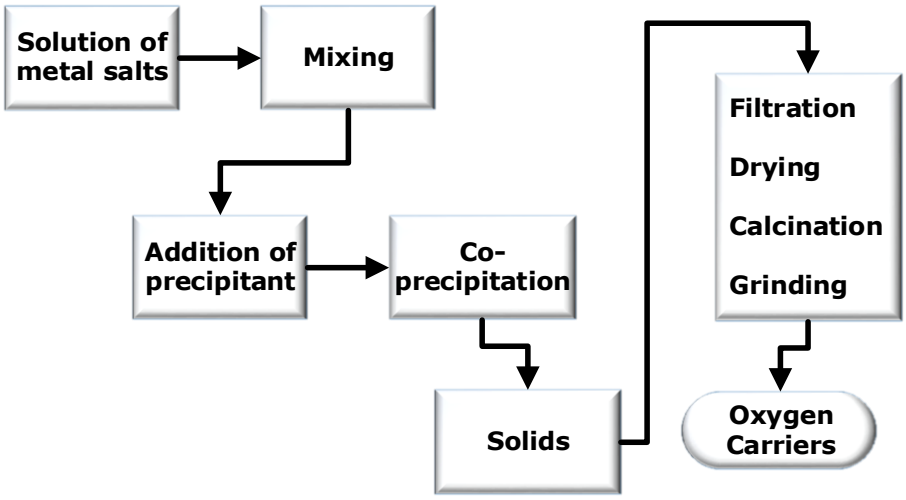

Figure 3.2: Preparation of the co-precipitated oxygen carriers.

The chemical precursors namely iron (III) nitrate, manganese (II) nitrate, zirconia (II) nitrate and ceria nitrate (from Sigma Aldrich) were dissolved in distilled water to obtain aqueous solutions. For instance, equal molar ratios of 28.7 g of $Mn(NO_3)_2 \cdot 6H_2O$, 40.4 g of $Fe(NO_3)_2 \cdot 9H_2O$ and 33.9 g $Zr(NO_3)_2 \cdot 6H_2O$ were dissolved in 200-500 ml deionized water. After mixing the solutions together, ammonia water (35% solution) was added slowly to the solutions under constant stirring conditions until its pH value reached about 7 in order to obtain a co-precipitate. The co-precipitate was aged for 2 hours and then filtered to remove excess water. Subsequently, the co-precipitate was dried in a vacuum oven at 378 K for about 24 hours. After drying, the co-precipitate was calcined in the furnace at temperature of 1323 K for 2 hours. After calcination, the co-precipitated oxygen carriers obtained were crushed (by using mortar and pestle) and sieved into different particle sizes: 75-250 μm and 300-850 μm.

During the initial design phase of the oxygen carrier materials formulations, preliminary synthesis was carried out to check if there is any potential effect of the mixing order of the active components. The aim was to ensure that appropriate synthesis order was followed, which could result

in an oxygen carrier with potentially suitable CLC characteristics. Bimetallic carrier with equimolar amounts of manganese and iron supported on zirconia was chosen for this test and it was confirmed that the effect of order of mixing was not significant on the performance of the synthesized materials (Appendix A).

The co-precipitated oxygen carriers studied in this work (presented in more detail in Chapters 4 - 7) are categorized into the following groups:

- Monometallic manganese oxide or iron oxide with support.
- Bimetallic manganese-iron oxide with low zirconia content - 20 wt. %.
- Bimetallic manganese-iron oxide with high zirconia content - 44 wt. %.
- Bimetallic manganese-iron oxide with combined zirconia-ceria support.

The mass ratio of the active metals in the co-precipitated oxygen carriers vary between 20 and 80 parts. The zirconia content of the OCs varies from 10% to 62% W/W, whereas the ceria content varies from 10% to 31% with the remaining material being the active metal oxides.

In this work, the synthesized oxygen carriers designated by the notations are presented in Tables 3.1 to 3.3. For the notations, the metal oxides mass fractions are followed by the support and calcination temperature. M, F, Z or Ce in the names of the oxygen carriers denotes manganese oxide, iron oxide, zirconium oxide or ceria oxide respectively. For instance, M8FZCe5-1050 means an oxygen carrier containing 80 wt. % Mn_3O_4 and 20 wt. % Fe_2O_4 supported on 44 wt. % ZrO_2 and CeO_2 and calcination of 1323 K.

Table 3.1: Composition of monometallic oxygen carriers

Oxygen carrier	Metal oxide composition (wt. %)	Support composition (wt. %)		True density (Kg/m^3)
		ZrO_2	CeO_2	
M5Z5-1050	38	62	-	5298
M6Z4-1050	60	40	-	-
M8Z5-1050	80	20	-	-
M5ZCe5-1050	38	31	31	6093
F5Z5-1050	39	61	-	4408
F1	100	-	-	-
M5Z5-450	38	62	-	-

Table 3.2: Composition of the mixed oxide oxygen carriers with zirconia.

Oxygen carrier	Metal oxide composition (Wt. %) {Mn_3O_4/ (Mn_3O_4+Fe_2O_3)}	Support composition (ZrO_2) [Wt %]	True density (Kg/m^3)
M8FZ5-1050	80	44	4678
M6FZ5-1050	67	44	4470
M5FZ5-1050	49	44	5412
M3FZ5-1050	33	44	5061
M2FZ5-1050	20	44	4646
M8FZ2-1050	80	20	-
M6FZ2-1050	67	20	-
M5FZ2-1050	49	20	-
M3FZ2-1050	33	20	-
M2FZ2-1050	20	20	-
M5FZ5-1050(1)	49	44	-
M5FZ5-1050(2)	49	44	-

Table 3.3: Composition of the mixed oxide oxygen carriers with zirconia-ceria support.

Oxygen carrier	Metal oxide composition (Wt. %) {Mn_3O_4/ (Mn_3O_4+ Fe_2O_3)}	Support composition (Wt. %)		Calcination temperature (K)	True density (gcm^{-3})
		ZrO_2	CeO_2		
M8FZCe5-1050	80	22	22	1323	6093
M6FZCe5-1050	67	22	22	1323	5279
M5FZCe5-1050	49	22	22	1323	5406
M3FZCe5-1050	33	22	22	1323	5677

3.3 Instrument: Thermogravimetric Analyser

A thermogravimetric analyser (Pyris 1 TGA, Perkin Elmer) was used to investigate and compare the reduction-oxidation reactivity, recyclability and thermal stability of the co-precipitated oxygen carriers. Furthermore, the TGA was used to study the effect of parameters such as, particle size, temperature and others on the oxygen carriers' behaviours for CLC application.

The Pyris 1 TGA is a computer-controlled analyser. The main components are the microbalance and furnace element. The microbalance of the Pyris 1 TGA operates as a high gain electromechanical servo system that permits detection of weight changes as small as 0.1 µg. The schematic view of the TGA is shown in Figure 3.3.

An important advantage of using the Pyris 1 TGA system is the automation function. This allows for the operation of programmable sequences involving temperatures, flow rates and data acquisition. The Thermal

Analysis Gas Station (TAGS) (gas flow controllers), furnace temperature and programme method were all automatically controlled through the Pyris software and allows for automatic sequence of sample runs and data analysis. Consequently, experiments were set up to run automatically for long periods of time permitting more efficient use of the thermal analysis system. This mode of operation ensures that required experimental parameters are repeated accurately during multi-cyclic CLC operation.

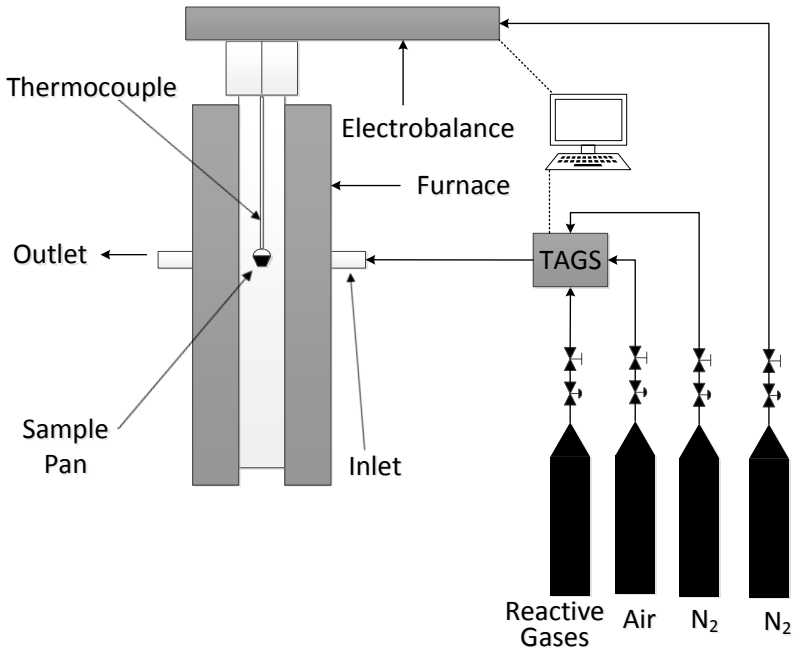

Figure 3.3: Schematic of the Thermogravimetric analyser.

3.3.1 Experimental Procedure

The CLC performance of the oxygen carriers was evaluated by subjecting about 20 mg oxygen carrier samples for reactivity and stability test in TGA. The gases used as fuel for the experiment were hydrogen (H_2), carbon monoxide (CO) and methane (CH_4). The oxygen carrier was progressively heated (20^{o}C/min) under a nitrogen atmosphere to the desired temperature. Thereafter, the OC was exposed to successive reduction and

oxidation conditions by injection of gaseous fuel and air with nitrogen purge (15 mins) between each reaction phase to avoid possible formation of flammable gas mixtures inside the instrument. The weight and furnace temperature data were continuously recorded by the data acquisition unit. Five multi-cycles (otherwise specified) of reduction and oxidation were performed in the TGA for the oxygen carrier. Also, some selected oxygen carriers were subjected to long term multi-cycle CLC test. All experiments were conducted at ambient pressure conditions and relevant experimental parameters for the evaluation of the oxygen carriers are summarized in Table 3.4. To ensure the integrity of the experiment and minimum variations in the data, routine calibration checks were performed on the equipment and repeat test runs were carried out. Examples of repeated test runs conducted are shown in Figures C.1 and C.2 in Appendix C.

Table 3.4: Summary of the experimental parameters

Oxygen carriers	Feed gas concentration (%)						Reaction time (min)		Particle size (μm)	Purging gas	Purging time (min)	Feed flow rate (ml/min)	Reaction temperature (K)
	Reduction					Oxidation	Reduction	Oxidation					
	H_2	CO	CH_4	CO_2	N_2	Air							
Monometalic	5	0	0	0	Bal.	100	76	50-80	75-250, 300-850	N_2	15	20	973-1173
Monometalic	0	10	0	0	Bal.	100	30	30	75-250	N_2	15	50	973-1173
Monometalic	0	0	10	25	Bal.	100	5	30	75-250	N_2	15	50	973-1173
Mixed Oxide OC (ZrO_2)	5	0	0	0	Bal.	100	76	50-80	75-250, 300-850	N_2	15	20	973-1173
Mixed Oxide OC (ZrO_2)	0	10	0	0	Bal.	100	30	30	75-250, 300-850	N_2	15	50	973-1173
Mixed Oxide OC (ZrO_2)	0	0	10	25	Bal.	100	5	30	75-250	N_2	15	50	973-1173
Mixed Oxide (Zr_2O/CeO)	5	0	0	0	Bal.	100	76	50-80	75-250	N_2	15	20	973-1173
Mixed Oxide (Zr_2O/CeO)	0	10	0	0	Bal.	100	30	30	75-250	N_2	15	50	973-1173
Mixed Oxide (Zr_2O/CeO)	0	0	10	25	Bal.	100	5	30	75-250	N_2	15	50	973-1173

3.4 Effect of Mass Transfer

In heterogeneous reactions, limitation from mass transfer plays an important role on the rate of conversion, rate of reaction and product formation. The oxygen carrier which is in the solid phase is embedded in the gaseous reacting species. Thus, the reaction rate depends on the mass transfer or diffusion between these phases (Klaewkla, Arend and Hoelderich, 2011).

In the sequence of heterogeneous reaction, the mass transfer of reactants occurs first, from the bulk fluid to the external surface of the particle (oxygen carrier). Then, the reactants diffuse into and through the pores within the particle from the external surface, whilst reaction takes place on the surface of the pores (Fogler, 2013). If the mass transfer or diffusion steps are fast as compared to the reaction, there is no mass transfer limitation from the bulk to the particle surface and from the particle surface to the active site in the pore. Under these situations, the mass transfer steps have no effect on the reaction rate. On the other hand, if the mass transfer or diffusion steps are slow, then the mass transfer limitation will become an important factor with respect to the overall reaction rate (Fogler, 2013). Furthermore, diffusion or mass transfer limitation is dependent on the flow conditions and the size of solid particles. Thus, the mass transfer limitation can be reduced by varying these parameters (Fogler, 2013).

Generally, the two methods to determine if effect of mass transfer is significant are by experiment and calculation. The most reliable method is by experiment (Satterfield, 1996). In this study, steps have been taken to reduce mass transfer controlling the solid-gas reactions. For instance,

small, well-spread sample masses were used in the experiments. In addition, experiments were conducted to check the effect of various gas flows and mass of sample on reaction kinetics (see Figures C.3 and C.4 in Appendix C). Almost similar reaction rates were observed with all gas flows and mass of samples. Moreover, theoretical calculations obtained for the mass transfer coefficients and effectiveness factors demonstrate that measurements were under chemical reaction control (see Appendix F). Thus, it could be concluded that mass transfer is not rate limiting in these experiments and chemical reaction seems to be the only resistance controlling the reaction rate for the oxygen carriers investigated in this work.

3.5 Evaluation Performance of the Oxygen Carriers

As previously mentioned, the oxygen carriers were subjected to TGA experiments following the procedure in Section 3.3.1. From these tests, reactivity data were obtained from the weight variations during the reduction and oxidation cycles as a function of time. Oxygen carrier reactivity corresponding to the fourth cycle was used given that the rates of the materials would have stabilized. For the purpose of comparison, the reactivity of the oxygen carriers was analysed in terms of oxygen transfer capacity (OTC), oxygen transfer rates and cyclic redox stability of the materials. Furthermore, the oxygen carrier reactivity (using hydrogen, carbon monoxide or methane as fuels) was evaluated in terms of effect of temperature, number of cycles and particle size.

The relevant calculations used to evaluate the reactivity of the oxygen carriers using the data obtained from the TGA are presented hereafter.

Ro (oxygen ratio) is the theoretical maximum amount of oxygen that can be transferred to the fuel and is expressed as:

$$R_o = \frac{(M_{oxd} - M_{red})}{M_{oxd}} \quad (22)$$

However, given that the OCs in this work is combined with inert materials, the effective value of the oxygen transfer capacity (Roc) of oxygen carrier depends on the fraction of active metal oxide (X_{oc}) in the composite material and is defined as:

$$R_{oc} = X_{oc} R_o \quad (23)$$

The conversion for reduction and oxidation of the oxygen carriers can be defined according to Equations 24 and 25.

$$\text{Fractional reduction (X)} = \frac{M_{oxd} - M}{M_{oxd} - M_{red}} = \frac{M_{oxd} - M}{M_{oxd} R_{oc}} \quad (24)$$

$$\text{Fractional oxidation (X)} = 1 - \frac{M_{oxd} - M}{M_{oxd} - M_{red}} \quad (25)$$

Where M is the instantaneous mass of the OC, M_{red} is the mass of the OC fully reduced. M_{oxd} is the mass of OC fully oxidized.

In this study, the fractional reduction and oxidation conversions were calculated using the TGA data of the fourth cycle unless specified otherwise.

The reaction rates for the reduction and oxidation were calculated from TGA conversion data using the following expression:

$$\frac{d\mathrm{w}}{d\mathrm{t}} = R_{oc}\frac{d\mathrm{X}}{d\mathrm{t}} \tag{26}$$

Where dw/dt is the rate of mass based conversion or rate of oxygen transport (ROT), dX/dt is the rate of reaction and w (mass conversion) is defined as

$$\mathrm{w} = \frac{\mathrm{M}}{\mathrm{M_{oxd}}} \tag{27}$$

3.6 Characterization of the Oxygen Carriers

Fresh and reacted oxygen carriers were characterized to appraise their morphology and near surface chemistry, true density, surface area and possible chemical transformations that occurred during the calcination process as well as reactivity investigations. The techniques employed include: Scanning Electron Microscopy-Energy Dispersive Spectroscopy (SEM-EDX), X-Ray Diffraction (XRD), Nitrogen Adsorption Isotherm and pycnometry. An overview of the applications of these analytical techniques used for the characterization of the oxygen carriers is presented in the following Sections 3.6.1 to 3.6.4.

3.6.1 SEM-EDX Analysis of the Oxygen Carriers

Scanning Electron Microscopy (SEM) is a technique that uses a beam of electrons to scan the surface of a sample in order to build a 3-dimensional image of the specimen. Scanning Electron Microscopy (SEM) (Philips XL-

30) equipped with Energy Dispersive X-ray (EDX) spectroscopy was used to image the morphology of the fresh and reacted oxygen carriers and appraise the near surface chemistry. The oxygen carrier samples were sputter coated with either carbon or platinum before imaging. In most cases, the electron beam energy was 15 kV. The images obtained from scanning electron microscope for the fresh and reacted oxygen carrier particles and the observed changes are discussed in Chapters 4 – 7.

3.6.2 Phase Identification of the Oxygen Carriers

X-ray diffraction (XRD) was used to identify the phases present in each oxygen carrier. The samples were crushed into fine powders and usually pressed into a sample holder so that a smooth flat surface is obtained. Subsequently, the samples were analysed using a Bruker, D8 Advance X-ray diffractometer with Cu-Kα (wavelength= 1.5406 A$^{\circ}$) radiation operating at 40 kV and 35 mA. A stepwise approach with a step size of 0.1° and residence time of 5 s at each step over the angular range (2θ) was used to generate the XRD patterns. Data analysis was conducted with EVA and XRD analytical results obtained were correlated with references and standards of the International Centre for Diffraction Data (ICDD) and Joint Committee on Powder Diffraction Standards (JCPDS).

The XRD results and phases present in the fresh oxygen carriers after calcination and selected re-oxidized oxygen carriers after reduction by methane are presented and discussed in Chapters 4 – 7.

3.6.3 Particle Density Measurements

The apparent density of the oxygen carriers was measured by the particle density analyser - AccuPyc II (Micrometrics). Each oxygen carrier sample was placed in a 10 cm^3 sample holder with at least two-third of the sample holder's volume occupied by the sample. The masses of the empty holder and that of holder containing sample were recorded. The samples were then placed into the analyser chamber and subjected to an automatic procedure operating under pressure and using helium as analysing gas. The densities of selected oxygen carriers are presented in Tables 3.1 - 3.3.

3.6.4 Surface Area Analysis

The specific surface area of the oxygen carrier particles was evaluated via Krypton sorption at 77.4 K in a Micrometrics ASAP 2420 Accelerated Surface Area and Porosimetry System. The Brunauer–Emmett–Teller (BET) method was used to calculate the specific surface area of the particles using a relative pressure (P/Po) between 0.05 - 0.3 with nine data points. The measurement results are shown in Table G.1 in Appendix G. Some examples of the BET isotherms and BET surface area plots are also shown in Appendix G.

In the current chapter, the development of the oxygen carriers and characterization of these oxygen carriers using the described analytical equipment were presented. The experimental results and discussions are presented in details in the following Chapters 4 - 7. Each chapter corresponds to a batch of the co-precipitated oxygen carriers as previously highlighted in Section 3.2. Furthermore, the subsections in each chapter present results and discussions on the OCs performance in hydrogen,

carbon monoxide and methane as fuel as well as results from SEM-EDX, XRD analysis.

4 MONOMETALLIC OXYGEN CARRIERS: BEHAVIOUR IN DIFFERENT GASES

The co-precipitated monometallic oxygen carriers consist of five oxygen carrier materials denoted as M5Z5-1050, M6Z5-1050, M8Z5-1050, M5ZCe5-1050 and F5Z5-1050 (see Table 3.1).

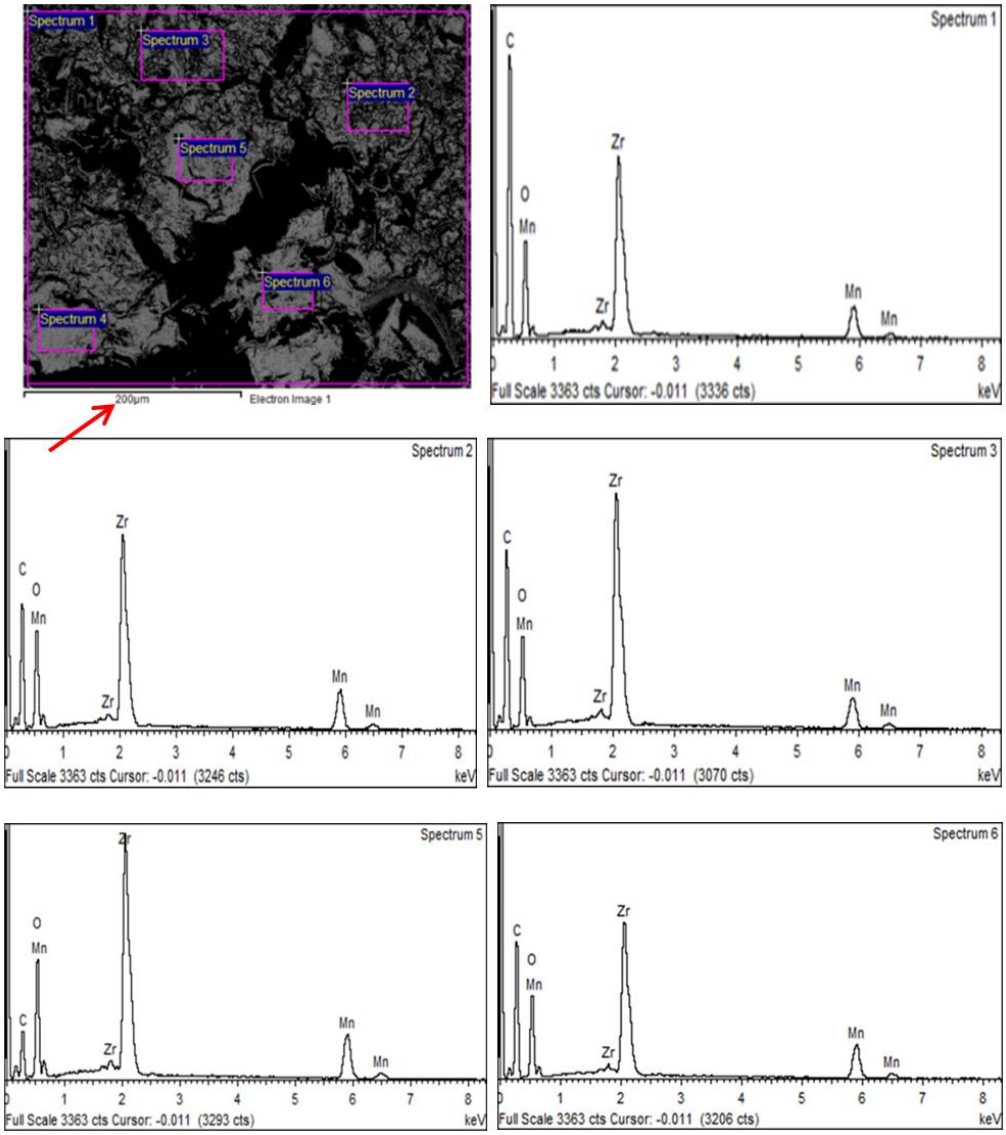

Figure 4.1: SEM-EDX image of fresh M5Z5-1050 particles after calcination at 1323 K in air for 2 h showing distribution of the elements. Scale bar indicated by the arrow represents 200 µm.

The co-precipitation technique allows for the synthesis of chemically well-dispersed particles as illustrated in Figure 4.1 for sample M5Z5-1050 at a scale of 200 μm. The rectangle in the inset image shows the selected EDX inspection field of the sample. Also, the resulting spectrum reveals that Mn and Zr are the main elements present in the OC. Furthermore, regarding chemical composition, the elements appears to be well dispersed in the selected field.

The following sections present in detail the behaviour of the co-precipitated monometallic oxygen carriers following the order hydrogen (H_2), carbon monoxide (CO) and methane (CH_4).

4.1 Reduction/Oxidation in Hydrogen

4.1.1 Reactivity

Reactivity tests for the five co-precipitated monometallic oxygen carriers (OCs) were carried out in TGA as detailed in the previous chapter on methodology. Figure 4.2 shows the fractional conversion for the OCs. In addition, mechanically mixed unsupported iron oxide, F(MEC) and impregnated Mn oxide supported on zirconia, M(IMP) were included as reference. Figure 4.2 indicates that whereas all the co-precipitated Mn oxide OCs reached full reduction conversion, the impregnated Mn oxide OC reached reduction conversion of 60%. Also, M5Z5-1050 reached fractional reduction conversion of 0.3 in 1.9 times faster than Mn oxide prepared via impregnation M(IMP).

It is known that ceria can actively participate and enhance chemical reactions (Galvita et al., 2013). Here, addition of ceria did not enhance the

performance of M5Z5-1050. On the contrary, M5Z5-1050 was more reactive than M5ZCe5-1050 and was 2.3 and 1.5 times faster than M5ZCe5-1050 in reduction and oxidation respectively (Table 4.1). The possible reason for slower reactivity of M5ZCe5-1050 will be discussed in Section 4.4.

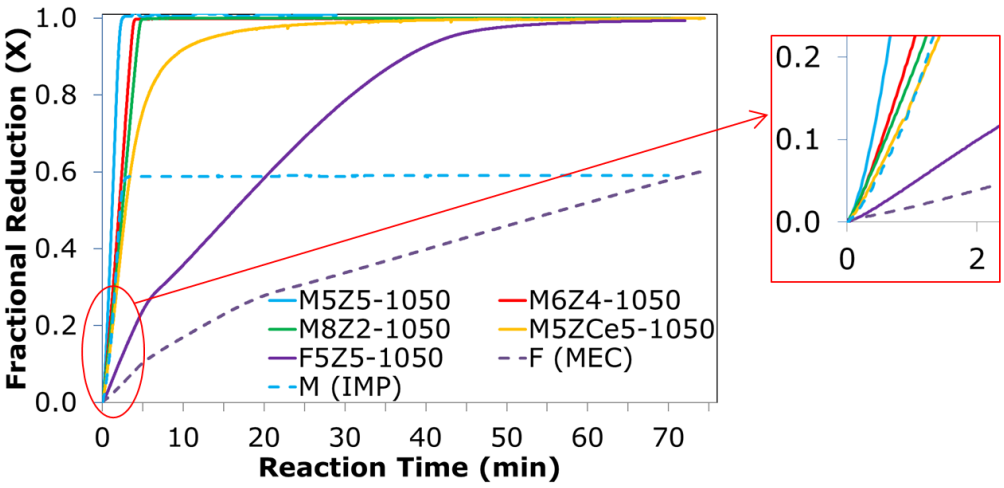

(a) Reduction

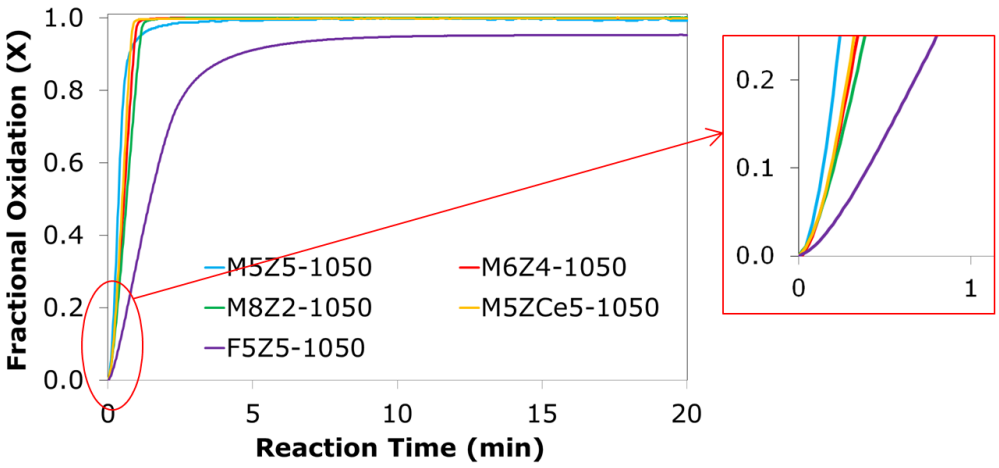

(b) Oxidation

Figure 4.2: Fractional conversion as a function of time for the co-precipitated monometallic oxygen carriers for the (a) 4th reduction cycles in 5% H_2 and (b) 4th oxidation cycles in air at 1173 K, particle size of 75-250 µm and feed gas flow rate of 20 ml/min for the transition from Fe_2O_3 to Fe and from Mn_3O_4 to MnO. Supported manganese oxide M(IMP) prepared by impregnation and unsupported mechanically mixed iron oxide F(MEC) were included as reference.

Clearly, the impact of zirconia on reactivity could be observed in Figure 4.2 and Table 4.1. For instance, in reduction and oxidation, reactivity of co-precipitated Mn oxide OCs with zirconia support increased with increasing zirconia content in the composite material. Similar behaviour was observed for Fe-based OC. Here, remarkable improvement in reactivity was observed for supported Fe OC (F5Z5-1050) over the pure unsupported Fe OC F(MEC) prepared via mechanical mixing. F5Z5-1050 achieved fractional conversion of 0.3 about 3.3 times faster in reduction reaction compared to F(MEC).

Table 4.1: Time needed to reach fractional conversion of 0.3 and 0.95 for the reduction of monometallic oxygen carriers by hydrogen and oxidation by air for the 4^{th} cycles.

Oxygen carriers	**Time for X=0.3 (s)**		**Time for X=0.95 (s)**	
	Reduction	**Oxidation**	**Reduction**	**Oxidation**
M5Z5-1050	48	15	126	64
M6Z4-1050	78	22	218	55
M8Z2-1050	96	26	264	68
M5ZCe5-1050	108	22	762	49
M(IMP)	94	-	-	-
F5Z5-1050	432	56	2526	524
F(MEC)	1410	-	-	-

The rates of reaction for the oxygen carriers are presented in Figure 4.3. The TGA data revealed that the maximum rate of reaction of Mn based OCs supported on zirconia increased with increasing zirconia content in reduction and oxidation reactions. Furthermore, M5Z5-1050 exhibited the highest maximum reaction rate such that this rate was 2.5 and 1.3 times

that of M5ZCe5-1050 and 7.8 and 4.1 times that of F5Z5-1050 in reduction and oxidation respectively.

As expected, F5Z5-1050 exhibited multistep reactions consisting of the transformations Fe_2O_3 →Fe_3O_4 → FeO →Fe. From Figure 4.3, the initial fast reduction reaction step up to conversion of 0.11 corresponds to reduction to Fe_3O_4. The rate continues to decrease until conversion of 0.3 which coincides with reduction to FeO and then much slower rate to Fe. Nevertheless, it is worth noting that the time taken to reach 30% conversion (reduction to FeO) was about 3.3 times faster for F5Z5-1050 compared to pure iron oxide F(MEC). It has been suggested that there is potential to exploit reduction of Fe_2O_3 to FeO or Fe systems for CLC if special configuration of fuel reactors was applied (Adánez et al., 2012). Perhaps the co-precipitated F5Z5-1050 which offers remarkable fast kinetics for the transformation of Fe_3O_4 to FeO could be considered for this application.

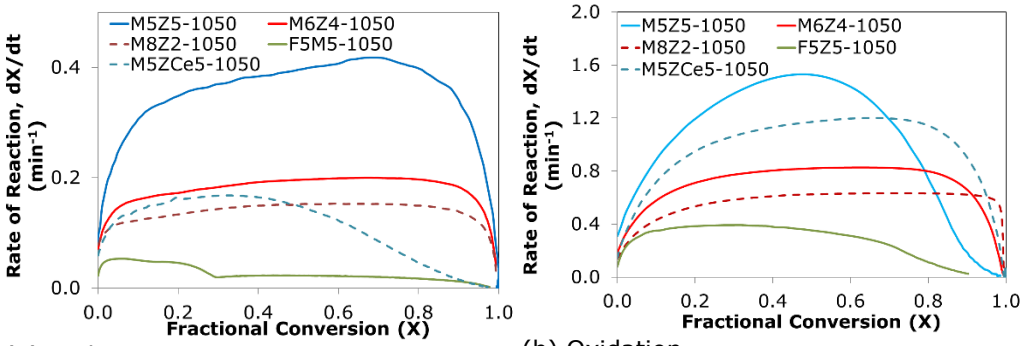

(a) Reduction (b) Oxidation

Figure 4.3: Rate of reaction as a function of fractional conversion for the co-precipitated monometallic oxygen carriers for the (a) 4th reduction cycles in 5% H_2 and (b) 4th oxidation cycles in air at 1173 K, particle size of 75-250 μm and feed gas flow rate of 20 ml/min for the transition from Fe_2O_3 to Fe and from Mn_3O_4 to MnO.

Figure 4.4 shows the maximum rate of mass conversion achieved by this batch of monometallic oxygen carriers in reduction and oxidation cycles. From the results, it is clear that M5Z5-1050 exhibit the highest maximum rate of mass conversion in reduction reaction. Furthermore, its rate was about 2.5 and 1.3 times that of M5ZCe5-1050 in reduction and oxidation respectively. Also, the maximum rate of mass conversion for M5Z5-1050 was 1.8 times that of F5Z5-1050 in reduction. On the other hand, the maximum rate of mass conversion for F5Z5-1050 was 1.1 times that of M5Z5-1050 in oxidation. This higher maximum rate of mass conversion value for F5Z5-1050 may possibly be due to its higher Roc and observed increased reactivity in oxidation cycle.

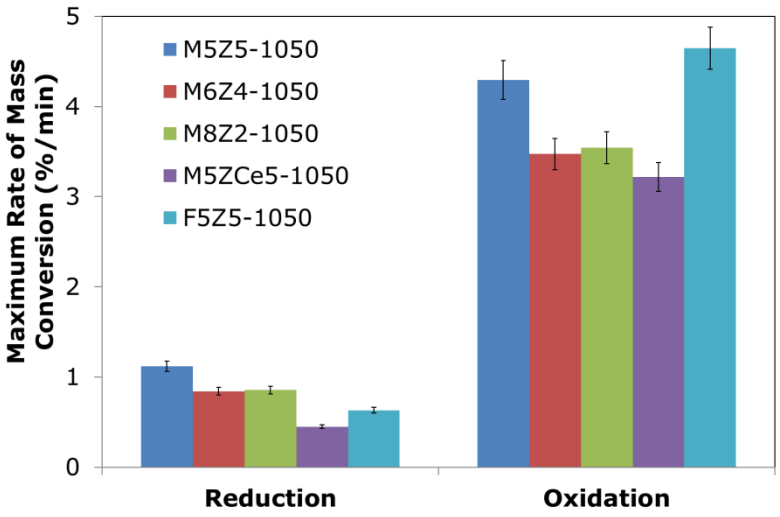

Figure 4.4: Comparison of maximum rate of mass conversion for oxygen carriers M5Z5-1050, M6Z4-1050, M8Z2-1050, M5ZCe5-1050 and F5Z5-1050 at 1173 K for the 4th reduction cycles in 5% H_2 and 4th oxidation cycles in air at 1173 K, particle size of 75-250 µm and feed gas flow rate of 20 ml/min for the transition from Fe_2O_3 to Fe and from Mn_3O_4 to MnO.

4.1.2 Stability and Effect of Repeated Cycles

For the CLC process, it is desirable that the oxygen carrier should be able to undergo multiple cycles and maintain its reactivity. Thus, the stability of

the solid particles becomes important for long-term operation. Figure 4.5 shows the stability performance for the monometallic OCs for five redox cycles. As can be observed, these particles demonstrate relatively stable rate of mass conversion during this test.

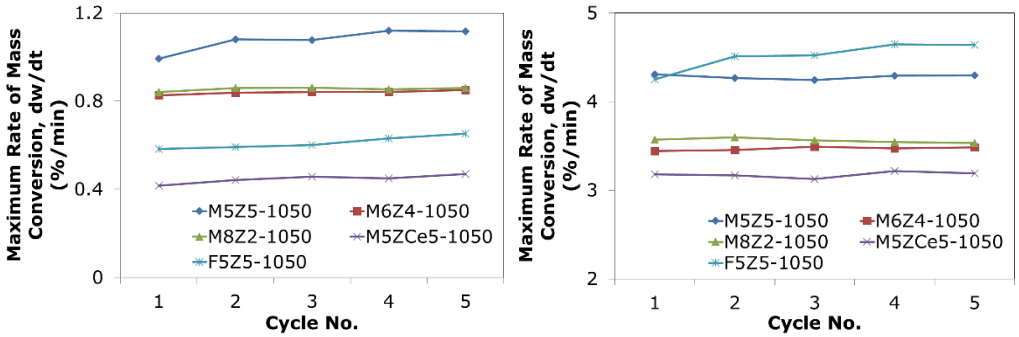

(a) Reduction (b) Oxidation

Figure 4.5: Effect of number of reaction cycles on maximum rate of mass conversion for M5Z5-1050, M6Z4-1050 M8Z2-1050, M5ZCe5-1050 and F5Z5-1050 oxygen carriers for the (a) reduction cycles in 5% H_2 and (b) oxidation cycles in air at 1173 K, particle size of 75-250 μm and feed gas flow rate of 20 ml/min for the transition from Fe_2O_3 to Fe and from Mn_3O_4 to MnO.

4.1.3 Effect of Temperature on Reactivity

In order to establish if the reactivity observed for M5Z5-1050 and F5Z5-1050 was temperature-dependent, redox experiments were conducted at 1173 K, 1073 K and 973 K. Clearly, from Figure 4.6, both the reactivity and the extent of conversion were function of temperature during the redox reaction.

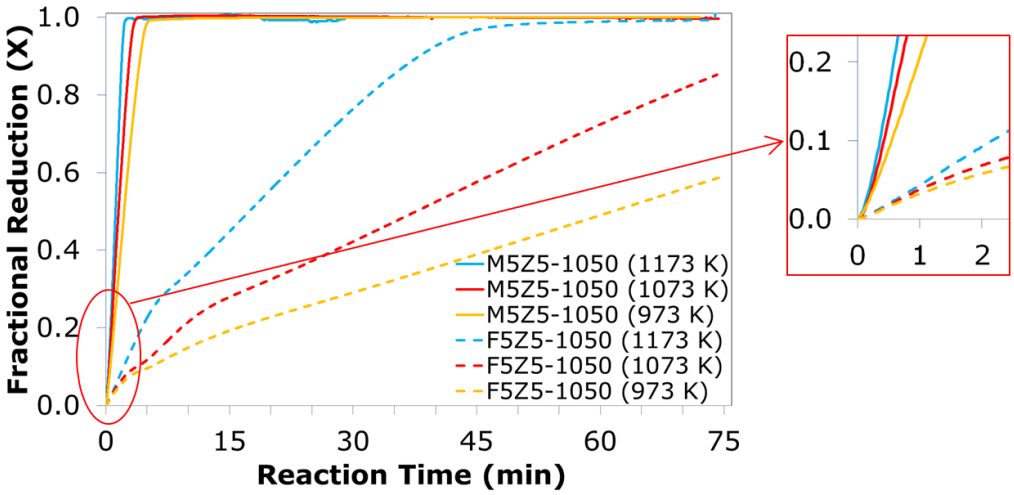

(a) Reduction

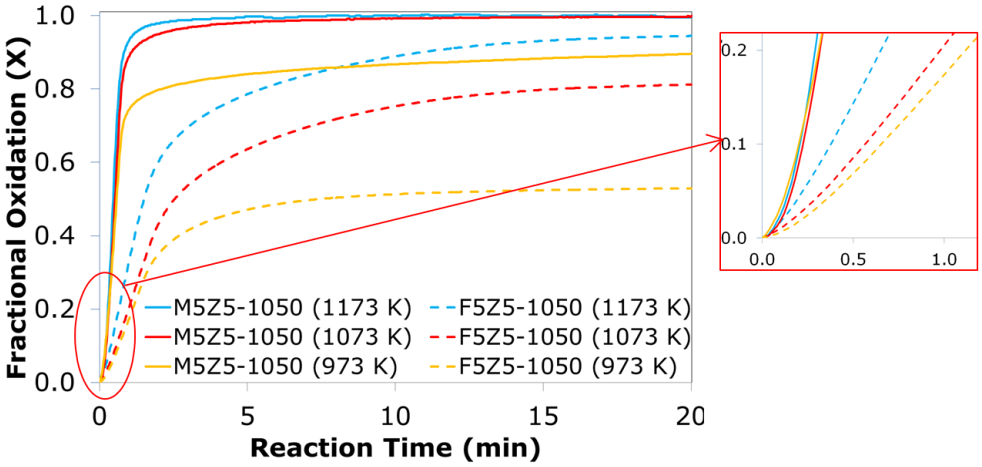

(b) Oxidation

Figure 4.6: Effect of temperature on fractional conversion versus reaction time for M5Z5-1050 and F5Z5-1050 oxygen carriers at 973 K, 1073 K and 1173 K for the (a) 2nd reduction cycles in 5% H_2 and (b) 2nd oxidation cycles in air with particle size of 75-250 µm and feed gas flow rate of 20 ml/min for the transition from Fe_2O_3 to Fe and from Mn_3O_4 to MnO.

Figure 4.6 shows that reactivity increased with increasing reaction temperature for both OCs in reduction and oxidation. This temperature effect appears to be more significant for F5Z5-1050 compared to M5Z5-1050. For instance, at reduction reaction temperature of 973 K, the time taken to reach fractional conversion 0.3 was 4 times and 1.8 times slower

than at 1173 K for F5Z5-1050 and M5Z5-1050 correspondingly. Furthermore, time to achieve fractional reduction conversion of 0.3 for F5Z5-1050 appeared to nearly double with each decreasing reaction temperature.

Similar trend in temperature-effect could be observed for maximum rate of reaction and maximum rate of mass conversion during the redox reactions. As shown in Figure 4.7 higher maximum rates values are achieved with increasing reaction temperatures.

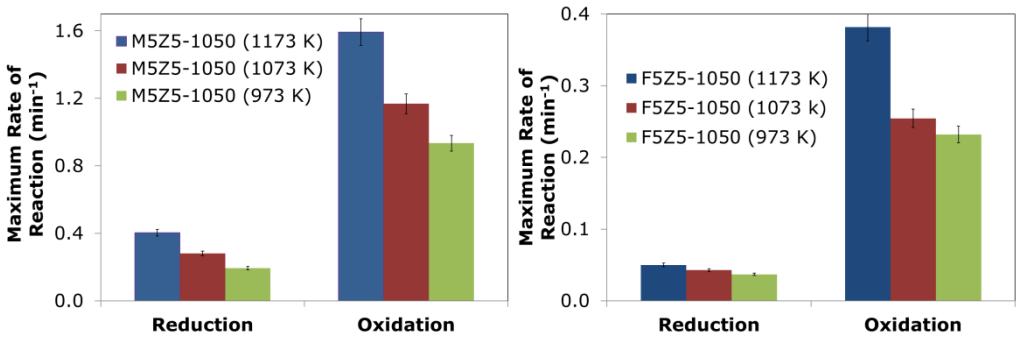

(a) (b)

Figure 4.7: Effect of temperature on maximum rate of mass conversion for monometallic oxygen carrier (a) M5Z5-1050 (b) F5Z5-1050 for the 2nd reduction cycles in 5% H_2 and 2nd oxidation cycles at 973 K, 1073 K and 1173 K, particle size of 75-250 µm and feed gas flow rate of 20 ml/min for the transition from Fe_2O_3 to Fe and from Mn_3O_4 to MnO.

4.1.4 Effect of Particle Size

The M5Z5-1050 and F5Z5-1050 particles were sieved into larger particle size fractions of 300-850 µm in order to investigate possible effect of particle size on reactivity. The reactivity profile presented in Figure 4.8 revealed that the small particle size OCs displayed higher reactivity compared to large particle size in reduction and oxidation cycles.

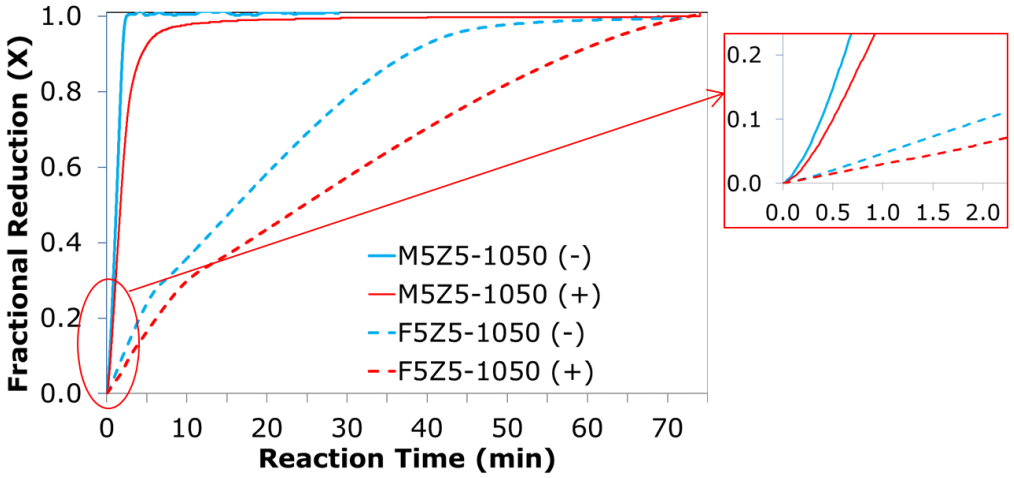

(a) Reduction

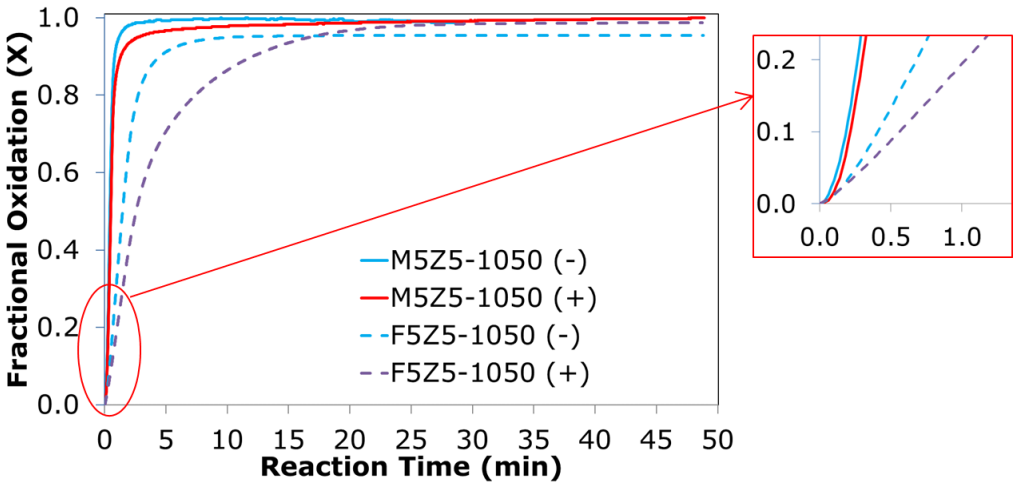

(b) Oxidation

Figure 4.8: Effect of particle size on the reactivity of M5Z5-1050 and F5Z5-1050 oxygen carriers for the (a) 4th reduction cycles in 5% H_2 and (b) 4th oxidation cycles in air at 1173 K and feed gas flow rate of 20 ml/min for the transition from Fe_2O_3 to Fe and from Mn_3O_4 to MnO. Particle sizes: (—) 75-250 µm, (+) 300-850 µm.

Figure 4.9 shows that the value of the maximum rate of reaction slightly depends on the size fractions and the extent of variations depend on the reduction-oxidation process being considered. This variation is more significant for F5Z5-1050 in oxidation reaction where 75-250 µm particles

displayed nearly twice maximum rate of reaction value compare to the large particle size fractions.

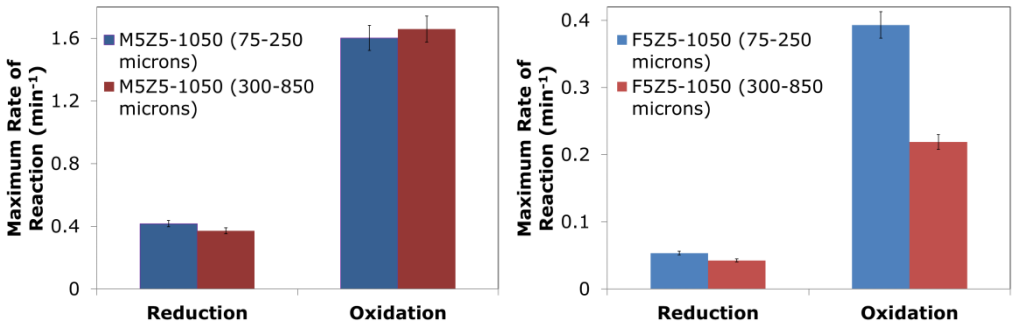

(a) (b)

Figure 4.9: Effect of particle size on maximum rate of reaction for (a) M5Z5-1050 (b) F5Z5-1050 for the 4th reduction cycles in 5% H_2 and 4th oxidation cycles at 1173 K and feed gas flow rate of 20 ml/min for the transition from Fe_2O_3 to Fe and from Mn_3O_4 to MnO. Particle sizes of 75-250 μm and 300-850 μm.

The effect of particle size presented in Figure 4.10 illustrates that the maximum rate of mass conversion value for M5Z5-1050 was relatively maintained for both particles sizes. This may suggest that the resistance due to mass transfer could be regarded as negligible for the M5Z5-1050 particle sizes. The computed effectiveness factor (η) for the small particle sized M5Z5-1050 was close to unity with low value of Thiele modulus (ϕ) (Table F.4, Appendix F) indicating the absence of internal mass transfer limitations. However, the effectiveness factor (η) for the large particle sized M5Z5-1050 was 0.92 which shows some slight diffusional limitations.

On the other hand, from the effectiveness factor (η) obtained for F5Z5-1-50 (Table F.4, Appendix F), whereas the large particle size sample was limited by internal mass transfer, this was not the case for the small particle size. This results correlates with the observed reactivity for the small and large particle sizes of F5Z5-1050.

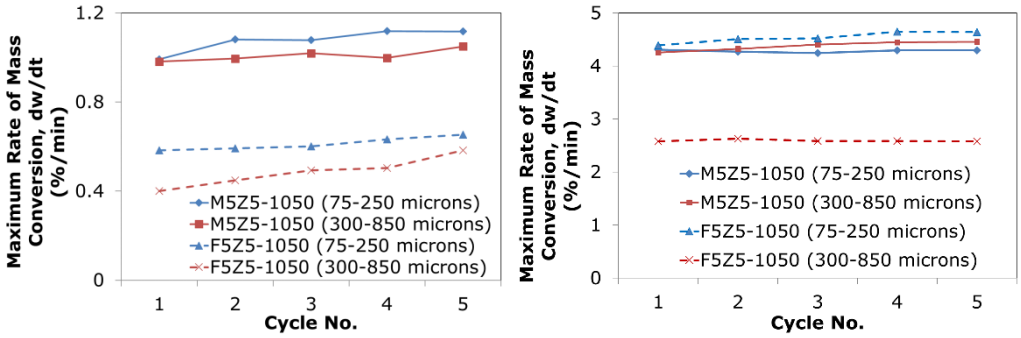

(a) Reduction (b) Oxidation

Figure 4.10: Effect of particle size on maximum rate of mass conversion versus cycle number for M5Z5-1050 and F5Z5-1050 oxygen carriers for the (a) reduction cycles in 5% H_2 and (b) oxidation cycles in air at 1173 K and feed gas flow rate of 20 ml/min for the transition from Fe_2O_3 to Fe and from Mn_3O_4 to MnO. Particle sizes: (—) 75-250 µm, (+) 300-850 µm.

4.1.5 Long Term Recyclability of the Monometallic Oxygen Carrier: M5Z5-450

Preliminary investigation was conducted on the co-precipitated M5Z5-450 sample following the same procedure and conditions already outlined in chapter 3. This particle was evaluated for long-term operation which involved thirty consecutive redox cycles as shown in Figure 4.11. Suprisingly, the TGA mass loss profile for M5Z5-450 oxygen carrier indicates reasonable recyclability and appears to maintain its stability through thirty multi-cycle CLC operations. Hence, given the demonstrated performance in terms of reactivity and recyclability, M5Z5-450 could potentially be suitable for chemical looping combustion process.

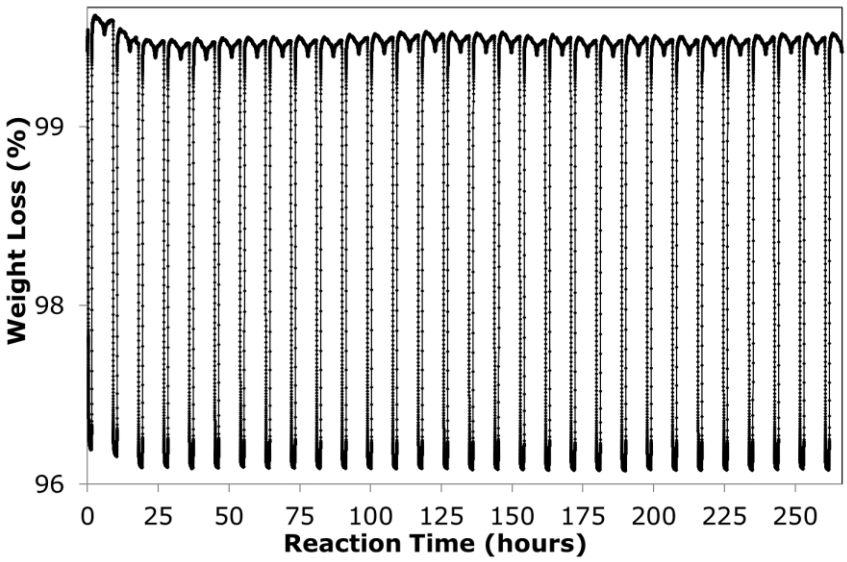

Figure 4.11: Long-term recyclability of M5Z5-450 oxygen carrier for reduction cycles in 5% H_2 and oxidation cycles in air at 1173 K, particle size of 75-250 μm and feed gas flow rate of 20 ml/min for the transition from Mn_3O_4 to MnO.

4.2 Reduction/Oxidation in Carbon Monoxide

4.2.1 Reactivity

Three co-precipitated monometallic oxygen carriers namely M5Z5-1050, F5Z5-1050 and M5ZCe5-1050 (Table 3.1) were selected for further tests in the TGA with carbon monoxide. Similar to findings obtained in H_2, the reactivity profile (Figure 4.12) shows that M5Z5-1050 was more reactive than F5Z5-1050 and M5ZCe5-1050. Furthermore, M5Z5-1050 at a fractional conversion of 0.3 was about 2.5 and 1.4 times faster than M5ZCe5-1050 (Table 4.2). This trend was found to be nearly same for that observed in H_2. Nevertheless, M5Z5-1050 tends to have slowed reactivity towards the end of oxidation cycle such that M5ZCe5-1050 reached 95% conversion faster than M5Z5-1050 and maximum rate of reaction for M5ZCe5-1050 at this point was 5.3 times that of M5Z5-1050 (Figure 4.12b). Comparable behaviour to this was also observed at 95% conversion using H_2.

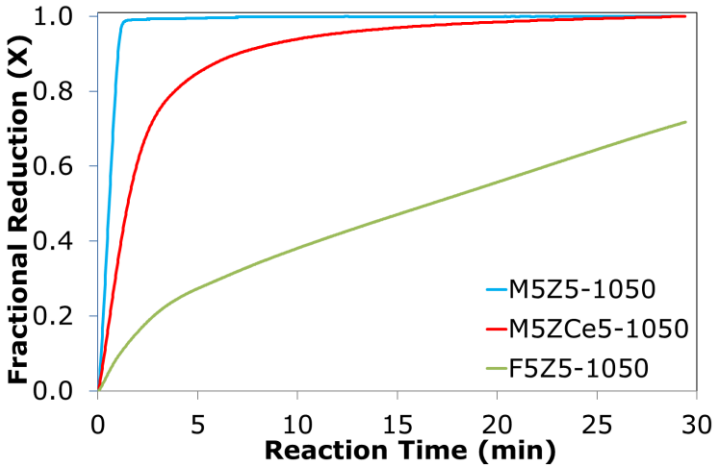

(a) Reduction

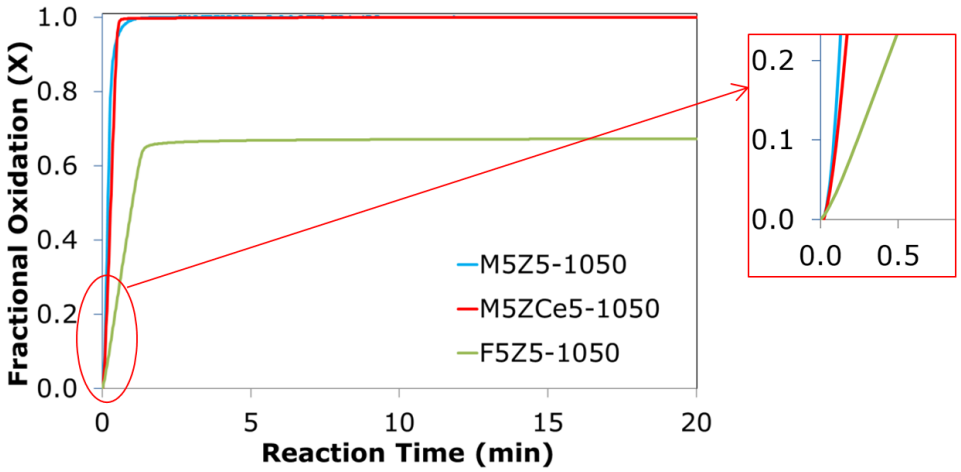

(b) Oxidation

Figure 4.12: Fractional conversion as a function of time for the co-precipitated monometallic oxygen carriers M5Z5-1050, M5ZCe5-1050 and F5Z5-1050 for the (a) 4th reduction cycles in 10% CO and (b) 4th oxidation cycles in air at 1173 K, particle size of 75-250 μm and feed gas flow rate of 50 ml/min for the transition from Fe_2O_3 to Fe and from Mn_3O_4 to MnO.

Table 4.2: Time needed to reach fractional conversion (X) of 0.3 and 0.95 for reduction of monometallic oxygen carriers by CO and oxidation by air: M5Z5-1050, M5ZCe5-1050, and F5Z5-1050.

Oxygen carriers	**Time for X=0.3 (s)**		**Time for X=0.95 (s)**	
	Reduction	**Oxidation**	**Reduction**	**Oxidation**
M5Z5-1050	21	8	65	30
M5ZCe5-1050	53	11	643	29
F5Z5-1050	366	37	-	-

Figure 4.13 shows that the maximum oxidation rate is higher than the maximum reduction rate for all the oxygen carriers. The maximum rate of reaction of M5Z5-1050 was observed to be 2.4 and 1.6 times that of M5ZCe5-1050 and 7.4 and 5.5 times that of F5Z5-1050 in reduction and oxidation respectively. Similar to the trend observed in H_2, F5Z5-1050 exhibited multistep reactions consisting of the transformations Fe_2O_3 →Fe_3O_4 → FeO →Fe. However, only the fast reaction step from Fe_2O_3 → FeO is shown in Figure 4.13.

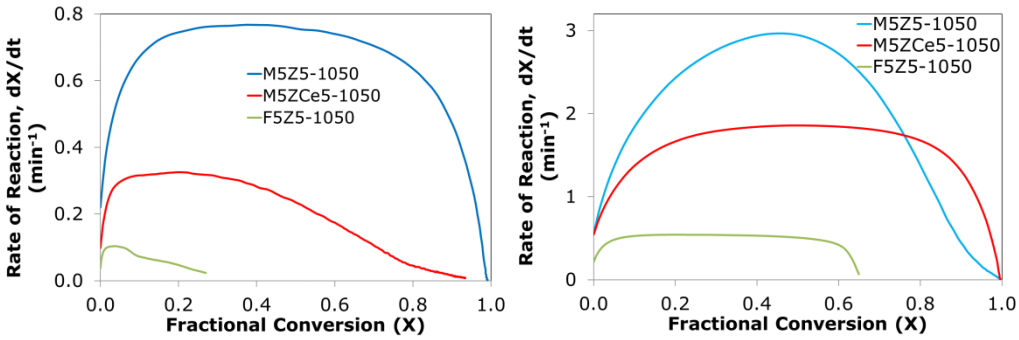

(a) Reduction (b) Oxidation

Figure 4.13: Rate of reaction as a function of fractional conversion for monometallic oxygen carriers M5Z5-1050, M5ZCe5-1050 and F5Z5-1050 for the (a) 4th reduction cycles in 10% CO and (b) 4th oxidation cycles in air at 1173 K, particle size of 75-250 µm and feed gas flow rate of 50 ml/min for the transition from Fe_2O_3 to Fe and from Mn_3O_4 to MnO.

The maximum rate of mass conversion for the oxygen carriers is shown in Figure 4.14. M5Z5-1050 shows the highest maximum rate of mass conversion for reduction. Additionally, its maximum rate of mass conversion was 1.7 and 1.2 times that of F5Z5-1050. Similar trend was observed in H_2 in the reduction cycle.

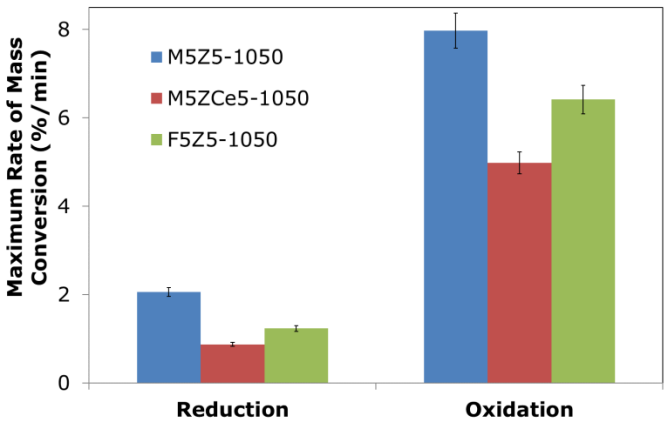

Figure 4.14: Comparison of maximum rate of mass conversion for oxygen carriers M5Z5-1050, M5ZCe-1050 and F5Z5-1050 for the 4th reduction cycles in 10% CO and 4th oxidation cycles in air at 1173 K, particle size of 75-250 µm and feed gas flow rate of 50 ml/min for the transition from Fe_2O_3 to Fe and from Mn_3O_4 to MnO.

4.2.2 Stability and Effect of Repeated Cycles

The stability performance for the monometallic oxygen carriers is presented in Figure 4.15. These particles demonstrated relatively stable rate of mass conversion for the five cycles in the TGA. M5Z5-1050 and M5ZCe5-1050 exhibited relatively stable maximum rate of mass conversion through the five cycles in reduction and oxidation. Moreover,

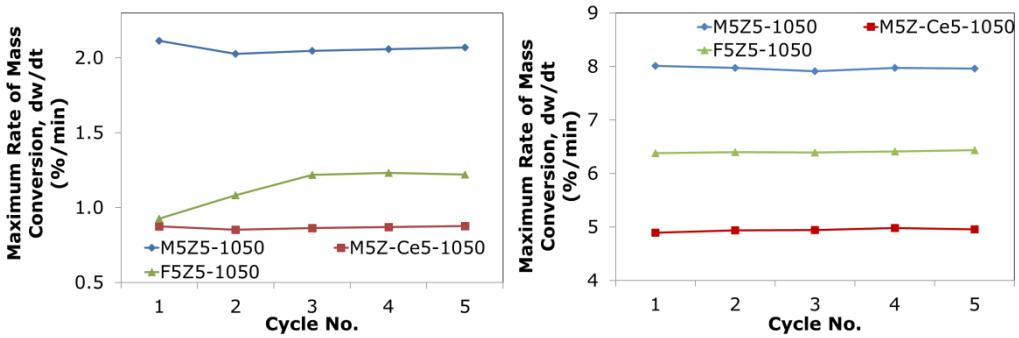

(a) Reduction (b) Oxidation

Figure 4.15: Effect of number of reduction-oxidation cycles on maximum rate of mass conversion for M5Z5-1050, M5ZCe5-1050 and F5Z5-1050 oxygen carriers for the (a) reduction cycles in 10% CO and (b) oxidation cycles in air at 1173 K, particle size of 75-250 µm and feed gas flow rate of 50 ml/min for the transition from Fe_2O_3 to Fe and from Mn_3O_4 to MnO.

F5Z5-1050 showed an initial increase in the maximum rate of mass conversion during reduction up to the third cycle and then maintained stable rate in the remaining cycles.

4.2.3 Effect of Temperature

The M5Z5-1050 OC exhibited the highest reactivity as observed in the previous sections. Hence, further investigation was conducted to ascertain possible effect of reaction temperature on its reactivity. Figure 4.16 shows the fractional conversion during the reduction and oxidation cycles for the reaction temperatures: 973 K, 1073 K and 1173 K.

M5Z5-1050 exhibited higher reactivity at reaction temperatures of 1073 K and 1173 K in reduction and oxidation cycles. Similar to behaviour obtained in H_2, M5Z5-1050 at reaction temperature 973 K displayed fast reaction up to conversion of 0.8 and thereafter slowed down in reactivity.

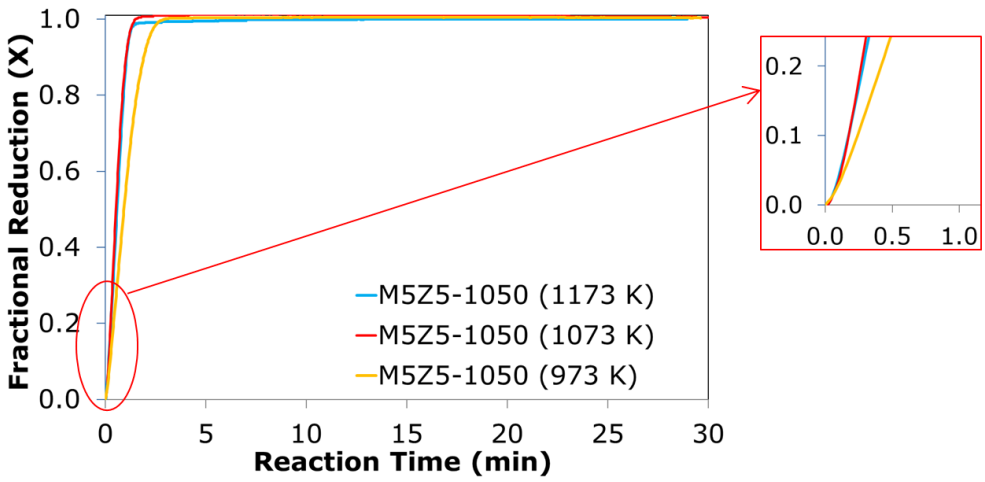

(a) Reduction

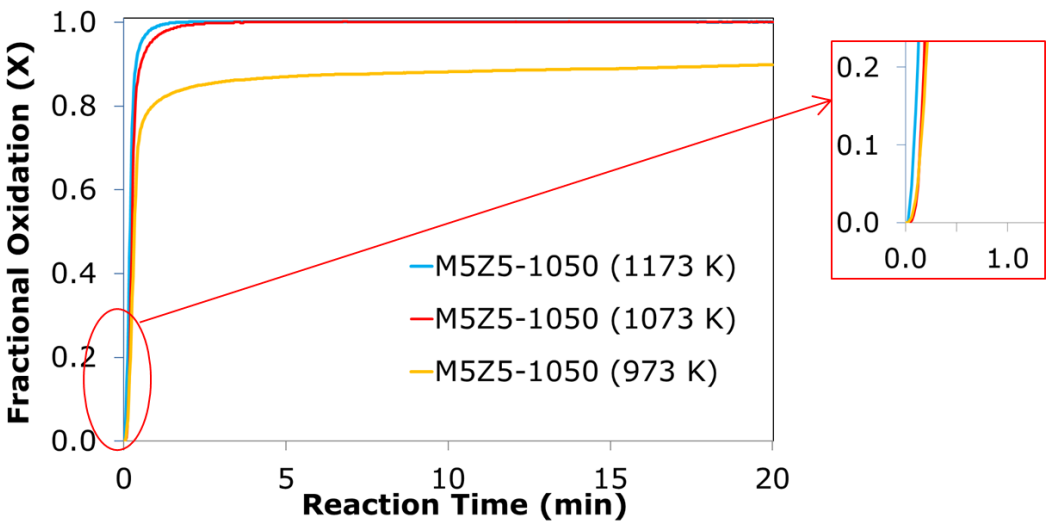

(b) Oxidation

Figure 4.16: Effect of temperature on fractional conversion for M5Z5-1050 oxygen carrier for the (a) 2nd reduction cycles in 10% CO and (b) 2nd oxidation cycles in air at 973 K, 1073 K and 1173 K, particle size of 75-250 μm and feed gas flow rate of 50 ml/min for the transition from Mn_3O_4 to MnO.

Figure 4.17 shows the effect of temperature on rate of reaction of M5Z5-1050. The oxidation rate appears to be at least 3.7 times faster than reduction rate regardless of the operating temperature. Temperature-effect on maximum rate of reaction appears not to be substantial for M5Z5-1050 at 1173 K and 1073 K; the maximum rate of reaction followed the order 1073 K > 1173 K > 973 K in reduction and oxidation. These results, thus suggest that the optimal temperature for the co-precipitated M5Z5-1050 could be 1173 K or 1073 K for CLC.

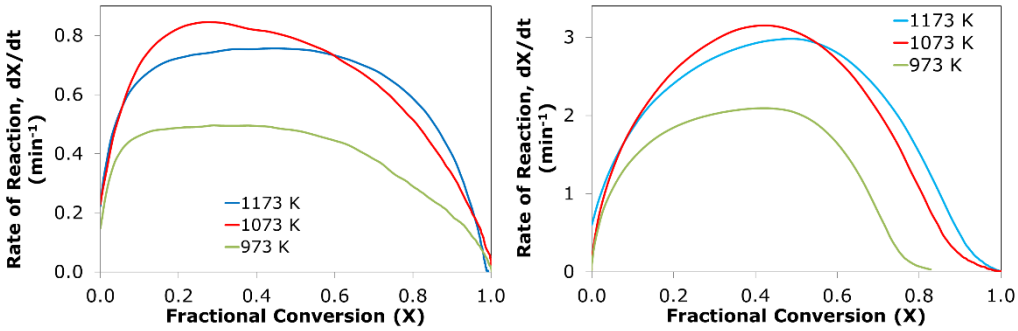

(a) Oxidation (b) Reduction

Figure 4.17: Effect of temperature on rate of reaction for M5Z5-1050 oxygen carrier for the (a) 2nd reduction cycles in 10% CO and (b) 2nd oxidation cycles in air at 973 K, 1073 K and 1173 K, particle size of 75-250 μm and feed gas flow rate of 50 ml/min for the transition from Mn_3O_4 to MnO.

4.3 Reduction/Oxidation in Methane

4.3.1 Reactivity

The reactivity of M5Z5-1050, M5ZCe5-1050 and F5Z5-1050 using methane as fuel were evaluated in TGA. Here, it was assumed that iron oxide in F5Z5-1050 was reduced to FeO. Figure 4.18 shows the conversion versus time curves for the different OCs.

The results indicate that M5Z5-1050 exhibit very fast kinetics and reached full conversion in approximately 47 s and 44 s in reduction and oxidation respectively. Moreover, reactivity of M5Z5-1050 at fractional conversion of 0.3 was 2.1 and 1.3 times faster than M5ZCe5-1050 in reduction and oxidation respectively. It is thus obvious that M5Z5-1050 is more reactive than M5ZCe5-1050 and F5Z5-1050 in reduction and oxidation as was previously observed in H_2 and CO.

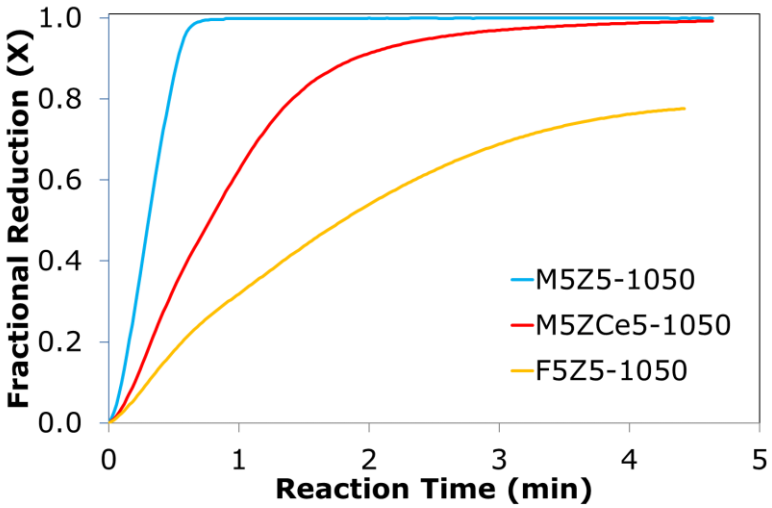

(a) Reduction

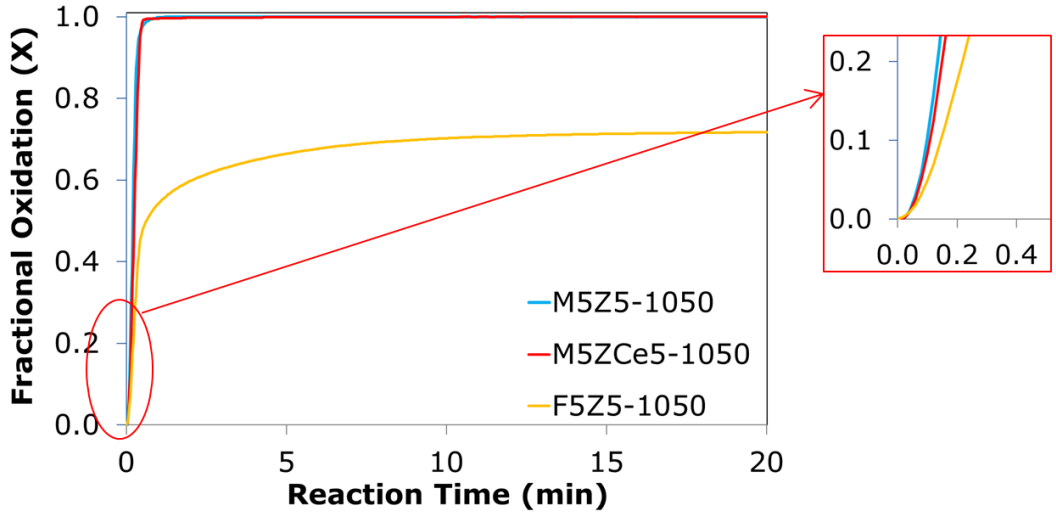

(b) Oxidation

Figure 4.18: Fractional conversion as a function of time for the co-precipitated monometallic M5Z5-1050, M5ZCe5-1050 and F5Z5-1050 oxygen carriers for the (a) 4th reduction cycles in 10% CH_4 and (b) 4th oxidation cycles in air at 1173 K, particle size of 75-250 µm and feed gas flow rate of 50 ml/min for the transition from Mn_3O_4 to MnO and from Fe_2O_3 to FeO.

Interestingly, higher reactivity was observed for F5Z5-1050 (Table 4.3). In methane, F5Z5-1050 reached conversion of 0.3 in 15% of the time needed for reduction in CO.

Table 4.3: Time needed to reach fractional conversion (X) of 0.3 and 0.95 for the reduction of the monometallic oxygen carriers by CH_4 and oxidation by air.

Oxygen carriers	Time for X=0.3 (s)		Time for X=0.95 (s)	
	Reduction	Oxidation	Reduction	Oxidation
M5Z5-1050	13	8	35	23
M5ZCe5-1050	27	10	144	25
F5Z5-1050	55	17	-	-

Clearly, the maximum oxidation rates of the oxygen carriers were higher than reduction rates as shown in Figure 4.19. The result demonstrates that M5Z5-1050 displayed the highest maximum rate of reaction in reduction and was found to be 2.8 and 1.5 times that of M5ZCe5-1050 in reduction and oxidation respectively. Somewhat similar trend was observed in H_2 and CO. Also, possibly due to improved reactivity of F5Z5-1050 in CH_4, the maximum rate of reaction for M5Z5-1050 was 3.8 and 2.2 times that of F5Z5-1050 in reduction and oxidation respectively. In contrast, these values were about twice in CO and H_2.

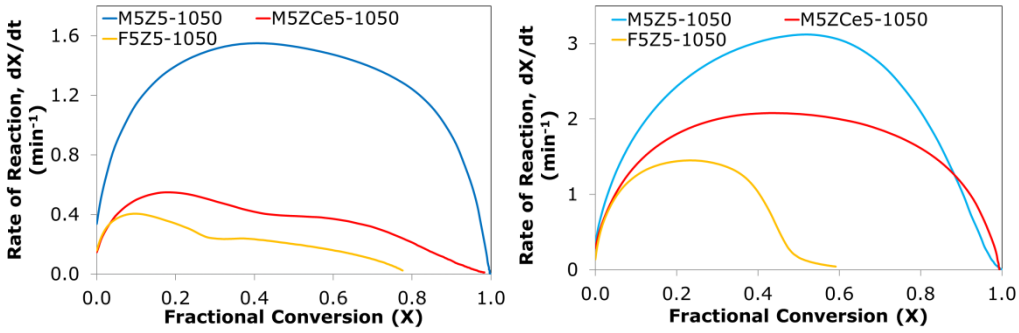

(a) Reduction (b) Oxidation

Figure 4.19: Rate of reaction as a function of fractional conversion for the monometallic oxygen carriers M5Z5-1050, M5ZCe5-1050 and F5Z5-1050 for the (a) 4th reduction cycles in 10% CH_4 and (b) 4th oxidation cycles in air at 1173 K, particle size of 75-250 µm and feed gas flow rate of 50 ml/min for the transition from Mn_3O_4 to MnO and from Fe_2O_3 to FeO.

Figure 4.20 shows that M5Z5-1050 displayed the highest rate of mass conversion in reduction and oxidation. This result is thus similar to that achieved in CO. Comparable to the trend observed in CO; M5Z5-1050 rate of mass conversion was 2.6 and 1.5 times that of F5Z5-1050 in reduction and oxidation respectively.

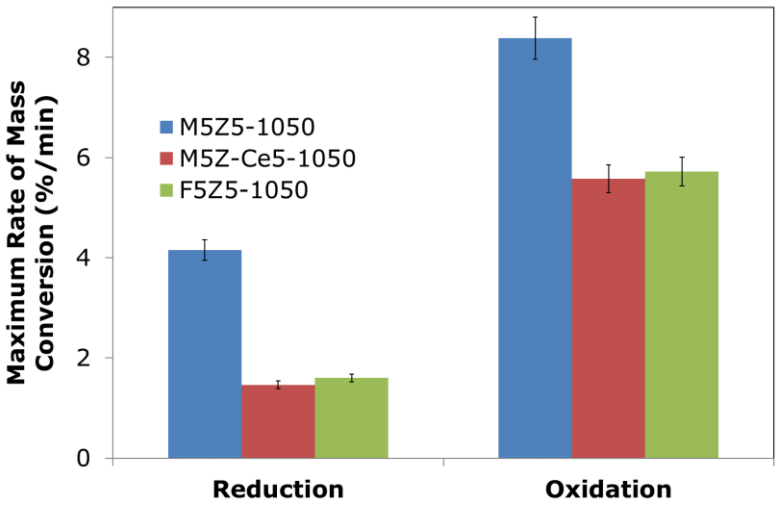

Figure 4.20: Comparison of maximum rate of mass conversion for M5Z5-1050, M5ZCe5-1050 and F5Z5-1050 oxygen carriers for the 4th reduction cycles in 10% CH_4 and 4th oxidation cycles in air at 1173 K, particle size of 75-250 µm and feed gas flow rate of 50 ml/min for the transition from Mn_3O_4 to MnO and from Fe_2O_3 to FeO.

4.3.2 Stability and Effect of Repeated Cycles

Figure 4.21 shows plot of maximum rate of mass conversion versus number of cycles which could provide indication of stability of the oxygen carriers. M5Z5-1050 and M5ZCe5-1050 displayed relatively stable rate of mass conversion for reduction and oxidation cycles in methane. Furthermore, M5Z5-1050 showed an increased maximum rate of mass conversion from first cycle to second cycle. This typical behaviour of M5Z5-1050 in CH_4 may be due the OC undergoing restructuring and then activates after the first reduction cycle. Also, F5Z5-1050 maximum rate of

mass conversion appears to increase with increasing number of cycles as shown in Figure 4.21. This seems to correlate with its mass loss profile and tends to progressively increase with increasing number of cycles as presented in Figure 4.22.

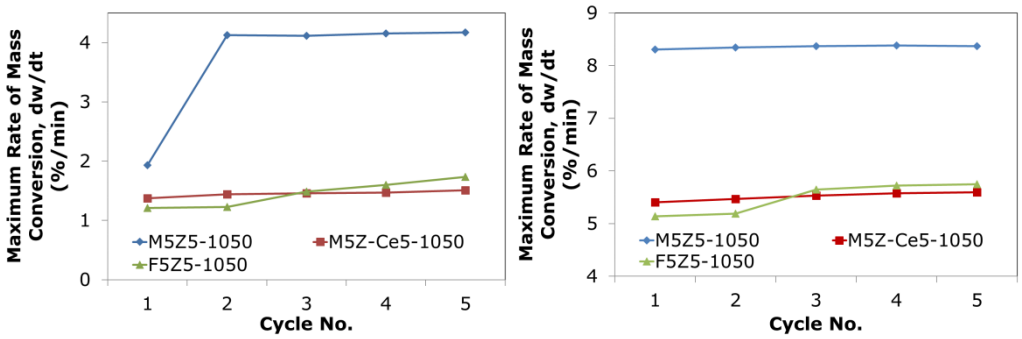

(a) Reduction (b) Oxidation

Figure 4.21: Effect of number of reduction-oxidation cycles on maximum rate of mass conversion for M5Z5-1050, M5ZCe5-1050 and F5Z5-1050 oxygen carriers for the (a) reduction cycles in 10% CH_4 and (b) oxidation cycles in air at 1173 K, particle size of 75-250 µm and feed gas flow rate of 50 ml/min for the transition from Mn_3O_4 to MnO and from Fe_2O_3 to FeO.

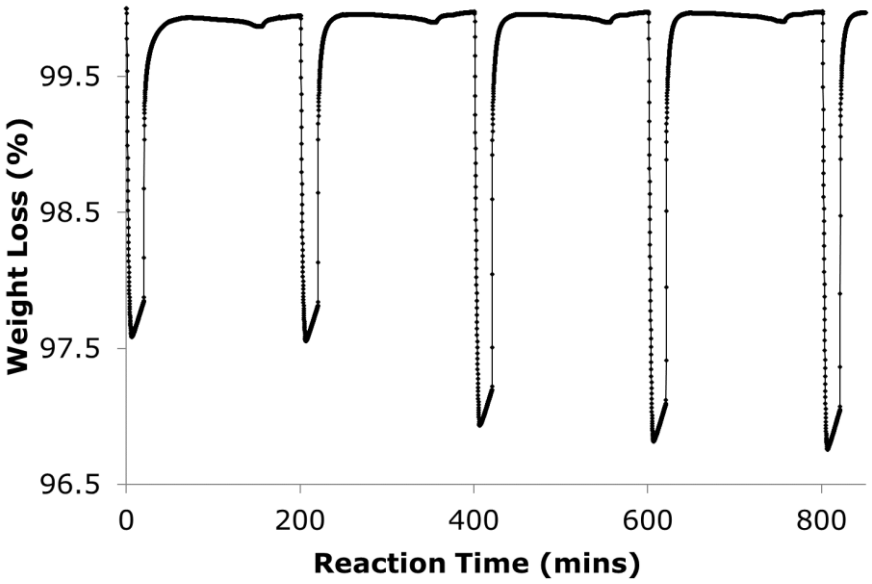

Figure 4.22: Cyclic reduction-oxidation performance of F5Z5-1050 for the reduction cycles in 10% CH_4 and oxidation cycles in air at 1173 K, particle size of 75-250 µm and feed gas flow rate of 50 ml/min for the transition from Fe_2O_3 to FeO.

4.3.3 Long-Term Recyclability of the Monometallic Oxygen Carrier: M5Z5-1050

In comparison to all the investigated oxygen carriers, the M5Z5-1050 OC exhibited the highest reactivity. Consequently, this particle was further evaluated in methane for long-term operation and the result of thirty multi-cycle tests is presented in Figure 4.23. The TGA mass loss profile for co-precipitated M5Z5-1050 oxygen carrier indicated reasonable recyclability and appears to maintain its stability through the multi-cycle redox test.

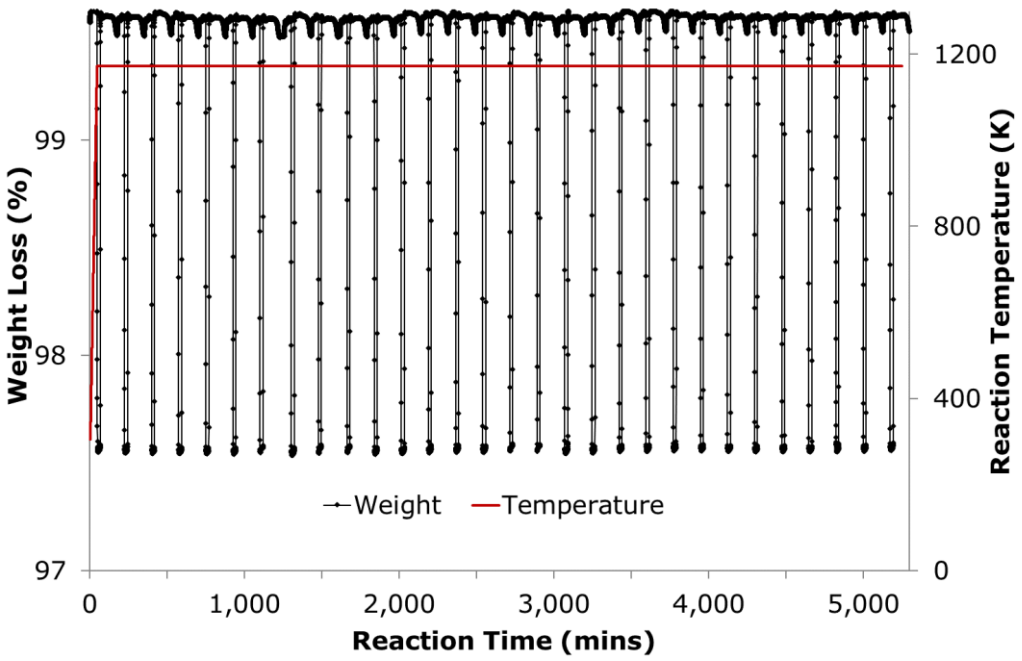

Figure 4.23: Long-term recyclability of M5Z5-1050 oxygen carrier for the reduction cycles in 10% CH_4 and oxidation cycles in air at 1173 K, particle size of 75-250 µm and feed gas flow rate of 50 ml/min for the transition from Mn_3O_4 to MnO.

In addition, the result in Figure 4.21 suggests that the maximum rate of mass conversion for M5Z5-1050 was not significantly affected by the consecutive reduction and oxidation cycles. Hence, given the demonstrated

performance in terms of reactivity and recyclability, M5Z5-1050 OC could potentially be suitable for chemical looping combustion process.

4.4 Characterization of Fresh and Reacted Oxygen Carriers

The fresh and reacted particles were characterized in order to gain understanding of possible chemical and morphological transformations in the oxygen carriers. These analyses are essential in order to establish structure-activity relationships for the oxygen carriers. Figure 4.24 displays the SEM image of the oxygen carriers. Generally, from Figures 4.24 - 4.25, all the manganese oxide based OCs did not form agglomerates. In comparison to other Mn oxide OC, the M5Z5-1050 which exhibited the highest reactivity appears to have become more porous after reaction in the fuel. The increased pores perhaps are the reason for its high reactivity. It is supposed that these pores could provide more active sites for gaseous fuel oxidation and facilitate mass transfer in the material. Besides, the computed effectiveness factor (η) for M5Z5-1050 was close to unity with low value of Thiele modulus (ϕ) (Table F.4, Appendix F) indicating the absence of internal mass transfer limitations. From the post experiment results presented in Figure 4.24, the increased pores for reactions in each gas tend to correlate well with the increased reactivity observed for the OCs following the order CH_4 > CO > H_2.

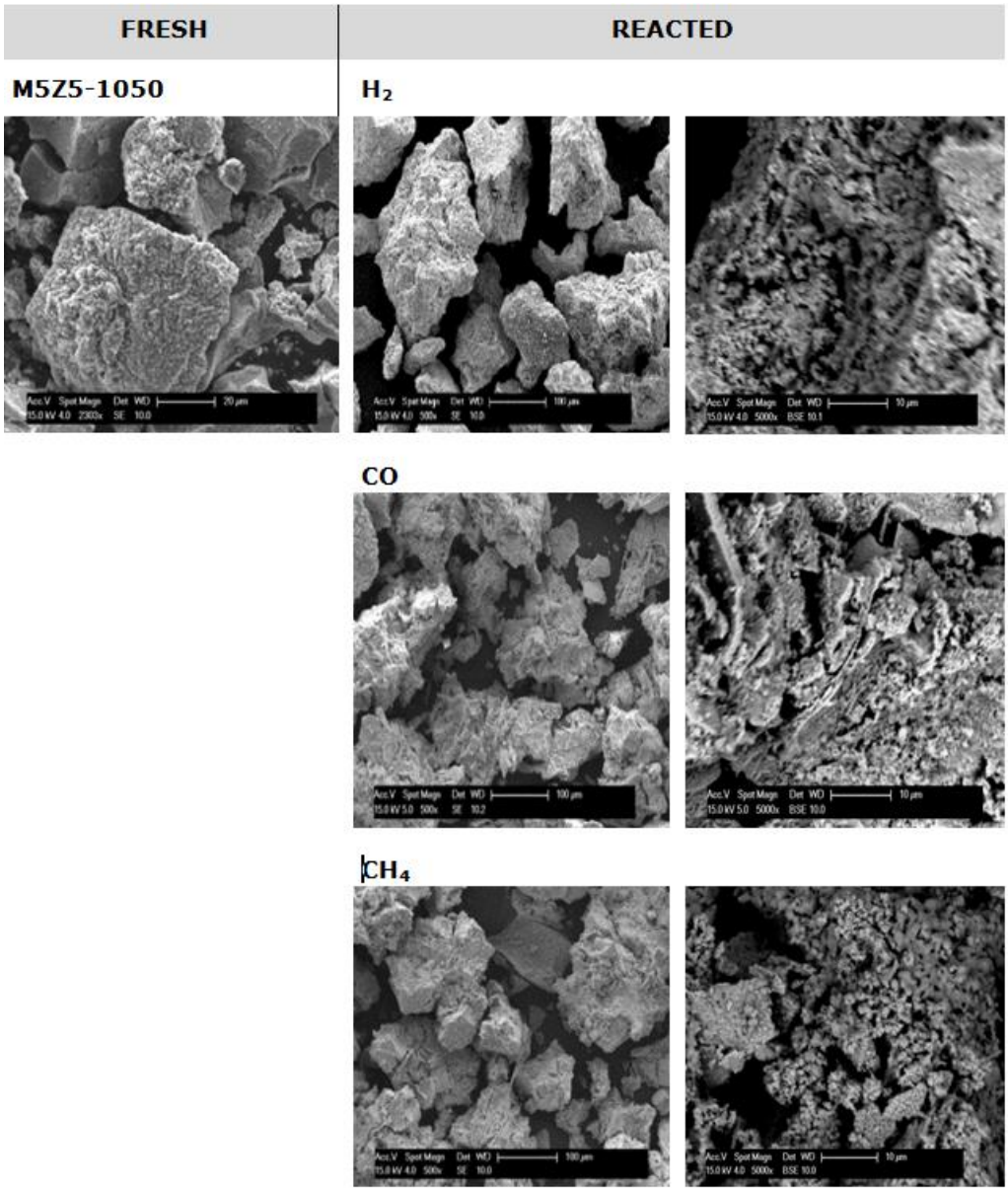

Figure 4.24: SEM images of the unreacted M5Z5-1050 particles after calcination at 1323 K for 2 h and reacted M5Z5-1050 particles after five redox cycles at 1173 K in different gases (H_2, CO and CH_4). The backscattered images at the right column confirm the existence of pores at a magnification of 5000X.

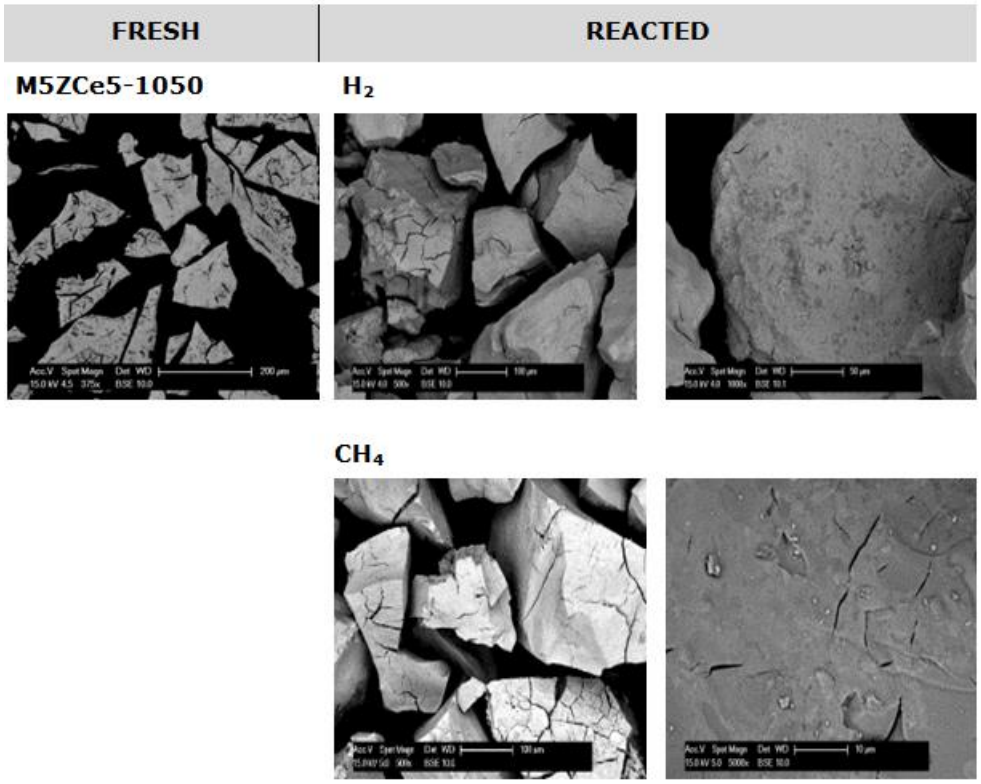

Figure 4.25: SEM images of polished unreacted M5ZCe5-1050 particles after calcination at 1323 K for 2 h and reacted M5ZCe5-1050 particles after five redox cycles at 1173 K in H_2 or CH_4. The surface of the particles appears to be smooth after the reactions.

Ceria can actively participate and enhance chemical reactions (Galvita et al., 2013). It is clear however that addition of ceria did not enhance the reactivity performance of M5Z5-1050. Manganese oxide is known to have the tendency to react or form irreversible compounds with supports resulting in phases of no or low reactivity (Zafar et al., 2005). However, for these co-precipitated OCs, there was no such interaction between the active components and support as can be observed in Table 4.4. It is thus suggested that the reason for the lower reactivity for M5Z5Ce-1050 is likely due to the smoother and less porous surface of this OC as shown in Figure 4.25.

On the other hand, after reaction in H_2, F5Z5-1050 formed lumps and featured voids which appear to be interconnected and without pores on the surface (Figure 4.26). This observation could be one of the reasons for its lower reactivity in comparison to the monometallic Mn based oxygen carriers.

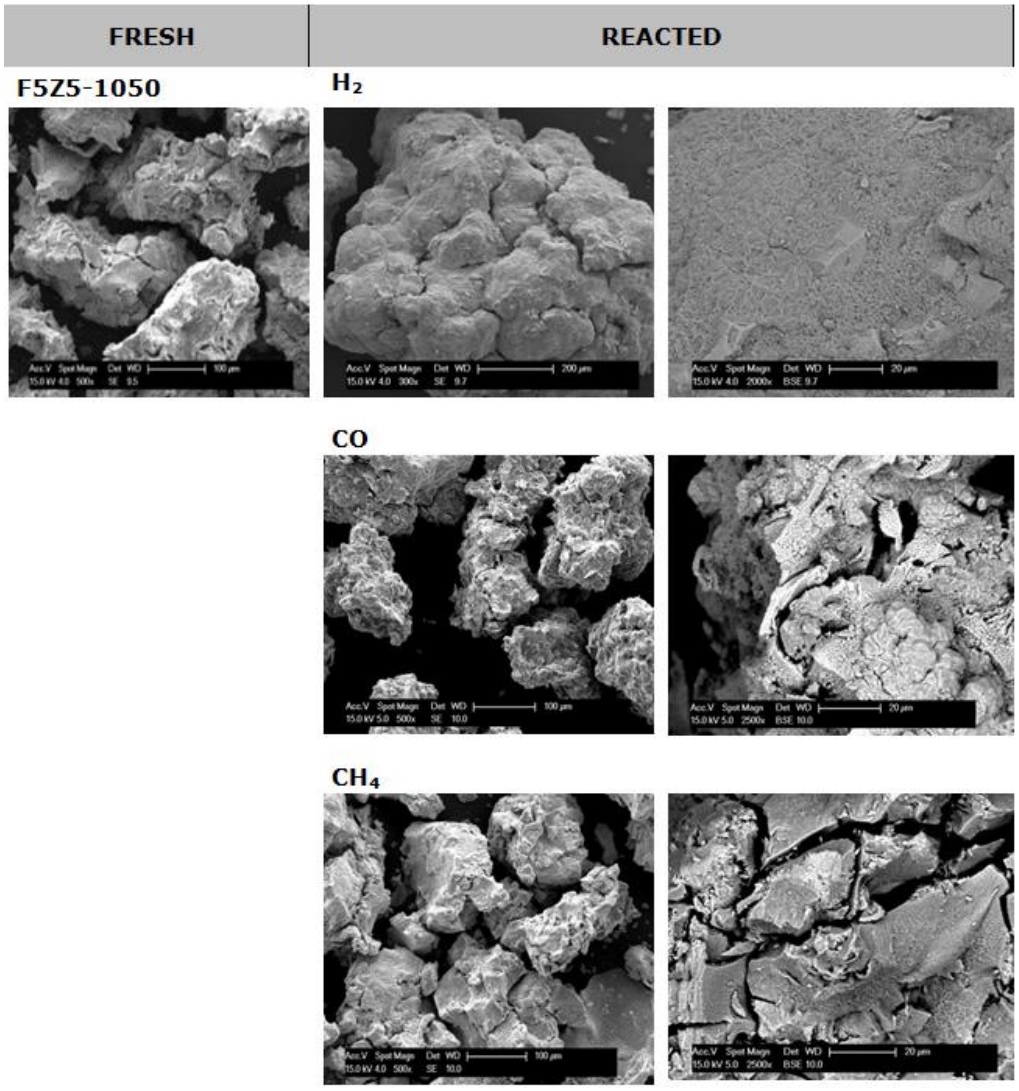

Figure 4.26: SEM images of the unreacted F5Z5-1050 particles after calcination at 1323 K for 2 h and reacted F5Z5-1050 particles after five redox cycles at 1173 K in H_2, CO or CH_4. The images at the right column (with scale bar corresponding to 20 μm) confirm the occurrence of pores in reactions with CO or CH_4.

Table 4.4: Phase Composition of the Oxygen Carriers identified by X-ray Diffraction.

Oxygen carrier	Fresh	After re-oxidation
M5Z5-1050	m-ZrO_2 t- Mn_3O_4	m-ZrO_2 t- Mn_3O_4
M6Z4-1050	m-ZrO_2 t- Mn_3O_4 t-ZrO_2	—
M8Z5-1050	m-ZrO_2 t- Mn_3O_4 t-ZrO_2	—
M5ZCe5-1050	t- Mn_3O_4 t-$(Zr_{0.88}Ce_{0.12})O_2$ c-$Ce_{0.75}Zr_{0.25}O_2$	—
F5Z5-1050	m-ZrO_2 r-Fe_2O_3 t-ZrO_2	m-ZrO_2 r-Fe_2O_3

Key: m-monoclinic, t-tetragonal, c-cubic, r-rhombo

4.5 Conclusions

1. The co-precipitated Mn-oxide based oxygen carriers are more reactive than impregnated Mn oxide OC as well as mechanical mixed iron oxide oxygen carrier.
2. The reactivity of the co-precipitated monometallic oxygen carriers depends on fuel used for combustion and for the reduction reaction, this generally followed the order CH_4 > CO > H_2.
3. It could be inferred that homogenous dispersion of the active metal phase on the support (Figure 4.1) via the co-precipitation technique, and the addition of zirconia contributes to the high reactivity of the oxygen carriers.
4. The best performance was obtained with the M5Z5-1050 oxygen carrier which exhibited high reactivity both in the

reduction and the oxidation processes for the conditions used in this work.

5 BIMETALLIC OXYGEN CARRIERS WITH LOW ZIRCONIA CONTENT SUPPORT: BEHAVIOUR IN DIFFERENT GASES

Various combinations of manganese oxide and iron oxide supported with low zirconia content (20 wt. %) were synthesized, namely: M8FZ2-1050, M6FZ2-1050, M5FZ2-1050, M3FZ2-1050 and M2FZ2-1050 (See Table 3.2). These were evaluated by TGA using hydrogen, carbon monoxide or methane as fuel. Typically, the individual elements (Mn, Fe and Zr) appear to be well dispersed in the composite material. This is illustrated in Figure 5.1 for the sample M8FZ2-1050. The elemental concentrations (indicated by unique colour) show that Mn, Fe, and Zr are well dispersed (at a scale of 70 μm) without position of exclusions.

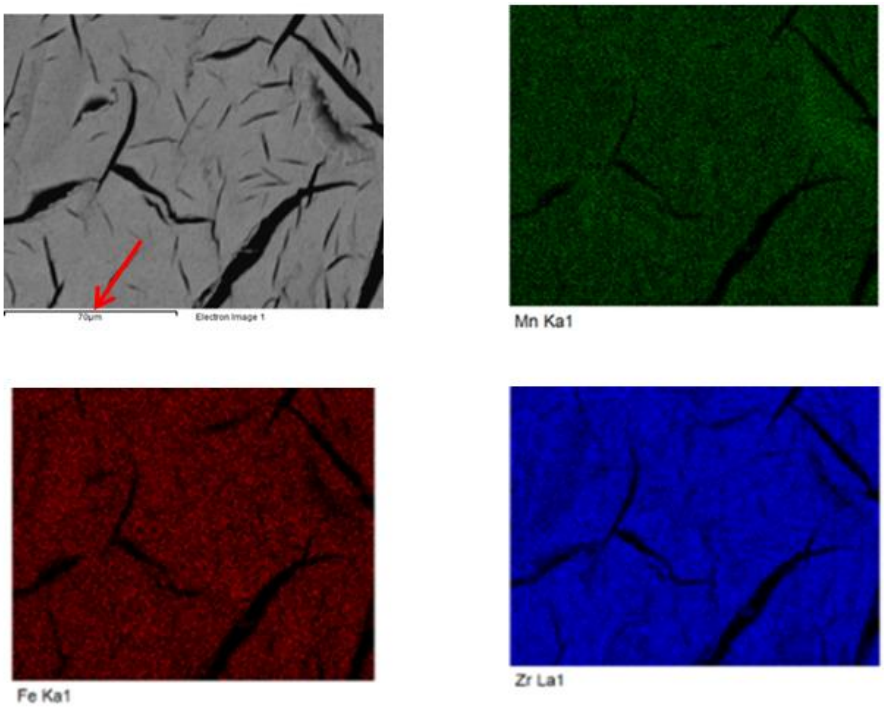

Figure 5.1 SEM-EDX map of fresh M8FZ2-1050 after calcination at 1323 K in air for 2 h showing distribution of the elements. The scale bar indicated by the arrow represents 70 μm. The SEM-EDX analysis confirms Mn, Fe and Zr are well dispersed.

Hereafter, the behaviour of this batch of bimetallic oxygen carriers is presented in this chapter following the same sequence used in the preceding chapter.

5.1 Reduction/Oxidation in Hydrogen

5.1.1 Reactivity

The fractional conversions of the redox reactions for the five oxygen carriers (M8FZ2-1050, M6FZ2-1050, M5FZ2-1050, M3FZ2-1050 and M2FZ2-1050) are presented in Figure 5.2. Clearly, the reactivity of the oxygen carriers is dependent on the single metal oxide compositions in the composite material. Generally, in reduction and oxidation, the reactivity of the OCs increases with increasing fraction of manganese oxide content exception for M3FZ2-1050 which displayed slightly higher reactivity than M5FZ2-1050.

Furthermore, all OCs showed an initial fast reaction step followed by a slow step in the reduction cycles. M8FZ2-1050, M3FZ2-1050 and M5FZ2-1050 reached full conversion while M6FZ2-1050 and M2FZ2-1050 achieved conversion of 0.85 and 0.89 respectively.

The Mn-rich OC was fastest to reach fractional conversion of 0.3 whereas the Fe-rich oxide OC reached the same conversion for longer time as presented in Figure 5.3. This result thus, correlates well with the trend in the reactivity observed in Chapter 4, where the monometallic manganese oxide OCs exhibited very fast reactions compared to iron oxide OCs which displayed much slower reactivity.

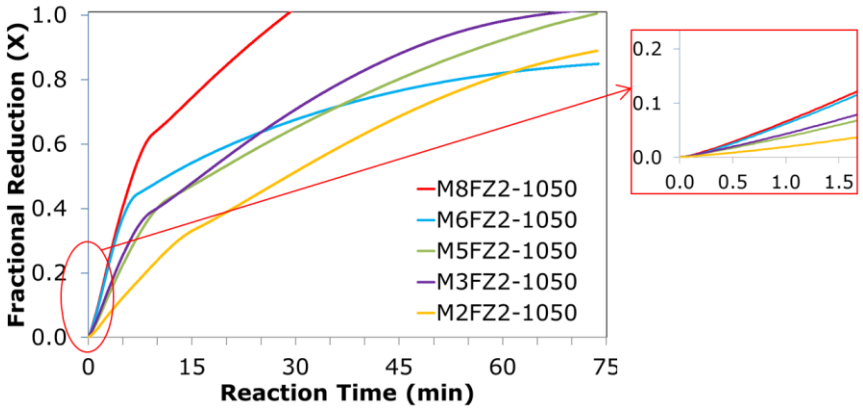

(a) Reduction

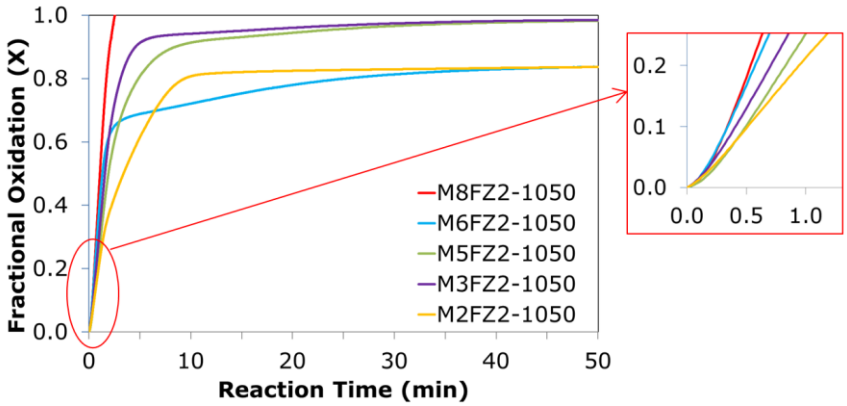

(b) Oxidation

Figure 5.2: Fractional conversion as a function of time for bimetallic oxygen carriers with 20 wt. % zirconia for the (a) 4th reduction cycles in 5% H_2 and (b) 4th oxidation cycles in air at 1173 K, particle size of 75-250 μm and feed gas flow rate of 20 ml/min for the transition from Fe_2O_3 to Fe and from Mn_3O_4 to MnO.

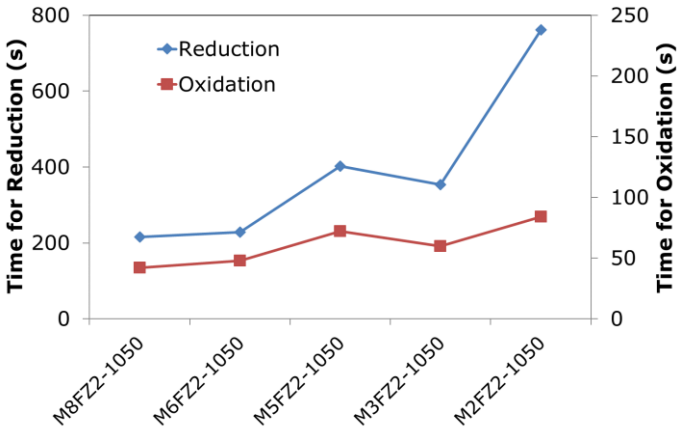

Figure 5.3: Time needed to reach fractional conversion of 0.3 for the bimetallic oxygen carriers with 20 wt. % zirconia for the 4th reduction cycles in 5% H_2 and 4th oxidation cycles in air at 1173 K, particle size of 75-250 μm and feed gas flow rate of 20 ml/min for the transition from Fe_2O_3 to Fe and from Mn_3O_4 to MnO.

A comparison of reduction and oxidation rates for the different oxygen carriers is presented in Figure 5.4. Clearly, oxidation rates were faster than reduction rates for all OCs. Also, as expected (see Section 4.1.1), the reactivity trend suggests that the synergistic effect of Mn on Fe varies with the ratios of the single oxides in the composite material. Furthermore, the maximum rate of reaction of OCs in reduction and oxidation increased with increasing manganese oxide content in the composite material except for M3FZ2-1050 which exhibited higher maximum rate of reaction than M5FZ2-1050.

Two step reactions were quite pronounced for M2FZ2-1050 compared to other OCs. Perhaps, this is not surprising given that M2FZ2-1050 has a high fraction of iron oxide and the defined feature in Figure 5.4 could be reflecting the transition between the different oxidation states of $Fe_2O_3 \rightarrow Fe_3O_4 \rightarrow FeO$. This feature was absent or much weakened for the other OCs suggesting that Mn facilitated the transition between the different oxidation states of Fe.

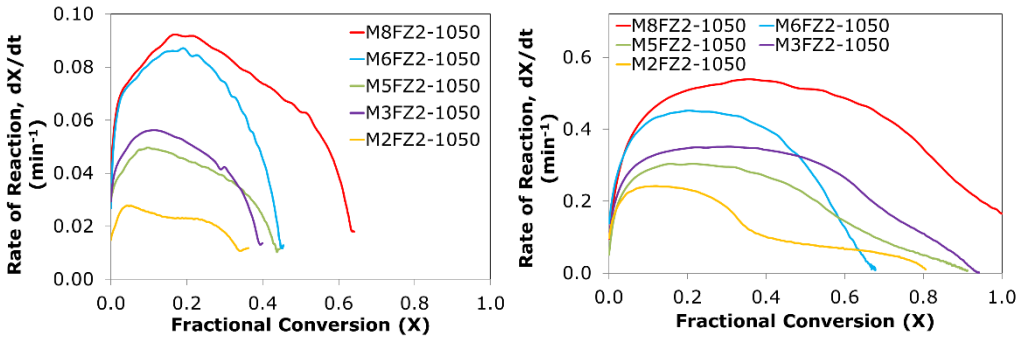

(a) Reduction (b) Oxidation

Figure 5.4: Rate of reaction as a function of fractional conversion for bimetallic oxygen carriers with 20 wt. % zirconia for the (a) 4th reduction cycles in 5% H_2 and (b) 4th oxidation cycles in air at 1173 K, particle size of 75-250 μm and feed gas flow rate of 20 ml/min for the transition from Fe_2O_3 to Fe and from Mn_3O_4 to MnO.

Figure 5.5 shows the maximum rates of mass conversion for the five composite materials. The trend observed in the maximum rate of reduction and oxidation did not translate to similar trend in the maximum rate of mass conversion. This disparity is apparently due to the differences in the oxygen transport capacity of the metal oxides as reflected in Section 2.5.2. Whereas M6FZ2-1050 and M3FZ2-1050 displayed approximately the same maximum rate of mass conversion in reduction, M3FZ2-1050 exhibited the highest rate of mass conversion in oxidation cycle. Moreover, the maximum rate of mass conversion of M3FZ2-1050 was about 17% and 26% more than that of M8FZ2-1050.

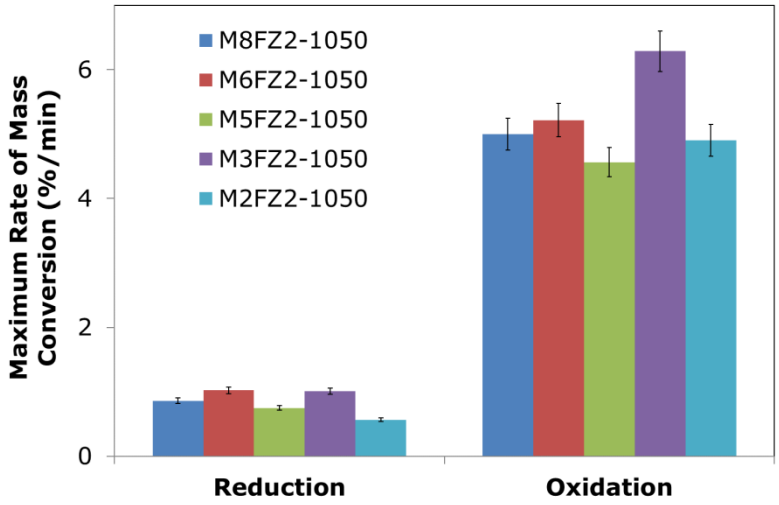

Figure 5.5: Maximum rate of mass conversion for bimetallic oxygen carriers with 20 wt % zirconia for the 4th reduction cycles in 5% H_2 and 4th oxidation cycles in air at 1173 K, particle size of 75-250 µm and feed gas flow rate of 20 ml/min for the transition from Fe_2O_3 to Fe and from Mn_3O_4 to MnO.

5.1.2 Stability and Effect of Repeated Cycles

Figure 5.6 shows that M3FZ2-1050 demonstrated stable redox cycles and maintained relatively stable Roc through the five-cycle test. It is interesting to note that all the other oxygen carriers showed relatively similar stable regeneration behaviour. These results indicate that zirconia

is a suitable support for the co-precipitated Mn-Fe oxygen carriers regardless of the active components composition in the composite material.

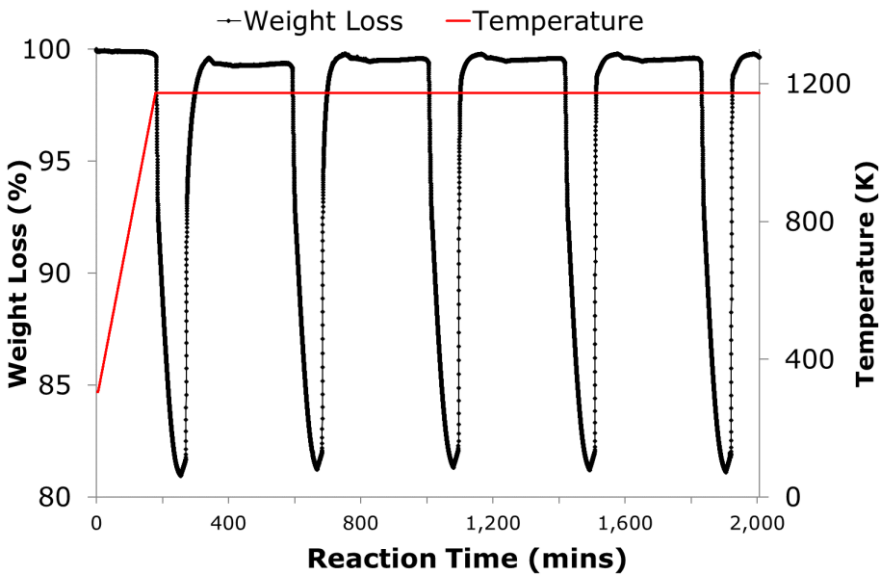

Figure 5.6: Cyclic reduction-oxidation performance of M3FZ2-1050 for the reduction cycles in 5% H_2 and oxidation cycles in air at 1173 K, particle size of 75-250 µm and feed gas flow rate of 20 ml/min for the transition from Fe_2O_3 to Fe and from Mn_3O_4 to MnO**.**

Furthermore, the stability of this batch of bimetallic oxygen carrier was evaluated in terms of maximum rate of mass conversion with regards to repeated cycles. The results shown in Figure 5.7 indicate that the maximum rates of mass conversion for the OCs exhibited an initial decrease between 11% and 39% from the first to the second reduction cycles. In addition, M6FZ2-1050 reduced at an average steady rate of 3% per cycle from the second reduction cycle. This behaviour could possibly be due to the internal restructuring of the fresh oxygen carrier in the first cycle. Other possible reason will be discussed in Section 5.3.

In contrast to the behaviour observed in reduction reaction, the maximum rates of mass conversion during oxidation were relatively stable for all

oxygen carriers through the five cycles. Nevertheless, from the fourth oxidation cycle, M2FZ2-1050, M3FZ2-1050 and M5FZ2-1050 displayed slight downward trend in the maximum rates of mass conversion as shown in Figure 5.7b.

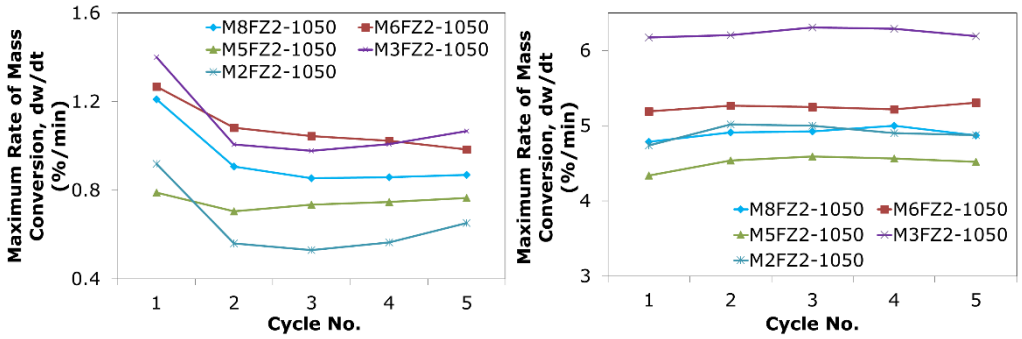

(a) Reduction (b) Oxidation

Figure 5.7: Maximum rate of mass conversion versus cycle number for bimetallic oxygen carriers with 20 wt. % zirconia for the (a) 4th reduction cycles in 5% H_2 and (b) 4th oxidation cycles in air at 1173 K, particle size of 75-250 µm and feed gas flow rate of 20 ml/min for the transition from Fe_2O_3 to Fe and from Mn_3O_4 to MnO.

5.1.3 Effect of Particle Size

The fractional conversion (X) for all the oxygen carriers for the two size fractions (75-250 and 300- 850 µm) are presented in Figure 5.8 and 5.9. Clearly, the oxygen carriers of 75-250 µm size fractions exhibited higher reactivity compared to the larger particle sizes. Also, the reduction conversions reached by the 300-850 µm size OCs achieved lower conversions compared to 75-250 µm OCs except for M8FZ2-1050. For instance, the conversion for M3FZ2-1050 larger particle size was reduced by about 25% in reduction and oxidation reactions relative to the small particle size OC.

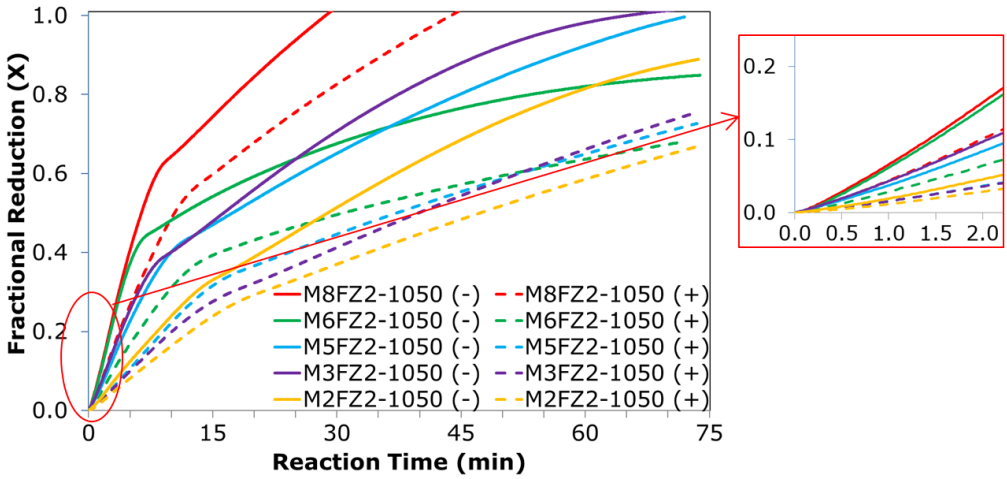

Figure 5.8: Effect of particle size on the reactivity of bimetallic oxygen carriers with 20 wt. % zirconia for the 4th reduction cycles in 5% H_2 at 1173 K and feed gas flow rate of 20 ml/min for the transition from Fe_2O_3 to Fe and from Mn_3O_4 to MnO. Particle sizes: (—) 75-250 µm, (+) 300-850 µm.

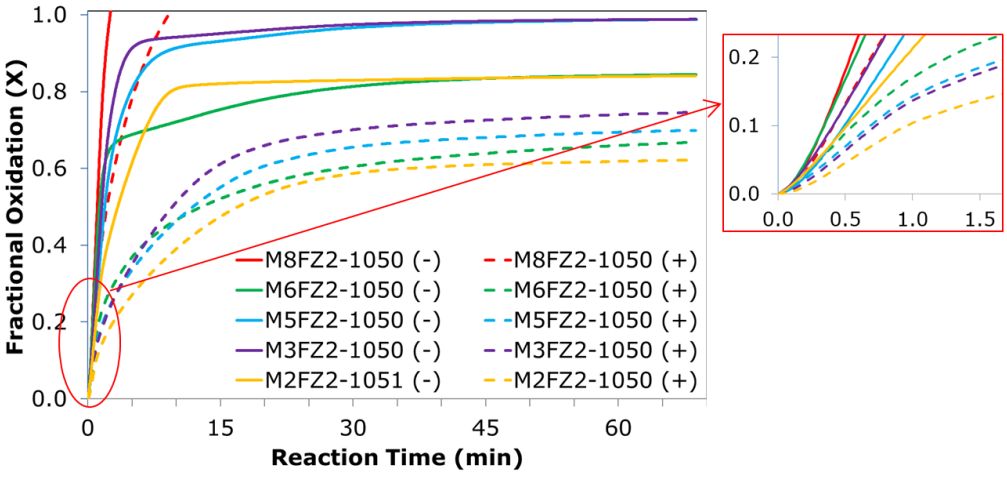

Figure 5.9: Effect of particle size on the reactivity of the bimetallic oxygen carriers with 20 wt. % zirconia for the 4th oxidation cycles in air at 1173 K and feed gas flow rate of 20 ml/min for the transition from Fe_2O_3 to Fe and from Mn_3O_4 to MnO. Particle sizes: (—) 75-250 µm, (+) 300-850 µm.

Moreover, it was observed that the small particle size reached fractional conversion (X) of 0.3 between 1.4 to 4.2 times faster compared to larger sized particles (Figure 5.10).

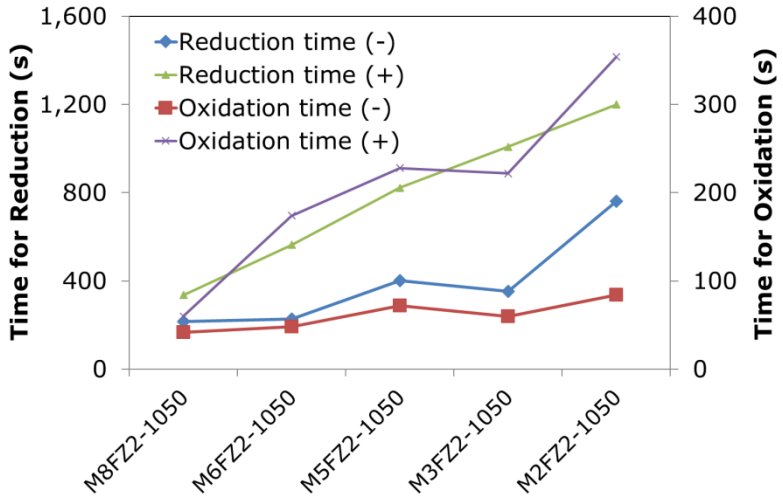

Figure 5.10: Time needed to reach fractional conversion of 0.3 for the bimetallic oxygen carriers with 20 wt. % zirconia for the 4th reduction cycles in 5% H_2 and 4th oxidation cycles in air at 1173 K. Particle sizes: (—) 75-250 µm, (+) 300-850 µm.

Additionally, Table 5.1 shows the effect of particle size on maximum rate of conversion. The result showed that for OCs with 33 - 67 wt. % Mn content, the reactivity for smaller size fractions were about or more than twice that of the corresponding 300-850 µm in oxidation and reduction. Similarly, smaller size fractions for M8FZ2-1050 and M2FZ2-1050 were about 1.4 to 1.8 times more reactive in reduction and oxidation reactions.

Table 5.1: Effect of particle size on maximum rate of mass of conversions bimetallic oxygen carriers with 20 wt. % zirconia.

Oxygen carriers	**Relative maximum rate of mass conversion ratio (75-250 /300-850 µm)**	
	Reduction	**Oxidation**
M8FZ2-1050	1.4	1.5
M6FZ2-1050	2.3	2.1
M5FZ2-1050	2.1	1.8
M3FZ2-1050	2.7	2.0
M2FZ2-1050	1.5	1.8

Generally, the observed particle size effect for this batch of oxygen carriers suggests there is possible significant internal mass transfer limitation due to the low zirconia content. This agrees well with the observed findings from SEM analysis (Section 5.3) and values of the effectiveness factor (η) which were far less than unity as well as high values of Thiele modulus (ϕ) (Table F.5, Appendix F). The results from material characterization (SEM images) after reactivity show that the OCs with low zirconia content with the exception of M8FZ2-1050 formed agglomerates using H_2 as reacting gas. The agglomeration of these OCs resulted in the internal mass transfer limited reactions. The onset of internal mass transfer resistance can be attributed to the effect of deactivation by sintering which occurs when there is reduced reactivity as a result of the loss of active surface area at the onset of agglomeration. This leads to the closure of internal pores and subsequently limiting the internal mass transfer process from the external surface to the internal pore surface (Klaewkla, Arend and Hoelderich, 2011; Rahaman, 2015; Fogler, 2006).

5.1.4 Comparison of Mass Loss Profile for the Different Particle Size Fractions

Figure 5.11 and Figure 5.12 show the TGA mass loss profile of M3FZ2-1050 for 75-250 and 300-850 μm size fractions respectively. The mass loss for the smaller size fraction was relatively maintained for the redox multi-cycles.

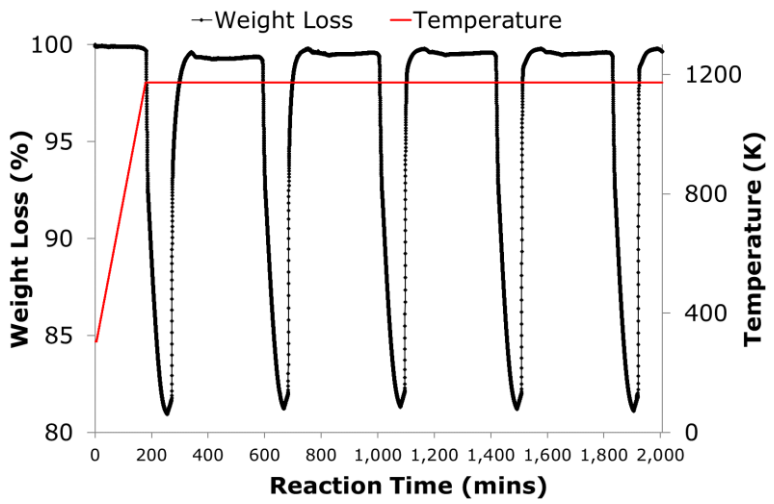

Figure 5.11: Cyclic reduction-oxidation performance of M3FZ2-1050 for the reduction cycles in 5% H_2 and oxidation cycles in air at 1173 K, particle size of 75-250 µm and feed gas flow rate of 20 ml/min for the transition from Fe_2O_3 to Fe and from Mn_3O_4 to MnO.

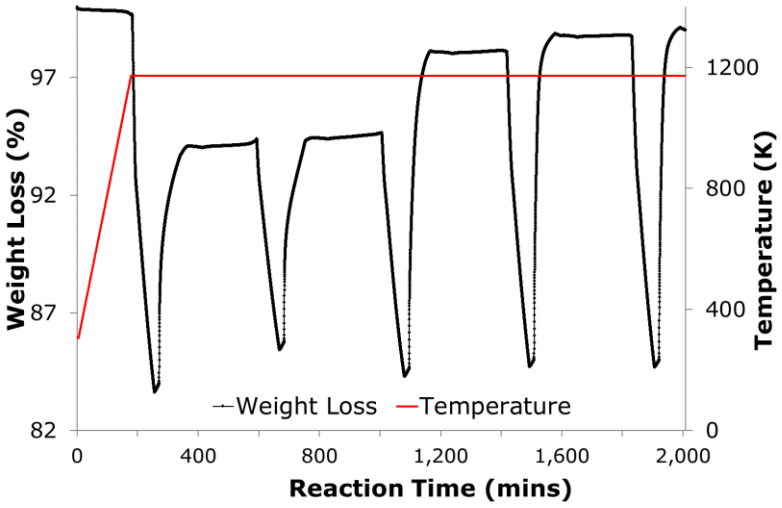

Figure 5.12: Cyclic reduction-oxidation performance of M3FZ2-1050 for the reduction cycles in 5% H_2 and oxidation cycles in air at 1173 K, particle size of 300-850 µm and feed gas flow rate of 20 ml/min for the transition from Fe_2O_3 to Fe and from Mn_3O_4 to MnO.

On the other hand, reduction of about 71% in the mass loss was observed for the larger particle size after the first cycle. Thereafter, these OCs seems to activate from the third cycle. This characteristic behaviour (with varying reduction of mass loss between 11 to 71%) was observed for all

the other OCs of particle size 300-850 μm regardless of metal oxide compositions. Similar characteristic behaviour was also observed for the maximum rate of mass conversion for these larger particle size oxygen carriers.

From these results, it was thus concluded that for the bimetallic oxygen carriers with a low zirconia content support of 20 wt. %, the 75-250 μm size OCs exhibit better performance in terms of reactivity than OCs of 300-850 μm size for CLC using hydrogen as fuel.

5.2 Reduction/Oxidation in Carbon Monoxide

5.2.1 Reactivity

From the previous section in which results using H_2 were presented, it was observed that M8FZ2-1050 and M3FZ2-1050 exhibited the best performance in H_2. Consequently, these OCs were selected for further test in TGA using carbon monoxide as fuel. The results presented in Figure 5.13 revealed that M8FZ2-1050 displayed higher reactivity than M3FZ2-1050 in reduction and oxidation. This result is thus similar to that obtained in reaction with H_2. Also, M8FZ2-1050 reached fractional conversion (X) of 0.95 in oxidation in 49 s while M3FZ2-1050 was much slower and reached conversion 0.82 in reduction.

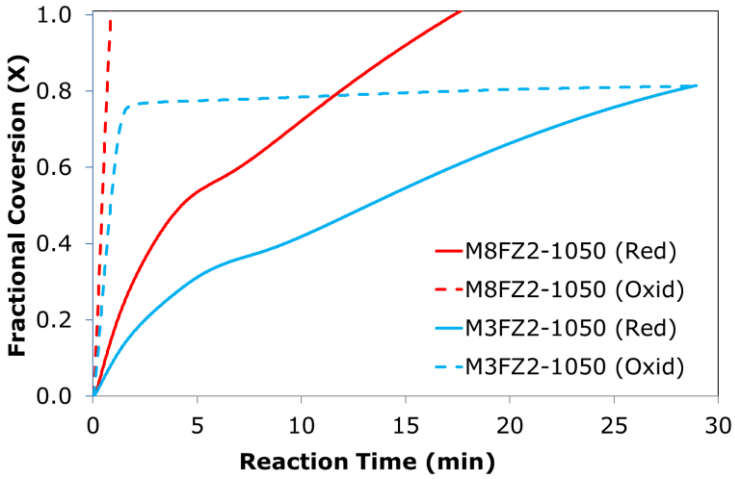

Figure 5.13: Fractional conversion as a function of time for M8FZ2-1050 and M3FZ2-1050 oxygen carriers for the 4th reduction cycles in 10% CO and 4th oxidation cycles in air at 1173 K, particle size of 75-250 µm and feed gas flow rate of 50 ml/min for the transition from Fe_2O_3 to Fe and from Mn_3O_4 to MnO. (Red) signifies reduction and (Oxid) oxidation.

The time needed to reach fractional conversions (X) of 0.3 is presented in Table 5.2. The reduction reactions for M8FZ2-1050 and M3FZ2-1050 were 1.9 and 1.3 times faster in CO than in H_2 respectively. Correspondingly, their oxidation reactions were 2.3 and 1.9 times faster in oxidation. Hence, it could be concluded that reactions in CO was faster than in H_2.

Table 5.2: Time needed to reach fractional conversion (X) of 0.3 for M8FZ2-1050 and M3FZ2-1050 oxygen carriers with 20 wt. % zirconia.

Oxygen carriers	Reduction time (s)	Oxidation time (s)
M8FZ2-1050	112	18
M3FZ2-1050	272	31

The rate of reaction as a function of the fractional conversion for the fast reaction step is shown in Figure 5.14. Obviously, M8FZ2-1050 has higher rate of reaction for all values of fractional conversion (X). Moreover, the

maximum rate of reaction for M8FZ2-1050 was nearly twice that of M3FZ2-1050. Interestingly, similar to the oxidation reaction in H_2, M8FZ2-1050 exhibited fast reaction which was relatively sustained through the entire conversion period.

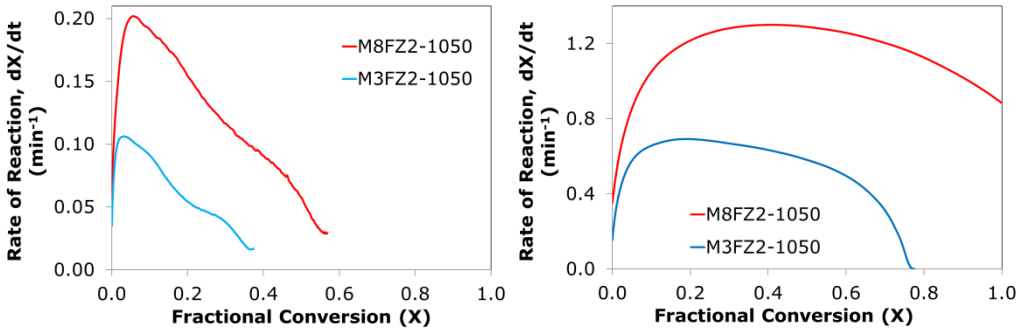

(a) Reduction (b) Oxidation

Figure 5.14: Rate of reaction as a function of fractional conversion for M8FZ2-1050 and M3FZ2-1050 oxygen carriers for the (a) 4th reduction cycles in 10% CO and (b) 4th oxidation cycles in air at 1173 K, particle size of 75-250 µm and feed gas flow rate of 50 ml/min for the transition from Fe_2O_3 to Fe and from Mn_3O_4 to MnO.

As previously highlighted, the maximum rate of reaction of M8FZ2-1050 was about twice that of M3FZ2-1050. However, a comparison of the maximum rate of mass conversion for these OCs showed that M3FZ2-1050 exhibited slightly higher rate of about 1% and 3% than M8FZ2-1050 in reduction and oxidation respectively (Figure 5.15). Again, this variation may be attributed to the differences in the oxygen transport capacity of the metal oxides as reflected in Section 2.7.2.

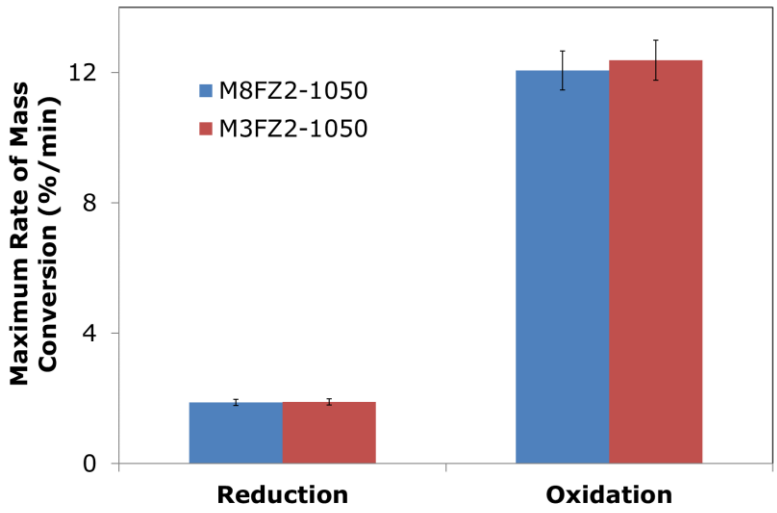

Figure 5.15: Maximum rate of mass conversion for M8FZ2-1050 and M3FZ2-1050 oxygen carriers for the 4th reduction cycles in 10% CO and 4th oxidation cycles in air at 1173 K, particle size of 75-250 μm and feed gas flow rate of 50 ml/min for the transition from Fe_2O_3 to Fe and from Mn_3O_4 to MnO.

5.2.2 Stability and Effect of Repeated Cycles

The stability performance of M8FZ2-1050 and M3FZ2-1050 for the five-cycle test is presented in Figure 5.16. The maximum rates of mass conversion for the OCs were relatively stable through the five cycles in oxidation reactions. On the other hand, an initial decrease was observed in reduction cycle for both OCs. This behaviour was similar to that observed in H_2. After this initial decrease, M8FZ2-1050 maximum rate of mass conversion remained stable whereas that for M3FZ2-1050 exhibited slightly downward trend. The possible reason for this behaviour could be due to agglomeration of particles observed for the OC which will be discussed in Section 5.3.

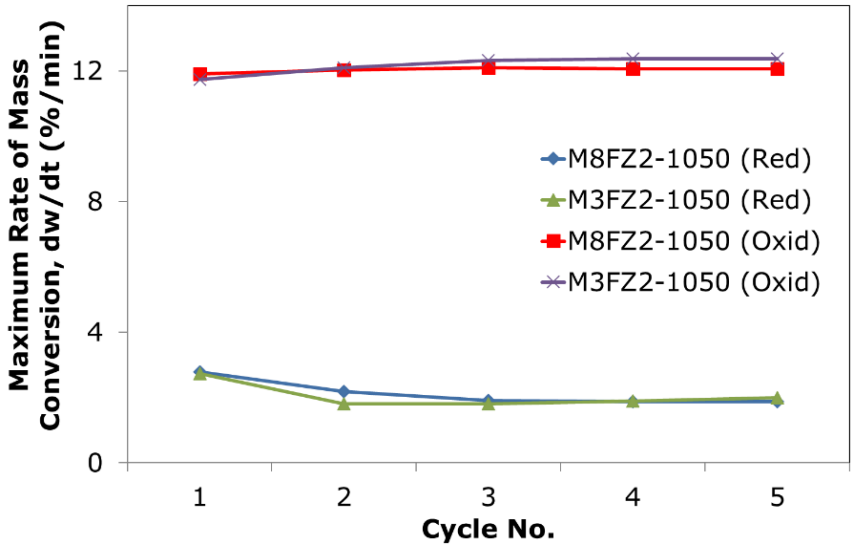

Figure 5.16: Maximum rate of mass conversion versus cycle number for M8FZ2-1050 and M3FZ2-1050 oxygen carriers for the reduction cycles in 10% CO and oxidation cycles in air at 1173 K, particle size of 75-250 μm and feed gas flow rate of 50 ml/min for the transition from Fe_2O_3 to Fe and from Mn_3O_4 to MnO. (Red) signifies reduction and (Oxid) oxidation.

5.2.3 Effect of Particle Size

An investigation for any potential effect of particle size was conducted for M3FZ2-1050 and the results for the third redox cycle are presented in Figure 5.17. The conversion reached by the 300-850 μm particle size OC was 47% and 50% lower than that achieved by OC of 75-250 μm particle size.

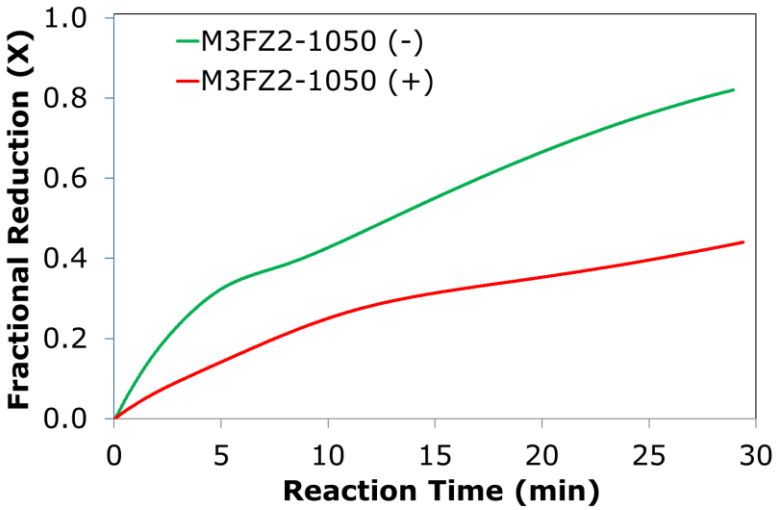

(a) Reduction

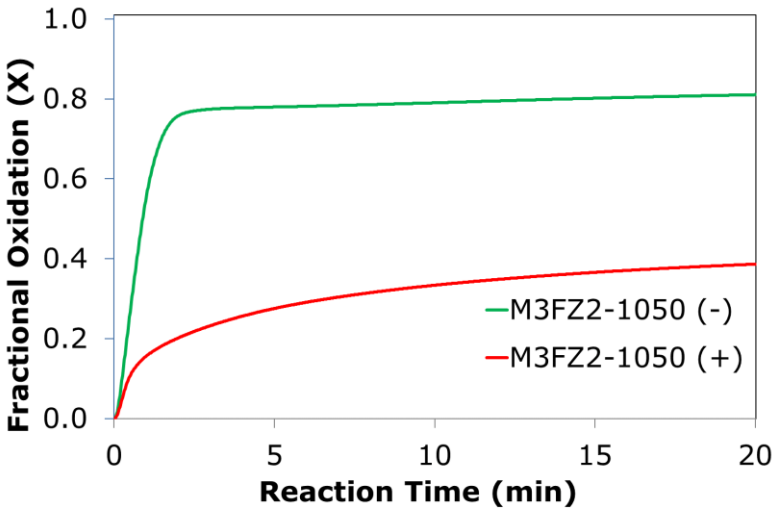

(b) Oxidation

Figure 5.17: Effect of Particle Size on reactivity of M3FZ2-1050 for the 3rd reduction cycle in 10% CO and 3rd oxidation cycle in air at 1173 K and feed gas flow rate of 50 ml/min for the transition from Fe_2O_3 to Fe and from Mn_3O_4 to MnO. Particle sizes: (—) 75-250 μm, (+) 300-850 μm.

Furthermore, the time to reach fractional conversion of 0.3 by the larger particle size OC was increased by 3 and 12 times in reduction and oxidation respectively (Table 5.3).

Table 5.3: Effect of particle size: on time needed to reach fractional conversion (X) of 0.3 for the bimetallic oxygen carriers with 20 wt. % zirconia.

Oxygen carriers	Reduction time (s)		Oxidation time (s)	
	75-250 µm	300-850 µm	75-250 µm	300-850 µm
M3FZ2-1050	254	787	31	377

Also, the maximum rate of mass conversion values for the OC in the smaller size fraction was considerably higher than that for OC in the larger size fraction in reduction and oxidation respectively (Table 5.4). This observation is similar to that obtained in reaction with hydrogen. The values of the effectiveness factor (η) for both particle sizes were far less than unity as well as having high values of Thiele modulus (ϕ) (Table F.5, Appendix F) indicating presence of internal mass transfer resistance. The results from material characterization (SEM images in Section 5.3) after reactivity show that M3FZ2-1050 with low zirconia content formed agglomerates using CO as reacting gas. The agglomeration of this OC resulted in internal mass transfer limiting these reactions.

Table 5.4: Effect of particle size on maximum rate of mass conversion: mixed oxides/20 wt. % zirconia in CO (3rd Cycle).

Oxygen carriers	Relative maximum rate of mass conversion ratio (75-250 microns/300-850 microns)	
	Reduction	Oxidation
M3FZ2-1050	2.4	2.2

From these results, it was concluded that the impact of particle size on conversion of the OC was greater in CO compared to H_2. In addition, the

use of 300-850 μm size fractions offered no improved benefit on the reactivity of M3FZ2-1050.

5.3 Characterization of Fresh and Reacted Oxygen Carriers

The SEM analysis of the bimetallic oxygen carriers with low zirconia content were carried out to help establish any possible structure-activity relationship for the oxygen carriers. The SEM images of the surface morphology (at a scale of 20 – 500 μm) of the samples after reactivity investigations are shown in Figure 5.18. Also, included in Figure 5.18, is an SEM image of unreacted M8FZ2-1050 particle. From Figure 5.18 it could be observed that the Mn-rich oxygen carrier (M8FZ2-1050) is least affected using low zirconia content (20 wt. %) as support. Whereas the other OCs where found to have formed agglomerates, the M8FZ2-1050 particles did not agglomerate. Furthermore, the iron-rich sample, M2FZ2-1050 was found to have developed ruptured particles as seen in Figure 5.18e. These observations are likely due to the rather low zirconia content support. In addition, particle agglomeration was also observed for the reaction in CO as shown in Figure 5.19. It is thus suggested that using 20 wt. % zirconia as support was not sufficient to maintain mechanical integrity of the particles during the redox reactions.

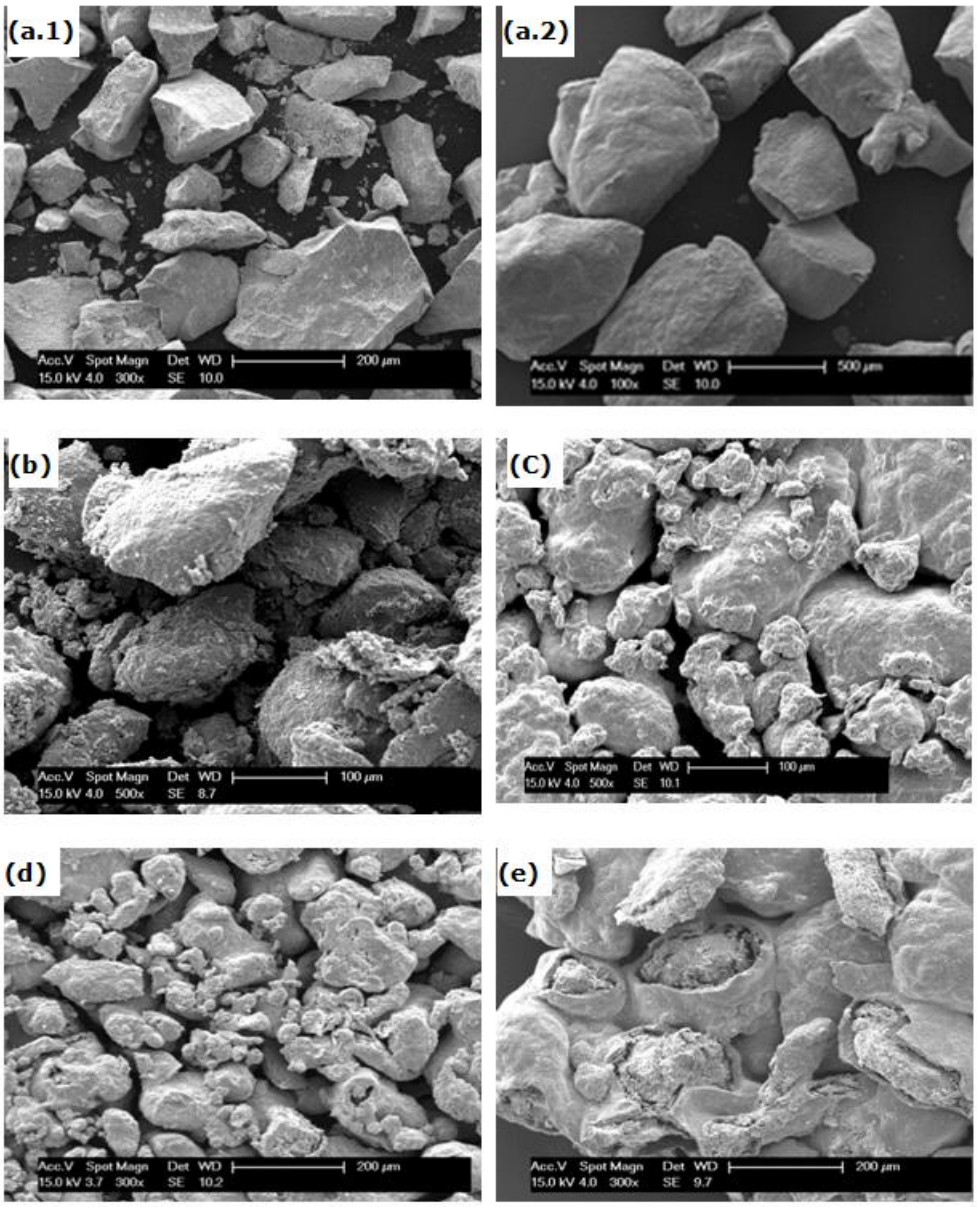

Figure 5.18: SEM images of fresh and reacted bimetallic oxygen carriers (with 20 wt. % zirconia) after five redox cycles at 1173 K in H_2 and air. (a.1) Unreacted M8FZ2-1050 particles after calcination at 1323 K for 2 h. Reacted particles after five redox cycles at 1173 K in H_2: (a.2) M8FZ2-1050 (b) M6FZ2-1050 (c) M5FZ2-1050 (d) M3FZ2-1050 and (e) M2FZ2-1050. The bimetallic oxygen carrier particles (20 wt. % zirconia) agglomerates after the redox reaction except for M8FZ2-1050.

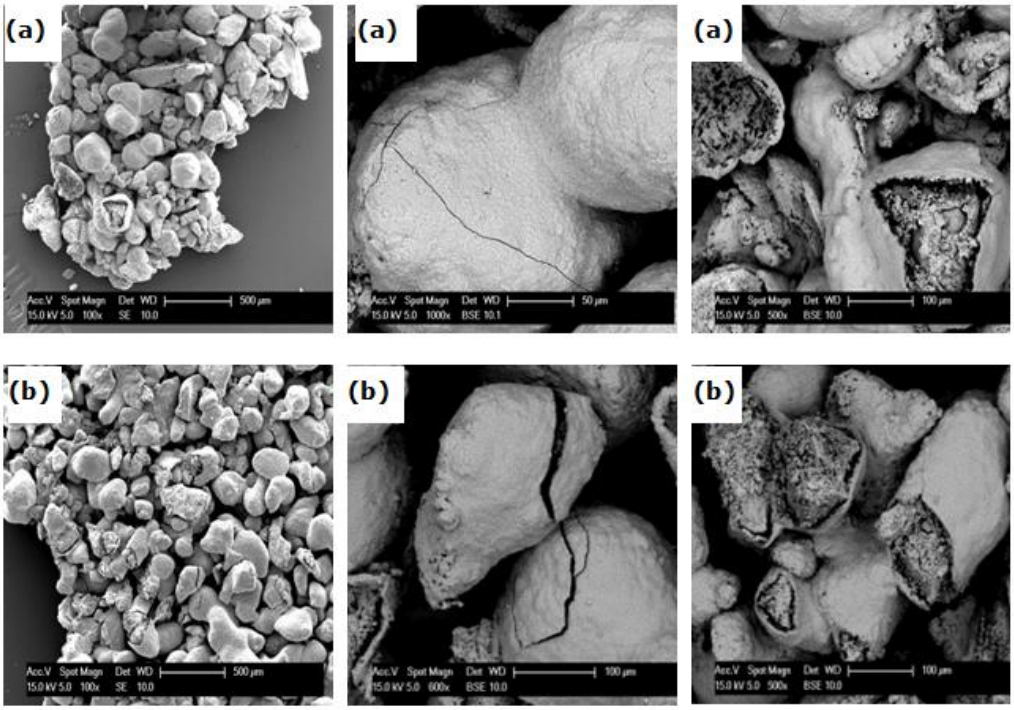

Figure 5.19: SEM images of reacted bimetallic oxygen carriers with 20 wt. % zirconia after five redox cycles at 1173 K in CO and air. (a) M2FZ2-1050 (b) M3FZ2-1050. The bimetallic oxygen carriers form agglomerate and fractures after the redox reactions.

The XRD results presented in Table 5.5 shows that for M8FZ2-1050, no separate peaks were observed for iron oxide. Thus, suggesting that iron oxide is likely incorporated into the cubic bixbyite structure of manganese oxide. Conversely, for iron-rich OC, M2FZ2-1050, no separate peaks for manganese oxide was observed. These observations correlate well with the reactivity results from the TGA where M8FZ2-1050 exhibits the highest reactivity while M2FZ2-1050 was the least reactive.

Table 5.5: Phase composition of the bimetallic oxygen carriers with a low zirconia content (20 wt. %) identified with X-ray Diffraction.

Oxygen carrier	Crystalline phase
M8FZ2-1050	m-ZrO_2 Baddeleyite c-Mn_2O_3 Bixbyite t-ZrO_2
M6FZ2-1050	m-ZrO_2 Baddeleyite c-$MnFe_2O_4$ Jakobsite c-Mn_2O_3 Bixbyite t-ZrO_2
M5FZ2-1050	m-ZrO_2 Baddeleyite c-$MnFe_2O_4$ Jakobsite c-Mn_2O_3 Bixbyite r-Fe_2O_3 Hematite
M3FZ2-1050	m-ZrO_2 Baddeleyite r-Fe_2O_3 Hematite c-Mn_2O_3 Bixbyite t-ZrO_2
M2FZ2-1050	m-ZrO_2 Baddeleyite r-Fe_2O_3 Hematite

Key: m-monoclinic, t-tetragonal, c-cubic, r-rhombo

5.4 Conclusions

The results from this chapter indicate that:

1. Some co-precipitated oxygen carriers supported on zirconia (20 wt. %) could potentially find application for CLC.
2. The Mn-rich OC, M8FZ2-1050 OC appear to have demonstrated the best performance compared to other oxygen carriers in this batch.
3. Generally, reactivity of these oxygen carriers in carbon monoxide was faster compared to reaction in hydrogen.

4. Moreover, some of these oxygen carriers were found to have formed agglomerates during the TGA experiments especially for reactions in hydrogen. It was speculated that this shortcoming could be avoided by increasing the zirconia content in the composite material.

   Against the backdrop of the shortcoming observed on the bimetallic oxygen carriers with low zirconia content support (20 wt. %), a series of co-precipitated bimetallic oxygen carriers with high zirconia content support (44 wt. %) was synthesized and investigated in TGA. Hereafter, the behaviour of these series of oxygen carriers are presented and analysed in detail in the next chapter.

6 BIMETALLIC OXYGEN CARRIERS WITH HIGH ZIRCONIA CONTENT SUPPORT: BEHAVIOUR IN DIFFERENT GASES.

Against the backdrop of the findings in the preceding chapter, co-precipitated bimetallic oxygen carriers with high zirconia content (44 wt. %) was synthesized and denoted as M8FZ5-1050, M6FZ5-1050, M5FZ5-1050, M3FZ5-1050, and M2FZ5-1050 (see Table 3.2). The elements (Mn, Fe and Zr) appear to be well dispersed in the composite material. This is illustrated in Figure 6.1, which shows that the elemental concentrations of Mn, Fe and Zr (indicated by unique colours) in the M5FZ5-1050 are well dispersed at a scale of 50 μm.

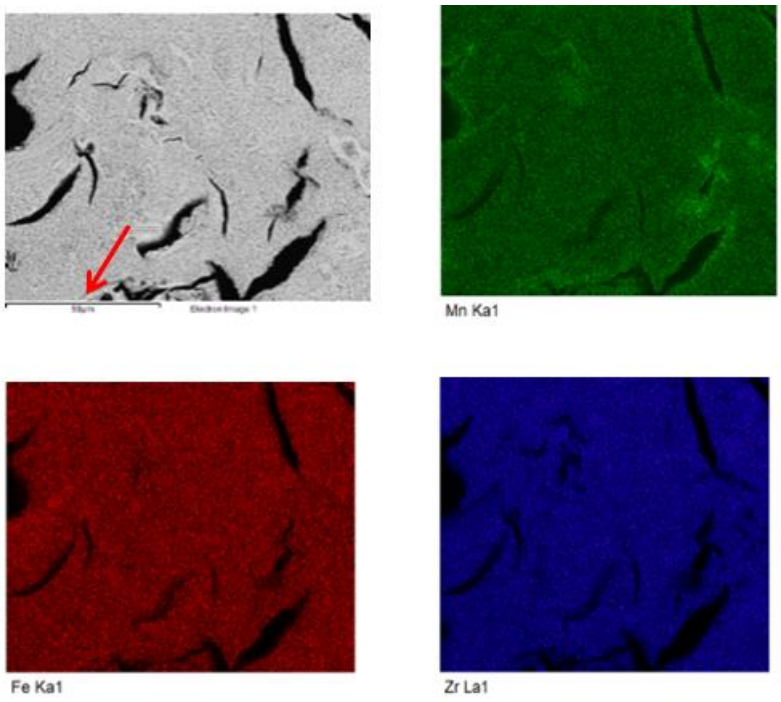

Figure 6.1: SEM-EDX map of fresh M5FZ5-1050 after calcination at 1323 K for 2 h showing distribution of the elements. The scale bar indicated by the arrow represents 50 μm. The SEM-EDX analysis confirms Mn, Fe and Zr are well dispersed.

The behaviour of this batch of co-precipitated bimetallic oxygen carriers with high zirconia content (44 wt. %) were investigated in TGA utilizing hydrogen, carbon monoxide or methane as fuel. The results obtained are presented in this chapter.

6.1 Reduction/Oxidation in Hydrogen

6.1.1 Reactivity

Co-precipitated bimetallic oxygen carriers supported on zirconia (44 wt. %) namely M8FZ5-1050, M6FZ5-1050, M5FZ5-1050, M3FZ5-1050, and M2FZ5-1050 (see Table 3.2) were investigated in TGA and the results on fractional conversion are presented in Figure 6.2. The synergistic effect observed here, is similar to the trend obtained for the co-precipitated bimetallic series supported on zirconia (20 wt. %). As shown in Figure 6.2, reactivity increased with increasing Mn content in reduction and oxidation reactions.

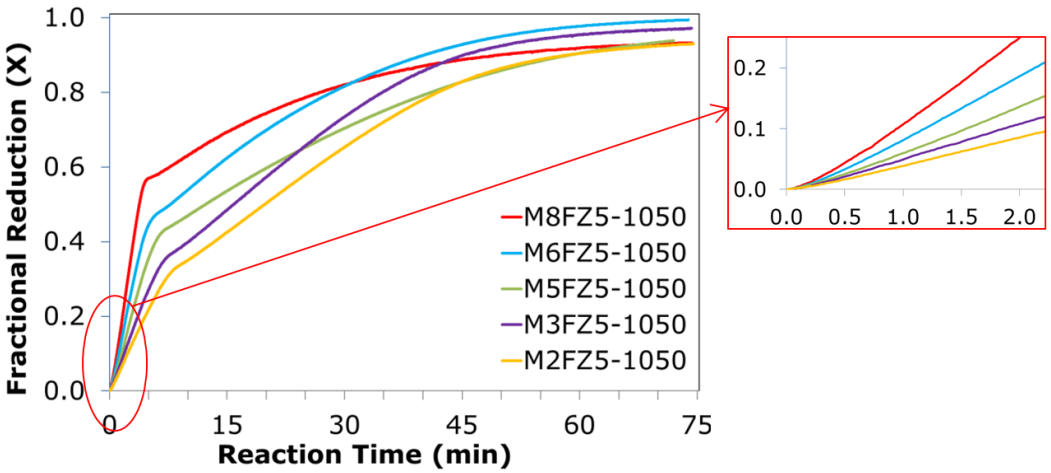

(a) Reduction

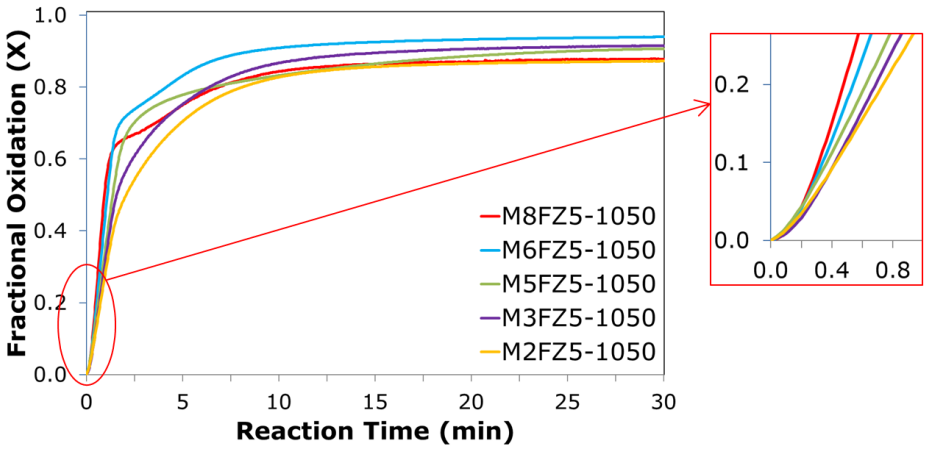

(b) Oxidation

Figure 6.2: Fractional conversion as a function of time for bimetallic oxygen carriers with 44 wt. % zirconia for the (a) 4th reduction cycles in 5% H_2 and (b) 4th oxidation cycles in air at 1173 K, particle size of 75-250 µm and feed gas flow rate of 20 ml/min for the transition from Fe_2O_3 to Fe and from Mn_3O_4 to MnO.

Also, the fractional conversions for the reduction reaction were 93%, 99%, 94%, 97% and 93% for M8FZ5-1050, M6FZ5-1050, M5FZ5-1050, M3FZ5-1050, and M2FZ5-1050 respectively. Furthermore, the time required by these OCs to achieve fractional conversion of 0.3 is presented in Figure 6.3.

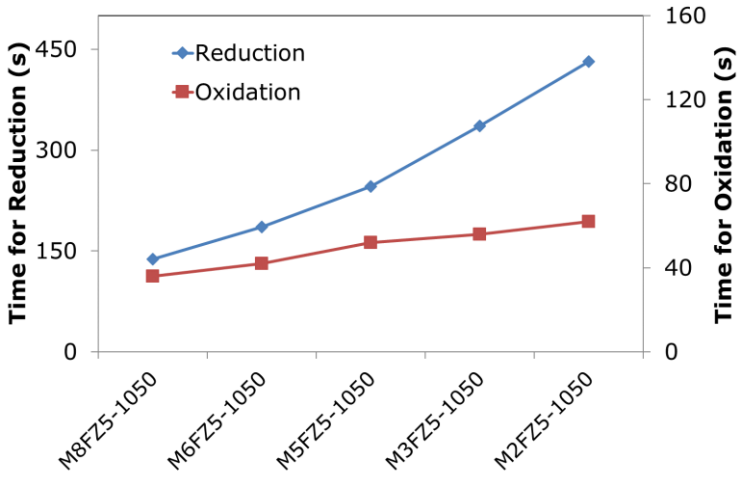

Figure 6.3: Time needed to reach fractional conversion of 0.3 for the bimetallic oxygen carriers with 44 wt. % zirconia for the 4th reduction cycles in 5% H_2 and 4th oxidation cycles in air at 1173 K, particle size of 75-250 µm and feed gas flow rate of 20 ml/min for the transition from Fe_2O_3 to Fe and from Mn_3O_4 to MnO.

The rate of reaction versus fractional conversion (X) for this series of OCs is shown in Figure 6.4. The maximum rate of reaction increased with increasing manganese content in the reduction and oxidation reactions.

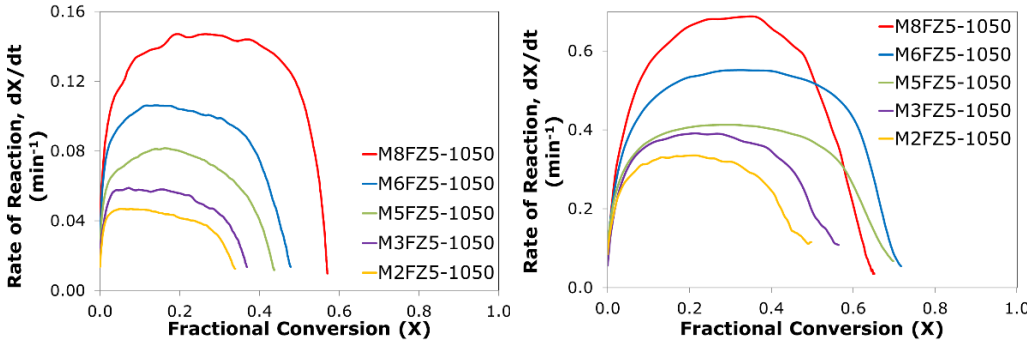

(a) Reduction (b) Oxidation

Figure 6.4: Rate of reaction as a function of fractional conversion for bimetallic oxygen carriers with 44 wt. % zirconia at 1173 K for the (a) 4th reduction cycles in 5% H_2 and (b) 4th oxidation cycles in air at 1173 K, particle size of 75-250 μm and feed gas flow rate of 20 ml/min for the transition from Fe_2O_3 to Fe and from Mn_3O_4 to MnO.

Also, in reduction and oxidation, the extent of fractional conversion for the fast reaction step was found to be increasing with manganese content except for M8FZ5-1050 in oxidation period (see Figure 6.4). The maximum rate of mass conversion for the oxygen carriers is presented in Figure 6.5; showing that this increases with increasing Mn content in reduction reaction.

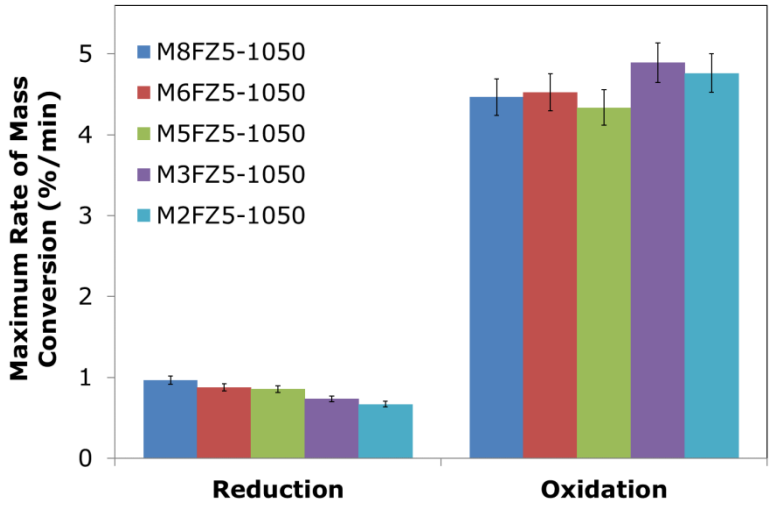

Figure 6.5: Maximum rate of mass conversion for bimetallic oxygen carriers with 44 wt. % zirconia for the 4th reduction cycles in 5% H_2 and 4th oxidation cycles in air at 1173 K, particle size of 75-250 µm and feed gas flow rate of 20 ml/min for the transition from Fe_2O_3 to Fe and from Mn_3O_4 to MnO.

6.1.2 Stability and Effect of Repeated Cycles

Figure 6.6 shows the stable performance of bimetallic M3FZ5-1050 oxygen carrier in hydrogen and air at 1173 K for five multi-cycles. As observed, the weight loss during redox reactions was somewhat stable suggesting no appreciable change in the Roc with repeated cycles. Similar regeneration behaviour was observed for other OCs in this batch during consecutive redox cycles. In comparison to the oxygen carriers with low zirconia content of 20 wt. %, (Section 5.1.2), it could be inferred that increasing the amount of zirconia to 44 wt. % does not appear to negatively alter the regeneration ability of the OCs.

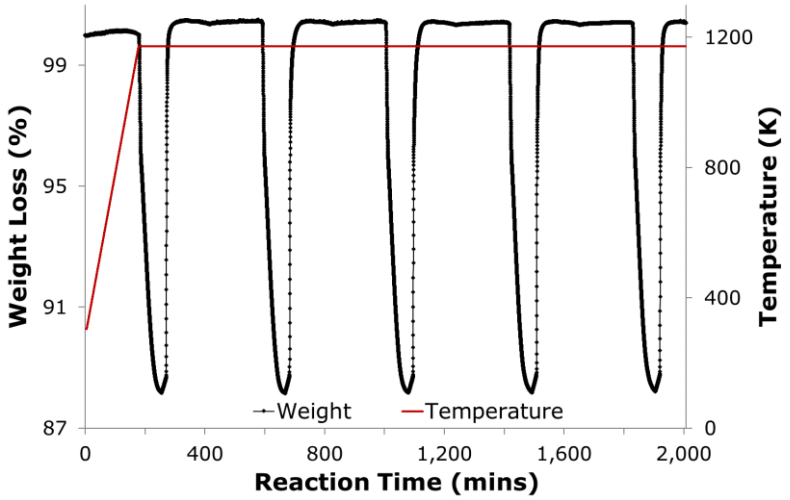

Figure 6.6: Cyclic reduction-oxidation performance of M3FZ5-1050 for the reduction cycles in 5% H_2 and oxidation cycles in air at 1173 K, particle size of 75-250 µm and feed gas flow rate of 20 ml/min for the transition from Fe_2O_3 to Fe and from Mn_3O_4 to MnO.

The stability of the OCs in terms of maximum rate of mass conversion with number of cycles is presented in Figure 6.7. In reduction, the maximum rate of mass conversion was observed to increase with number of cycles for Mn-rich OCs (i.e. M8FZ5-1050 and M6FZ5-1050). The maximum rate of mass conversion showed an increase of 12% in the fifth cycle compared to the first cycle.

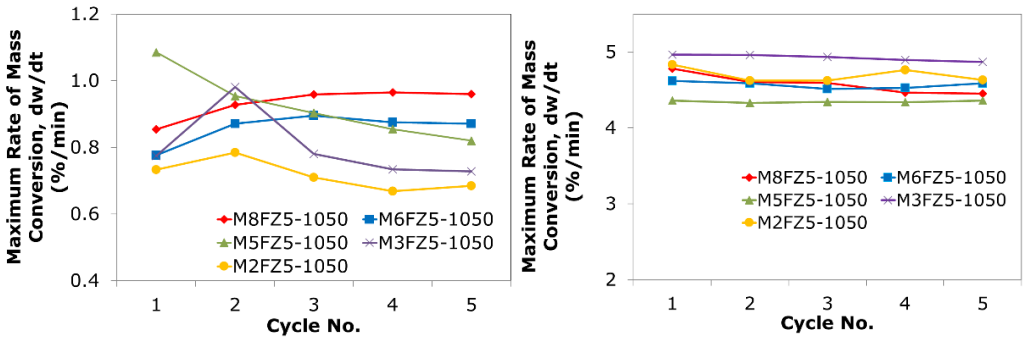

(a) Reduction (b) Oxidation

Figure 6.7: Maximum rate of mass conversion versus cycle number for bimetallic oxygen carriers with 44 wt. % zirconia for the (a) 4th reduction cycles in 5% H_2 and (b) 4th oxidation cycles in air at 1173 K, particle size of 75-250 µm and feed gas flow rate of 20 ml/min for the transition from Fe_2O_3 to Fe and from Mn_3O_4 to MnO.

However, M3FZ5-1050 and M2FZ5-1050 maximum rate of mass conversions initially increased in the second cycle and then gradually reduced as from the third cycle. On the other hand, M5FZ5-1050 progressively reduced at an average rate of 5% per cycle from the second reduction cycle. This behaviour may possibly be due to these OCs undergoing de-alloying during the reduction reaction (Bhavsar et al., 2014). On the contrary, somewhat different trend was observed during oxidation in which all OCs showed relatively stable rate of mass conversion except M8FZ5-1050.

6.1.3 Effect of Particle Size

The effect of particle size was investigated for the M5FZ5-1050 OC. This is to elucidate any potential effect given the decrease of its maximum rate of mass conversion as observed in Section 6.1.2. There seem to be less significant difference in reactivity for the particle sizes as presented in Figure 6.8.

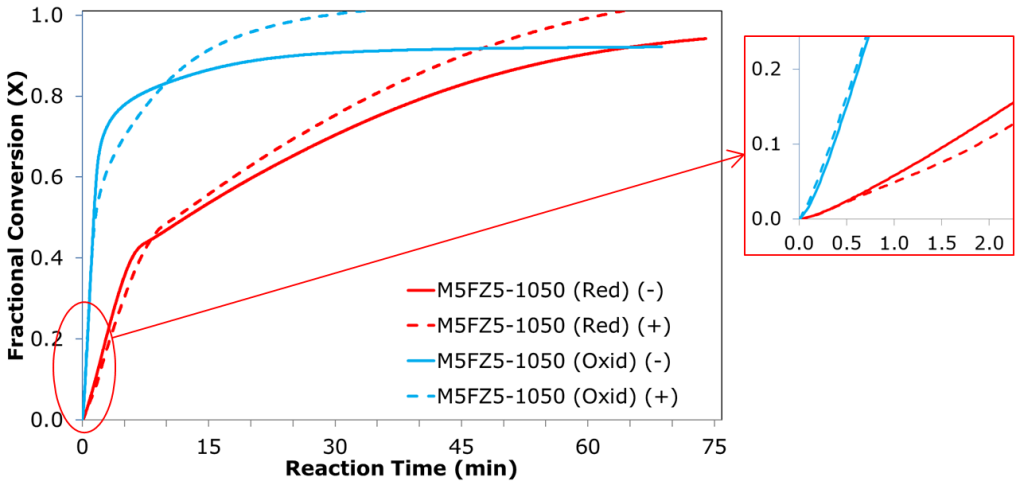

Figure 6.8: Effect of particle size on fractional conversion for M5FZ5-1050 oxygen carrier for the 3rd reduction cycles in 5% H_2 and 3rd oxidation cycles in air at 1173 K and feed gas flow rate of 20 ml/min for the transition from Fe_2O_3 to Fe and from Mn_3O_4 to MnO. Particle sizes: (—) 75-250 µm, (+) 300-850 µm.

Whereas 300-850 µm size OC exhibited complete conversion, the smaller particle only reached 94% and 92% for oxidation and reduction respectively. Also, smaller size fraction OC reached fractional reduction conversion of 0.3 about 1.2 times faster than the larger particle as can be deduced from Table 6.1.

Table 6.1: Time needed to reach fractional conversion of 0.3 for M5FZ5-1050 oxygen carrier in hydrogen for the third cycle.

Oxygen carriers	Reduction time (s)	Oxidation time (s)
M5FZ5-1050 (75-250 µm)	246	52
M5FZ5-1050 (300-850 µm)	296	52

The particle size effect in terms of maximum rate of mass conversion (Figure 6.9) showed that the rate of mass conversion is lower in both reduction and oxidation for larger particle size OCs compared to the smaller particle size.

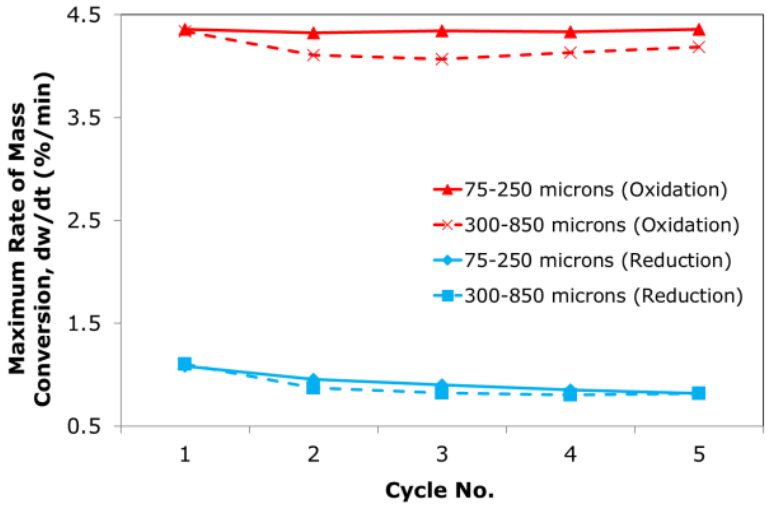

Figure 6.9: Effect of particle size on maximum rate of mass conversion for M5FZ5-1050 oxygen carrier for the reduction cycles in 5% H_2 and oxidation cycles in air at 1173 K, particle size of 75-250 µm and 300-850 µm respectively and feed gas flow rate of 20 ml/min for the transition from Fe_2O_3 to Fe and from Mn_3O_4 to MnO.

From the above findings, it could be concluded that particle size effect was not quite significant which suggests that diffusion limitation may be negligible and the reaction was predominantly chemical controlled. This agrees well with the calculated values of the effectiveness factor (η) for both particle sizes which were close to unity as well as low values of Thiele modulus (ϕ), indicating absence of internal mass transfer limitations (Table F.4, Appendix F). The results from material characterization (SEM images) after reactivity show that M5FZ5-1050 did not agglomerate using H_2 as reacting gas (Section 6.4).

6.1.4 Effect of Temperature

The preceding results for the bimetallic oxygen carriers with high zirconia content support showed that M8FZ5-1050 oxygen carrier tends to exhibit the best performance. Consequently, the effect of temperature on its reactivity was examined in the TGA and the result is presented in Figure 6.10. Generally, reactivity increases with increasing reaction temperature in both reduction and oxidation. Nevertheless, reactivity at 973 K appears to be higher than that of 1073 K for the initial 28% of the oxidation cycle.

In comparison to reaction at 1173 K, the time needed to achieve fractional reduction conversion of 0.3 was 1.8 and 2.8 times more for reaction temperatures 1073 K and 973 K respectively. Similar trend was obtained for the oxidation reaction where reaction temperatures at 1073 K and 973 K require 1.3 and 1.5 times longer to reach fractional conversion of 0.3 respectively.

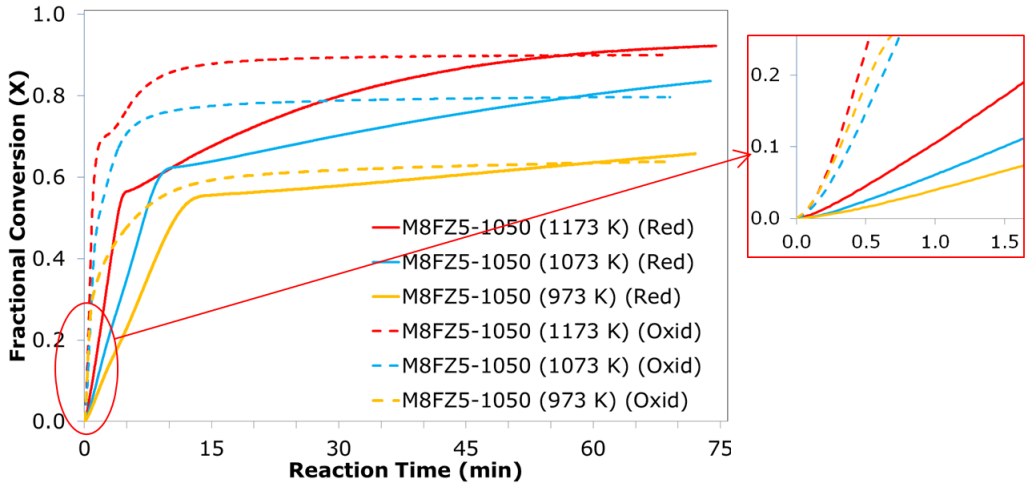

Figure 6.10: Effect of temperature on fractional conversion for M8FZ5-1050 oxygen carrier at 973 K, 1073 K and 1173 K for the 2nd reduction cycles in 5% H_2 and 2nd oxidation cycles in air, particle size of 75-250 µm and feed gas flow rate of 20 ml/min for the transition from Fe_2O_3 to Fe and from Mn_3O_4 to MnO.

The effect of temperature on maximum rate of reaction for M8FZ5-1050 in H_2 is presented in Figure 6.11. In the reduction reaction, the maximum rate of reaction tends to increase with increasing reaction temperature. Moreover, in oxidation reaction, the extent of conversion increased with increasing reaction temperature. The trend for reduction cycle was quite different from that of oxidation given that OC at 1073 K exhibit slightly higher extent of reaction. Clearly, from Figure 6.11a, two step reactions could be observed with the lower reaction temperatures (1073 K and 973 K) in the reduction cycle.

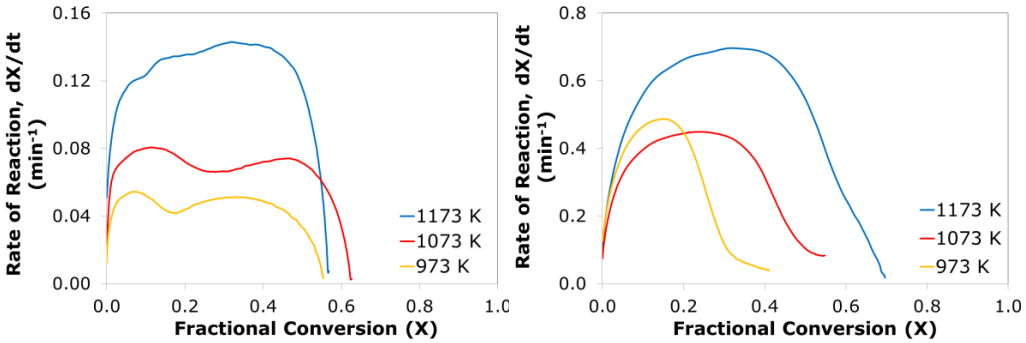

(a) Reduction (b) Oxidation

Figure 6.11: Effect of temperature on maximum rate of reaction versus fractional conversion for M8FZ5-1050 at 973 K, 1073 K and 1173 K for the (a) 2nd reduction cycles in 5% H_2 and (b) 2nd oxidation cycles in air, particle size of 75-250 μm.

The effect of temperature on maximum rate of mass conversion values for M8FZ5-1050 were lower for reaction temperatures (973 K and 1073 K) compared to that of 1173 K. It could be inferred that the maximum rate of mass conversion of reaction at 1173 K was 1.8 and 1.5 times that of reaction at 1073 K and 973 K respectively. Similar trend was observed for the oxidation reaction (Table 6.2).

Table 6.2: Effect of temperature on maximum rate of mass conversion for M8FZ5-1050; ratio of maximum rate of mass conversion at 1173 K to 1073 K and 973 K in hydrogen for the second cycle.

Oxygen carrier	Reaction temperature (K)	Ratio of maximum rate of mass conversion (1173 K/reaction temperature)	
		Reduction	Oxidation
M8FZ5-1050	1073	1.8	1.6
	973	1.5	1.5

Table 6.3 shows the effect of temperature on the oxygen transport capacity (Roc) for M8FZ5-1050. The Roc is dependent on the reaction temperature. The Roc decreases with decreasing temperature in both

reduction and oxidation cycles. This trend correlates well with the behaviour observed in the reactivity of the OC at these temperatures.

Table 6.3: Effect of temperature on the oxygen transport capacity for M8FZ5-1050 for the second cycle at 973 K, 1073 K and 1173 K in hydrogen.

Oxygen carrier	Reaction temperature (K)	Ratio of oxygen transport capacity (1173 K/reaction temperature)	
		Reduction	Oxidation
M8FZ5-1050	1073	1.1	1.1
	973	1.4	1.4

From the above findings with respect to temperatures effect, it was concluded that the optimal reaction temperature for the bimetallic oxygen carrier (M8FZ5-1050) is 1173 K.

6.2 Reduction/Oxidation in Carbon Monoxide

The behaviour of these series of bimetallic oxygen carriers with high zirconia content (44 wt. %) were also investigated in TGA using carbon monoxide as fuel. The results obtained are presented and discussed in this section.

6.2.1 Reactivity

As shown in Figure 6.12, reactivity of the OCs in the reduction cycle increased with increasing Mn content except for M2FZ5-1050 which exhibit slightly higher reactivity than M3FZ5-1050. The OCs achieved 74% to 88% conversion in reduction reaction whereas in oxidation, the conversion achieved was 70% to 95%.

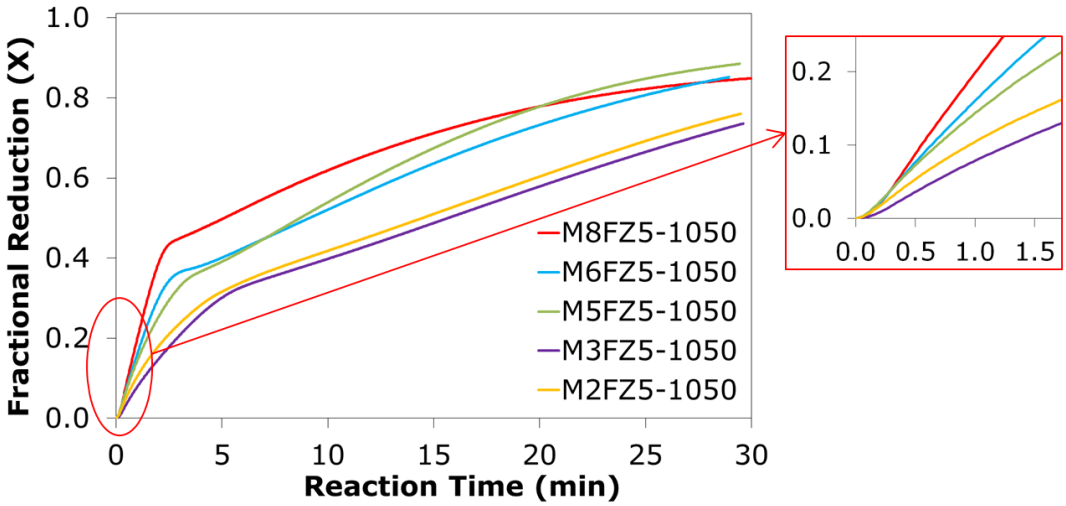

(a) Reduction

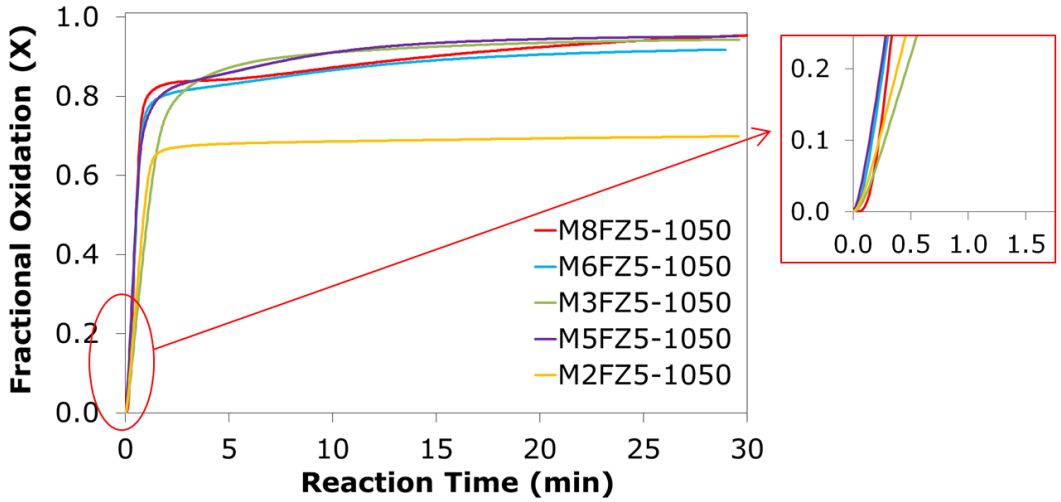

(b) Oxidation

Figure 6.12: Fractional reduction a function of reaction time for the bimetallic oxygen carriers with 44 wt. % zirconia for the (a) 4th reduction cycles in 10% CO and (b) 4th oxidation cycles in air at 1173 K, particle size of 75-250 μm and feed gas flow rate of 50 ml/min for the transition from Fe_2O_3 to Fe and from Mn_3O_4 to MnO.

Furthermore, it can be deduced that reaction of the OCs is faster in the oxidation than in reduction reaction as shown in Figure 6.13. Generally, the reactivity of this batch of bimetallic oxygen carrier in carbon monoxide was faster than in hydrogen. For instance, time needed to achieve conversion of 0.3 in either reduction or oxidation cycle in H_2 was about 1.4

to 2.5 times more than the time in CO for all OC except for M2FZ5-1050 in reduction.

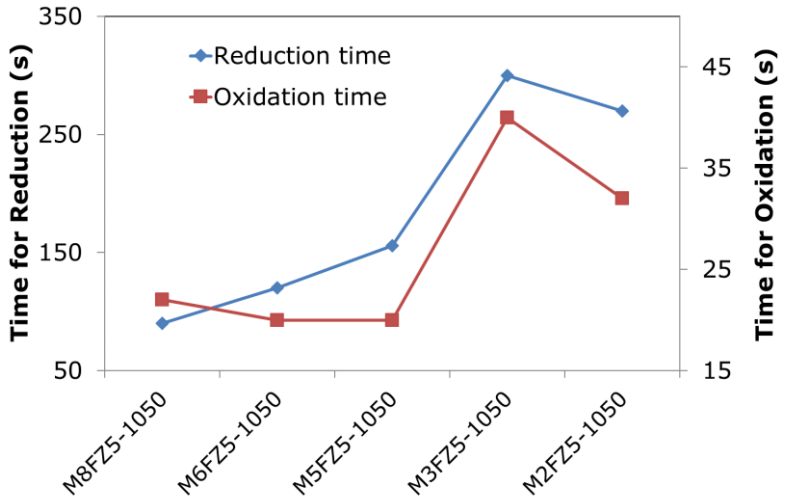

Figure 6.13: Time needed to reach fractional conversion of 0.3 for the bimetallic oxygen carriers with 44 wt. % zirconia for the 4th reduction cycles in 10% CO and 4th oxidation cycles in air at 1173 K, particle size of 75-250 μm and feed gas flow rate of 50 ml/min for the transition from Fe_2O_3 to Fe and from Mn_3O_4 to MnO.

The rate of reaction versus fractional conversion for the five OCs in this batch is presented in Figure 6.14. Again, it was observed that the maximum rate of reaction increases with increasing Mn content in the reduction and oxidation cycles with exception of M2FZ5-1050. Figure 6.14 reveals that the Mn-rich OC (M8FZ5-1050) has the highest maximum rate of reaction and extent of reaction (for the fast reaction step) of 45% and 95% in reduction and oxidation respectively. Moreover, the maximum rate of reaction for M8FZ5-1050 is 1.4 and 2.5 times that of M5FZ5-1050 and M2FZ5-1050 respectively.

It should be noted that the maximum rate of reaction in reduction and oxidation cycles for the OCs in CO were about 1.3 to 2.6 times the maximum rate of reaction in H_2.

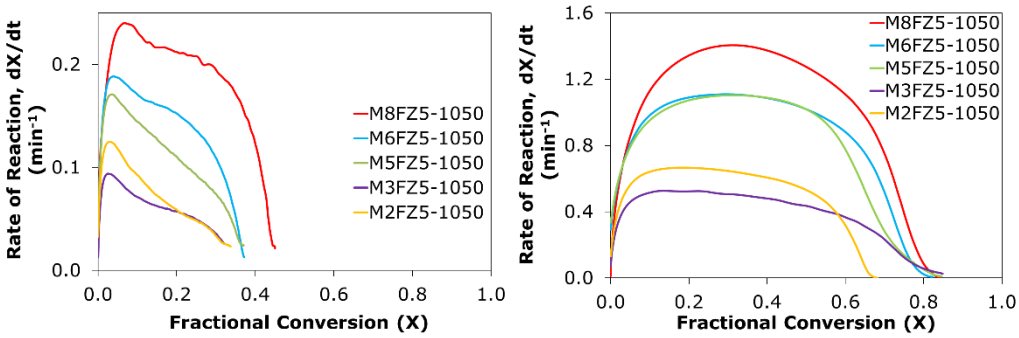

(a) Reduction (b) Oxidation

Figure 6.14: Rate of reaction as a function of fractional conversion for bimetallic oxygen carriers with 44 wt. % zirconia for the (a) 4th reduction cycles in 10% CO and (b) 4th oxidation cycles in air at 1173 K, particle size of 75-250 μm and feed gas flow rate of 50 ml/min for the transition from Fe_2O_3 to Fe and from Mn_3O_4 to MnO.

On the other hand, a different trend was observed for the maximum rate of mass conversion. Figure 6.15 showed that M5FZ5-1050 has the highest maximum rate of mass conversion in oxidation and reduction cycles. Furthermore, M5FZ5-1050 has a maximum rate of mass conversion that was about 1.2 times that of M8FZ5-1050. This was followed by M2FZ5-1050 which has maximum rate of mass conversion value that is about 1.1 times of M8FZ5-1050.

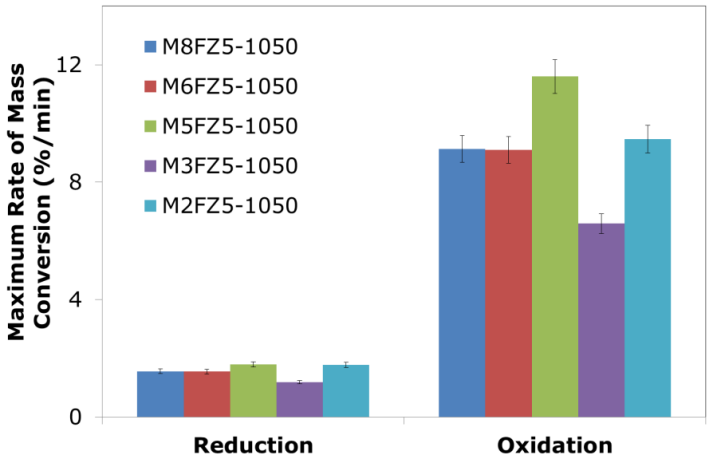

Figure 6.15: Maximum rate of mass conversion for bimetallic oxygen carriers with 44 wt. % zirconia for the 4th reduction cycles in 10% CO and 4th oxidation cycles in air at 1173 K, particle size of 75-250 μm and feed gas flow rate of 50 ml/min for the transition from Fe_2O_3 to Fe and from Mn_3O_4 to MnO.

6.2.2 Stability and the Effect of Repeated Cycles

For CLC, it is desirable that the oxygen carrier should be able to undergo multiple cycles and maintain its reactivity. Thus, the stability of the solid particles becomes important for long-term operation. Figure 6.16 shows the stability of the bimetallic oxygen carriers under discussion with respect to their maximum rate of mass conversion versus number of cycles. The results indicated that all OCs showed upward trend in the maximum rate of mass conversion with increasing number of reduction cycles except M5FZ5-1050. The M5FZ5-1050 showed somewhat decreasing maximum rate of mass conversion with number of cycles at average rate of 9% per cycle from the second reduction cycle.

In oxidation (Figure 6.16b), all the OCs showed slight reduction after the first cycle and then exhibited relatively stable maximum rate of mass conversion for the remaining cycles.

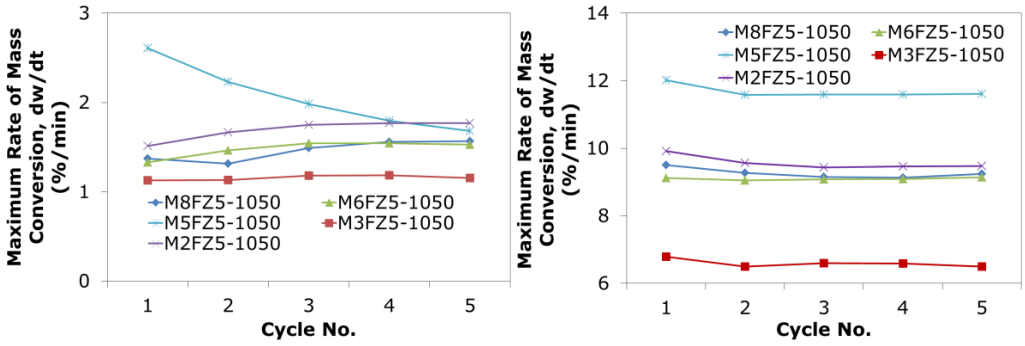

(a) Reduction (b) Oxidation

Figure 6.16: Maximum rate of mass conversion versus number of cycles for bimetallic oxygen carriers with 44 wt. % zirconia for the (a) reduction cycles in 10% CO and (b) oxidation cycles in air at 1173 K, particle size of 75-250 μm and feed gas flow rate of 50 ml/min for the transition from Fe_2O_3 to Fe and from Mn_3O_4 to MnO.

Stability in terms of oxygen transport capacity and number of cycles varies depending on the oxygen carrier composition as shown in Figure 6.17. For instance, M8FZ5-1050 and M3FZ5-1050 showed Roc that was stable across the five cycles. However, M5FZ5-1050 initially reduced after first cycle and then showed slight progressive reduction in subsequent cycles. This behavior is similar to the trend observed in Figure 6.16 and Figure 6.7 where the rate of mass conversion of M5FZ5-1050 was observed to be reducing as the number of cycle increases. The possible reason for this behavior has been mentioned in Section 6.1.2 and further detail will be highlighted in Section 6.4.

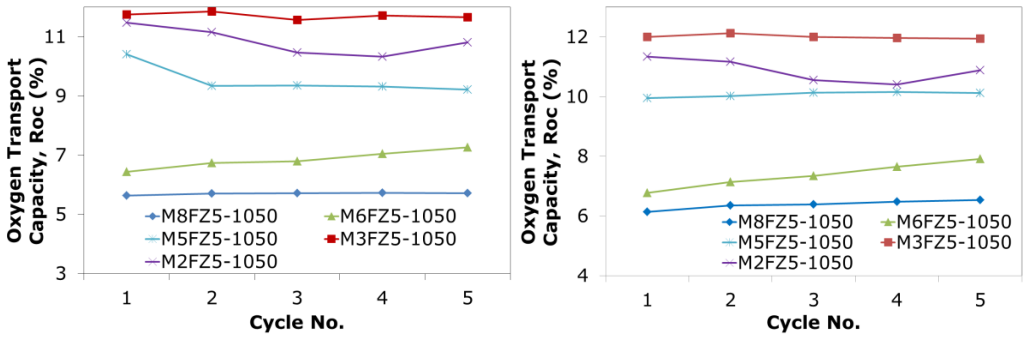

(a) Reduction (b) Oxidation

Figure 6.17: Oxygen transport capacity versus no of cycles for the bimetallic oxygen carriers with 44 wt. % zirconia for the (a) reduction cycles in 10% CO and (b) oxidation cycles in air at 1173 K, particle size of 75-250 μm and feed gas flow rate of 50 ml/min for the transition from Fe_2O_3 to Fe and from Mn_3O_4 to MnO.

6.2.3 Effect of Particle Size

In the preceding section, it was observed that in reduction, Fe-rich OC, M2FZ5-1050 displayed low reactivity; however, the maximum rate of mass conversion was relatively high in CO. Consequently, effect of particle size on its reactivity was investigated and the result is presented in Figure 6.18. The results showed that reactivity was higher for the small particle

size (75-250 μm) OC than for the larger size fraction (300-850 μm) OC. Whereas the small particle size fraction reached fractional conversions of 74% and 71%, the larger particle size fraction reached fractional conversions of 56% and 52% in reduction and oxidation respectively. Furthermore, in reduction and oxidation cycle, the larger particle required about twice the time needed by the small particle size to achieve fractional conversion of 0.3.

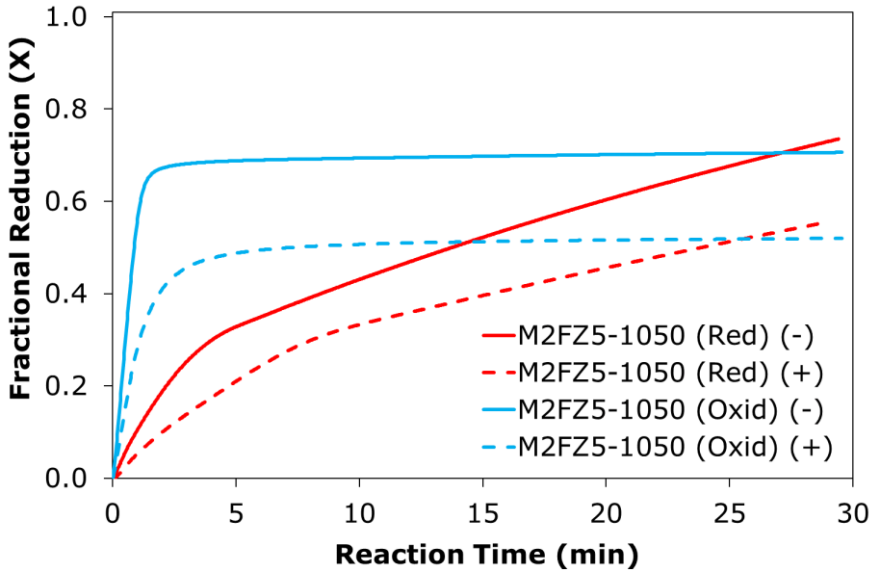

Figure 6.18: Effect of particle size on fractional conversion versus time for M2FZ5-1050 for the 3rd reduction cycles in 10% CO and 3rd oxidation cycles in air at 1173 K and feed gas flow rate of 50 ml/min for the transition from Fe_2O_3 to Fe and from Mn_3O_4 to MnO. Particle sizes: (—) 75-250 μm, (+) 300-850 μm.

Figure 6.19 shows that the small particle size fraction (75-250 μm) has a higher rate of reaction than the large particle size fraction. In the reduction cycle, both size fractions appear to have the same extent of reaction corresponding likely to Fe reduction to FeO. Also, in oxidation, the extent of reaction for the small particle size is about 1.4 times that of the larger particle size fraction.

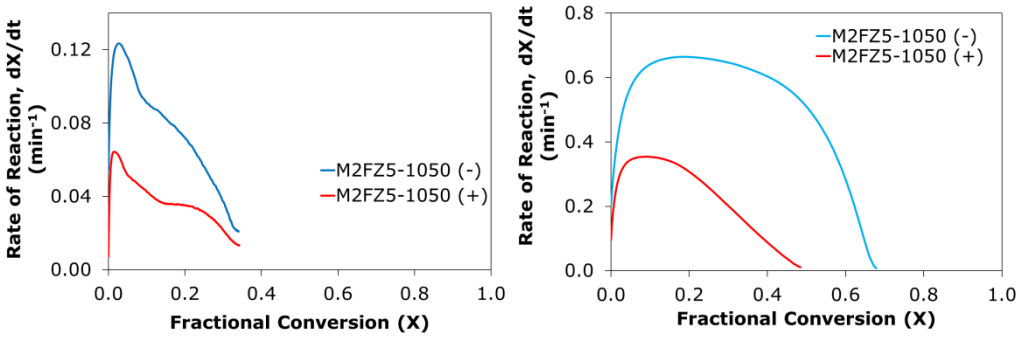

(a) Reduction (b) Oxidation

Figure 6.19: Effect of particle size on rate of reaction versus fractional conversion for M2FZ5-1050 for the (a) 3rd reduction cycles in 10% CO and (b) 3rd oxidation cycles in air at 1173 K, particle size of 75-250 μm and feed gas flow rate of 50 ml/min for the transition from Fe_2O_3 to Fe and from Mn_3O_4 to MnO. Particle sizes: (-) 75-250 μm and (+) 300-850 μm.

From the above results, it could be observed that in addition to chemical controlled reaction, diffusion limitation appeared to be quite significant in the reaction. This agrees with the calculated values of the effectiveness factor (η) for both particle sizes which were far less than unity as well as high values of Thiele modulus (ϕ), indicating presence of internal mass transfer limitations (Table F.4, Appendix F). The results from material characterization (SEM images) after reactivity also show that M2FZ5-1050 form agglomerates using CO as reacting gas (Section 6.4). The agglomeration of this OC resulted in internal mass transfer limiting these reactions.

6.3 Reduction/Oxidation in Methane

The reactivity of the five bimetallic oxygen carriers with 44 wt. % zirconia was investigated to elucidate their behaviour with methane in CLC. The results obtained and discussions on the findings will be the focus of the next section.

6.3.1 Reactivity

Figure 6.20 shows that in CH_4, the OCs reactivity was quite fast reaching fractional conversions of 0.3 in less than 60 s (see Figure 6.21). Furthermore, the OCs reached 65% - 79% reduction conversions and 65% - 97% oxidation conversions. Interestingly, in comparison to reaction in CH_4, the time taken to achieve 30% conversion in CO was about 2.3 to 6 and 1.3 to 2.1 times longer in reduction and oxidation cycles respectively.

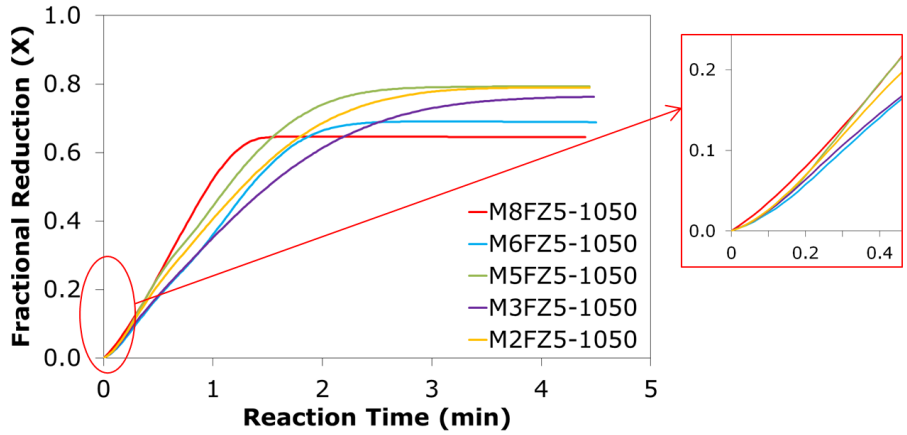

(a) Reduction

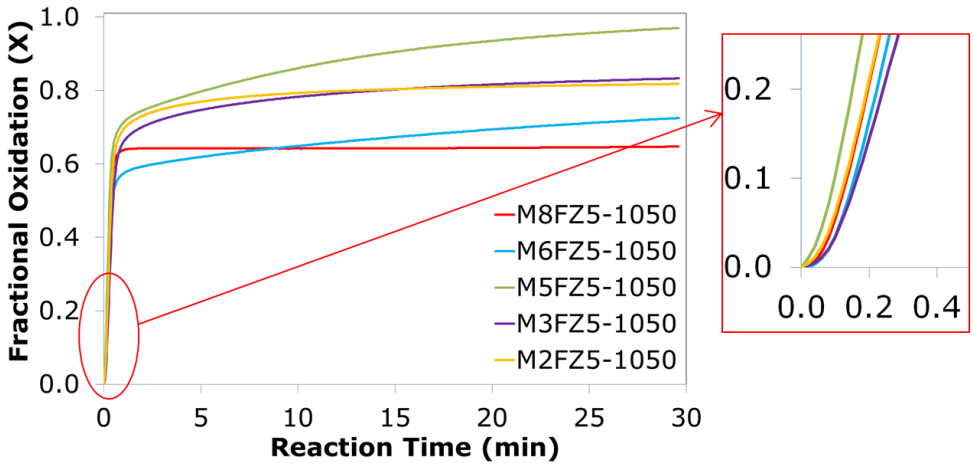

(b) Oxidation

Figure 6.20: Fractional conversion as a function of time for bimetallic oxygen carriers with 44 wt. % zirconia for the (a) 4th reduction cycles in 10% CH_4 and (b) 4th oxidation cycles in air at 1173 K, particle size of 75-250 µm and feed gas flow rate of 50 ml/min for the transition from Fe_2O_3 to FeO and from Mn_3O_4 to MnO.

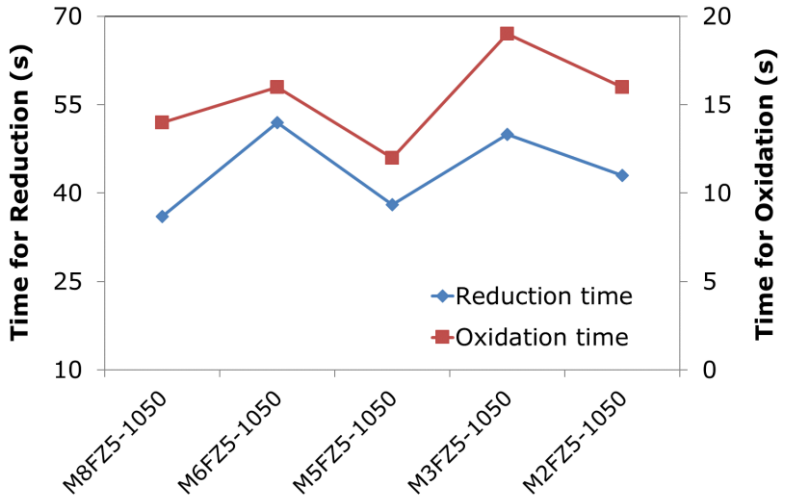

Figure 6.21: Time needed to reach fractional conversion of 0.3 for the bimetallic oxygen carriers with 44 wt. % zirconia for the 4th reduction cycles in 10% CH_4 and 4th oxidation cycles in air at 1173 K, particle size of 75-250 µm and feed gas flow rate of 50 ml/min for the transition from Fe_2O_3 to FeO and from Mn_3O_4 to MnO.

Figure 6.22a shows that the extent of reaction for each OCs in reduction was the same as the total conversion achieved by the respective OCs within the reaction time. This observation could be attributed to the very fast reactions observed for the OCs. Also, the rate of reduction reaction was found to vary depending on the manganese content. For instance, the rate of reaction of all OCs (except M8FZ5-1050) tends to slow down appreciably between conversion of 0.2 and 0.3 and thereafter rise to another maximum reaction rate or gradually slow down. The Mn-rich OCs (M6FZ5-1050 and M5FZ5-1050) fall into the category that rises to a second maximum rate of reaction. On the other hand, the iron-rich OCs (M3FZ5-1050 and M2FZ5-1050) attained only one maximum rate of reaction before gradually slows down to zero at the end. This behaviour could be an indication that the process involves two different reaction mechanisms which contributes to the overall rate.

Clearly from Figure 6.22b, the variations in rate of reactions observed in the reduction cycle were not observed in the oxidation reaction.

Interestingly, in reduction and oxidation period, the OCs maximum rates of reaction in CH_4 are about 2.4 to 4.5 and 1.5 to 3 times higher than in CO as fuel.

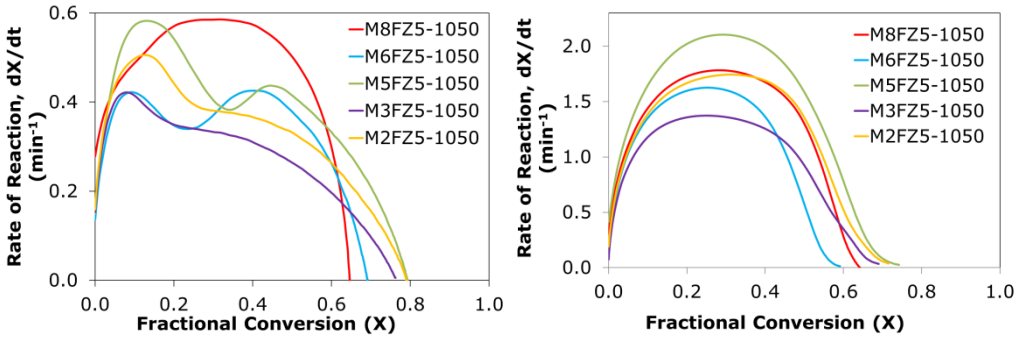

(a) Reduction (b) Oxidation

Figure 6.22: Rate of reaction as a function of fractional conversion for bimetallic oxygen carriers with 44 wt. % zirconia content for the (a) 4th reduction cycles in 10% CH_4 and (b) 4th oxidation cycles in air at 1173 K, particle size of 75-250 µm and feed gas flow rate of 50 ml/min for the transition from Fe_2O_3 to FeO and from Mn_3O_4 to MnO.

The maximum rate of mass conversion for this batch of bimetallic oxide in CH_4 for the fourth cycle is presented in Figure 6.23. M5FZ5-1050 has the highest maximum rate of mass conversion in oxidation and reduction cycles. The maximum rate of mass conversion for M5FZ5-1050 in CH_4 was about 1.1 and 1.3 times that of M8FZ5-1050 while M2FZ5-1050 was about 1.1 and 1.2 times that of M8FZ5-1050 during reduction and oxidation respectively. This observation is somewhat similar to the trend observed in CO (see Section 6.2.1).

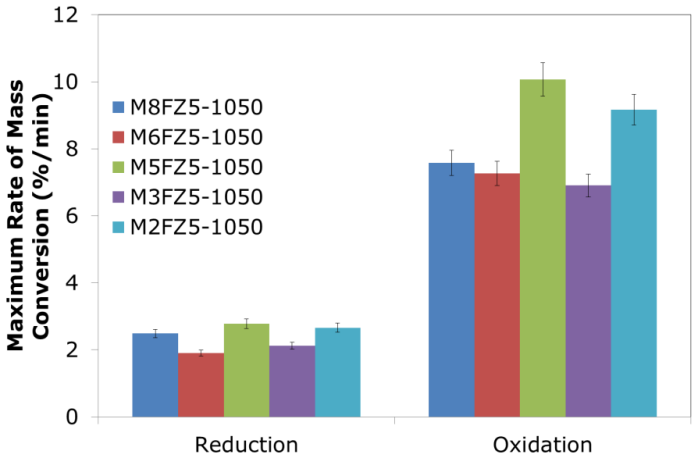

Figure 6.23: Maximum rate of mass conversion for the bimetallic oxygen carriers with 44 wt. % zirconia content for the 4th reduction cycles in 10% CH_4 and 4th oxidation cycles in air at 1173 K, particle size of 75-250 µm and feed gas flow rate of 50 ml/min for the transition from Fe_2O_3 to FeO and from Mn_3O_4 to MnO.

6.3.2 Stability and Effect of Repeated Cycles

Typical mass loss profile of this batch of oxygen carriers is shown in Figure 6.24. The TGA data for M8FZ5-1050 revealed that the oxygen released in both reduction and oxidation was relatively stable during the multi-redox cycle. Considerably similar profile with slight variations in the oxygen released was obtained for the other OCs.

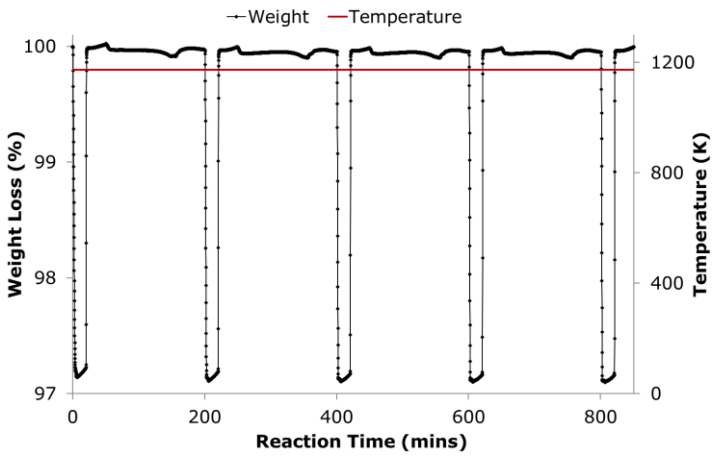

Figure 6.24: Cyclic reduction-oxidation performance of M8FZ5-1050 for reduction cycles in 10% CH_4 and 4th oxidation cycles in air at 1173 K, particle size of 75-250 µm for the transition from Fe_2O_3 to FeO and from Mn_3O_4 to MnO.

The stability of the OCs in terms of maximum rate of mass conversion is shown in Figure 6.25. Figure 6.25a shows that all OCs except M8FZ5-1050 and M6FZ5-1050 exhibited an initial decrease in maximum rate of mass conversion from first to second cycle. M5FZ5-1050 displayed the highest decrease of the maximum rate of mass conversion during reduction reaction of about 52%. This rate progressively reduced further at an average of 10% per cycle from the second cycle. This behaviour appears to be characteristic for M5FZ5-1050 given that similar progressive decrease in the maximum rate of mass conversion was observed in H_2 and CO.

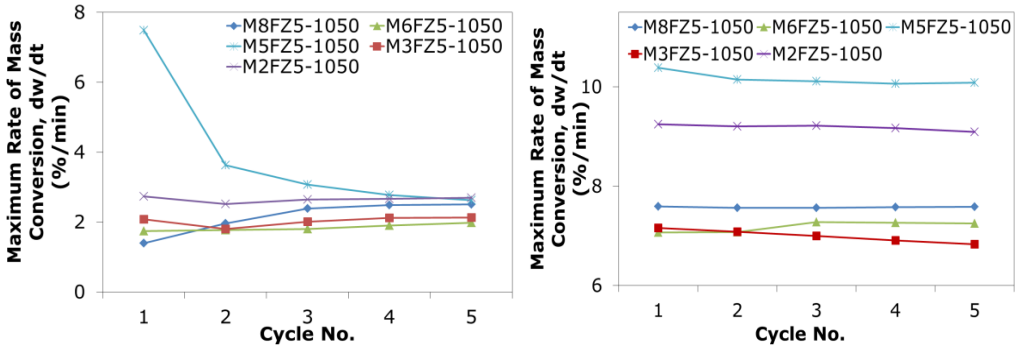

(a) Reduction (b) Oxidation

Figure 6.25: Maximum rate of mass conversion versus number of cycles for the bimetallic oxygen carriers with 44 wt. % zirconia for the (a) reduction cycles in 10% CH_4 and (b) oxidation cycles in air at 1173 K, particle size of 75-250 µm and feed gas flow rate of 50 ml/min for the transition from Fe_2O_3 to FeO and from Mn_3O_4 to MnO.

6.4 Characterization of Fresh and Reacted Oxygen Carriers

The fresh and reacted particles of the bimetallic oxygen carriers with high zirconia content were characterized to gain understanding of the chemical and morphological transformations in the oxygen carriers. Figures 6.26 to 6.30 show the SEM image for each oxygen carrier sample at a scale of 20 – 100 µm. Whereas almost all the bimetallic OCs with 20 wt. % zirconia content formed agglomerates, all the OCs in this batch did not agglomerate (Figures 6.26 to 6.28) except the Fe-rich OCs (M3FZ5-1050

and M2FZ5-1050) which agglomerates in H_2 and CO (Figures 6.29 to 6.30). Thus, these findings suggest that zirconia content of 44 wt. % was quite sufficient to maintain the mechanical integrity of the Mn-Fe particles during the redox reactions. The OCs appear to become more porous after reaction in the fuels and these pores could provide more active sites for gaseous fuel oxidation. The increased pores after the reactions in each gas tend to correlate with the increased reactivity observed for OCs following the order CH_4 > CO > H_2. This observation was rather obvious for Mn-rich OCs which exhibited higher reactivity than the less reactive Fe-rich oxygen carriers.

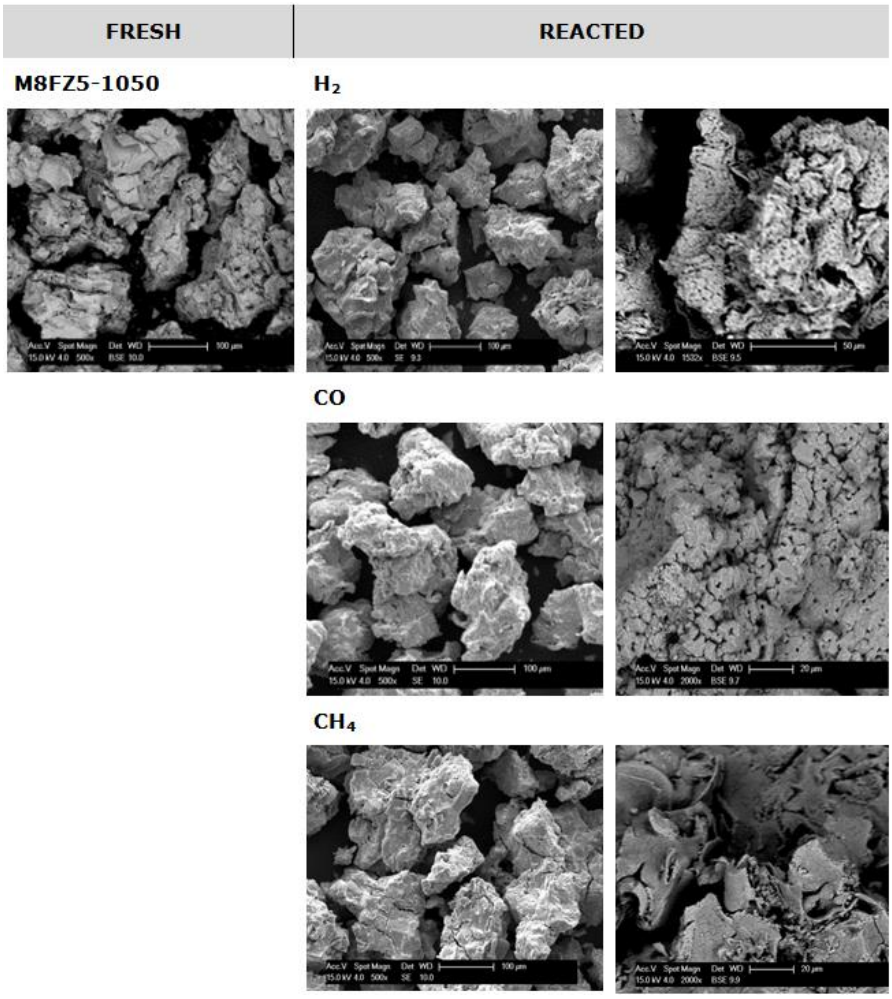

Figure 6.26: SEM images of fresh bimetallic M8FZ5-1050 particles with 44 wt. % zirconia after calcination at 1323 K for 2 h and reacted M8FZ5-1050 particles after five redox cycles at 1173 K in H_2, CO or CH_4 and air. The images (middle column) show particles without agglomeration and the occurrence of pores (right column) after the redox reaction in the different gases.

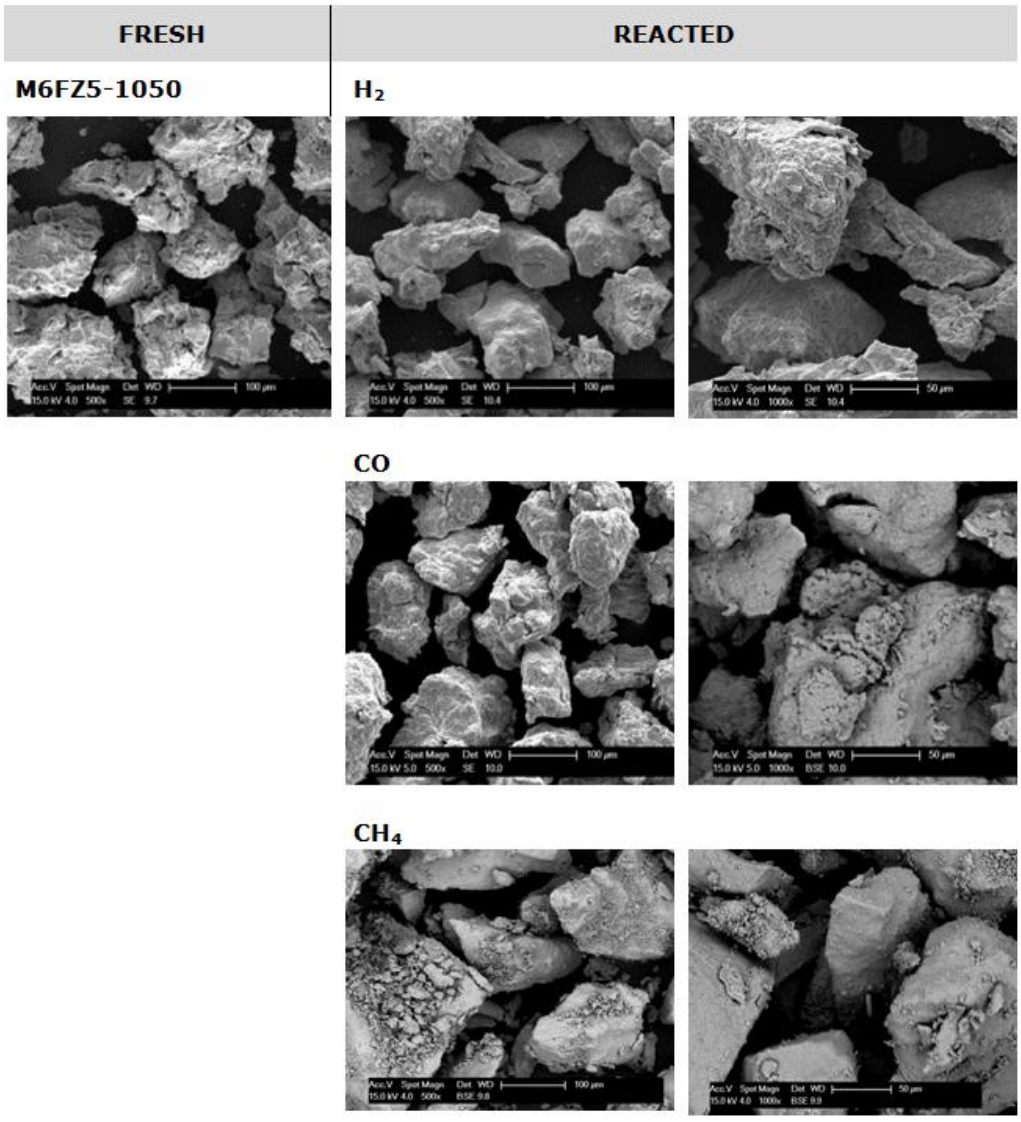

Figure 6.27: SEM images of fresh bimetallic M6FZ5-1050 particles with 44 wt. % zirconia after calcination at 1323 K for 2 h and reacted particles after five redox cycles at 1173 K in H_2, CO or CH_4 and air.

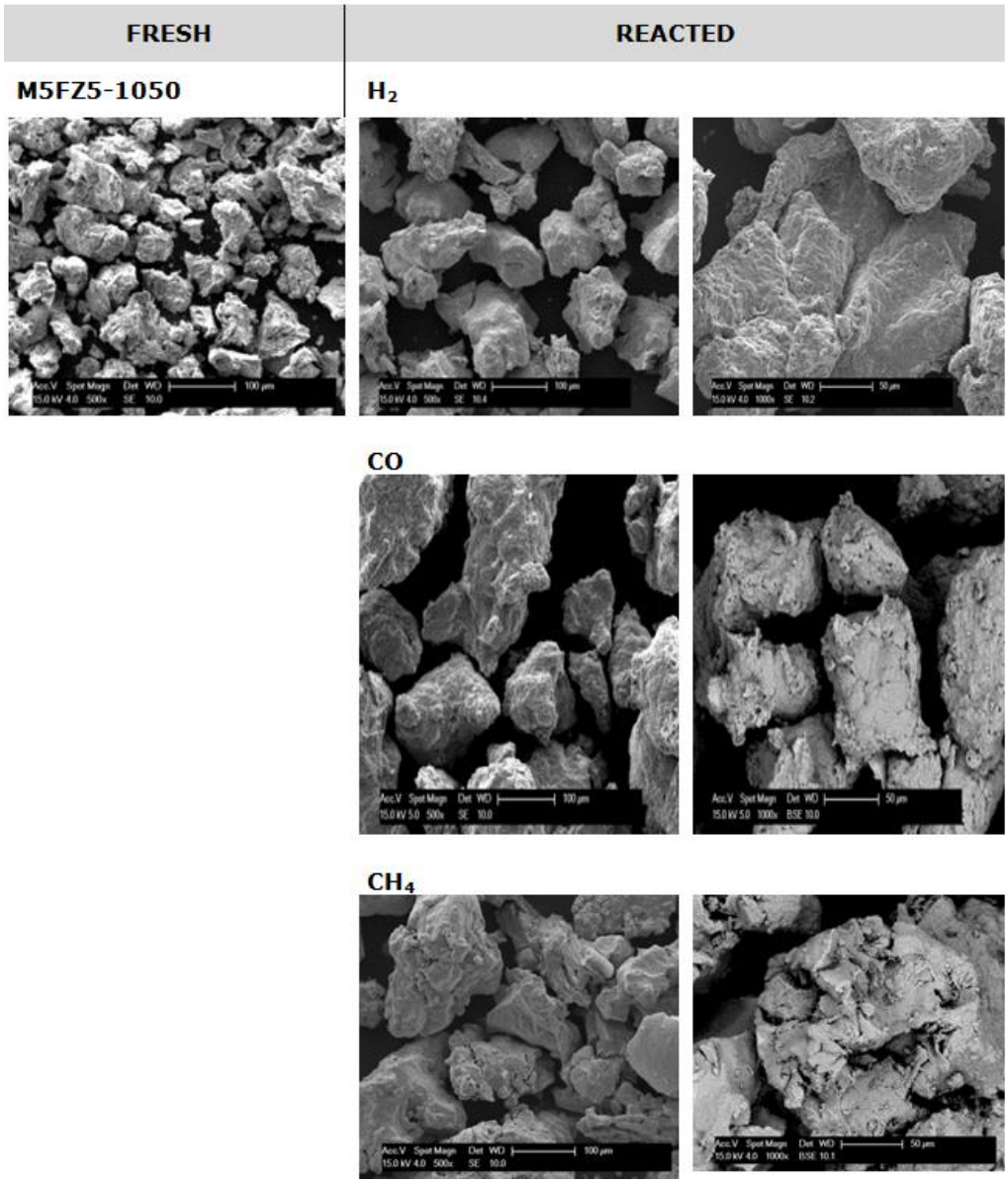

Figure 6.28: SEM images of fresh bimetallic M5FZ5-1050 particles with 44 wt. % zirconia after calcination at 1323 K for 2 h and reacted M5FZ5-1050 particles after five redox cycles at 1173 K in H_2, CO or CH_4 and air.

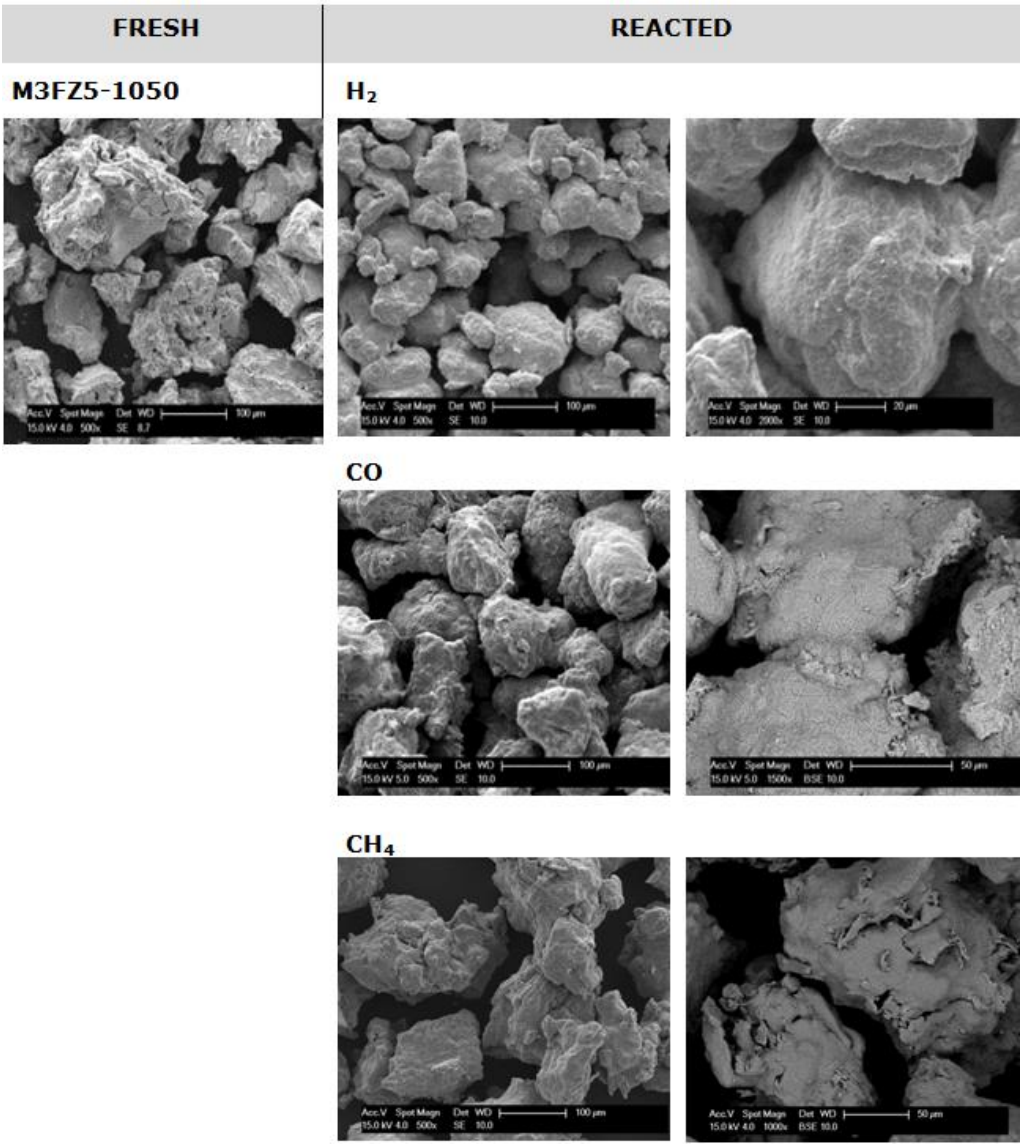

Figure 6.29: SEM images of fresh bimetallic M3FZ5-1050 particles with 44 wt. % zirconia after calcination at 1323 K for 2 h and reacted M3FZ5-1050 particles after five redox cycles at 1173 K in H_2, CO or CH_4 and air.

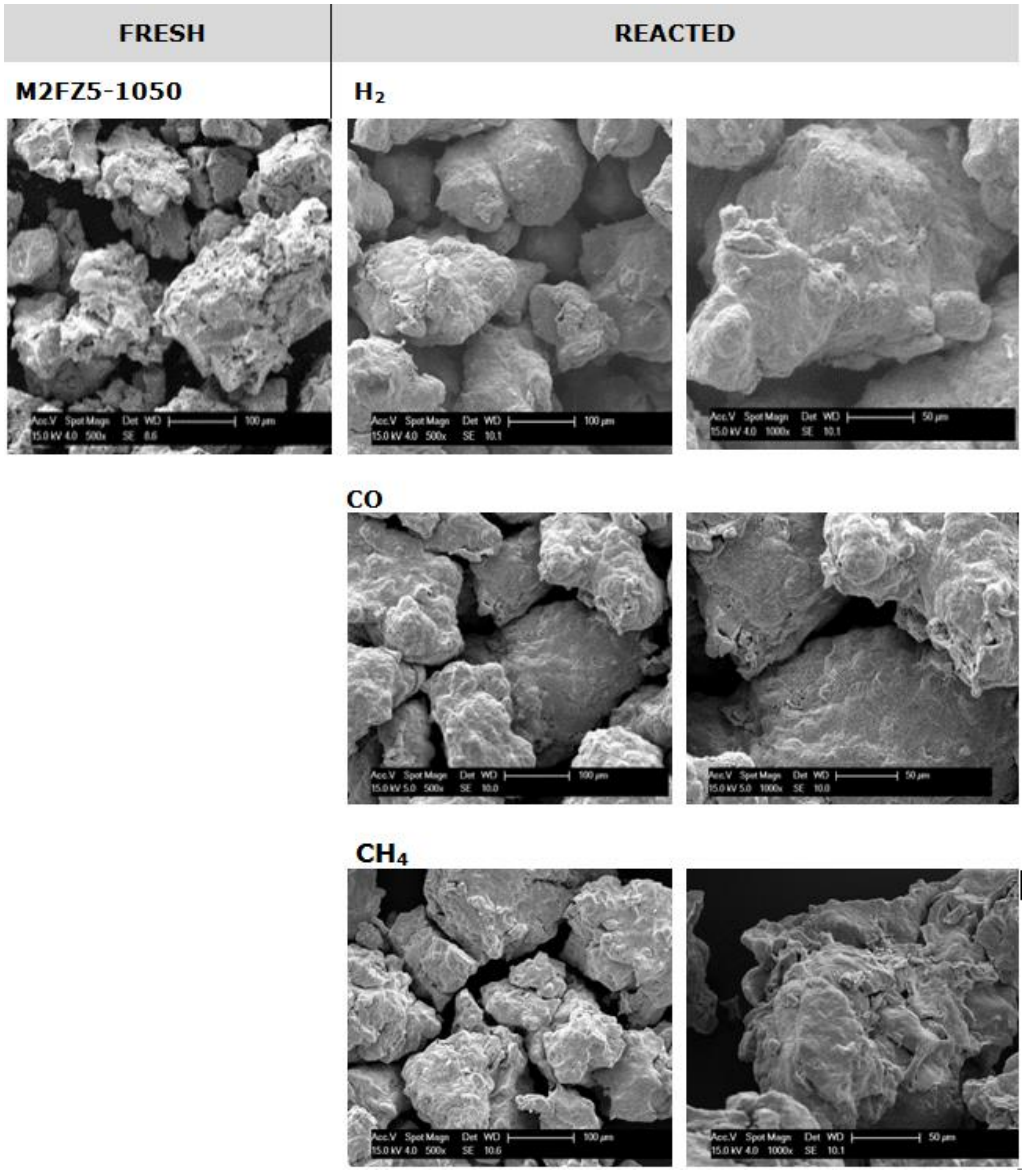

Figure 6.30: SEM images of fresh bimetallic M2FZ5-1050 particles with 44 wt. % zirconia after calcination at 1323 K for 2 h and reacted M2FZ5-1050 particles after five redox cycles at 1173 K in H_2, CO or CH_4 and air.

The XRD results presented in Table 6.4 is clear evidence that there was no interaction between the active phase and the support through the formation of irreversible compounds which could have altered the reactivity of the oxygen carrier. Hence, zirconia is a suitable support for the co-precipitated Mn-Fe oxide oxygen carriers. Furthermore, the XRD results obtained for the reacted particles show that there was no occurrence of phase transformation after reaction with CH_4 and regeneration in air. This

implies that these bimetallic OCs successfully maintained their crystal structure during the multi reduction-oxidation cycles in methane.

Table 6.4: Phase composition of bimetallic oxygen carriers with 44 wt. % zirconia identified by X-ray Diffraction

Oxygen carrier	**Fresh**	**Re-Oxidation**
M8FZ5-1050	m-ZrO_2 Baddeleyite c-$MnFe_2O_4$ Jakobsite	m-ZrO_2 Baddeleyite c-$MnFe_2O_4$ Jakobsite
M6FZ5-1050	m-ZrO_2 Baddeleyite c-$MnFe_2O_4$ Jakobsite c-Mn_2O_3 Bixbyite	m-ZrO_2 Baddeleyite c-$MnFe_2O_4$ Jakobsite c-Mn_2O_3 Bixbyite
M5FZ5-1050	m-ZrO_2 Baddeleyite c-$MnFe_2O_4$ Jakobsite c-Mn_2O_3 Bixbyite r-Fe_2O_3 Hematite	m-ZrO_2 Baddeleyite c-$MnFe_2O_4$ Jakobsite c-Mn_2O_3 Bixbyite
M3FZ5-1050	m-ZrO_2 Baddeleyite c-$MnFe_2O_4$ Jakobsite r-Fe_2O_3 Hematite	m-ZrO_2 Baddeleyite c-$MnFe_2O_4$ Jakobsite r-Fe_2O_3 Hematite
M2FZ5-1050	m-ZrO_2 Baddeleyite c-$FeMnO_3$ Bixbyite r-Fe_2O_3 Hematite	m-ZrO_2 Baddeleyite r-Fe_2O_3 Hematite c-$MnFe_2O_4$ Jakobsite

Key: m-monoclinic, c-cubic, r-rhombo

The XRD reveals that unreacted M5FZ5-1050 has three active component phases present ($MnFe_2O_4$, Mn_2O_{3-} bixbyte and Fe_2O_3). However, after reduction in CH_4 and regeneration in air, the Fe_2O_3 was not detected by the XRD. This could suggest possible incorporation of the iron oxide into the cubic structure of $MnFe_2O_4$. Otherwise, it could be that any Fe_2O_3 present in the reacted sample was below the detection limit of the instrument.

6.5 Conclusions

1. The co-precipitated technique was found to yield bimetallic oxygen carriers with high degree of dispersion of the elements in the composite material.
2. After reactions with the fuels, the bimetallic oxygen carriers with high zirconia content (44 wt. %) did not form agglomerates. This is in contrast to the agglomeration of particles observed for the bimetallic oxygen carriers with low zirconia content (20 wt. %). This result thus, concludes that zirconia content of 44 wt. % was quite sufficient to maintain the mechanical integrity of this batch of Mn-Fe particles during the redox reactions.
3. Generally, the reactivity in methane was rather fast (reaching 30% conversion in less than 60 s) and the slow step reaction was not quite pronounced regardless of active components composition in the samples. Furthermore, the OCs reactivity in the three gases followed the order CH_4> CO> H_2.
4. For the three reaction temperatures investigated in hydrogen, it was concluded that the optimal reaction temperature for the Mn-rich oxygen carrier (M8FZ5-1050) was 1173 K.

The current chapter presented the findings on the behaviour of the bimetallic oxygen carriers with high zirconia content. However, it is known that ceria can actively participate in chemical reaction. Hence, a combination of ceria and zirconia was used as support for the bimetallic Mn-Fe oxygen carriers. The result obtained is the focus of the next chapter.

7 BIMETALLIC OXYGEN CARRIERS SUPPORTED ON CERIA AND ZIRCONIA: BEHAVIOUR IN DIFFERENT GASES

Ceria can actively participate and enhance chemical reactions (Galvita et al., 2013). Consequently, for this batch of oxygen carriers, combined support of ceria and zirconia was used in order to elucidate any possible enhancement on the performance of the oxygen carriers. The four co-precipitated oxygen carriers denoted as M8FZCe5-1050, M6FZCe5-1050, M5FZCe5-1050 and M3FZCe5-1050 (See Table 3.3) were evaluated for chemical looping combustion.

The SEM-EDX elemental map of the polished OC shows that the active component (Mn, Fe,) were homogeneously dispersed in the supports (Zr and Ce) as illustrated in Figure 7.1 for the sample M5FZCe5-1050.

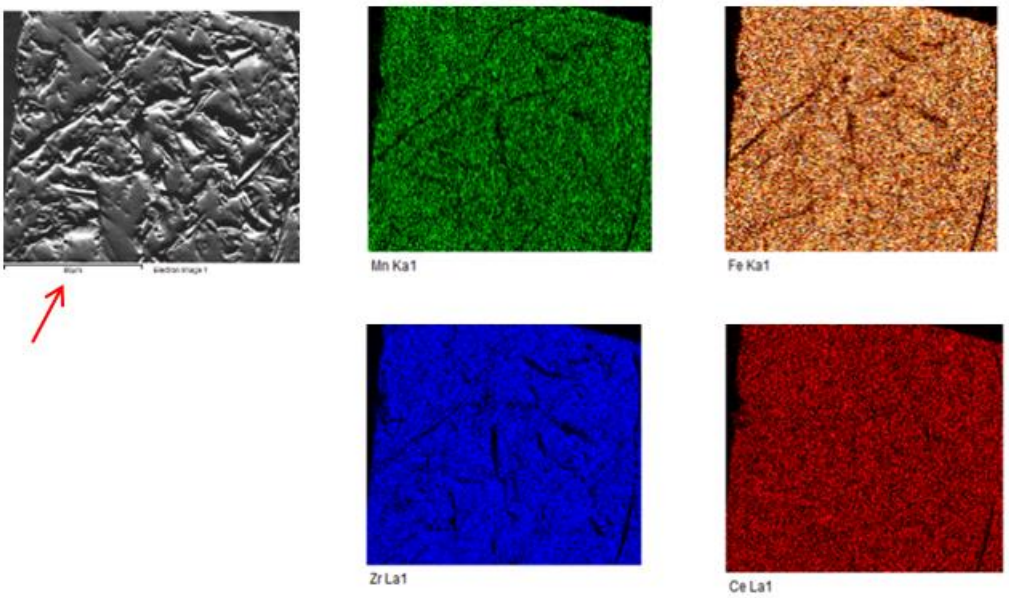

Figure 7.1: SEM-EDX map of fresh M5FZCe5-1050 after calcination at 1323 K in air for 2 h showing distribution of the elements. The scale bar corresponds to 80 μm. The SEM-EDX analysis confirms Mn, Fe, Zr and Ce are well dispersed.

The elemental concentrations (indicated by unique colours) in Figure 7.1 show that Mn, Fe, Zr and Ce are well dispersed without position of exclusions at a scale of 80 μm.

Hereafter, the results and discussions on the performance of the bimetallic oxygen carriers with ceria and zirconia support is presented and discussed. The behaviour of these OCs in hydrogen, carbon monoxide and methane will be presented following the same structure in the preceding chapter.

7.1 Reduction/Oxidation in Hydrogen

7.1.1 Reactivity

Co-precipitated bimetallic oxygen carriers with combined support of zirconia and ceria (M8FZCe5-1050, M6FZCe5-1050, M5FZCe5-1050 and M3FZCe5-1050) were investigated in TGA using hydrogen as fuel. The results of the OCs fractional conversions are presented in Figure 7.2. All the OCs reached full conversion in reduction and oxidation except M8FZCe5-1050 which displayed 99% conversion in oxidation within the reaction time of the experiment. However, it could be observed that reactivity varies depending on the composition of the oxygen carrier.

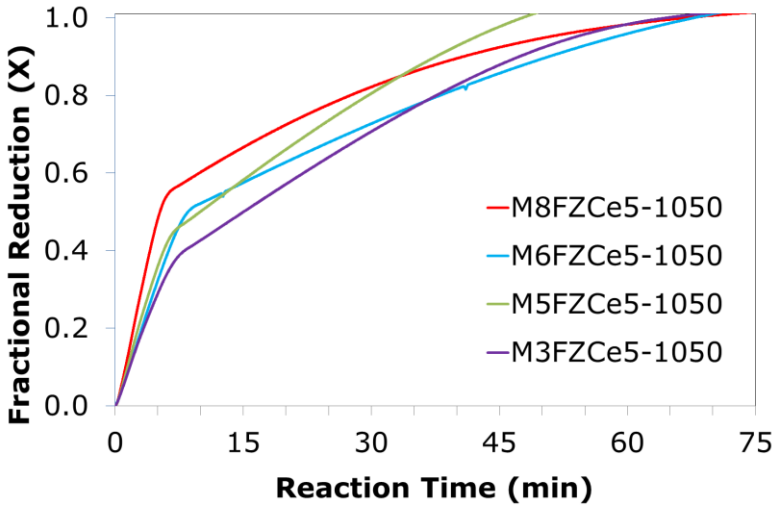

(a) Reduction

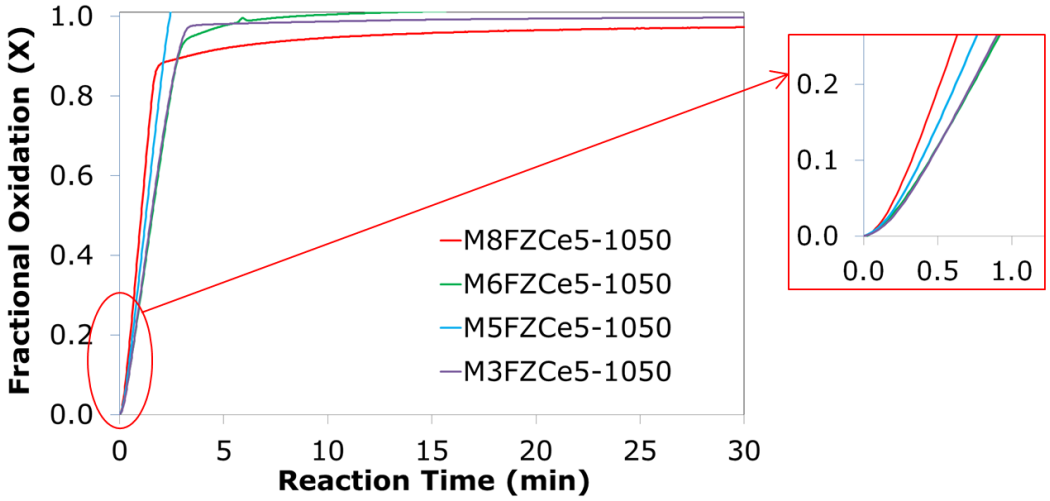

(b) Oxidation

Figure 7.2: Fractional reduction and oxidation versus time for the bimetallic oxygen carriers with zirconia-ceria support for the (a) 4th reduction cycles in 5% H_2 and (b) 4th oxidation cycles in air at 1173 K, particle size of 75-250 µm and feed gas flow rate of 20 ml/min for the transition from Fe_2O_3 to Fe and from Mn_3O_4 to MnO.

The Mn-rich OC (M8FZCe5-1050) was fastest to reach fractional conversion of 0.3 whereas the Fe-rich oxide OC (M3FZCe5-1050) reached the same conversion for longer time as presented in Figure 7.3. The results show that M8FZCe5-1050 oxygen carrier appears to be most reactive in both oxidation and reduction.

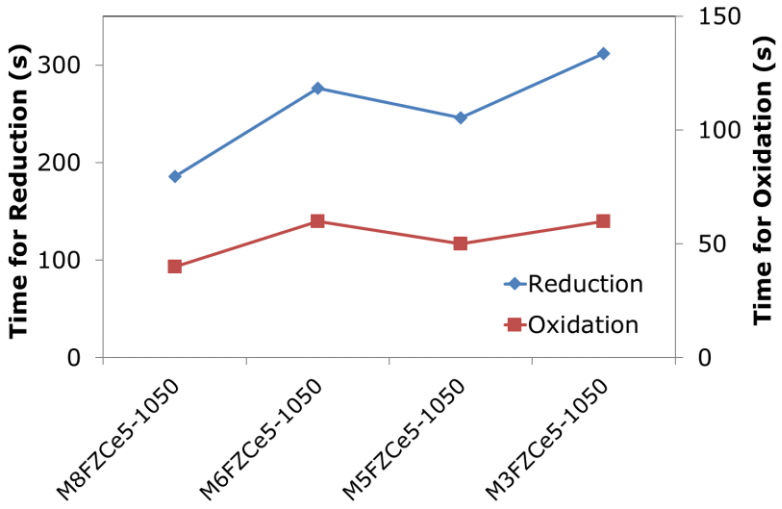

Figure 7.3: Time needed to reach fractional conversion of 0.3 for the bimetallic oxygen carriers with zirconia-ceria support for the 4th reduction cycles in 5% H_2 and 4th oxidation cycles in air at 1173 K, particle size of 75-250 µm and feed gas flow rate of 20 ml/min for the transition from Fe_2O_3 to Fe and from Mn_3O_4 to MnO.

Figure 7.4 show that M8FZCe5-1050 has the highest maximum rate of reaction which is 1.3 times that of M5FZCe5-1050 in reduction and oxidation. Also, the extent of reaction appears to increase with increasing Mn content in reduction. However, in oxidation, M5FZCe5-1050 has the highest extent of reaction whereas M8FZCe5-1050 achieved the least value of 0.89 for the fast reaction step as shown in Figure 7.4.

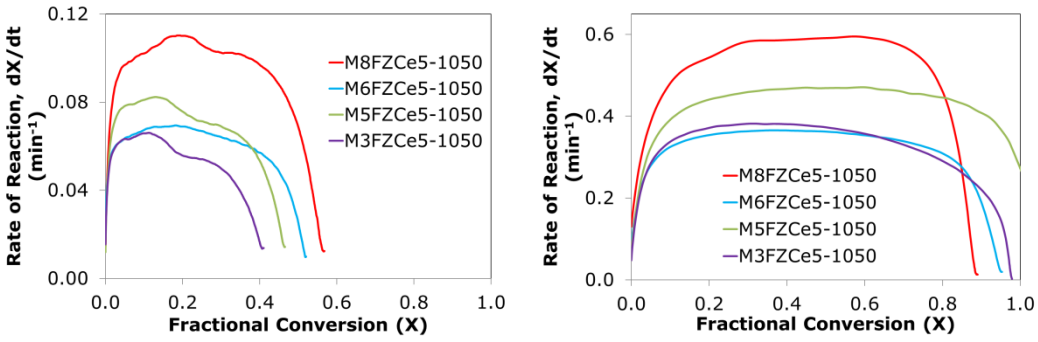

(a) Reduction (b) Oxidation

Figure 7.4: Rate of reaction as a function of fractional conversion for bimetallic oxygen carriers with zirconia-ceria support for the (a) 4th reduction cycles in 5% H_2 and (b) 4th oxidation cycles in air at 1173 K, particle size of 75-250 µm and feed gas flow rate of 20 ml/min for the transition from Fe_2O_3 to Fe and from Mn_3O_4 to MnO.

M5FZ5-1050 and the Fe-rich OC (M3FZ5-1050) and exhibited slightly higher maximum rate of mass conversion as presented in Figure 7.5. Furthermore, M5FZCe5-1050 has the highest maximum rate of mass conversion and was 1.2 and 1.3 times that of M8FZCe5-1050 in reduction and oxidation respectively.

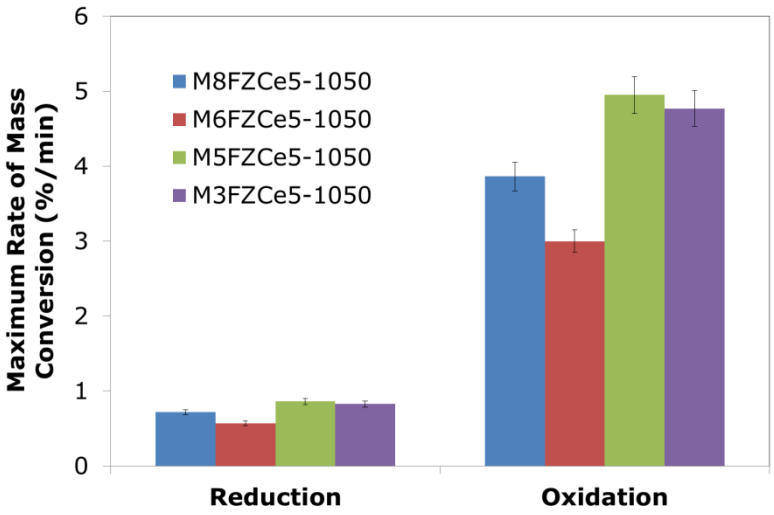

Figure 7.5: Maximum rate of mass conversion for bimetallic oxygen carriers with zirconia-ceria support for the 4th reduction cycles in 5% H_2 and 4th oxidation cycles in air at 1173 K, particle size of 75-250 μm and feed gas flow rate of 20 ml/min for the transition from Fe_2O_3 to Fe and from Mn_3O_4 to MnO.

7.1.2 Stability and Effect of Repeated Cycle

All OCs in this batch were relatively stable and their Roc tends to increase with increasing number of cycle in reduction and oxidation as shown in Figure 7.6.

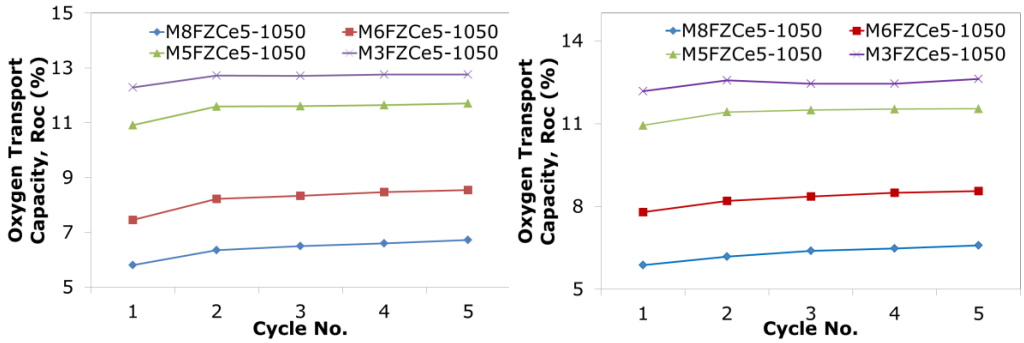

(a) Reduction (b) Oxidation

Figure 7.6: Oxygen transport capacity versus no of cycles for the bimetallic oxygen carriers with zirconia-ceria support for the (a) reduction cycles in 5% H_2 and (b) oxidation cycles in air at 1173 K, particle size of 75-250 µm and feed gas flow rate of 20 ml/min for the transition from Fe_2O_3 to Fe and from Mn_3O_4 to MnO.

Similarly, the maximum rate of mass conversion for all OCs showed increasing maximum rate of mass conversion with increasing number of cycles during reduction reaction (Figure 7.7). The average rates of increase of the maximum rate of mass conversion for the OCs from the second cycle were: 8%, 5%, 5% and 4% per cycle for M8FZCe5-1050, M6FZCe5-1050, M5FZCe5-1050 and M3FZCe5-1050 respectively. However, in oxidation, all OCs showed relatively stable maximum rate of mass conversion through the cycles except M5FZCe5-1050 which displayed initial reduction from first to second cycle but afterward appear to be stable.

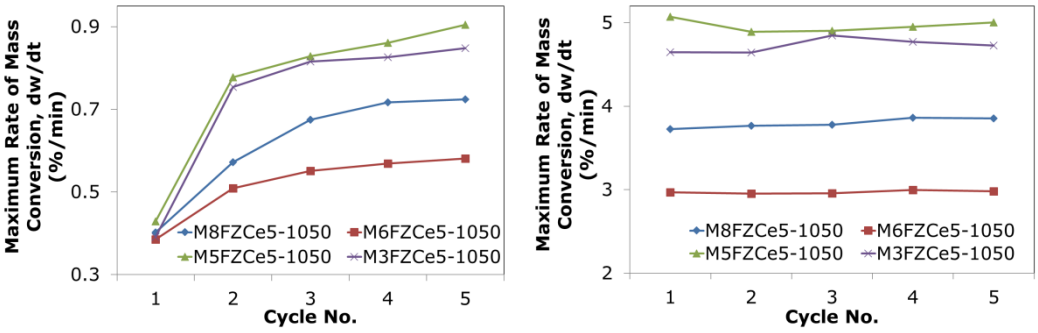

(a) Reduction (b) Oxidation

Figure 7.7: Maximum rate of mass conversion versus cycle number for the bimetallic oxygen carriers with zirconia-ceria support for the reduction cycles in 5% H_2 and oxidation cycles in air at 1173 K, particle size of 75-250 µm and feed gas flow rate of 20 ml/min for the transition from Fe_2O_3 to Fe and from Mn_3O_4 to MnO.

As previously reported in Section 6.2.2, the counterpart of M5FZCe5-1050 OC without ceria i.e. M5FZ5-1050 was found to exhibit characteristic behaviour of progressive decrease in the maximum rate of mass conversion as the number of cycles increased using hydrogen as fuel. Surprisingly, the use of ceria and zirconia appear to have altered the thermodynamics of iron and manganese oxides in the OC and thus reversed the progressive decrease in the maximum rate of mass conversion trend as shown in Figure 7.7.

Against the backdrop of the findings, the next section will highlight the effect of ceria support on the co-precipitated oxygen carriers' reactivity and oxygen transport capacity (Roc).

7.1.3 Effect of Ceria Support on Reactivity

The addition of ceria to zirconia as support tends to have more pronounced effect on the rate of reactions of the Mn-rich OCs than the Fe-rich OCs in H_2 (Table 7.1). For instance, in reduction, addition of ceria to zirconia as support reduced the maximum rate of reaction of Mn-rich OCs (M8FZ5-1050 and M6FZ5-1050) by 30%. Similar decrease in reactivity was observed in the oxidation reactions of these OCs. Also, the addition of ceria resulted to an increase in the extent of fractional conversion of all OCs. On the average, this increase was 10% in reduction and 43% in oxidation except for M8FZ5-1050 in reduction. Furthermore, the addition of ceria improved the oxygen carrier Roc by an average of 10% in reduction and 13% in oxidation (Table 7.2).

Table 7.1: Effect of ceria support on reactivity of the bimetallic oxygen carriers in H_2.

Oxygen carriers	Maximum rate of reaction ratio (ZrCe/Zr)		Extent of fractional conversion ratio (ZrCe/Zr)	
	Reduction	Oxidation	Reduction	Oxidation
M8FZCe5-1050/ M8FZ5-1050	0.7	0.9	1.0	1.4
M6FZCe5-1050/ M6FZ5-1050	0.7	0.7	1.1	1.3
M5FZCe5-1050/ M5FZ5-1050	1.0	1.1	1.1	1.4
M3FZCe5-1050/ M3FZ5-1050	1.1	1.0	1.1	1.6

Table 7.2: Effect of ceria support on the oxygen transport capacity of the bimetallic oxygen carriers.

Oxygen carriers	Oxygen transport capacity ratio (ZrCe/Zr)	
	Reduction	Oxidation
M8FZCe5-1050/ M8FZ5-1050	1.1	1.1
M6FZCe5-1050/ M6FZ5-1050	1.0	1.1
M5FZCe5-1050/ M5FZ5-1050	1.2	1.2
M3FZCe5-1050/ M3FZ5-1050	1.1	1.1

7.2 Reduction/Oxidation in Carbon Monoxide

7.2.1 Reactivity

Figure 7.8 presents the fractional conversions of these OCs from TGA data using CO as fuel. Clearly, reactivity in oxidation is faster than in reduction. Furthermore, similar to the trend observed in H_2, the Mn-rich OC (M8FZCe5-1050) was most reactive followed by M5FZCe5-1050 and the

least reactive was Fe-rich OC (M3FZCe5-1050) as shown in Figure 7.8. Additionally, in oxidation, M8FZCe5-1050 was the most reactive whereas the least reactive was M3FZCe5-1050.

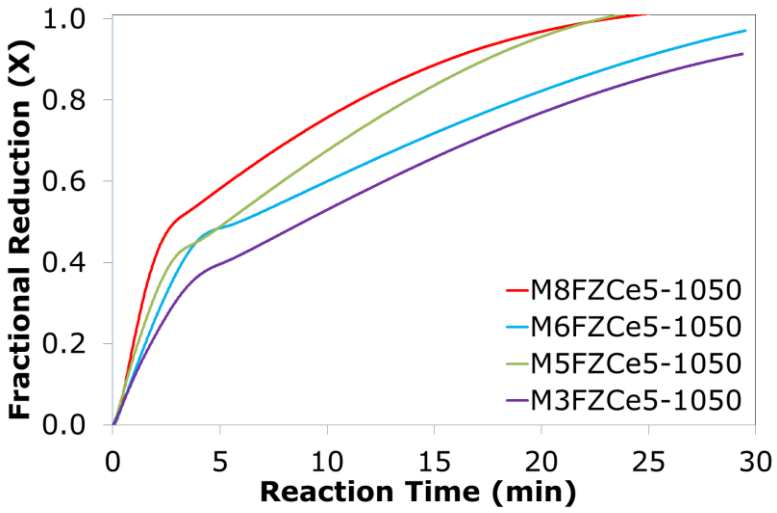

(a) Reduction

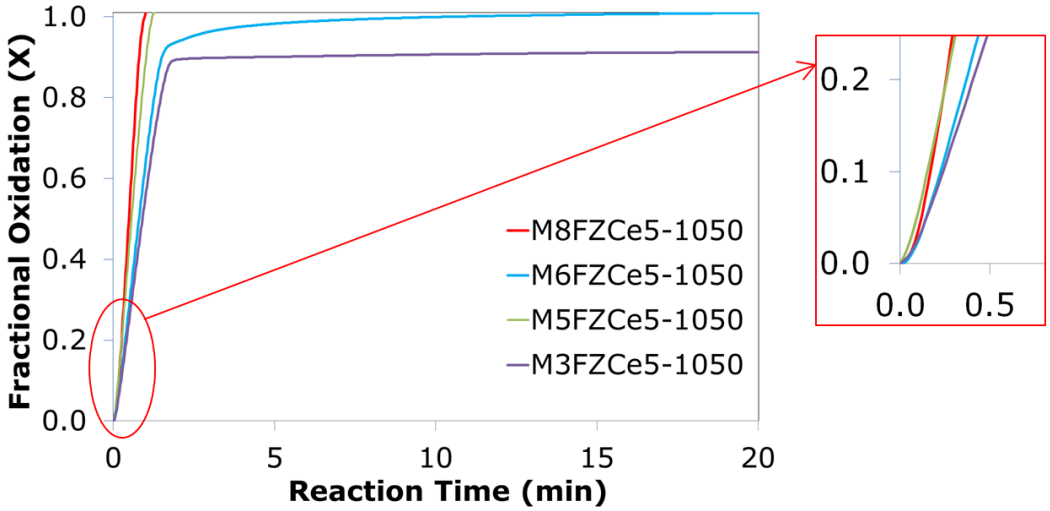

(b) Oxidation

Figure 7.8: Fractional reduction and oxidation versus time for the bimetallic oxygen carriers with zirconia-ceria support for the (a) 4th reduction cycles in 10% CO and (b) 4th oxidation cycles in air at 1173 K, particle size of 75-250 μm and feed gas flow rate of 50 ml/min for the transition from Fe_2O_3 to Fe and from Mn_3O_4 to MnO.

M8FZCe5-1050 and M5FZCe5-1050 reached full conversion within the reaction time in reduction. The time required to reach conversion of 0.3 is

shown in Figure 7.9. Moreover, the time needed to reach 30% conversion in oxidation and reduction is twice less than the time required in H_2 to achieve same fractional conversion.

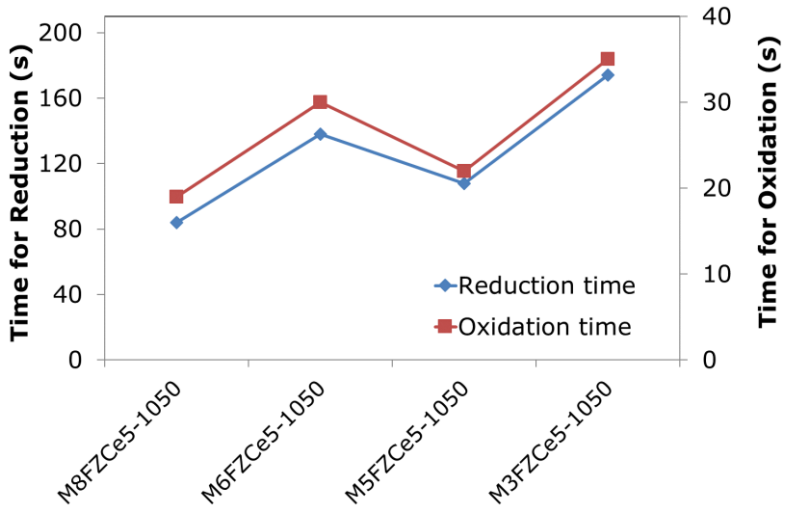

Figure 7.9: Time needed to reach fractional conversion of 0.3 for the bimetallic oxygen carriers with zirconia-ceria support for the 4th reduction cycles in 10% CO and 4th oxidation cycles in air at 1173 K, particle size of 75-250 μm and feed gas flow rate of 50 ml/min for the transition from Fe_2O_3 to Fe and from Mn_3O_4 to MnO.

Figure 7.10 shows that M8FZCe5-1050 has the highest maximum rate of reaction in both reduction and oxidation cycles followed by M5FZCe5-1050, M6FZCe5-1050 and M3FZCe5-1050. Similar trend in reduction-oxidation cycles was observed in H_2 as previously presented in Section 7.1.1. Moreover, the maximum rate of reaction for M8FZCe5-1050 was about 1.4 times that of M5FZCe5-1050 in reduction and oxidation which is approximately same as that observed for reaction in H_2.

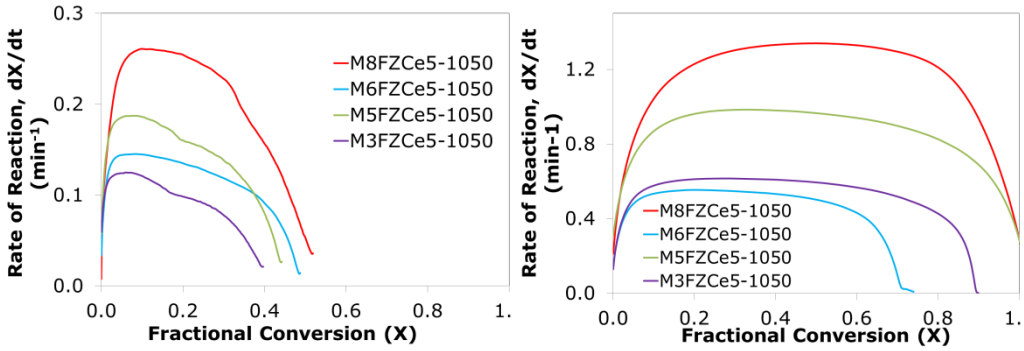

(a) Reduction (b) Oxidation

Figure 7.10: Rate of reaction as a function of fractional conversion for bimetallic oxygen carriers with zirconia-ceria support for the (a) 4th reduction cycles in 10% CO and (b) 4th oxidation cycles in air at 1173 K, particle size of 75-250 μm and feed gas flow rate of 50 ml/min for the transition from Fe_2O_3 to Fe and from Mn_3O_4 to MnO.

Furthermore, the maximum rate of mass conversion for M5FZCe5-1050 was about 1.2 times that of M8FZCe5-1050 in reduction and oxidation (Figure 7.11).

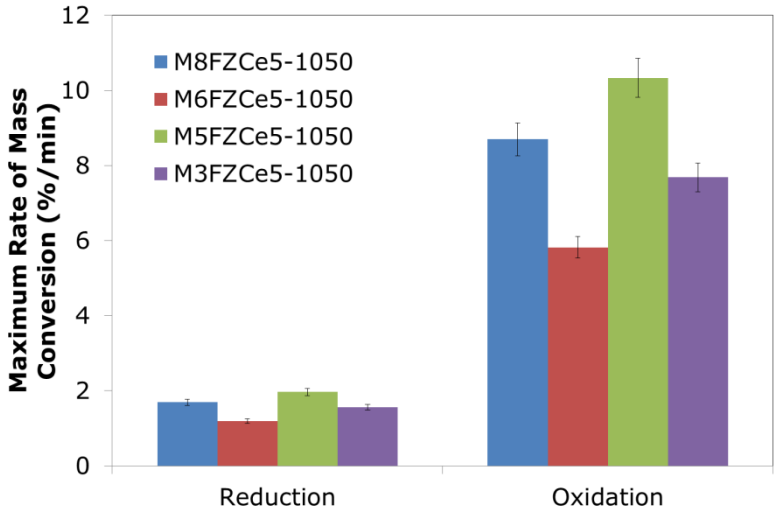

Figure 7.11: Maximum rate of mass conversion for the bimetallic oxygen carriers with zirconia-ceria support for the 4th reduction cycles in 10% CO and 4th oxidation cycles in air at 1173 K, particle size of 75-250 μm and feed gas flow rate of 50 ml/min for the transition from Fe_2O_3 to Fe and from Mn_3O_4 to MnO.

7.2.2 Stability and Effect of Repeated Cycles

Generally, the oxygen carriers were relatively stable in the multi-redox cycles as shown in Figure 7.12. Furthermore, all the OCs showed an initial increase from first to second cycle except M8FZCe5-1050 and thereafter maintained their Roc in the remaining cycles.

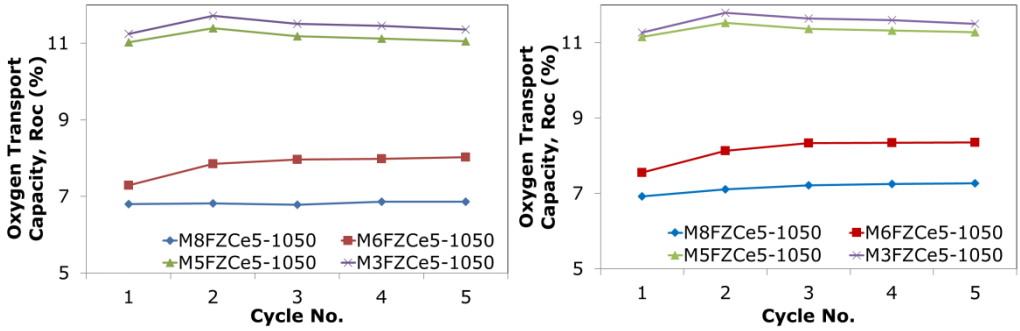

(a) Reduction (b) Oxidation

Figure 7.12: Oxygen transport capacity versus no of cycles for the bimetallic oxygen carriers with zirconia-ceria support for the (a) 4th reduction cycles in 10% CO and (b) 4th oxidation cycles in air at 1173 K, particle size of 75-250 μm and feed gas flow rate of 50 ml/min for the transition from Fe_2O_3 to Fe and from Mn_3O_4 to MnO.

In reduction, all OCs showed increasing maximum rate of mass conversion with increasing number of cycles in reduction reaction as shown in Figure 7.13a. Similar to the findings in H_2, the maximum rate of mass conversion for the OCs increased at an average rate of 2% to 5% per cycle from the second reduction cycle. In oxidation, all OCs showed relatively stable maximum rate of mass conversion through the five cycles as shown in Figure 7.13.

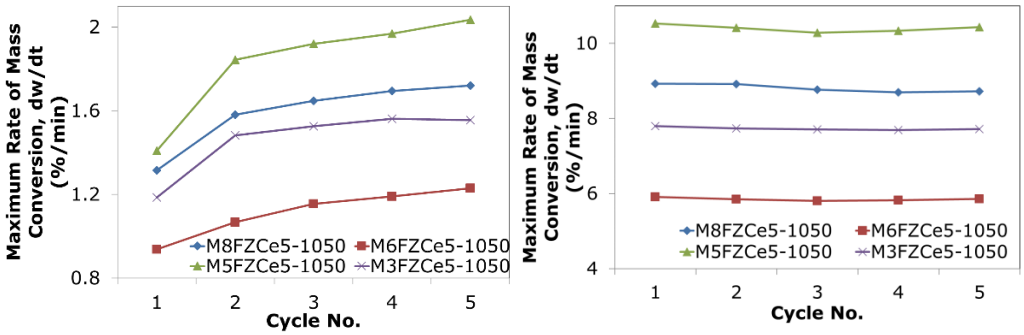

(a) Reduction (b) Oxidation

Figure 7.13: Maximum rate of mass conversion versus cycle number for the bimetallic oxygen carriers with zirconia-ceria support for the (a) reduction cycles in 10% CO and (b) oxidation cycles in air at 1173 K, particle size of 75-250 μm and feed gas flow rate of 50 ml/min for the transition from Fe_2O_3 to Fe and from Mn_3O_4 to MnO.

7.3 Reduction/Oxidation in Methane

7.3.1 Reactivity

The reactivity of the four OCs namely: M8ZCe5-1050, M6ZCe5-1050, M5ZCe5-1050 and M3ZCe5-1050 was evaluated in TGA using methane as fuel. Figure 7.14 shows the fractional conversion versus time curves for the different oxygen carriers. The results indicated that reactivity in CH_4 were quite in oxidation and reduction reactions.

Also, as observed in Figure 7.14, reactivity of the OCs increases with increasing Mn content in both reduction and oxidation period. This behaviour is slightly different when compared to H_2 and CO where M5FZCe5-1050 was the next most reactive OC after M6ZCe5-1050 in both oxidation and reduction.

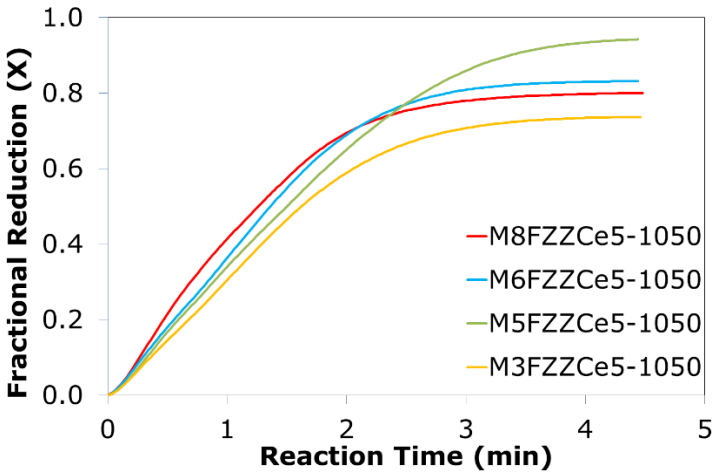

(a) Reduction

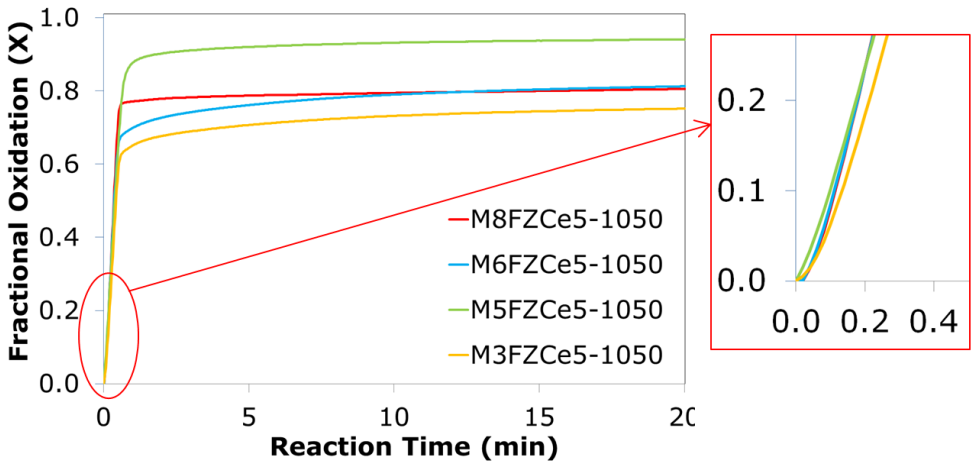

(b) Oxidation

Figure 7.14: Fractional reduction and oxidation versus time for the bimetallic oxygen carriers with zirconia-ceria support for the (a) 4th reduction cycles in 10% CH_4 and (b) 4th oxidation cycles in air at 1173 K, particle size of 75-250 μm and feed gas flow rate of 50 ml/min for the transition from Fe_2O_3 to FeO and from Mn_3O_4 to MnO.

The result presented in Figure 7.15 shows that time needed to reach 30% conversion in reduction and oxidation was less than 60 s. The time needed to reach the same fractional reduction conversion of 0.3, was 4.4 to 5.6 times more in H_2 and 2 to 2.9 times more in CO. Likewise, for the fractional oxidation conversion, the time needed was 3 to 4.6 times more in H_2 and 1.5 to 2.3 times more in CO. Thus, this result shows that

reactivity of the bimetallic Mn-Fe oxygen carriers with zirconia-ceria support was highest in CH_4 compared to reactivity in H_2 and CO.

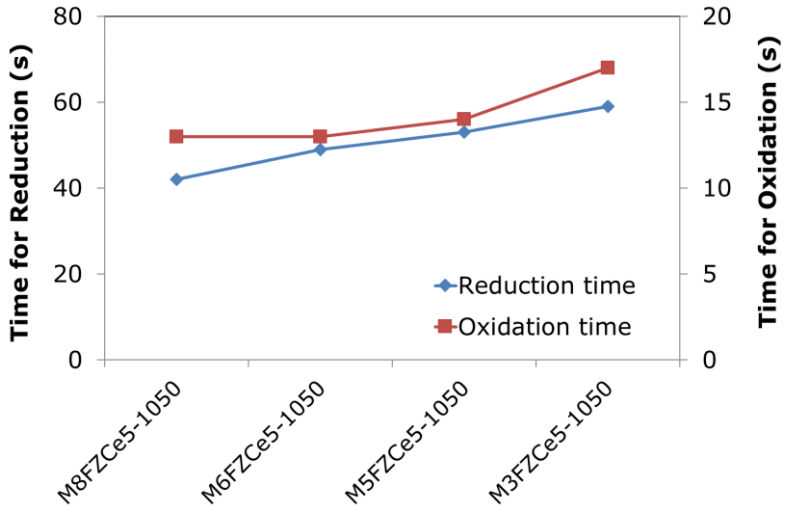

Figure 7.15: Time needed to reach fractional conversion of 0.3 for the bimetallic oxygen carriers with zirconia-ceria support for the 4th reduction cycles in 10% CH_4 and 4th oxidation cycles in air at 1173 K, particle size of 75-250 μm and feed gas flow rate of 50 ml/min for the transition from Fe_2O_3 to FeO and from Mn_3O_4 to MnO.

The OCs rate of reaction as a function of the fractional conversion is shown in Figure 7.16. The results reveal that in reduction and oxidation, maximum rate of reaction of the OCs increased with increasing Mn content. Similar to observations in H_2 and CO, Mn-rich OC (M8FZCe5-1050) has the highest maximum rate of reaction in oxidation and reduction. Furthermore, the maximum rate of reaction of M8FZCe5-1050 was about 1.2 times that of M5FZCe5-1050 in both reduction and oxidation. This trend is nearly similar to that obtained for reactions in H_2 and CO.

As shown in Figure 7.16, M5FZCe5-1050 exhibited the highest extent of reaction in oxidation and reduction. Similarly, this same trend was observed in H_2 and CO during oxidation reaction.

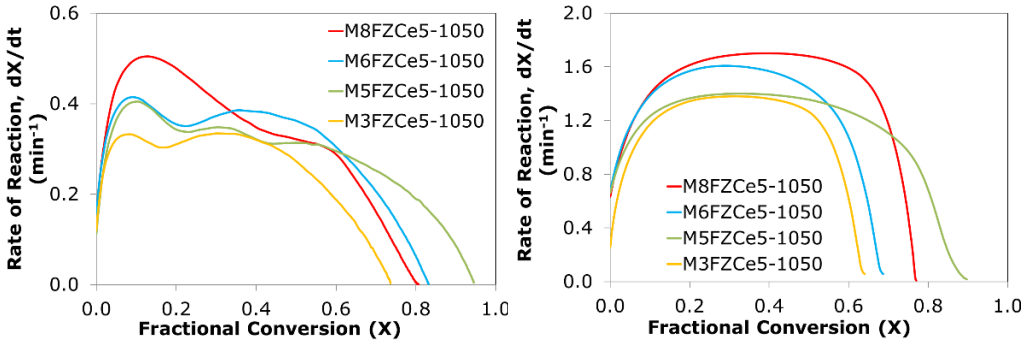

(a) Reduction (b) Oxidation

Figure 7.16: Rate of reaction versus Fractional Conversion: Mixed Oxides/44% Zirconia-Ceria for the (a) 4th reduction cycles in 10% CH_4 and (b) 4th oxidation cycles in air at 1173 K, particle size of 75-250 μm and feed gas flow rate of 50 ml/min for the transition from Fe_2O_3 to FeO and from Mn_3O_4 to MnO.

The maximum rate of mass conversion was highest for M8FZCe5-1050 as shown in Figure 7.17. This rate was approximately 1.1 times that of M5FZCe5-1050. This observation is different to that obtained in H_2 and CO where M5FZCe5-1050 achieved higher maximum rate of mass of conversion compared to M8FZCe5-1050.

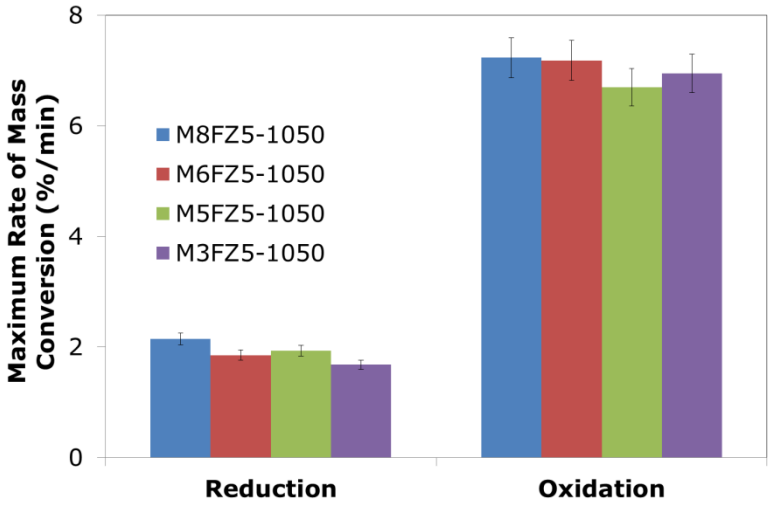

Figure 7.17: Maximum rate of mass conversion as a function of fractional conversion for bimetallic oxygen carriers with zirconia-ceria support for the 4th reduction cycles in 10% CH_4 and 4th oxidation cycles in air at 1173 K, particle size of 75-250 μm and feed gas flow rate of 50 ml/min for the transition from Fe_2O_3 to FeO and from Mn_3O_4 to MnO.

7.3.2 Stability and Effect of Repeated Cycle

The Roc for the oxygen carriers appear to increase gradually with increasing number of cycles in reduction and oxidation as shown in Figure 7.18 which is somewhat similar to the activation tendency behaviour observed in H_2 and CO. Moreover, in reduction, the OCs showed an increasing Roc at an average rate of 1.2 to 1.8% per cycle from the third cycle and in oxidation, the average rate was 1.3 to 1.8% per cycle from the second cycle.

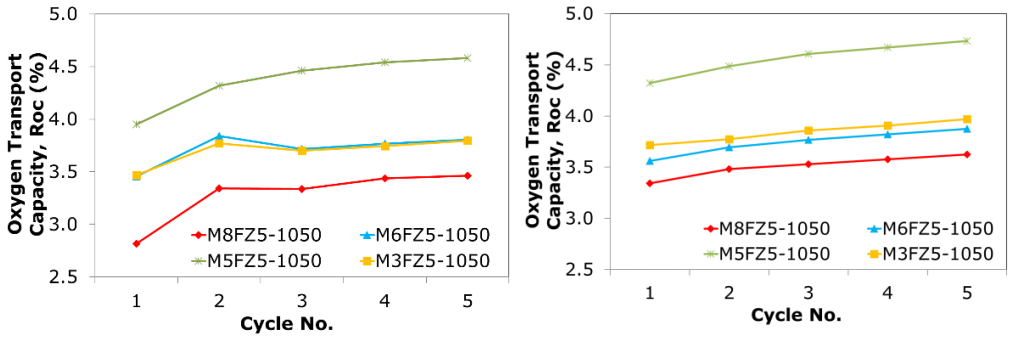

(a) Reduction (b) Oxidation

Figure 7.18: Oxygen transport capacity versus no of cycles for the bimetallic oxygen carriers with zirconia-ceria support for the (a) reduction cycles in 10% CH_4 and (b) oxidation cycles in air at 1173 K, particle size of 75-250 μm and feed gas flow rate of 50 ml/min for the transition from Fe_2O_3 to FeO and from Mn_3O_4 to MnO.

Likewise, as shown in Figure 7.13, the OCs showed relatively increasing maximum rate of mass conversion with increasing number of cycles in reduction and oxidation. In reduction, the maximum rate of mass conversion of the OCs increased at average rate of 1% to 7% per cycle from the third cycle. Similar trend was observed for reactions in H_2 and CO as fuel.

Again, it is worth noting that M5FZCe5-1050 activation tendency behaviour observed in CH_4 (Figure 7.19) as well as in H_2 and CO is a reversal of the typical progressive reduction behaviour observed for the corresponding OC with zirconia support (i.e. M5FZ5-1050). Furthermore, Bhavsar et al. (2014) used only ceria as support for Fe and Mn oxygen carrier synthesized via incipient wetness technique (impregnation) and observed that ceria could not maintain the integrity of the bimetallic phase during redox operation. In this study, the use of combined ceria and zirconia support appear to have altered the thermodynamics of iron and manganese oxides, hence the observed remarkable behaviour by the oxygen carrier. This result is in agreement that ceria can actively participate and enhance chemical reactions (Galvita et al., 2013). Further confirmation to this finding will be highlighted in Section 7.5.

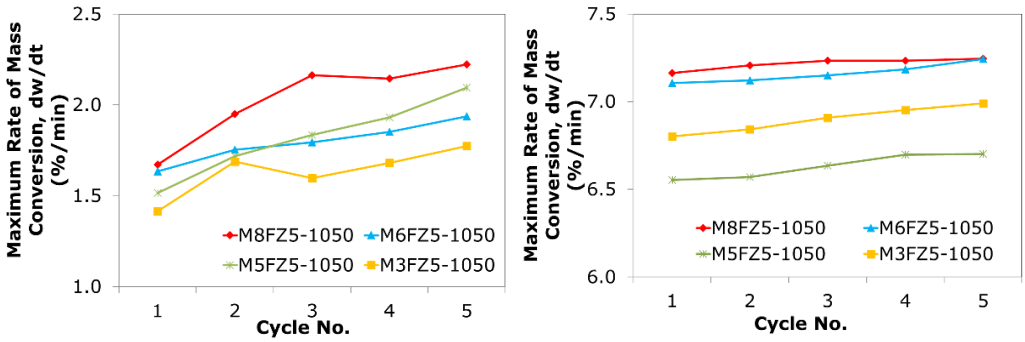

(a) Reduction (b) Oxidation

Figure 7.19: Maximum rate of mass conversion versus cycle number for the bimetallic oxygen carriers with zirconia-ceria support for the (a) reduction cycles in 10% CH_4 and (b) oxidation cycles in air at 1173 K, particle size of 75-250 μm and feed gas flow rate of 50 ml/min for the transition from Fe_2O_3 to FeO and from Mn_3O_4 to MnO.

7.4 Long-Term Recyclability of Bimetallic Oxygen Carrier Supported on Zirconia-Ceria Support.

In comparison to the investigated oxygen carriers in this batch, the Mn-rich OC (M8FZCe5-1050) exhibited the highest reactivity. Therefore, this

particle was further evaluated for long-term operation which involved thirty consecutive redox cycles presented in Figure 7.20. The co-precipitated M8FZCe5-1050 oxygen carrier indicates reasonable recyclability with activation tendency behaviour (Figure 7.20). The result suggests that addition of ceria as support has promotional effect on the behaviour of the oxygen carriers.

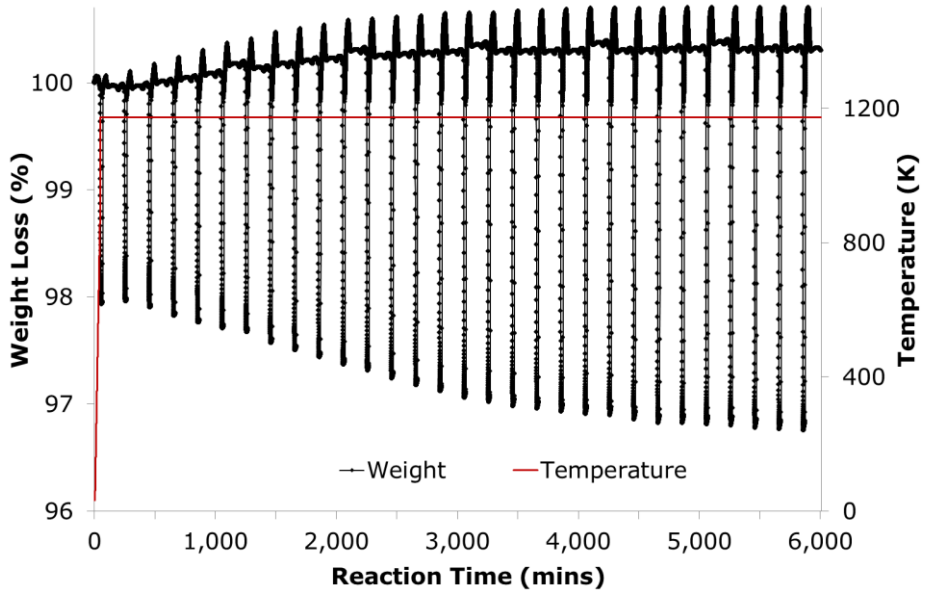

Figure 7.20: Long-term recyclability of M8FZCe5-1050 oxygen carrier for the reduction cycles in 10% CH_4 and oxidation cycles in air at 1173 K, particle size of 75-250 µm and feed gas flow rate of 50 ml/min for the transition from Fe_2O_3 to FeO and from Mn_3O_4 to MnO.

7.5 Characterization of Fresh and Reacted Oxygen Carriers

The fresh and reacted particles of the bimetallic oxygen carriers with ceria and zirconia support were characterized to gain understanding of possible chemical and morphological transformations in the oxygen carriers. These analyses are helpful to establish possible structure-activity relationship for the oxygen carriers. Figures 7.21 to 7.24 show the SEM image of the OCs at a scale of 20–100 µm. Generally, Mn-rich OCs (M8FZCe5-1050 and

M6FZCe5-1050) did not form agglomerates regardless of the reacting gas (Figures 7.21-7.22). Also, M5FZCe5-1050 OC did agglomerate except in CO (Figure 7.23). On the other hand, the Fe-rich OC form agglomerates in H_2 as well as in CO (Figure 7.24). The larger pores observed in the reacted particles in CH_4 perhaps provide more active sites for gaseous fuel oxidation and thus contributes to the very high reactivity observed in CH_4 compared to H_2 and CO.

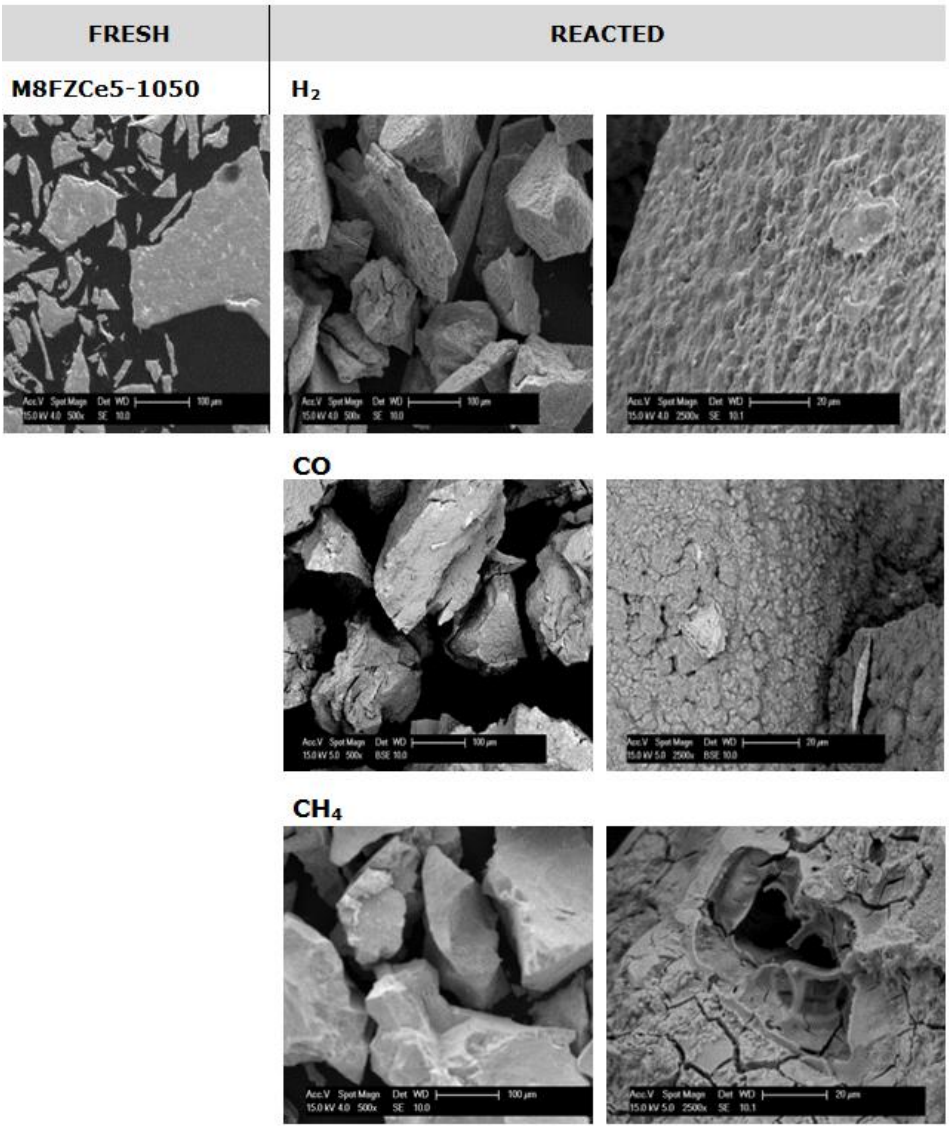

Figure 7.21: SEM images of the unreacted polished M8FZCe5-1050 particles after calcination at 1323 K for 2 h and reacted M8ZCe5-1050 particles after five redox cycles at 1173 K in H_2, CO or CH_4. The images show particles without agglomeration.

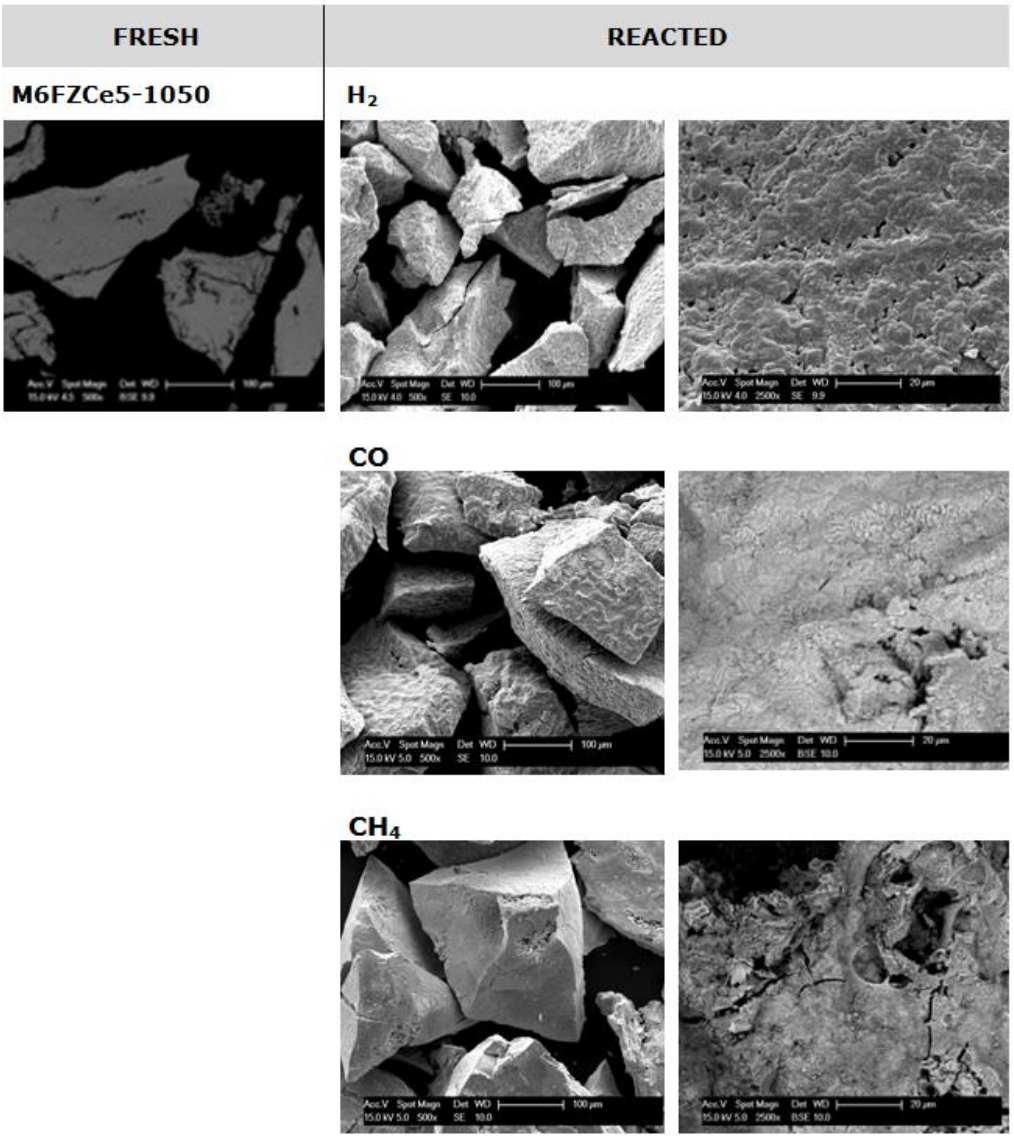

Figure 7.22: SEM images of the unreacted polished M6FZCe5-1050 particles after calcination at 1323 K for 2 h and the reacted particles after five redox cycles 1173 K in H_2, CO or CH_4. The images show particles without agglomeration and the presence of pores after the redox reaction.

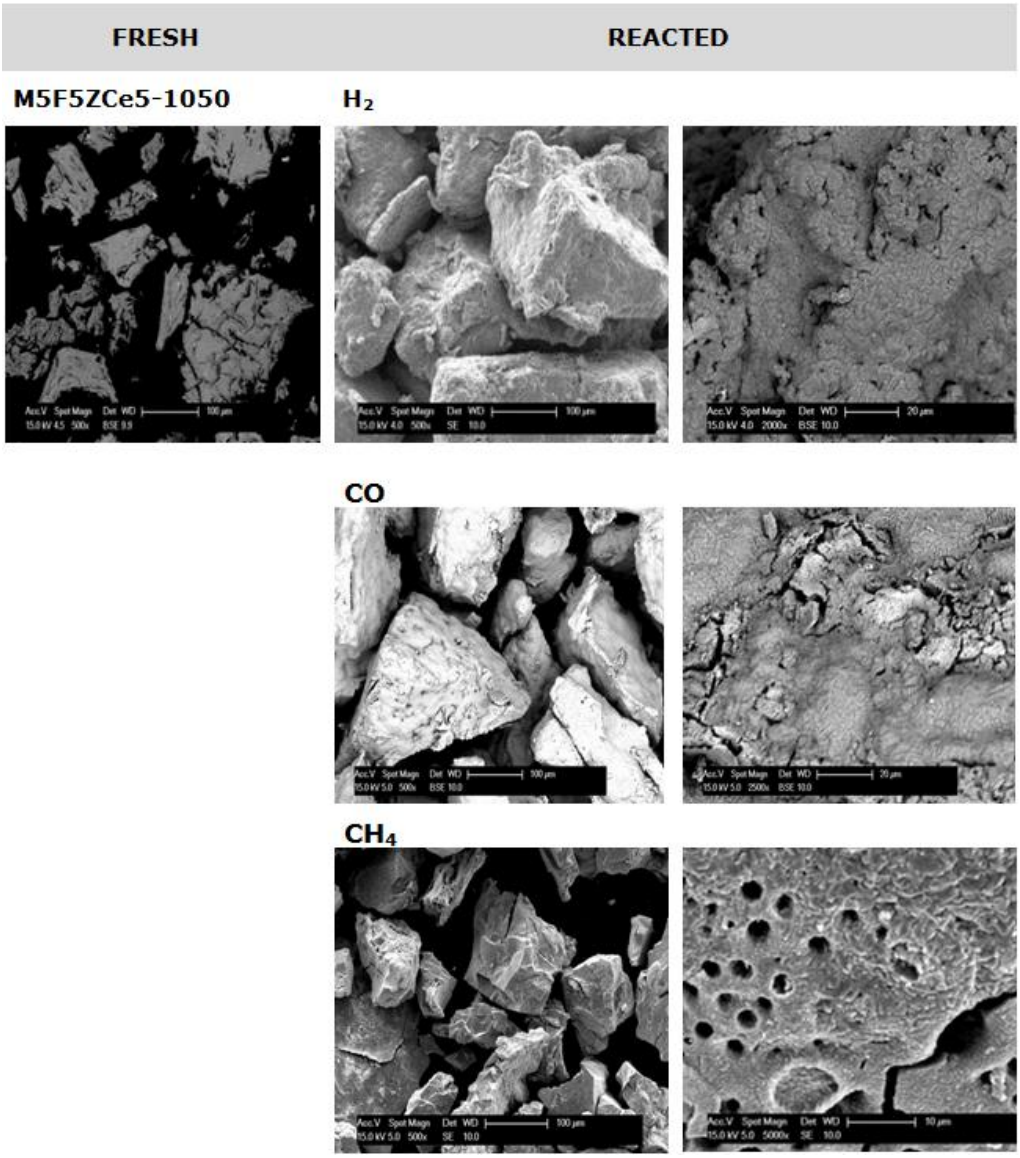

Figure 7.23: SEM images of the unreacted polished M5FZCe5-1050 particles after calcination at 1323 K for 2 h and reacted particles after five redox cycles at 1173 K in H_2, CO or CH_4. The images show particles without agglomeration and the presence of pores after the redox reaction in the different gases.

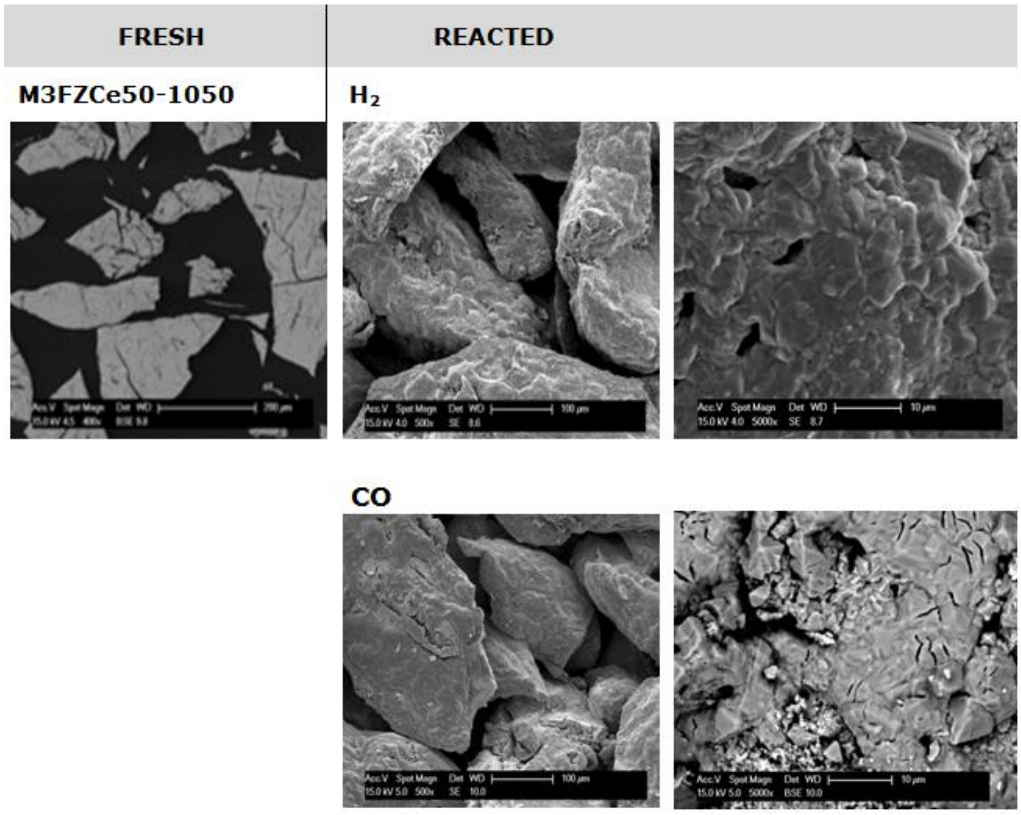

Figure 7.24: SEM images of the fresh M3FZCe5-1050 polished particles after calcination at 1323 K for 2 h and reacted M3FZCe5-1050 particles after five redox cycles at 1173 K in H_2 or CO

The XRD result presented in Table 7.3 revealed that zirconia and ceria combined to form Zr-rich phase and Ce-rich phase and no separate peak for either zirconia or ceria was identified by the XRD. However, it does appear the ceria migrates to the particle surface and participates in the redox reaction. This was confirmed by SEM-EDX analysis of reacted M8FZCe5-1050 in H_2 presented in Figure 7.25 at 60 μm scale. The rectangle in the inset image shows the selected EDX inspection field of the sample. The resulting spectrum reveals the presence of Ce peaks for spectrum 1 and 2 while negligible Ce peaks were observed for spectrum 3 and 4. This finding could be a contributing factor for the observed effects on the behaviour of Mn-Fe bimetallic OC with zirconia-ceria support compared to the corresponding zirconia only supported OC discussed earlier in this chapter.

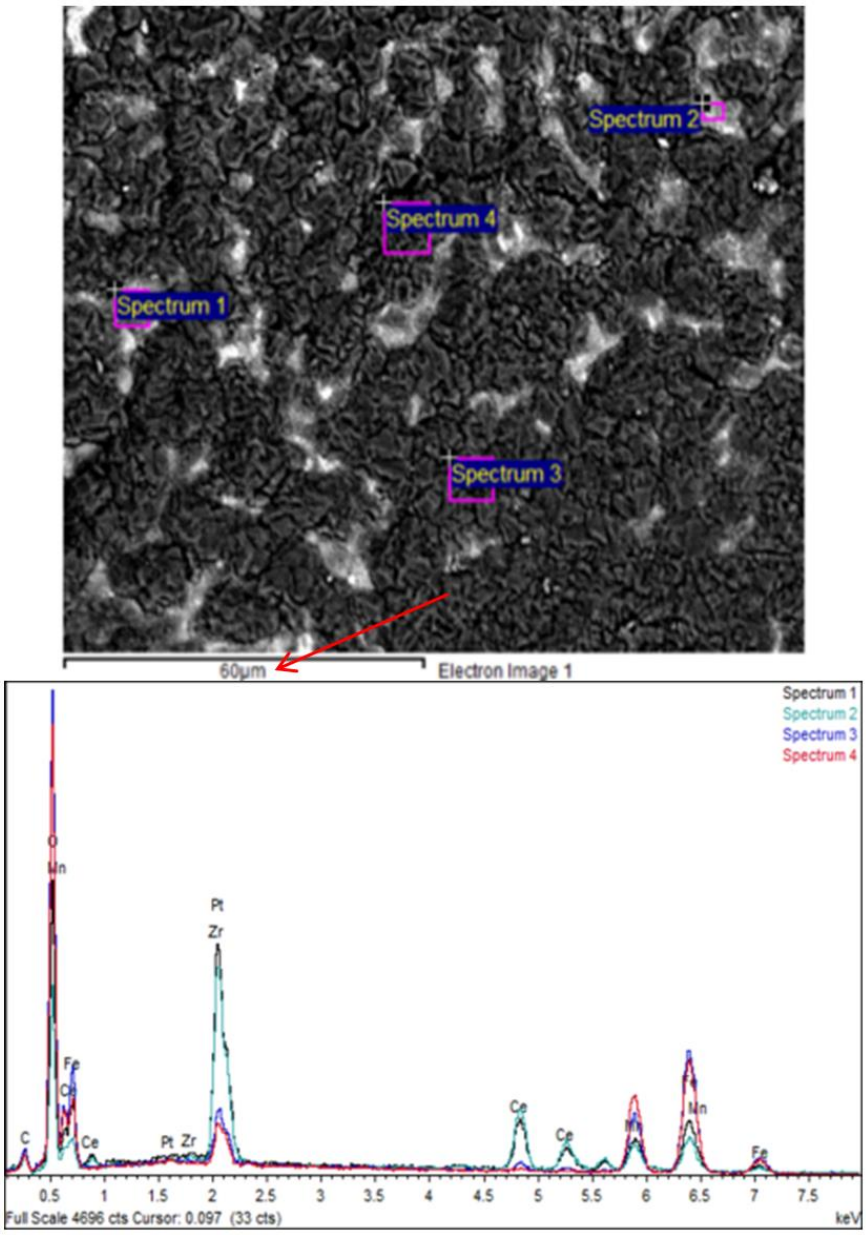

Figure 7.25: SEM-EDX image of reacted M8FZCe5-1050 particle after five redox cycles at 1173 K in H_2 and air. The scale bar indicated by the arrow represents 60 µm. The SEM-EDX analysis confirms the presence of Ce particles at the surface of the composite material.

Table 7.3: Phase composition of bimetallic oxygen carriers with zirconia-ceria identified by X-ray Diffraction.

Oxygen carrier	Fresh	Re-Oxidation
M8FZCe5-1050	t-$(Zr_{0.88}Ce_{0.12})O_2$ c-$Ce_{0.75}Zr_{0.25}O_2$ c-$MnFe_2O_4$ Jakobsite	t-$(Zr_{0.88}Ce_{0.12})O_2$ c-$MnFe_2O_4$ Jakobsite c-CeO_2 t- $Z_{r0.5}Ce_{0.5}O_2$
M6FZCe5-1050	t-$(Zr_{0.88}Ce_{0.12})O_2$ c-$Ce_{0.75}Zr_{0.25}O_2$ c-$MnFe_2O_4$ Jakobsite r-Fe_2O_3 Hematite	c-Mn_2O_3 Bixbyite c-$MnFe_2O_4$ Jakobsite t-$(Zr_{0.88}Ce_{0.12})O_2$ c-$Ce_{0.75}Zr_{0.25}O_2$ r-Fe_2O_3 Hematite
M5FZCe5-1050	t-$(Zr_{0.88}Ce_{0.12})O_2$ c-$Ce_{0.75}Zr_{0.25}O_2$ c-$MnFe_2O_4$ Jakobsite r-Fe_2O_3 Hematite	r-Fe_2O_3 Hematite c-$MnFe_2O_4$ Jakobsite t- $Z_{r0.5}Ce_{0.5}O_2$
M3FZCe5-1050	t-$(Zr_{0.88}Ce_{0.12})O_2$ c-$Ce_{0.75}Zr_{0.25}O_2$ c-$MnFe_2O_4$ Jakobsite r-Fe_2O_3 Hematite	—

Key: t-tetragonal, c-cubic, r-rhombo

7.6 Conclusions

The behaviour of the co-precipitated Mn-Fe bimetallic oxygen carriers with zirconia-ceria support has been studied and the following conclusions can be drawn:

1. The co-precipitated technique was found to yield bimetallic oxygen carriers with high degree of dispersion of the elements; Mn, Fe, Ce and Zr in the composite material.
2. The oxygen carrier reactivity in the three gases followed the order CH_4> CO> H_2: and most of the OCs did not form agglomerates during the redox reactions.

5. The Mn-rich sample M8FZCe5-1050 has the highest maximum rate of reaction in oxidation and reduction in the three gases; H_2, CO and CH_4.
6. Ceria exhibited a promoting effect on the OCs. in comparison to zirconia-only support, the addition of ceria support enhanced the performance of the bimetallic OCs and these exhibited activation tendency behaviour.
7. The use of combined zirconia-ceria reversed the characteristic progressive decrease in performance observed for M5FZ5-1050 oxygen carrier.

8 KINETICS OF CO-PRECIPITATED Mn_3O_4/ZrO_2

Kinetic studies provide the opportunity to obtain values of kinetic parameters for the determination of rate of reactions at reaction conditions different from that at which the original measurements were carried out (Brown, 2001). Hence, one of the main aims of kinetic studies of chemical reaction is to obtain the rate equation that best describes the extent of conversion of reactant(s) or of product(s) formation with time as the reaction progresses. To achieve this, experimentally obtained data are compared with predicted values derived from theoretical kinetic expressions. This gives the opportunity to decide which rate equation best describes the experimental measurements. The study may be at constant or varying temperature. Thus, kinetic analysis also provides opportunity to determine the influence of temperature on the rate of reaction (Galwey and Brown, 1998).

Several factors such as interaction of metal oxide with the support affect the activation energy for an oxygen carrier. Thus, it is necessary to obtain the kinetic data for every specific oxygen carrier (Adánez et al., 2012). Furthermore, very limited kinetic data exist for manganese oxide-based OCs in literature (Adánez et al., 2012; Zafar et al, 2007). Hence, the focus of this chapter is to examine the kinetics of the reduction and oxidation reactions of the most reactive co-precipitated monometallic OC (M5Z5-1050) obtained from this work using CH_4, H_2, CO and air respectively as reacting gases.

8.1 Kinetic Analysis

Fractional conversion was calculated using TGA data of the second cycle up to 95% conversion. Microsoft Excel and Prism version 6.00 for Windows (GraphPad Software) were used to aid data analysis. The fractional conversion (X) was defined in Section 3.4. The kinetic expression for the rate of solid-gas reaction can be described by the following equation:

$$\frac{d\mathrm{X}}{d\mathrm{t}} = f(\mathrm{X})k(\mathrm{T}) \tag{28}$$

where *f(*X*)* is a mathematical function that depends on the reaction model that describes the chemical or physical properties during the reaction process, t is the reaction time and *k(*T*)* is the reaction rate constant described by the Arrhenius equation (Equation 29).

$$k(\mathrm{T}) = A_o e^{(-E_a)/R\mathrm{T}} \tag{29}$$

where E_a is the activation energy, R is the gas constant (8.314 J K^{-1} mol^{-1}) and A_o is the pre-exponential factor. The kinetic parameters are calculated from the slope and intercept of ln(k(T)) versus 1/T based on the following equation.

$$\ln k(\mathrm{T}) = -\frac{E_a}{R\mathrm{T}} + \ln A_o \tag{30}$$

Equation 28 can be integrated analytically for reaction kinetics under isothermal conditions to yield:

$$g(\mathrm{X}) = \int_0^X \frac{d\mathrm{X}}{f(\mathrm{X})} = k\mathrm{t} \tag{31}$$

where *g(X)* is an integral mathematical form of the kinetic model.

Different kinetic models have been used to predict OCs conversion time dependence and operating condition effects on reaction rates. Commonly cited kinetic models can be categorized as reaction order, geometrical

contraction, diffusion, and nucleation and growth (Zhou et al, 2014). The f(X) and g(X) of the models considered in this work are shown in Table 8.1.

Methods used in this work to compare kinetic models to isothermal experimental data include: Hancock and Sharp (1972) method, and the fit quality of the fractional conversion versus time curve. The Hancock and Sharp (1972) approach is based on the nucleation model and is expressed as

$$\ln(-ln(1-\mathrm{X})) = \ln a + n \ln \mathrm{t} \qquad (31)$$

where *a* is a constant that relies on rate of nuclei formation and growth, *n* is the kinetic exponent. ln(-ln(1-X)) was plotted against ln t for experimental data 0.15<X<0.5, such that the value of *n*, points to the most suited model. In addition, deviation from straight line indicates multi step reaction conversion data.

Table 8.1: Rates and integral expressions for basic solid-state kinetic models.

No	Kinetic model	*f(X)*	*g(X)*	*n*
Reaction order model				
K2-O	Second-order	$(1-\mathrm{X})^2$	$(1-\mathrm{X})^{-1}-1$	0.83
K3-O	Third-order	$(1-\mathrm{X})^3$	$(1/2)((1-\mathrm{X})^{-2}-1)$	0.70
Geometrical contraction model				
C2-D	2-D (Contracting area)	$2(1-\mathrm{X})^{1/2}$	$(1-(1-\mathrm{X})^{1/2})$	1.11
C3-D	3-D (Contracting volume)	$3(1-\mathrm{X})^{2/3}$	$(1-(1-\mathrm{X})^{1/3})$	1.07
Nucleation and nuclei growth model				
N(n=n)	Avrami-Erofe'ev	$n(1-\mathrm{X})(-\ln(1-\mathrm{X}))^{(n-1)/n}$	$(-\ln(1-\mathrm{X}))^{1/n}$	*n*
Diffusion model				
D3-D	3-D (Jander)	$(3/2)(1-\mathrm{X})^{2/3}(1-(1-\mathrm{X})^{1/3})$	$(1-(1-\mathrm{X})^{1/3})^2$	0.54

The reaction of OCs in the fuel and air reactors is considered as non-catalytic gas-solid reaction. Gas-solid reactions generally follow intermediate steps that may involve the following parameters:

- gas diffusion to the porous particle surface through the bulk gas
- penetration and gas diffusion to the surface of the unreacted core through the product boundary layer
- chemical reaction between the gas and the solid
- adsorption of the gaseous reactants on the solid surface (Zafar et al., 2006; Adánez et al., 2012).

The kinetic model that explains a heterogeneous or gas-solid reaction is dependent on the controlling resistance during the reaction. It is therefore important to ensure that the reaction is chemically controlled and intrinsic surface reaction determines the overall reaction rate. The measures taken to achieve this aim are discussed in Section 3.4 and Appendix F. It could be noted that the estimated theoretical rates of reaction due to external mass transfer were substantially higher than the observed rates for all temperatures; which implies that external mass transfer was not controlling the reaction. In addition, an effectiveness factor close to unity was obtained for M5Z5-1050 indicating negligible presence of internal mass transfer resistance. Thus, it could be stated that in this kinetic study, reaction of reacting gases with the OC at conditions for CLC was predominantly chemically controlled.

8.2 Statistical Analysis

In statistical analysis and modelling, regression is used to estimate the relationships among variables and provide a means of predicting the dependent variable based on one or more independent variables and model

parameters. This involves fitting a line called the regression model or equation to the data points that minimize the errors (residuals). Consequently, on constructing the regression model, it is important to check the goodness of fit of the proposed model and the statistical significance of the estimated parameters. Common means of checking for the goodness of fit and statistical significance include the coefficient of determination (R-squared), the residual sum of squares (RSS), F-test of the overall fit and the use of Akaike Information Criterion with correction (AIC_C) (Motulsky and Christopoulos, 2003).

The residual sum of squares is the sum of the squares of the vertical distances (residuals predicted from actual experimental data) of the points from the curve. RSS provides the degree of discrepancy between the data and the regression model and provide a means of quantifying the accuracy of fit of each model. It is usually used as an optimality criterion in model selection. Thus, a small value of RSS shows a tight fit of the model to the experimental data. On the other hand, the coefficient of determination quantifies the goodness of fit. Hence, the coefficient of determination measures the extent to which the regression measures the total deviations of the dependent variable (Motulsky and Christopoulos, 2003).

In model selection, the model with more fitting parameters will virtually always fit the experimental data better (with a lower RSS) than the model with fewer numbers of free parameters. Also, it is recommended not to use only R-squared as a basis for model selection (Motulsky and Christopoulos, 2003). Thus, a statistical approach is needed to better decide if there is any substantial statistical difference between models fitted to the same experimental data but having different number of free parameters. The F-test and AIC_C are available statistical approach in model discrimination to

achieve this aim (Motulsky and Christopoulos, 2003; Kletting and Glatting, 2009).

F-test is a commonly used hypothesis-test for determining the most statistically significant model between versions with varied complexity. It is based on the difference between the RSS of the two models, the number of sample data points and the number of free parameters of each model. The goodness-of-fit and complexity of the models are quantified as the RSS of the data points from the model and the degrees of freedom respectively. The F ratio (*F*) is computed using the following equation.

$$F = \frac{(SS_1 - SS_2)/SS_2}{(df_1 - df_2)/df_2} \quad 32$$

where *SS* is the sum of squares, *df* is the degrees of freedom, and the numbers 1 and 2 denote the null (simpler) and alternative (more complex) models, respectively. The more complex model is accepted as statistically significant when the F ratio of the two models exceeds $F_{0.05}(df_1\text{-}df_2, df_2)$ (Motulsky and Christopoulos, 2003; Kletting and Glatting, 2009).

The Akaike Information Criterion with correction (AIC_C) is a method used in model selection for comparing models based on information theory. This method provides the means for measuring the relative quality of each model for a given set of experimental data and hence determines the most likely model to be correct. For the case of least square fit, the AIC_C is defined as

$$\mathrm{AIC_C} = \mathrm{AIC} + \frac{2K(K+1)}{N-K-1} \quad 33$$

$$\mathrm{AIC} = N \ln\left(\frac{SS}{N}\right) + 2K \quad 34$$

Where *N* is the number of data points, *K* is the number of free parameters fitted by the regression (+1 for the estimated sum-of-squares), and *SS* is

the sum of the square of the deviations (between the measurement and the curve). The model with the smallest value of AIC_C among the candidate models is selected as the best model (Motulsky and Christopoulos, 2003; Kletting and Glatting, 2009; Burnham and Anderson, 2002).

It has been noted that the AIC_C and F test do sometimes disagree in their selection of correct model. When the competing models are very similar, the F test tends to lean towards choosing the simpler model even when the more complex model is correct. In contrast to the F test, the AIC_C is theoretically better justified for the selection of models. Thus, in such instances, the choice of model is based on the AIC_C (Ludden, Beal and Sheiner, 1994; Kletting and Glatting, 2009).

In this work, the experimental data were fitted to the kinetic expressions in Table 8.1. The models in Table 8.1 include five one-parameter models (K2-O, K3-O, C2-D, C3-D, D3-D and one two-parameter model (N(n=n)). Also, there is a further one-parameter variant of the N(n=n) with the n value constant. The analysis procedure utilized involved selecting the model with least value of RSS among the one-parameter models and comparing the F ratio obtained for this model and the two-parameter model with the corresponding 95% upper quantile of the F-distribution, $F_{0.05}(df_1\text{-}df_2, df_2)$. If the F-ratio of the two models is greater than the $F_{0.05}(df_1\text{-}df_2, df_2)$, then the two-parameter model is selected as statistically significant. The result obtained is cross checked with the values of AIC_C computed.

8.3 Reduction Kinetics of M5Z5-1050 Oxygen Carrier in Methane

The effect of temperature on M5Z5-1050 sample in CH_4 is shown in Figure 8.1. Figure 8.1 shows that the reactivity of the OC is dependent on

temperature such that the reactivity increases with increasing reaction temperature.

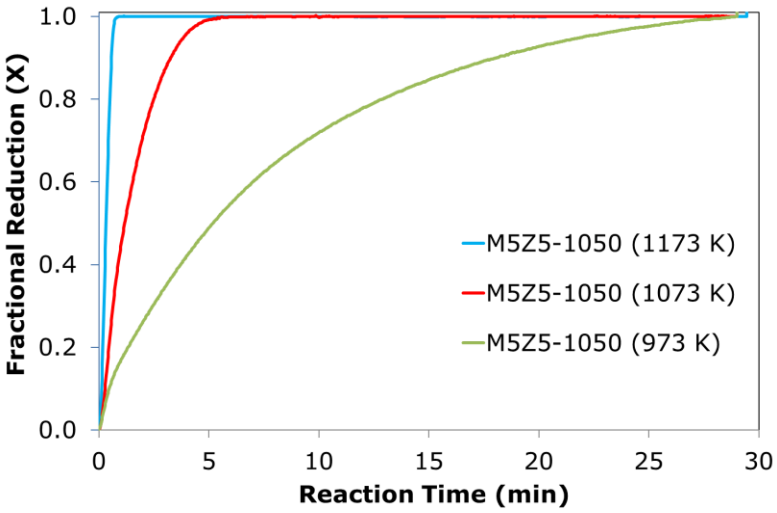

Figure 8.1: Fractional reduction versus time for monometallic oxygen carrier M5Z5-1050 at 973 K, 1073 K and 1173K for the 2nd reduction cycles in 10% CH_4 particle size of 75-250 μm and feed gas flow rate of 50 ml/min for the transition from Mn_3O_4 to MnO.

Applying the Hancock and Sharp (1972) method, the plot of ln(-ln(1-X)) versus ln t for M5Z5-1050 for temperature range 973-1173 K using 10% CH_4 in conversion range of $0.15<X<0.5$ is illustrated in Figure 8.2. The existence of a linear relationship is evident at the three temperatures investigated which implies that nucleation and growth process is constant through the reduction process; that is, constant *n* values at given reaction temperatures. This also means that the experimental reaction data for M5Z5-1050 could be described by a single kinetic model. The values of *n* obtained at the different temperatures ranges from 0.81 to 1.58. Models (from Table 8.1) with suitable kinetic mechanisms associated with these n values are: K2-O (n=0.83), C2-D (n=1.11), C3-D (1.07), and N (n=n).

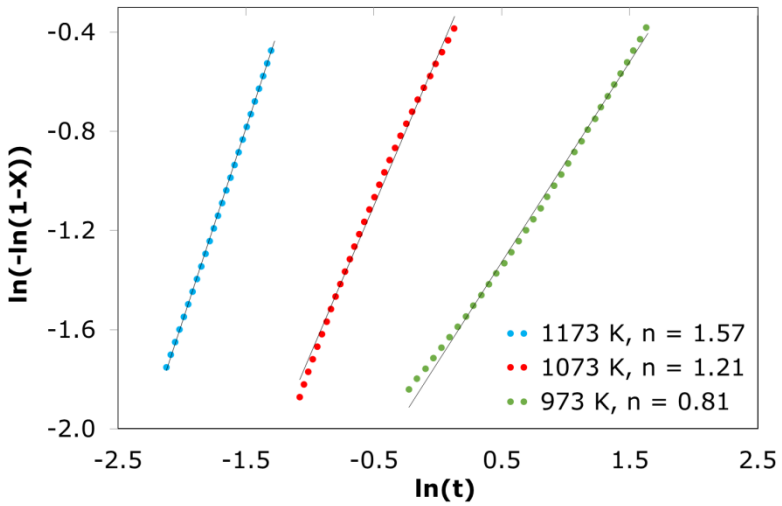

Figure 8.2: Sharp-Hancock plots for monometallic oxygen carrier M5Z5-1050 using 0.15<X<0.5 at 973 K, 1073 K and 1173K for the 2nd reduction cycles in 10% CH_4, particle size of 75-250 µm and feed gas flow rate of 50 ml/min for the transition from Mn_3O_4 to MnO.

Figures 8.4, 8.5 and 8.6 show the fit of the experimental reaction data to the fractional reduction conversion versus time curve for each of the kinetic models at temperatures 973 K, 1073 K and 1173 K respectively.

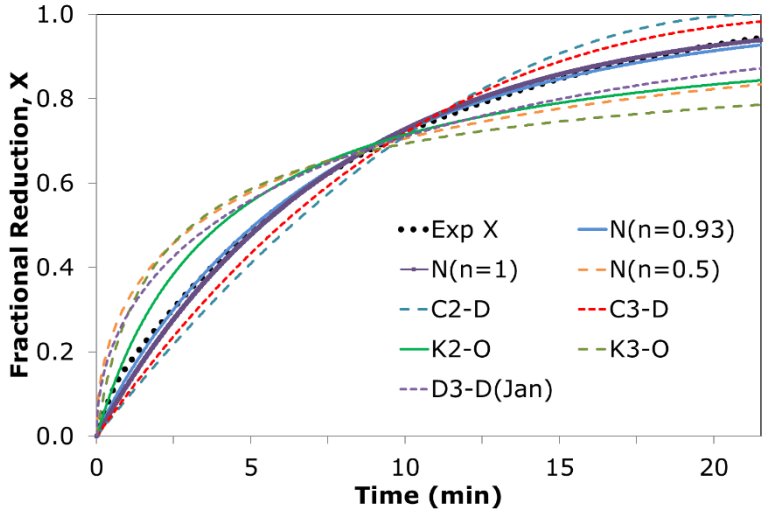

Figure 8.3: Curve fitting of experimental data (0<X<0.95) of M5Z5-1050 to various kinetic models at 973 K for the 2nd reduction cycle in 10% CH_4, particle size of 75-250 µm and feed gas flow rate of 50 ml/min for the transition from Mn_3O_4 to MnO.

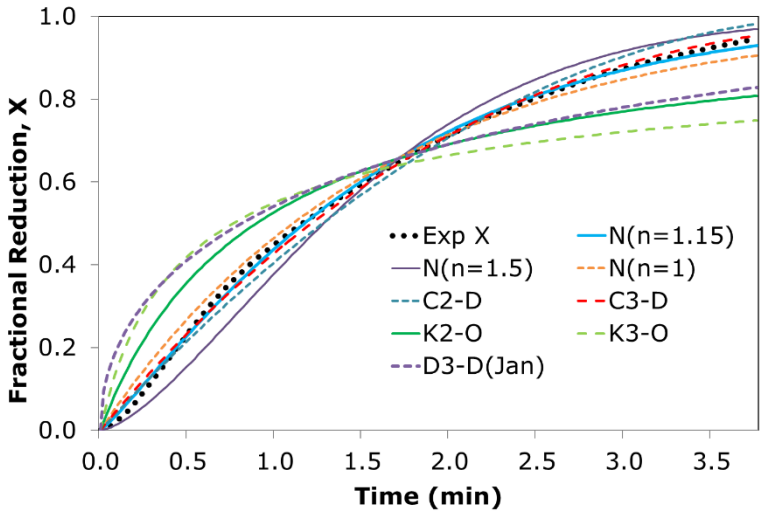

Figure 8.4: Curve fitting of experimental data (0<X<0.95) of M5Z5-1050 to various kinetic models at 1073 K for the 2nd reduction cycle in 10% CH_4, particle size of 75-250 μm and feed gas flow rate of 50 ml/min for the transition from Mn_3O_4 to MnO.

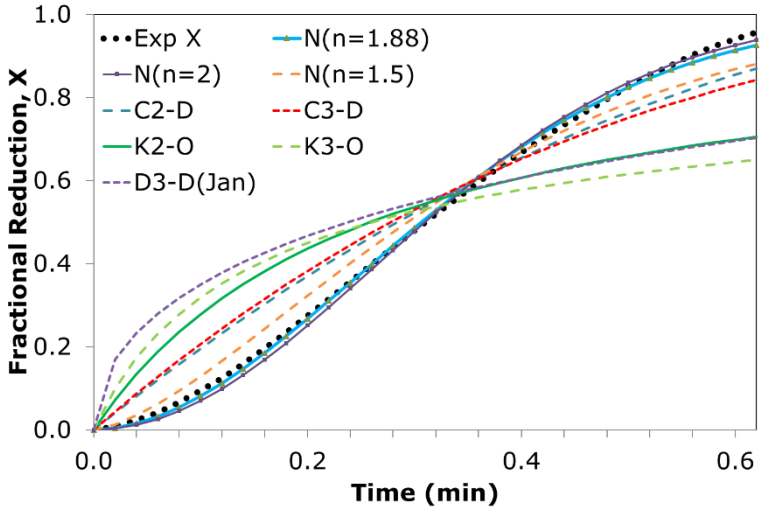

Figure 8.5: Curve fitting of experimental data (0<X<0.95) of M5Z5-1050 to various kinetic models at 1173 K for the 2nd reduction cycle in 10% CH_4, particle size of 75-250 μm and feed gas flow rate of 50 ml/min for the transition from Mn_3O_4 to MnO.

The parameters obtained for the kinetic models examined are presented in Tables 8.2, 8.3 and 8.4. All models shown in Tables 8.2, 8.3 and 8.4 are one-parameter models except for N(n=0.93), N(n=1.15) and N(n=1.88). The one-parameter model with the least RSS and highest R-squared was selected and then compared with the two-parameter model using F-test and AIC_C for each of the data sets. The nucleation models [N(n=0.93),

N(n=1.15) and N(n=1.88)] has the highest values of R-squared and lowest RSS values. Also, the AICC identifies the nucleation models as the most statistically significant models. Furthermore, the F-test of the nucleation model with regards to the other models gave values that are greater than the 95% upper quantile of the Fisher distribution for the three temperatures investigated. Therefore, the two-parameter nucleation model N(*n*=*n*) is the most suitable model for describing the reduction behaviour of M5Z5-1050 at the three temperatures studied.

Thus, the reaction of the OC proceeded through the generation of metallic nuclei and subsequent increase in the number of nuclei formation during the incubation period leading to increasing reaction rate. The nucleation continues with the reaction occurring uniformly over the solid surface and into the inner core of grains as illustrated in Figure 8.6. This reaction mechanism is generally typified by a sigmoid curve as illustrated in Figures 8.2, 8.3 and 8.5 (Adánez et al., 2012).

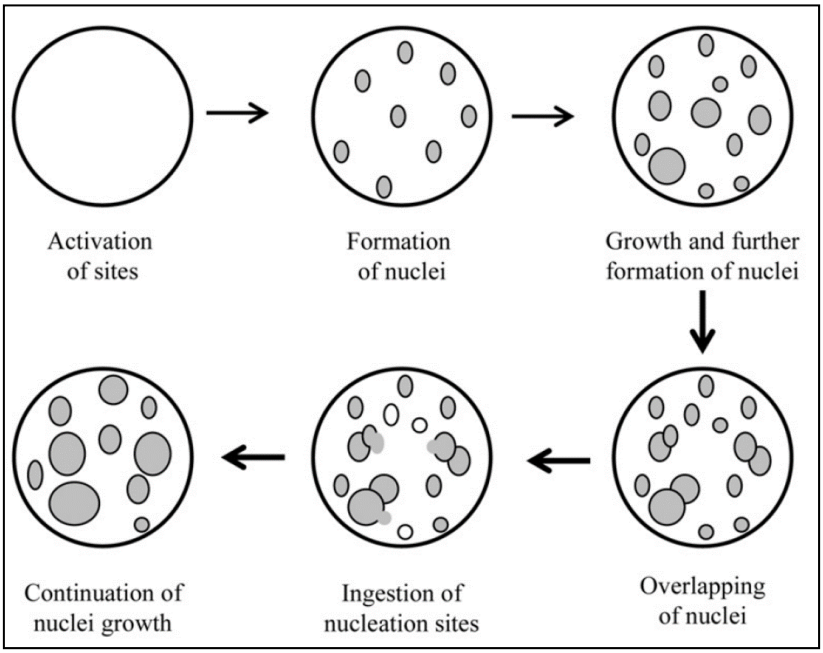

Figure 8.6: Schematic of nucleation and nuclei growth model (Hossain and de Lasa, 2010)

The geometrical contraction models (C2-D and C3-D) also show some good fit to the experimental reaction data at temperature of 1073 K (Figure 8.4) whereas C3-D had a better fit than C2-D at 973 K (Figure 8.3). This result is an agreement that nucleation process could be relatively fast at the temperature ranges for CLC such that the geometrical contraction model could reasonably fit the same experimental data as the nucleation model (Szekely et al., 1976; Sedor et al., 2008). Also, the diffusion controlled model D3-D(Jan) has decreasing quality of fit as the temperature increases showing a poorer fit to the experimental data and thus not suitable for describing the reduction reaction behaviour (Figure 8.3, 8.4 and 8.5).

Table 8.2: Parameters from fitting kinetic models to reaction experimental reduction data at 973 K using 10% CH_4. 95% upper quantile of the F-distribution $F_{0.05}$(df1-df2,df2) = 3.8501 for all the cases compared.

Models	**RSS**	**R^2**	**AIC_C**	**F-Test [Compared with N(n=0.93)]**	***K* (min^{-1})**
N(n=0.93)	0.0875	0.999	-10138		0.1317
N(n=0.5)	8.6606	0.864	-5191	105385	0.1497
N(n=1)	0.2598	0.996	-8967	2118	0.1301
C2-D	4.0593	0.936	-6007	48824	0.0463
C3-D	2.0449	0.968	-6745	24062	0.0345
K2-O	3.9935	0.937	-6024	48015	0.2506
K3-O	11.7479	0.816	-4862	143336	0.4827
D3-D(Jan)	4.8102	0.924	-5824	58054	0.0114

Table 8.3: Parameters from fitting kinetic models to reaction experimental reduction data at 1073 K using 10% CH_4. 95% upper quantile of the F-distribution $F_{0.05}$(df1-df2,df2) = 3.8914 for all the cases compared.

Models	**RSS**	**R^2**	**AIC_C**	**F-Test [Compared with N(n=1.15)]**	***K*** **(min^{-1})**
N(n=1.15)	0.0182	0.999	-1752.5		0.6213
N(n=1)	0.1207	0.992	-1394.7	1062	0.6281
N(n=1.5)	0.4205	0.971	-1157.5	4167	0.6114
C2-D	0.1488	0.990	-1354.8	1353	0.2298
C3-D	0.0339	0.998	-1636.0	163	0.1705
K2-O	1.4870	0.897	-917.5	15210	1.1179
K3-O	3.2324	0.776	-770.0	33283	1.9705
D3-D(Jan)	2.1025	0.854	-851.7	21583	0.0525

Table 8.4: Parameters from fitting kinetic models to reaction experimental reduction data at 1173 K using 10% CH_4. 95% upper quantile of the F-distribution $F_{0.05}$(df1-df2,df2) = 4.1709 for all the cases compared.

Models	**RSS**	**R^2**	**AIC_C**	**F-Test [Compared with N(n=1.88)]**	***K*** **(min^{-1})**
N(n=1.88)	0.0050	0.998	-273.7		2.6851
N(n=1.5)	0.0511	0.984	-201.7	278	2.6690
N(n=2)	0.0085	0.997	-259.1	21	2.6871
C2-D	0.1564	0.952	-165.9	913	1.0308
C3-D	0.2137	0.934	-155.9	1258	0.7410
K2-O	0.7097	0.781	-117.5	4247	3.8609
K3-O	1.0373	0.680	-105.3	6221	5.7556
D3-D(Jan)	0.9907	0.694	-106.8	5940	0.1786

Figure 8.7 shows the plot of ln(k(T)) versus 1/T based on the Arrhenius equation using k values obtained for the nucleation model. The value of activation energy obtained for the reduction of M5Z5-1050 was 142.8

KJ/mol and the pre-exponential factor 9.84 X 10^{+4} s^{-1}. The activation energy obtained is somewhat similar to that obtained by Zafar et al. (2007). The difference in the values could possibly be attributed to the difference in material investigated (40 wt. % Mn_3O_4 on Mg-ZrO_2), temperature range (1073 K – 1223 K), and preparation method (freeze granulation).

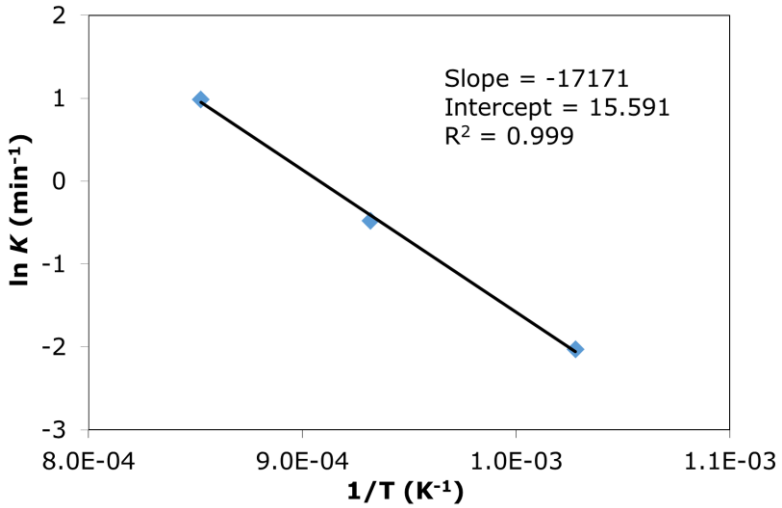

Figure 8.7: Arrhenius plot for experimental data of M5Z5-1050 at 973 K, 1073 K and 1173 K for the 2nd reduction cycle in 10% CH_4, particle size of 75-250 µm and feed gas flow rate of 50 ml/min for the transition from Mn_3O_4 to MnO.

8.4 Reduction Kinetics of M5Z5-1050 Oxygen Carrier in Hydrogen

The Hancock and Sharp (1972) method was also applied for M5Z5-1050 data for temperature range 973-1173 K using 5% H_2 as illustrated in Figure 8.8. A linear relationship was obtained with values of n ranging from 1.15 to 1.53 for the three temperatures with potential for the nucleation model N(n=n) and Geometrical contraction model C2-D being suitable models.

Figures 8.9, 8.10 and 8.11 show the fit of the experimental reaction data to the fractional reduction conversion versus time curve for each of the

kinetic models at temperatures 973 K, 1073 K and 1173 K respectively. The parameters obtained for the kinetic models examined are presented in Tables 8.5, 8.6 and 8.7. Similar to the reduction reaction in CH_4, the two-parameter nucleation models (N(n=1.61), N(n=1.60) and N(n=1.89) were the most statistically significant and suitable model for describing the reduction behaviour of M5Z5-1050 in H_2 at the three temperatures studied.

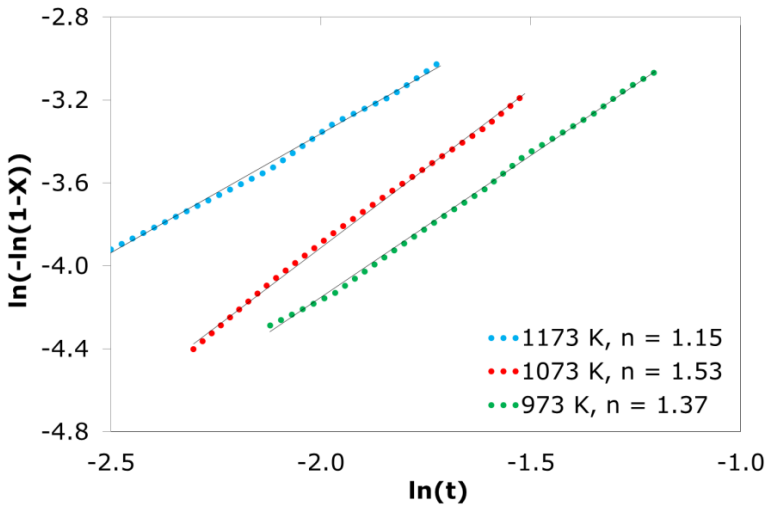

Figure 8.8: Sharp-Hancock plots for monometallic oxygen carrier M5Z5-1050 using 0.15<X<0.5 at 973 K, 1073 K and 1173K for the 2nd reduction cycles in 5% H_2, particle size of 75-250 μm and feed gas flow rate of 20 ml/min for the transition from Mn_3O_4 to MnO.

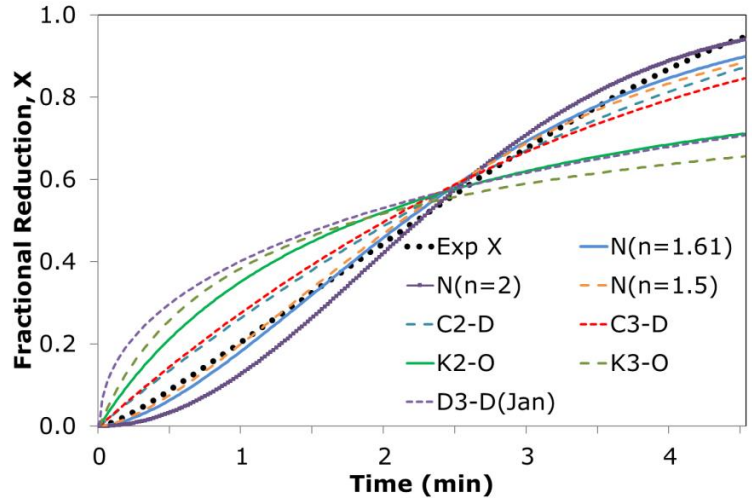

Figure 8.9: Curve fitting of experimental data (0<X<0.95) of M5Z5-1050 to various kinetic models at 973 K for the 2nd reduction cycle in 5% H_2, particle size of 75-250 μm and feed gas flow rate of 20 ml/min for the transition from Mn_3O_4 to MnO.

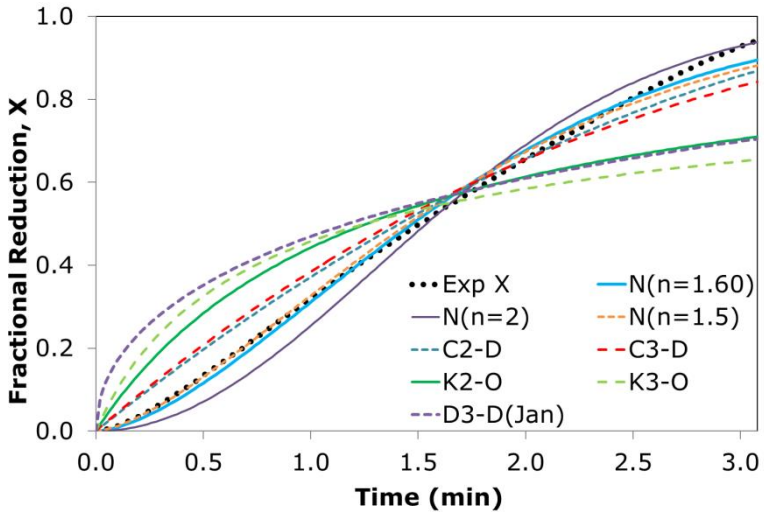

Figure 8.10: Curve fitting of experimental reduction data (0<X<0.95) of M5Z5-1050 to various kinetic models at 1073 K for the 2nd reduction cycle in 5% H_2, particle size of 75-250 μm and feed gas flow rate of 20 ml/min for the transition from Mn_3O_4 to MnO.

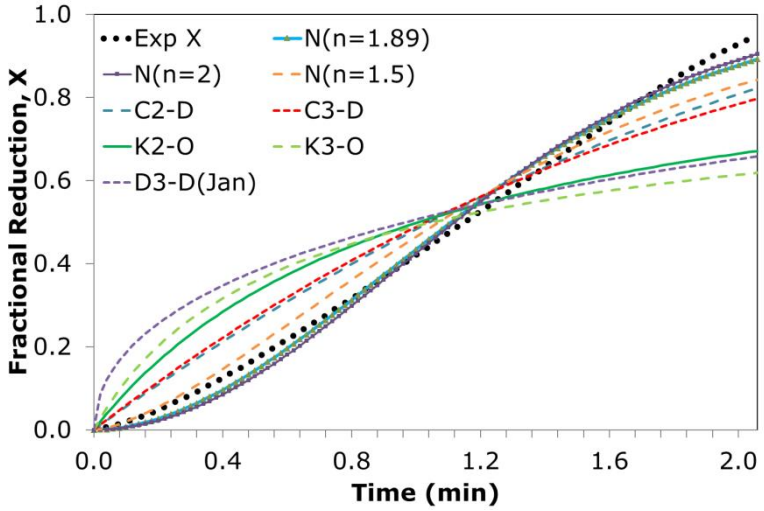

Figure 8.11: Curve fitting of experimental reduction data (0<X<0.95) of M5Z5-1050 to various kinetic models at 1173 K for the 2nd reduction cycle in 5% H_2, particle size of 75-250 μm and feed gas flow rate of 20 ml/min for the transition from Mn_3O_4 to MnO.

Table 8.5: Parameters from fitting kinetic models to experimental reduction data at 973 K using 5% H_2. 95% upper quantile of the F-distribution $F_{0.05}$(df1-df2,df2) = 3.883 for all the cases compared.

Models	**RSS**	**R^2**	**AIC_C**	**F-Test [Compared with N(n=1.61)]**	***K* (min^{-1})**
N(n=1.61)	0.0910	0.995	-1769		0.3704
N(n=1.5)	0.1202	0.994	-1708	72	0.3697
N(n=2)	0.3978	0.979	-1437	758	0.3713
C2-D	0.4512	0.977	-1408	890	0.1423
C3-D	0.7305	0.962	-1299	1581	0.1025
K2-O	3.5127	0.818	-942	8458	0.5455
K3-O	5.5070	0.715	-840	13387	0.8246
D3-D(Jan)	5.1950	0.731	-853	12616	0.0249

Table 8.6: Parameters from fitting kinetic models to experimental reduction data at 1073 K using 5% H_2. 95% upper quantile of the F-distribution $F_{0.05}$(df1-df2,df2) = 3.908 for all the cases compared.

Models	**RSS**	**R^2**	**AIC_C**	**F-Test [Compared with N(n=1.60)]**	***K* (min^{-1})**
N(n=1.6)	0.0520	0.996	-1243		0.5396
N(n=1.5)	0.0708	0.995	-1197	56	0.5385
N(n=2)	0.2720	0.980	-987	652	0.5410
C2-D	0.3105	0.977	-966	766	0.2071
C3-D	0.4995	0.963	-892	1326	0.1493
K2-O	2.4079	0.820	-647	6980	0.7928
K3-O	3.7863	0.717	-576	11064	1.1959
D3-D(Jan)	3.5944	0.731	-584	10495	0.0362

Table 8.7: Parameters from fitting kinetic models to experimental reduction data at 1173 K using 5% H_2. 95% upper quantile of the F-distribution $F_{0.05}$(df1-df2,df2) = 3.934 for all the cases compared.

Models	**RSS**	**R^2**	**AIC_C**	**F-Test [Compared with N(n=1.89)]**	***K*** **(min^{-1})**
N(n=1.89)	0.0597	0.994	-770		0.7420
N(n=1.5)	0.2007	0.978	-646	241	0.7313
N(n=2)	0.0694	0.992	-756	16	0.7435
C2-D	0.5377	0.942	-543	816	0.2806
C3-D	0.7028	0.924	-516	1098	0.2001
K2-O	2.0474	0.778	-404	3395	0.9907
K3-O	2.9282	0.683	-367	4899	1.4226
D3-D(Jan)	2.9937	0.675	-365	5011	0.0439

The Arrhenius plot using *k* values obtained for the nucleation model from Tables 8.5, 8.6 and 8.7 is shown in Figure 8.12. The value of activation energy obtained for the reduction of M5Z5-1050 in H_2 is 32.95 KJ/mol and the pre-exponential factor 3.623 X 10^{-1} s^{-1}. As stated earlier in this chapter, very limited kinetic data exist for manganese oxide-based OCs in literature. Nonetheless, activation energy up to 96 KJ/mol has been reported in literature for the reduction of other monometallic oxygen carriers using H_2 as fuel (Adánez et al., 2012).

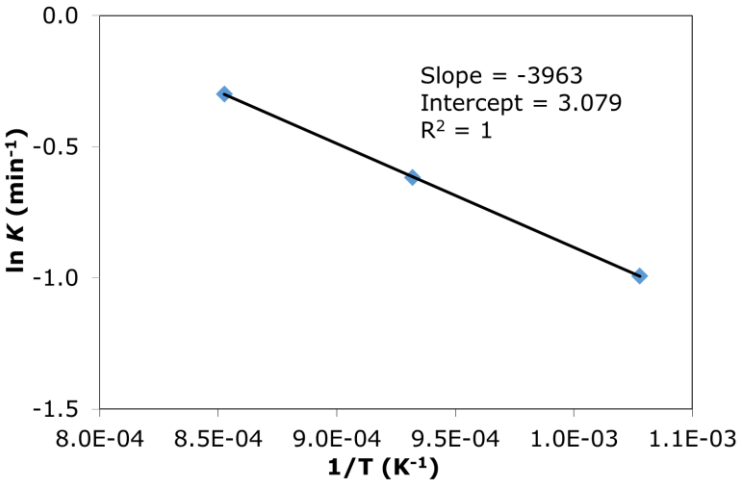

Figure 8.12: Arrhenius plot for experimental data of M5Z5-1050 at 973 K, 1073 K and 1173 K for the 2nd reduction cycle in 5% H_2, particle size of 75-250 µm and feed gas flow rate of 20 ml/min for the transition from Mn_3O_4 to MnO.

8.5 Reduction Kinetics of M5Z5-1050 Oxygen Carrier in Carbon Monoxide

The Hancock and Sharp (1972) method was also applied for M5Z5-1050 data for temperature range 973-1173 K using 10% CO as illustrated in Figure 8.13 to obtain linear relationships with n values ranging from 1.38 to 1.58 for the three temperatures with potential for the nucleation model N(n=n) being the suitable model.

Figures 8.14, 8.15 and 8.16 show the fit of the experimental reaction data to the fractional reduction conversion versus time curve for each of the kinetic models at temperatures 973 K, 1073 K and 1173 K respectively. Tables 8.8, 8.9 and 8.10 show the parameters obtained for the kinetic models examined. Similar to the reduction reaction in CH_4 or H_2, the two-parameter nucleation models (N(n=1.55), N(n=1.67) and N(n=1.72) were the most statistically significant and suitable model for describing the reduction behaviour of M5Z5-1050 in CO at the three temperatures studied.

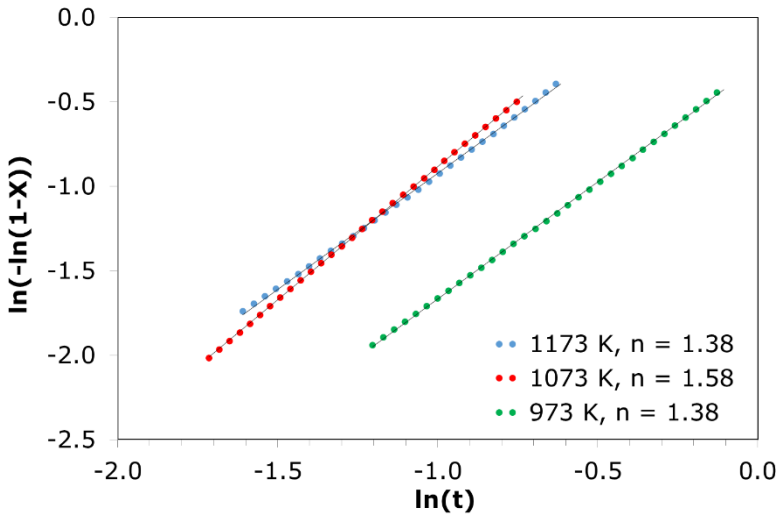

Figure 8.13: Sharp-Hancock plots for monometallic oxygen carrier M5Z5-1050 using 0.15<X<0.5 at 973 K, 1073 K and 1173K for the 2nd reduction cycles in 10% CO, particle size of 75-250 µm and feed gas flow rate of 50 ml/min for the transition from Mn_3O_4 to MnO.

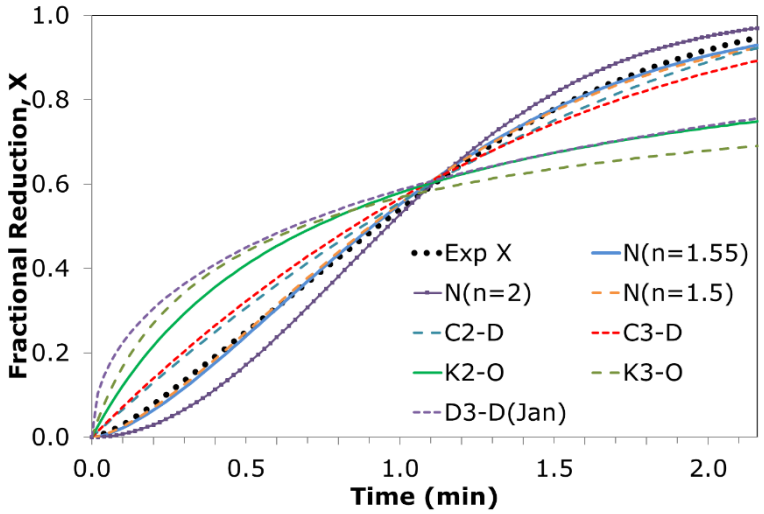

Figure 8.14: Curve fitting of experimental data (0<X<0.95) of M5Z5-1050 to various kinetic models at 973 K for the 2nd reduction cycle in 10% CO, particle size of 75-250 µm and feed gas flow rate of 50 ml/min for the transition from Mn_3O_4 to MnO.

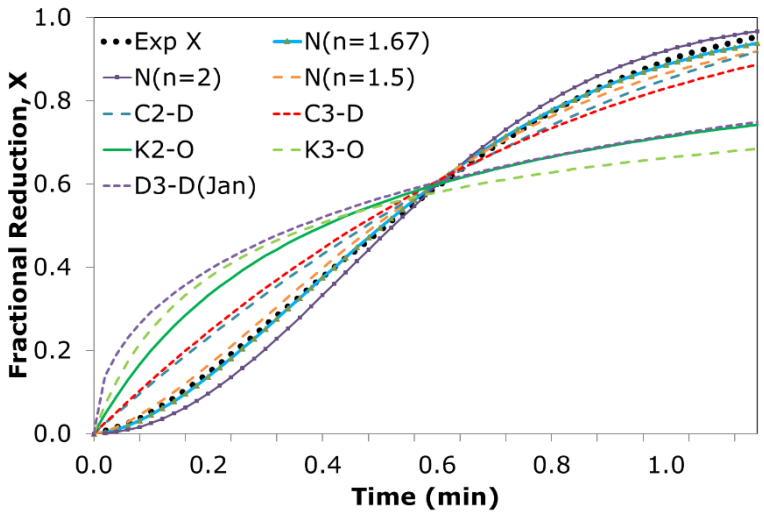

Figure 8.15: Curve fitting of experimental data (0<X<0.95) of M5Z5-1050 to various kinetic models at 1073 K for the 2nd reduction cycle in 10% CO, particle size of 75-250 μm and feed gas flow rate of 50 ml/min for the transition from Mn_3O_4 to MnO.

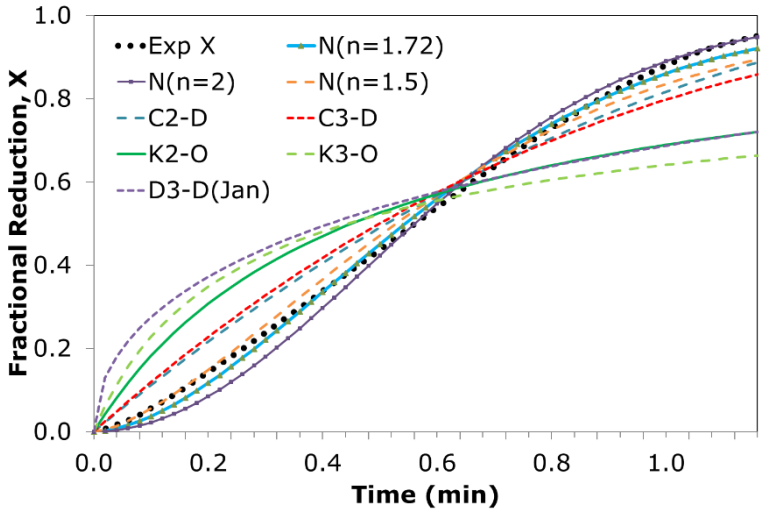

Figure 8.16: Curve fitting of experimental data (0<X<0.95) of M5Z5-1050 to various kinetic models at 1173 K for the 2nd reduction cycle in 10% CO, particle size of 75-250 μm and feed gas flow rate of 50 ml/min for the transition from Mn_3O_4 to MnO.

Table 8.8: Parameters from fitting kinetic models to experimental reduction data at 973 K using 10% CO. 95% upper quantile of the F-distribution $F_{0.05}$(df1-df2,df2) = 3.93 for all the cases compared.

Models	**RSS**	**R^2**	**AIC_C**	**F-Test [Compared with N(n=1.55)]**	***K*** **(min^{-1})**
N(n=1.55)	0.0106	0.999	-1000		0.8676
N(n=1.5)	0.0141	0.999	-972	35	0.8678
N(n=2)	0.2146	0.978	-675	2054	0.8662
C2-D	0.1379	0.986	-723	1281	0.3340
C3-D	0.2586	0.974	-655	2496	0.2430
K2-O	1.7394	0.825	-447	17407	1.3782
K3-O	2.8500	0.713	-393	28589	2.1852
D3-D(Jan)	2.4492	0.754	-410	24554	0.0650

Table 8.9: Parameters from fitting kinetic models to experimental reduction data at 1073 K using 10% CO. 95% upper quantile of the F-distribution $F_{0.05}$(df1-df2,df2) = 4.01 for all the cases compared.

Models	**RSS**	**R^2**	**AIC_C**	**F-Test [Compared with N(n=1.67)]**	***K*** **(min^{-1})**
N(n=1.67)	0.0037	0.999	-565		1.5901
N(n=1.5)	0.0240	0.996	-456	317	1.5905
N(n=2)	0.0587	0.990	-404	858	1.5893
C2-D	0.1409	0.976	-352	2138	0.6136
C3-D	0.2252	0.961	-324	3453	0.4454
K2-O	1.1225	0.806	-230	17433	2.4823
K3-O	1.7613	0.696	-203	27386	3.8875
D3-D(Jan)	1.5505	0.733	-210	24101	0.1175

Table 8.10: Parameters from fitting kinetic models to experimental reduction data at 1173 K using 10% CO. 95% upper quantile of the F-distribution $F_{0.05}$(df1-df2,df2) = 4.01 for all the cases compared.

Models	**RSS**	**R^2**	**AIC_C**	**F-Test [Compared with N(n=1.72)]**	***K*** **(min^{-1})**
N(n=1.72)	0.0188	0.997	-469		1.4835
N(n=1.5)	0.0493	0.991	-414	92	1.4807
N(n=2)	0.0574	0.990	-405	117	1.4839
C2-D	0.1741	0.969	-340	471	0.5719
C3-D	0.2641	0.953	-315	744	0.4127
K2-O	1.1112	0.800	-230	3311	2.2160
K3-O	1.6944	0.696	-205	5079	3.3771
D3-D(Jan)	1.5651	0.719	-210	4687	0.1030

The Arrhenius plot using *k* values obtained for the nucleation model from Tables 8.8, 8.9 and 8.10 is shown in Figure 8.17. The value of activation energy obtained for the reduction of M5Z5-1050 in CO is 26.37 KJ/mol and the pre-exponential factor 4.138 X 10^{-1} s^{-1}. As stated previously, there are very limited kinetic data for manganese oxide-based OCs in literature. Nonetheless, activation energy up to 75 KJ/mol has been reported for the reduction of other monometallic oxygen carriers using CO as fuel (Adánez et al., 2012).

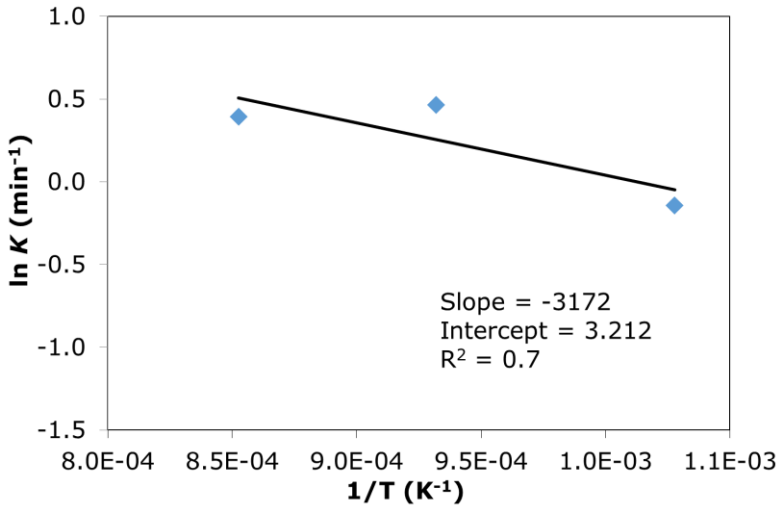

Figure 8.17: Arrhenius plot for experimental data of M5Z5-1050 at 973 K, 1073 K and 1173 K for the 2nd reduction cycle in 10% CO, particle size of 75-250 μm and feed gas flow rate of 50 ml/min for the transition from Mn_3O_4 to MnO.

8.6 Oxidation Kinetics of M5Z5-1050 Oxygen Carrier

Similar results to the other reacting gases were obtained for the oxidation reaction in air. A linear relationship was evident for the Hancock and Sharp (1972) plot at the three temperatures investigated with values of n obtained ranging from 1.94 to 3.09 as shown in Figure 8.18. The nucleation model N(n=n) seems to be the only model with suitable kinetic mechanisms associated with these n values.

Figures 8.19, 8.20 and 8.21 show the fit of the experimental reaction data to the fractional oxidation conversion versus time curve for each of the kinetic models at temperatures 973 K, 1073 K and 1173 K respectively.

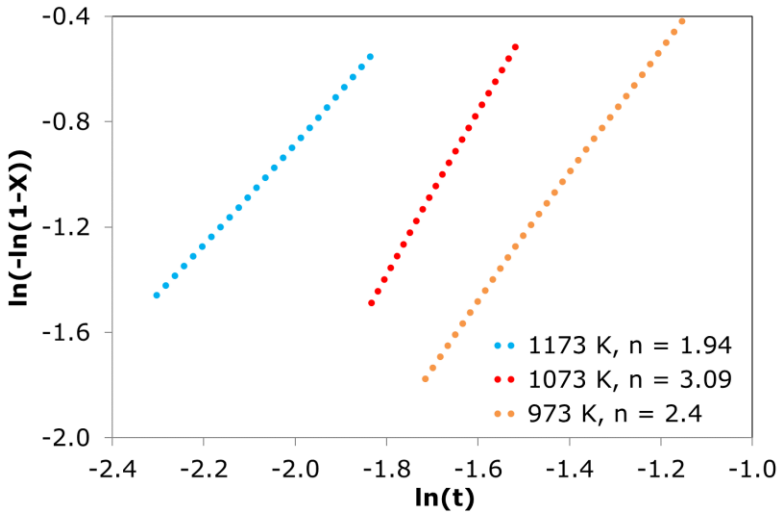

Figure 8.18: Sharp-Hancock plots for monometallic oxygen carrier M5Z5-1050 using 0.15<X<0.5 at 973 K, 1073 K and 1173K for the 2nd oxidation cycles in air, particle size of 75-250 μm and feed gas flow rate of 50 ml/min for the transition from MnO to Mn_3O_4.

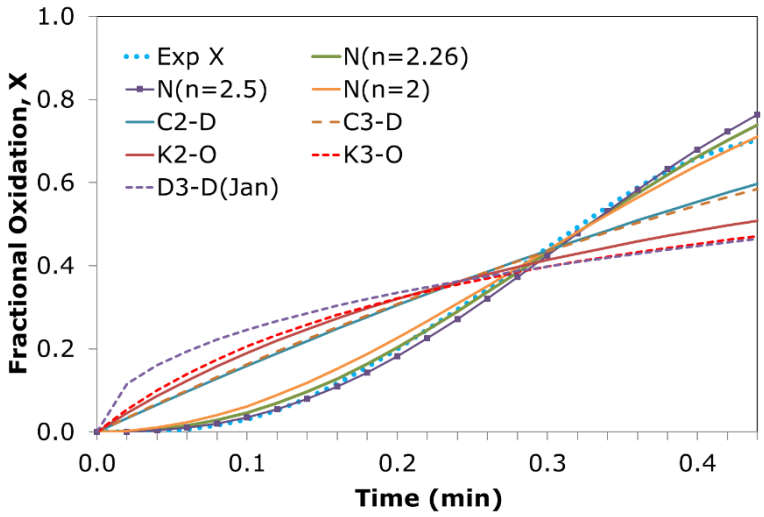

Figure 8.19: Curve fitting of experimental oxidation data (0<X<0.70) of M5Z5-1050 to various kinetic models at 973 K for the 2nd oxidation cycle in air, particle size of 75-250 μm and feed gas flow rate of 50 ml/min for the transition from MnO to Mn_3O_4.

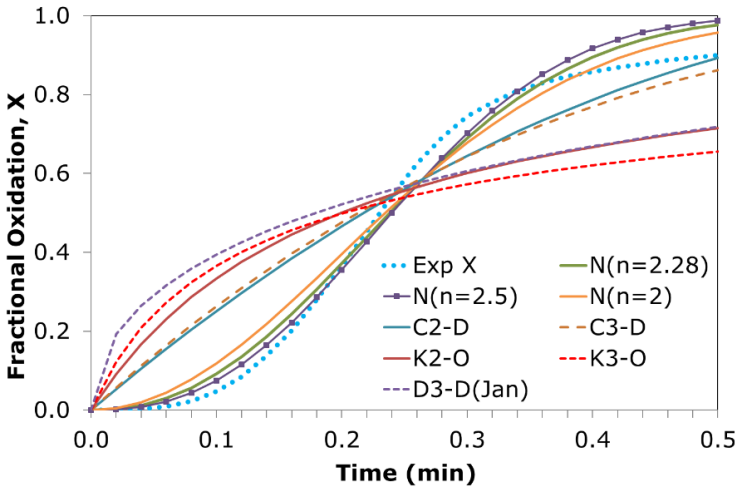

Figure 8.20: Curve fitting of experimental oxidation data (0<X<0.90) of M5Z5-1050 to various kinetic models at 1073 K for the 2nd oxidation cycle in air, particle size of 75-250 μm and feed gas flow rate of 50 ml/min for the transition from MnO to Mn_3O_4.

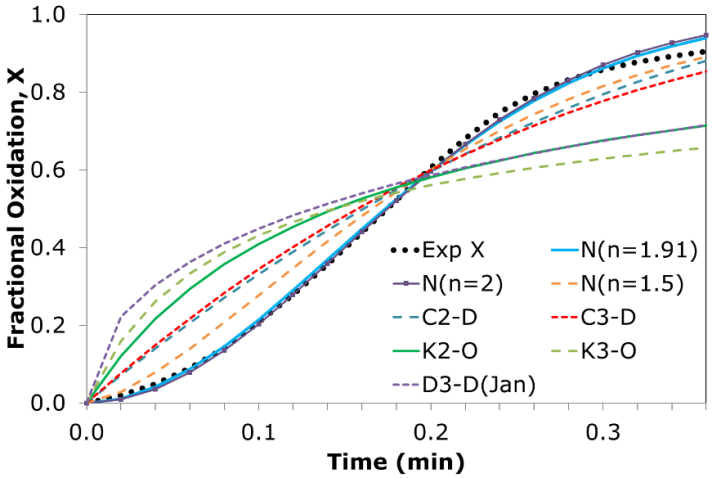

Figure 8.21: Curve fitting of experimental oxidation data (0<X<0.90) of M5Z5-1050 to various kinetic models at 1173 K for the 2nd oxidation cycle in air, particle size of 75-250 μm and feed gas flow rate of 50 ml/min for the transition from MnO to Mn_3O_4.

The parameters obtained for the kinetic models examined are presented in Tables 8.11, 8.12 and 8.13. The two-parameter nucleation models (N(n=2.26) was the most suitable model at reaction temperature of 973 K. At the temperature of 1073 K, the one-parameter model N(n=2.5) and the two-parameter-model N(n=2.28) had the same AIC_C values of -157. Nonetheless, comparison of both models using F test gave a value of 2.6

which is lower than the 95% upper quantile of the F distribution (value of 4.26). Thus, the one-parameter model N(N=2.5) becomes the winner model.

At the reaction temperature of 1173, N(n=2) was selected amongst the one-parameter models having the highest R-squared and lowest RSS and AIC_C values. Comparison of N(n=2) and the two-parameter model (N=1.91) gave an F test value of 4.4 which is lower than the 95% upper quantile of the F distribution (value of 4.45). This indicated a better statistical significance for the simpler model N(n=2). Nevertheless, N(n=1.91) had a lower value of AIC_C compared to N(n=2). As stated previously in Section 8.2, in instances where there is a conflict between the results from AIC_C and F test, the model with the lowest AIC_C is selected. Thus, the nucleation model N(n=1.91) is chosen as the most suitable model for describing the oxidation reaction of M5Z5-1050 in air at the temperature of 1173K.

Table 8.11: Parameters from fitting kinetic models to experimental oxidation data at 973 K using air. 95% upper quantile of the F-distribution $F_{0.05}$(df1-df2,df2) = 4.32 for all the cases compared.

Models	**RSS**	**R^2**	**AIC_C**	**F-Test [Compared with N(n=2.26)]**	***K* (min^{-1})**
N(n=2.26)	0.0037	0.997	-193		2.5906
N(n=2)	0.0104	0.993	-173	37	2.5306
N(n=2.5)	0.0087	0.994	-177	28	2.6312
C2-D	0.1911	0.867	-106	1051	0.8307
C3-D	0.2103	0.854	-103	1159	0.5768
K2-O	0.3578	0.751	-91	1986	2.3497
K3-O	0.4548	0.684	-86	2530	2.9232
D3-D(Jan)	0.5860	0.593	-80	3266	0.0806

Table 8.12: Parameters from fitting kinetic models to experimental oxidation data at 1073 K using air. 95% upper quantile of the F-distribution $F_{0.05}$(df1-df2,df2) = 4.26 for all the cases compared.

Models	RSS	R^2	AIC_C	F-Test [Compared with N(n=2.28)]	*K* (min^{-1})
N(n=2.28)	0.0478	0.985	-157		3.5722
N(n=2)	0.0593	0.982	-154	5.8	3.5445
N(n=2.5)	0.0531	0.984	-157	2.6	3.5964
C2-D	0.3313	0.899	-109	142.2	1.3450
C3-D	0.3877	0.881	-105	170.5	0.9676
K2-O	0.8967	0.726	-83	425.8	5.0072
K3-O	1.2266	0.625	-75	591.3	7.4327
D3-D(Jan)	1.1751	0.640	-76	565.5	0.2371

Table 8.13: Parameters from fitting kinetic models to experimental oxidation data at 1173 K using air. 95% upper quantile of the F-distribution $F_{0.05}$(df1-df2,df2) = 4.45 for all the cases compared.

Models	RSS	R^2	AIC_C	F-Test [Compared with N(n=1.91)]	*K* (min^{-1})
N(n=1.91)	0.0040	0.998	-153		4.7579
N(n=1.5)	0.0351	0.983	-115	133.2	4.7225
N(n=2)	0.0050	0.998	-152	4.4	4.7632
C2-D	0.1058	0.948	-94	435.4	1.8205
C3-D	0.1381	0.932	-89	573.5	1.3120
K2-O	0.4415	0.783	-67	1870.2	6.9261
K3-O	0.6457	0.682	-60	2743.2	10.4314
D3-D(Jan)	0.6054	0.702	-61	2570.9	0.3245

Figure 8.22 shows the Arrhenius plot using *k* values obtained for the nucleation model. The value of activation energy obtained for the oxidation of M5Z5-1050 in air was 28.83 KJ/mol and the pre-exponential factor

1.522 s^{-1}. This activation energy is somewhat similar to the 20 KJ/mol reported by Zafar et al. (2007).

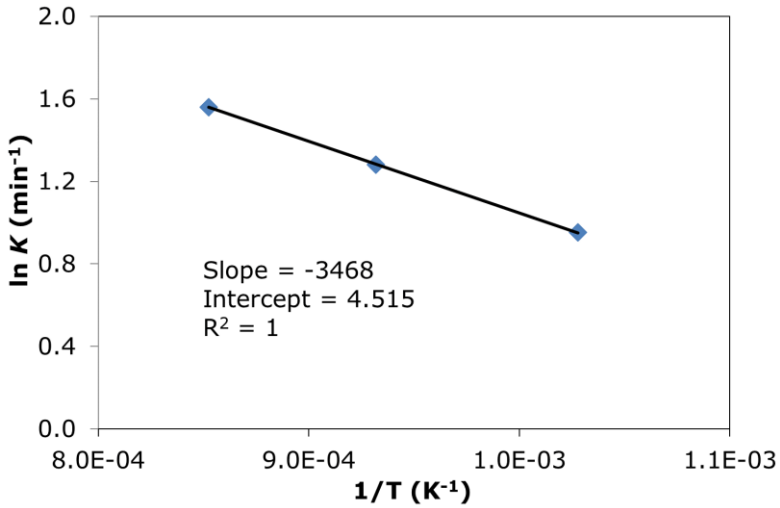

Figure 8.22: Arrhenius plot for experimental data of M5Z5-1050 at 973 K, 1073 K and 1173 K for the 2nd oxidation cycle in air, particle size of 75-250 µm and feed gas flow rate of 50 ml/min for the transition from MnO to Mn_3O_4.

8.7 Conclusions

The reduction and oxidation reaction kinetics of a promising monometallic oxide (M5Z5-1050) using CH_4, H_2, CO and air have been investigated at isothermal conditions (973-1173 K) using experimental reaction data from this work. Reaction models that were the most statistically significant and suitable for describing the reduction and oxidation behaviour of M5Z5-1050 in the reacting gases at the three temperatures studied were selected. The activation energy and pre-exponential factor were determined for the reduction and oxidation reactions. Measures were taken to ensure that the effect of mass transfer resistance was negligible. Thus, these reactions were chemically controlled and intrinsic surface reaction determined the overall reaction rates. The diffusion controlled model had poorer fit to the experimental data and not suitable for describing the reduction and oxidation reaction behaviour.

From the result of the kinetic study, the following conclusions can be drawn:

- The reduction and oxidation rates were dependent on the reaction temperatures.
- The nucleation model was the most suitable and statistically significant model to describe the reduction and oxidation reaction of the M5Z5-1050 in the reacting gases at all reaction temperatures.
- The values of activation energy obtained for the reduction reaction using CH_4, H_2 and CO were 142.8 KJ/mol, 32.95 KJ/mol and 26.37 KJ/mol respectively. Whereas, for the oxidation reaction, the activation energy obtained using air was 28.83 KJ/mol.
- The values of the activation energy obtained followed the order CH_4 > H_2 > CO. Generally, it has been reported that activation energy of oxygen carriers appears to follow the tendency CH_4 > H_2 > CO (Adánez et al., 2012).

The understanding gained from this kinetic study is of practical importance in real CLC application.

9 CONCLUSIONS AND FUTURE WORK

9.1 Conclusions

Novel research on co-precipitated oxygen carriers based on manganese oxide and iron oxide with zirconia and zirconia-ceria supports for chemical looping combustion (CLC) application has been developed. Against the back drop that only few works have been reported for manganese oxide and co-precipitated oxygen carriers, this study makes an original contribution towards bridging this knowledge gap. Moreover, insight into the fundamental behaviours of the co-precipitated Mn and Fe based OCs would aid the design and optimization of future materials development for CLC.

The developed oxygen carriers were evaluated for chemical looping combustion in terms of reactivity and stability in multicycle tests using hydrogen, carbon monoxide and methane as fuel. These materials were evaluated by TGA and characterised by SEM-EDX, XRD, BET and pycnometer. This study has led to the following conclusions:

1. Application of a well-designed co-precipitated synthesis technique yields high performance oxygen carriers for chemical looping combustion.
2. For the synthesis of Mn and Fe oxygen carriers via co-precipitation, the effect of mixing order of the precursor chemicals was not quite significant on the performance of the materials.
3. Generally, the co-precipitated oxygen carriers exhibited very stable reduction-oxidation operation in hydrogen, carbon monoxide and methane.

4. The co-precipitated monometallic Mn-oxide and Fe-oxide supported on zirconia exhibited faster kinetics compared to the corresponding oxides synthesized via impregnation and mechanical mixing method.

5. For co-precipitated Mn-Fe Oxide oxygen carriers, zirconia content of 44 wt. % is quite sufficient to maintain the mechanical integrity of the particles during redox reactions compared to zirconia content of 20 wt. %.
6. The use of ceria support enhanced the performance of the Mn-Fe oxygen carriers and these OCs exhibited activation tendency behaviour.
7. The use of combined zirconia-ceria support for bimetallic Mn-Fe oxide reversed the characteristic progressive decrease in the performance of the OC with equimolar composition.
8. The nucleation model was the most suitable and statistically significant kinetic model to describe the redox reaction of the most reactive OC in the reacting gases.
9. The values of the activation energy obtained followed the order CH_4 > H_2 > CO. The values of activation energy obtained for the reduction reaction using CH_4, H_2 and CO were 142.8 KJ/mol, 32.95 KJ/mol and 26.37 KJ/mol respectively. Whereas, for the oxidation reaction, the activation energy obtained using air was 28.83 KJ/mol
10. The co-precipitated manganese and iron oxide based oxygen carriers are promising for chemical looping combustion and could be optimized to provide a practical alternative to monometallic iron oxide oxygen carriers which exhibit very slow kinetics.

9.2 Suggestions for Further Work

This study has demonstrated that co-precipitated manganese oxide and iron oxide are promising for chemical looping combustion. The following areas of further investigation could be of interest:

- To have more information about phase changes in the co-precipitated oxygen carriers during the multicycle experiments, it is suggested that XRD can be used to investigate the residual particles after the reduction reactions.
- Also, the oxygen carrier particles could be characterized with respect to strength. Although, crushing strength testing is helpful, they are far from conclusive. Nevertheless, investigations into the strength of the co-precipitated oxygen carriers could help to establish any potential relationship between the crushing strength and performance of the oxygen carriers.
- Additionally, the TGA can be combined with analysis equipment such as a mass spectrometer to measure the evolved gas composition during the reduction and oxidation reactions.
- In this work, TGA was used as the main equipment for investigating the reduction and oxidation behaviour of the co-precipitated oxygen carriers. However, to gain understanding of the fluidizing behaviour of the co-precipitated Mn-Fe oxygen carriers, these materials could be investigated in a fluidized bed reactor.
- Another interesting study would be the evaluation of the co-precipitated oxygen carriers' effectiveness for solid fuel chemical looping combustion.

REFERENCES

Abad A., Mattisson, T., Lyngfelt A. and Johansson, M., 2007. The use of iron oxide as oxygen carrier in a chemical-looping reactor. *Fuel* 86, pp.1021–35.

Abad, A., Adánez, A., García-Labiano, F., de Diego, L. F., Gayán, P. and Celaya, J., 2007. Mapping of the range of operational conditions for Cu-, Fe-, and Ni-based oxygen carriers in chemical-looping combustion. *Chemical Engineering Science*, 62, pp.533 – 549.

Adánez, J., de Diego, L.F., Garcı´a-Labiano, F., Gaya´n, P. and Abad, A., 2004. Selection of Oxygen Carriers for Chemical-Looping Combustion. *Energy & Fuels*, 18, pp.371-377

Adánez, J., Abad, A., Garcia-Labiano, F., Gayan, P. & De Diego, L. F. 2012. Progress in Chemical-Looping Combustion and Reforming technologies. *Progress in Energy and Combustion Science,* 38, pp.215-282.

Adánez, J., Cuadrat, A., Abad, A., Gayan, P., de Diego, L.F. and Garcia-Labiano, F., 2010. Ilmenite Activation during Consecutive Redox Cycles in Chemical-looping Combustion. *Energy Fuels* 24, pp.1402–1413.

Aris, R. 1965. Introduction to the Analysis of Chemical Reactors. USA: Prentice Hall.

Azimi, G., Leion, H., Mattisson, T. and Lyngfelt, A., 2011. Chemical-looping with oxygen uncoupling using combined Mn-Fe oxides, testing in batch fluidized bed. *Energy Procedia*, 4, pp.370-377.

Azis, M.M., Jerndal, E., Leion, H., Mattisson, T. and Lyngfelt, A., 2010. On the Evaluation of Synthetic and Natural Ilmenite Using Syngas as Fuel in

Chemical Looping Combustion (CLC). *Chem. Eng. Res. Des.* 88, pp.1505–1514.

Benrabaa, R., Boukhlouf, H., Barama, S., Bordes-Richard, E., Vannier, R.N. and Barama, A., 2012. Structural, Textural and Acid-Base Properties of Nano-Sized NiFe2O4 Spinel Catalysts. *Catal. Lett*. 142(1), pp.42-49.

Benson, S. M. & Surles, T. 2006. Carbon Dioxide Capture and Storage: An Overview With Emphasis on Capture and Storage in Deep Geological Formations. *Proceedings of the IEEE,* 94, pp.1795-1805.

Bhavsar, S., Najera, M., More, A. and Veser, G., 2014. Chemical-looping processes for fuel-flexible combustion and fuel production. In: Shi, F., (ed) *Reactor and Process Design in Sustainable Energy Technology*. Amsterdam: Elsevier, pp.233-280. Available from: http://dx.doi.org/10.1016/B978-0-444-59566-9.00007-7.

Bhavsar, S., Tackett, B. and Veser, G., 2014. Evaluation of iron- and manganese-based mono- and mixed-metallic oxygen carriers for chemical looping combustion. *Fuel.* 136, pp.268–279.

Boot-Handford, M. E., Abanades, J. C., Anthony, E. J., Blunt, M. J., Brandani, S., Mac Dowell, N., Fernandez, J. R., Ferrari, M.-C., Gross, R., Hallett, J. P., Haszeldine, R. S., Heptonstall, P., Lyngfelt, A., Makuch, Z., Mangano, E., Porter, R. T. J., Pourkashanian, M., Rochelle, G. T., Shah, N., Yao, J. G., and Fennell, P. S., 2014. Carbon capture and storage update. *Energy Environ. Sci.*, 7(1), pp.130-189.

Brown, M. E., 2001. Introduction to thermal analysis: Techniques and Applications. Netherlands: Kluwer Academic Publishers Dordrecht, pp 181.

Burdyny, T. and Struchtrup, H., 2010. Hydrid membrane/cryogenic separation of oxygen from air for use in the oxy-fuel process. *Energy*; 35, pp.1884–97.

Burnham, K. P. and Anderson, D. R., 2002. Model selection and multi-model inference: a practical information-theoretic approach, 2nd ed. Springer-Verlag New York, Inc.

Cao Y, and Pan W., 2006. Investigation of chemical looping combustion by solid fuels. *Process Anal Energy Fuels*. 20, pp.1836–44.

Cao, Y., Casenas, B., and Pan, W.P., 2006. Investigation of chemical looping combustion by solid fuels. 2. Redox reaction kinetics and product characterization with coal, biomass, and solid waste as solid fuels and CuO as an oxygen carrier. *Energy and Fuels*, 20(5), pp. 1845-1854.

Chandel, M. K., Hoteit, A. and Delebarre, A., 2009. Experimental investigation of some metal oxides for chemical looping combustion in a fluidized bed reactor. *Fuel,* 88, pp.898-908.

Cheremisinoff, N. P., 2000. Handbook of Chemical Processing Equipment. Boston: Butterworth-Heinemann.

Chiu, P. and Ku, Y., 2012. Chemical Looping Process - A Novel Technology for Inherent CO2 Capture. *Aerosol and Air Quality Research*, 12, pp.1421–1432

Chuang, S.Y., Dennis, J.S., Hayhurst, A.N, and Scott, S.A., 2008. Development and performance, of Cu-based oxygen carriers for chemical-looping combustion. *Combustion and Flame*, 154(1-2), pp.109-21.

Crum, J. V., Riley, B. J. and Vienna, J. D., 2009. Binary Phase Diagram of the Manganese Oxide – Iron Oxide System. *J. Am. Ceram. Soc.* 92, pp.2378-2384.

Cuadrat, A., Abad, A., Adánez, J., de Diego, L.F., Garcia-Labiano, F. and Gayan, P., 2012. Behaviour of ilmenite as oxygen carrier in chemical looping combustion. *Fuel Process Technol.* 94, pp.101–12.

Daubert, T. E. and Fitzgerald, D. J., 1997. Viscosity. In: American Petroleum Institute, Refining Department, (ed) *Technical Data Book—Petroleum Refining, 6th ed*. Washington, DC.: American Petroleum Institute (API).

Davis, M and Davis, R., 2002. Fundamentals of Chemical Reaction Engineering. New York: McGrraw-Hill.

de Diego L.F., Garcia-Labiano F., Gayan P., Cylaya J., Palacios, J.M. and Adánez J, 2007. Operation of a10kWth chemical-looping combustor during 200h with a CuO–Al2O3 oxygen carrier. *Fuel.* 86 pp.1036–45.

de Diego L.F., Gayan, P., Garcia-Labiano, F., Celaya, J., Abad, A., and Adánez, J., 2005. Impregnated CuO/Al2O3 oxygen carriers for chemical-looping combustion: avoiding fluidized bed agglomeration. Energy Fuels. 19, pp.1850–6.

de Diego, L. F., Garc a-Labiano, F., Adánez, J., Gayán, P., Abad, A., Corbella, B. M., and Mar a Palacios, J., 2004. Development of Cu-based oxygen carriers for chemical-looping combustion. *Fuel*, 83(13), pp.1749–1757.

de Visser, E., Hendricks, C., Barrio, M., Molnvik, M.J, de Koeijer, G., Liljemark S., 2008. Dynamics CO_2 quality recommendations. *Int J Greenh Gas Control*. 2, PP.478–84

Dlugokencky, E. & Tans, P. (2012). Trends in Atmospheric Carbon Dioxide, NOAA/ESRL. [Accessed www.esrl.noaa.gov/gmd/ccgg/trends/].

Ebaid, M. S. Y. and Al-hamdan, Q. Z., 2015. Thermodynamic Analysis of Different Configurations of Combined Cycle Power Plants. *Mechanical Engineering Research*, 5(2), pp.89-113.

Ekström, C., Schwendig, F., Biede, O., Franco, F., Haupt, G., De Koeijer, G., Papapavlou, C. & Røkke, P. E. 2009. Techno-Economic Evaluations and Benchmarking of Pre-combustion CO2 Capture and Oxy-fuel Processes Developed in the European ENCAP Project. *Energy Procedia,* 1, 4233-4240.

Fan, L.-S. 2011. Chemical Looping Systems for Fossil Energy Conversions*,* Hoboken, New Jersey, John Wiley & Sons.

Fan, L.S., and Li, F., 2010. Chemical Looping Technology and Its Fossil Energy Conversion Applications. *Industrial & Engineering Chemistry Research*, 49(21) pp.10200-10211.

Fennell, P. (2015) Calcium and Chemical Looping Combustion: An Introduction. In: Fennell, P. and Anthony, B. (eds.) *Calcium and Chemical Looping Technology for Power Generation and Carbon Dioxide (CO2) Capture.* Cambridge, Woodhead Publishing, pp.3-12

Fogler, S. H., 2006. Elements of Chemical Reaction Engineering. New Jersey: Prentice-Hall Inc.

Fogler, S.H., 2013. Elements of Chemical Reaction Engineering. Essex: Pearson.

Fuller, E. N., Schettler, P. D. and Giddings, J. C., 1966. New Method for Prediction of Binary Gas-Phase Diffusion Coefficients. *Ind. Eng. Chem.* 58(5), pp.18-27.

Galvita, V.V., Poelman, H., Bliznuk, V., Detavernier, C. and Marin, G. B., 2013. CeO_2 Modified Fe_2O_3 for CO_2 Utilization via Chemical Looping. *Ind. Eng. Chem. Res.* 52, pp.8416−8426 dx.doi.org/10.1021/ie4003574

Galwey, A. K. and Brown, M. E., 1998. Kinetic Background to Thermal Analysis and Calorimetry in Handbook of Thermal Analysis and Calorimetry.: *Principles and Practice*. 1, Elsevier Science.

Garcia-Labiano, F., Adánez, J., de Diego, L. F, Gayan, P. and Abad, A., 2006. Effect of pressure on the behaviour of copper-, iron-, and nickel-based oxygen carrier for chemical-looping combustion. *Energy Fuels*. 20, pp.26–33.

Gitay, H., Suárez, A., Watson, R. T. & Dokken, D. J. 2002. Climate Change and Biodiversity. IPCC Technical Paper V. Available: https://docs.google.com/file/d/0B1gFp6Ioo3akUTBlTVQyc0puVEE/edit?pli=1

Golmen, L. G., 1999. CO_2 Ocean Sequestration as a Future Method to Reduce Atmospheric CO_2. Paper presented at the *Minisymposium on Carbon Dioxide Capture and Storage, October 22*. Chalmers University of Technology, Göteborg, Sweden.

Guo Q., Liu Y. and Tian, H., 2009. Recent Advances on Preparation and Characteristics of Oxygen Carrier Particles. *International Review of Chemical Engineering (I.RE.CH.E.)*, 1(4), pp.357-368

Hancock, J. D. and Sharp, J. H., 1972. Method of Comparing Solid-State Kinetic Data and Its Application to the Decomposition of Kaolinite, Brucite, and $BaCO_3$. *Journal of the American Ceramic Society*, 55, pp.74–77. doi:10.1111/j.1151-2916.1972.tb11213.x

Hoffmann, S., Bartlett, M., Finkenrath, M., Evulet, A. and Ursin, T. P., 2009. Performance and cost analysis of advanced combined cycles with precombustion CO_2 capture. *J Eng Gas Turbines Power*, 131(2), (021701-021701-7).

Hossain, M. M. and de Lasa, H. I., 2010. Reduction and oxidation kinetics of Co-Ni/Al_2O_3 oxygen carrier involved in a chemical-looping combustion cycles. *Chem Eng Sci.* 65, pp.98-106.

Hossain, M.; De Lasa, H., 2008. Chemical looping combustion (CLC) for inherent CO_2 separations-a review*. Chemical Engineering Science.* 63, pp.4433-4451.

ICF (ICF International), 2009. Developing a pipeline infrastructure for CO_2 capture and storage; issues and challenges. In: *Technical report prepared for INGAA Foundation*. pp.1-97.

IEA (International Energy Agency), 2001. Putting Carbon Back Into the Ground*.* [Online]. Available: http://www.ieaghg.org/docs/general_publications/putcback.pdf.

IEA (International Energy Agency), 2010. World energy outlook (WEO, 2010). International Energy Agency, Paris, France.

IEA (International Energy Agency), 2012. Carbon Capture and Storage. Available: http://www.iea.org/topics/ccs/

IEA (International Energy Agency), 2012. CO_2 Emissions From Fuel Combustion Highlights*.* [Online]. Available: http://www.iea.org/publications/freepublications/publication/CO2emissionfromfuelcombustionHIGHLIGHTS.pdf

IEA (International Energy Agency), 2014. CO_2 Emissions from fuel combustion highlights (2014 Edition). International Energy Agency, Paris, France

IEA (International Energy Agency), 2015. World energy outlook (WEO, 2015). International Energy Agency, Paris, France

Imtiaz, Q., Kierzkowska A.M., Broda, M. and Müller, C.R., 2012. Synthesis of Cu-rich, Al_2O_3-stabilized oxygen carriers using a coprecipitation technique: redox and carbon formation characteristics. *Environ. Sci. Technol*. 46(6), pp.3561–3566.

IPCC (Intergovernmental Panel on Climate Change), 2007. IPCC Fourth Assessment Report: Climate Change 2007. Available: http://www.ipcc.ch/publications_and_data/ar4/syr/en/spms1.html

IPCC (Intergovernmental Panel on Climate Change), 2013. Climate Change 2013: The Physical Science Basis. In: Stocker, T.F., D. Qin, G.-K. Plattner, M. Tignor, S.K. Allen, J. Boschung, A. Nauels, Y. Xia, V. Bex and P. M. Midgley (eds.) *Contribution of Working Group I to the Fifth Assessment Report of the Intergovernmental Panel on Climate Change*. Cambridge: Cambridge University Press, pp.1535.

IPCC (Intergovernmental Panel on Climate Change), 2014: Climate Change 2014: Synthesis report. In: R.K. Pachauri and L.A. Meyer (eds.) *Contribution of Working Groups I, II and III to the Fifth Assessment Report of the Intergovernmental Panel on Climate Change*. IPCC, Geneva, Switzerland, pp.151.

IPCC (Intergovernmental Panel on Climate Change), 2005. IPPC Carbon Dioxide Capture and Storage. Available: http://www.ipcc-wg3.de/special-reports/.files-images/SRCCS-WholeReport.pdf

IPPC (Intergovernmental Panel on Climate Change), 2007. Summary for policymakers. In: Climate Change 2007: Mitigation. Contribution of Working group III to the fourth assessment report of the IPCC. Available:http://www.ipcc.ch/publications_and_data/publications_and_data_reports.shtml#.UQcYCB3ZZFA

Jerndal, E., Mattisson, T. and Lyngfelt, A., 2006. Thermal analysis of chemical-looping combustion. *Chem Eng Res Des.* 84(9), pp.795-806 http://dx.doi.org/10.1205/cherd05020.

Johansson, M., Mattisson, T. and Lyagfelt, A., 2006. Use of $NiO/NiAl_2O_4$ Particles in a 10 kW Chemical-Looping Combustor. *Ind. Eng. Chem. Res.* 45, pp.5911–5919.

Jordal, K., Anheden, M., Yan, J. and Strömberg, L., 2004. Oxyfuel Combustion For Coal-Fired Power Generation With CO2 Capture - Opportunities and Challenges. *Proceedings of the 7th International Conference on Greenhouse Gas Control Technologies, 5-9th September*, Vancouver, Canada.

Kanniche, M., Gros-Bonnivard, R., Jaud, P., Valle-Marcos, J., Amann, J. and Bouallou, C., 2010. Pre-combustion, post-combustion and oxy-combustion in thermal power plant for CO_2 capture. *Applied Thermal Engineering* 30, pp.53–62.

Kehlhofer, R., Rukes, B., Hannemann, F. and Stirnimann, F., 2009. Combined-Cycle Gas & Steam Turbine Power Plants, 3rd ed., Tulsa, Oklahoma: PennWell Corporation.

Kerr, H. R., 2005. Capture and Separation Technology Gaps and Priority Research Needs In: THOMAS, D. C. and Benson, S. M. (eds.) *Carbon Dioxide Capture for Storage in Deep Geologic Formations – Results from*

the CO_2 Capture Project Capture and Separation of Carbon Dioxide from Combustion Sources. Oxford, UK: Elsevier.

Klaewkla, R., Arend, M., and Hoelderich, W. F., 2011. A Review of Mass Transfer Controlling the Reaction Rate in Heterogeneous Catalytic Systems. In: Nakajima, H (ed) *Mass Transfer - Advanced Aspects*. Rijeka, Croatia: InTech.

Kletting, P. and Glatting, G., 2009. Model selection for time-activity curves: The corrected Akaike information criterion and the F-test Z. *Med.Phys*. 19, pp.200–206.

Knovel, 2008. Knovel Critical Tables, 2nd ed. Available from: http://app.knovel.com/hotlink/toc/id:kpKCTE000X/knovel-critical-tables/knovel-critical-tables

Ksepko, E., Siriwardane, R. V., Tian, H., Simonyi, T. and Sciazko, M., 2012. Effect of H2S on Chemical Looping Combustion of Coal-Derived Synthesis Gas over Fe–Mn Oxides Supported on Sepiolite, ZrO_2, and Al_2O_3. *Energy & Fuels,* 26, pp.2461-2472.

Lambert, A., Briault, P. and Comte, E., 2010. Spinel mixed oxides as oxygen carriers for chemical looping combustion. *Proc 10th Int Conf Greenhouse Gas Technology (GHGT-10)*. Amsterdam, The Netherlands.

Lambert, A., Delquié, C., Clémençon, I., Comte, E., Lefebvre, V., Rousseau, J., 2009. Synthesis and characterization of bimetallic Fe/Mn oxides for chemical looping combustion. *Energ Procedia*. 1, pp.375-81

Lee, H. J.; Lee, J. D.; Linga, P.; Englezos, P.; Kim, Y. S.; Lee, M. S. and Kim, Y. D., 2010. Gas hydrate formation process for pre-combustion capture of carbon dioxide. *Energy*. 35(6), pp.2729-2733.

Leion, H., Mattisson, T., and Lyngfelt, A., 2009. Use of ores and industrial products as oxygen carriers in chemical-looping combustion. *Energy and Fuels*, 23(4), pp.2307-2315

Leung, D. Y. C., Caramanna, G. and Maroto-Valer, M. M., 2014. An overview of current status of carbon dioxide capture and storage technologies. *Renewable and Sustainable Energy Reviews.* 39, pp.426–443

Lindeberg, E., 2003. The Quality of a CO_2 Repository: What is Sufficient Retention Time of CO2 Stored Underground. *Greenhouse Gas Technologies, ,* 1, pp.255-260.

Linderholm, C. and Lyngfelt, A., 2014. Chemical-looping combustion of solid fuels. In: Fennell, P. and Anthony, B. (eds.) *Calcium and Chemical Looping Technology for Power Generation and Carbon Dioxide (CO_2) Capture.* Cambridge: Woodhead Publishing, pp.299-321.

Linderholm, C. and Schmitz, M., 2015. Chemical-looping combustion of solid fuels in a 100kW dual circulating fluidized bed system using Iron ore as oxygen carrier. *Journal of Environmental Chemical Engineering,* 4(1), pp.1029-1039. http://dx.doi.org/10.1016/j.jece.2016.01.006

Linderholm, C., Jerndal, E., Mattisson, T. and Lyngfelt, A., 2010. Investigation of NiO-based mixed oxides in a 300-W chemical-looping combustor, *Chemical Engineering Research and Design*, 88(5-6) pp.661-672.

Linderholm, C., Lyngfelt, A., Cuadrat, A., and Jerndal, E., 2012. Chemical-looping combustion of solid fuels e operation in 10 kW unit with two fuels, above-bed and in-bed fuel feed and two oxygen carriers, manganese ore and ilmenite. *Fuel*. 102, pp.808-822.

Ludden, T. M., Beal, S. L. and Sheiner, L. B., 1994. Comparison of the Akaike Information Criterion, the Schwarz criterion and the F test as guides to model selection. *Journal of Pharmacokinetics and Biopharmaceutics*, 22(5), pp.431–445.

Luo, S., Zeng, L. and Fan, L., 2015. Chemical looping technology: Oxygen carrier characteristics. *Annu. Rev. Chem. Biomol. Eng*. 6, pp.53–75

Lyngfelt, A., 2013. Chemical looping combustion (CLC). In: Scala, F. (ed) *Fluidized Bed Technologies for Near-Zero Emission Combustion and Gasification. Woodhead Publishing Series in Energy.* Cambridge: Woodhead Publishing, pp. 895-921

Lyngfelt, A., 2014, Chemical-looping combustion of solid fuels – status of development, *Applied Energy*, 113, pp.1869-1873.

Lyngfelt, A., 2015. Oxygen carriers for chemical looping combustion. In: Fennell, P. and Anthony, B. (eds.) *Calcium and Chemical Looping Technology for Power Generation and Carbon Dioxide (CO2) Capture.* Cambridge: Woodhead Publishing, pp.221-243

Lyngfelt, A., Leckner, B. and Mattisson, T. A., 2001. A fluidized-bed combustion process with inherent CO_2 separation; application of chemical-looping combustion. *Chemical Engineering Science.* 56, pp.3101–3113

Mattisson, T., Lyngfelt, A. and Leion, H., 2009. Chemical-looping with oxygen uncoupling for combustion of solid fuels. *Int J Greenhouse Gas Control*. 3, pp.11-19.

Miller, B. G., 2011. Clean Coal Engineering Technology. Oxford: Elsevier. pp.251-300.

Motulsky, H. J. and Christopoulos, A., 2003. Fitting models to biological data using linear and nonlinear regression. A practical guide to curve fitting. San Diego CA: GraphPad Software Inc. Available from: www.graphpad.com.

Myer, L., 2011. Global status of geologic CO_2 storage technology development. *United States carbon sequestration council report,* pp1-58.

Nandy, A., Loha, C., Gu, S., Sarkar, P., Karmakar, M.K. and Chatterjee, P.K., 2016. Present status and overview of Chemical Looping Combustion technology. *Renewable and Sustainable Energy Reviews.* 59(C), pp.597-619.

Olajire, A. A., 2010. CO_2 capture and separation technologies for end-of-pipe application – a review. *Energy.* 35, pp.2610–2628.

Perry, R. H. and Green, D. W., 1999. Chemical Engineer's Handbook, 7th ed. New York: McGraw-Hill.

Petrakopoulou, F., Boyano, A., Cabrera, M. and Tsatsaronis, G., 2011. Exergoeconomic and exergoenvironmental analyses of a combined cycle power plant with chemical looping technology. *International Journal of Greenhouse Gas Control*, 5(3), pp.475-482.

Pröll, T. and Hofbauer, H., 2011. Chemical Looping Combustion and Reforming. *Proceedings of the 9th European Conference on Industrial Furnaces and Boilers (INFUB-9)*, Estoril, Portugal, 26-29 April 2011.

Pröll, T., 2015. Fundamentals of chemical looping combustion and introduction to CLC reactor design. In: Fennell, P. and Anthony, B. (eds.) *Calcium and Chemical Looping Technology for Power Generation and Carbon Dioxide (CO_2) Capture.* Cambridge: Woodhead Publishing, pp.197-218

Rahaman, M. N., 2015. Sintering theory and fundamentals. In: Samal, P. and Newkirk, J. (eds) *ASM Handbook, Volume 7, Powder Metallurgy*. West Conshohocken, PA: ASM International, pp.203-229.

Riazi, M. R. and Whitson, C. H., 1966. Estimating Diffusion Coefficients of Dense Fluids. *Industrial and Engineering Chemistry Research*, 32(12), pp.3081–3088.

Riazi, M. R., 2005. Characterization and Properties of Petroleum Fractions: (MNL 50). West Conshohocken, PA: ASTM International

Rydén, M., Leion, H., Mattisson, T. and Lyngfelt, A., 2014. Combined oxides as oxygen-carrier material for chemical-looping with oxygen uncoupling, *Applied Energy*, 113, pp.1924-1932.

Rydén, M., Lyngfelt, A., and Mattisson, T., 2011. Combined manganese/iron oxides as oxygen carrier for chemical looping combustion with oxygen uncoupling (CLOU) in a circulating fluidized bed reactor system. *Energy Procedia*, 4, pp.341-348.

Satterfield, C. N., 1996. in industrial practice 2nd ed. Malabar, Florida: Krieger Publishing Company.

Satterfield, C. N., 1970. Mass transfer in heterogeneous catalysis. Cambridge: M.I.T. press.

Sedor, K., Hossain, M. M. and de Lasa, H. I., 2008. Reduction kinetics of a fluidizable nickel alumina oxygen carrier for chemical-looping combustion. *Can J Chem Eng*. 86, pp.323-34.

Shen, L., Zheng, M., Xiao, J. and Xiao, R., 2010. Sulfur behaviour in chemical looping combustion with NiO/Al_2O_3 oxygen carrier. *Combust Flame.* 157, pp.853-63.

Siriwardane, R., Riley, J., Tian, H. and Richards, G., 2016. Chemical looping coal gasification with calcium ferrite and barium ferrite via solid–solid reactions. *Applied Energy.* 165, pp.952–966.

Snape, C. E., Sun, C., Lakatos, J. and Perry, R., 2010. Patent Number: WO2008093137-A1.

Szekely, J., Evans, J.W. and Sohn, H. Y., 1979. Gas-solid reactions. New York: Academic Press Inc.

Thiruvenkatachari, R.; Su, S.; An, H. and Xiang Yu, X., 2009. Post combustion CO_2 capture by carbon fibre monolithic adsorbents. *Progress in Energy and Combustion Science.* 35(5), pp.438-455.

Toftegaard, M. B., Brix, J., Jensen, P.A., Glarborg, P. A. and Jensen, A. D., 2010. Oxy-fuel combustion of solid fuels. *Progress in Energy and Combustion Science.* 36, pp.581-625.

UN., 1998. Kyoto protocol to the United Nations framework convention on climate change. Available: http://unfccc.int/kyoto_protocol/items/2830.php/

Villa, R., Cristiani, C., Groppi, G., Lietti, L., Forzatti, P., Cornaro, U. and Rossini, S., 2003. Ni based mixed oxide materials for CH4 oxidation under redox cycle conditions*. J Molecular Catal A: Chem*. 204-205, pp.637-46.

Wall, T., Liua, Y., Spero, C., Elliott L., Khare, S., Rathnama, R., Zeenathal, F., Moghtaderi, B., Buhre, B., Shenge, C., Guptaf, R., Yamadac, T., Makinoc, K. and Yu, J., 2009. An overview on oxyfuel coal combustion—State of the art research and technology development. *Chemical Engineering Research and Design.* 87, 1003–1016

Wang, P., Means, N., Shekhawat, D., Berry, D. and Massoudi, M., 2015. Chemical-Looping Combustion and Gasification of Coals and Oxygen Carrier Development: A Brief Review. *Energies*. 8, pp.10605-10635. doi:10.3390/en81010605

Wilke, C. R., 1950. Diffusional Properties of Multicomponent Gases. *Chemical Engineering Progress*, 46(2), pp.95–104.

Wolf, J., Anheden, M. and Yan, J., 2001. Performance analysis of combined cycles with chemical looping combustion for CO_2 capture. *Proceedings of the 18th Annual International Pittsburg Coal Conference*, New Castle, New South Wales, Australia, pp.1122–1139.

Wolf, J., Anheden, M. and Yan, J., 2005. Comparison of nickel- and iron-based oxygen carriers in chemical looping combustion for CO_2 capture in power generation. *Fuel* 84, pp.993–1006.

Yamasaki, A., 2003. An overview of CO_2 mitigation options for global warming-emphasizing CO_2 sequestration. *Journal of Chemical Engineering of Japan.* 36, pp.361-375.

Yaws, C. L., (2012; 2013; 2014). Yaws' Critical Property Data for Chemical Engineers and Chemists. Available from: http://app.knovel.com/hotlink/toc/id:kpYCPDCECD/yaws-critical-property/yaws-critical-property

Yu, S., Chen, L., Zhao, Y., Li, H. and Zhang, X., 2015. A brief review study of various thermodynamic cycles for high temperature power generation systems. *Energy Conversion and Management,* 94, pp.68–83.

Zafar, Q., Abad, A., Mattisson, T. and Gevert, B., 2007. Reaction kinetics of freeze-granulated $NiO/MgAl_2O_4$ oxygen carrier particles for chemical-looping combustion. *Energy & Fuels*. 21, pp.610-8.

Zafar, Q., Mattisson, T. and Gevert, B., 2005. Integrated hydrogen and power production with CO_2 capture using chemical-looping reforming—redox reactivity of particles of CuO, Mn_2O_3, NiO and Fe_2O_3 using SiO_2 as a support. *Ind Energy Chem Res*. 44(10). pp.3485–3496.

Zhang N. and Lior, N., 2008. Two novel oxy-fuel power cycles integrated with natural gas reforming and CO_2 capture. *Energy.* 33, pp.340–51.

Zhou, Z., Han, L., and Bollas, G. M., 2014. Kinetics of NiO reduction by H_2 and Ni oxidation at conditions relevant to chemical-looping combustion and reforming. *International Journal of Hydrogen Energy*, 39(16), pp.8535-8556.

Appendix A: Impact of Order of Mixing of Precursor Solutions

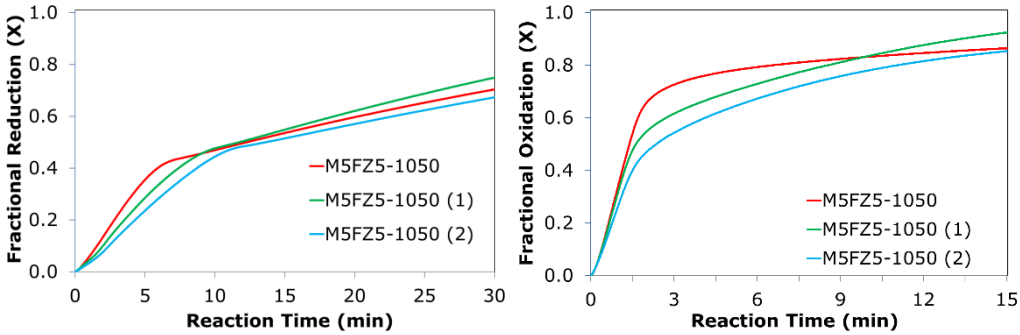

(a) Reduction (b) Oxidation

Figure A.1: Fractional conversion as a function of time of M5FZ5-1050 showing impact of order of mixing of precursor solutions for the (a) 4th reduction cycles in 5% H_2 and (b) 4th oxidation cycles in air at 1173 K, particle size of 75-250 μm and feed gas flow rate of 20 ml/min for the transition from Fe_2O_3 to Fe and from Mn_3O_4 to MnO.

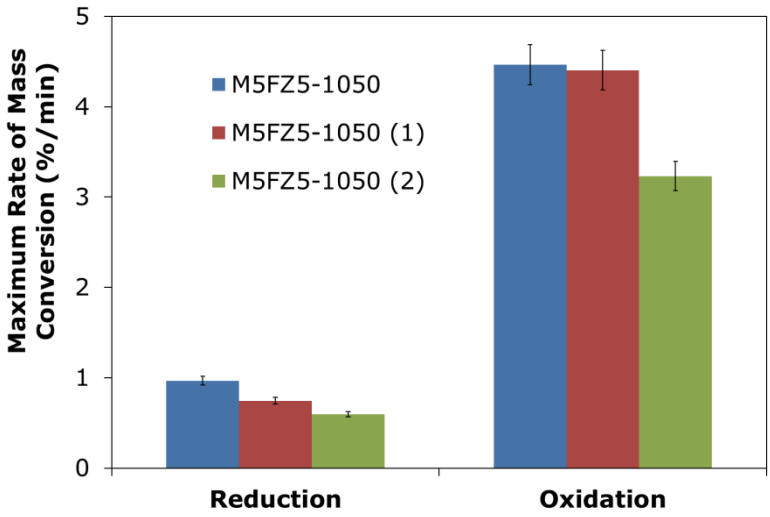

Figure A.2: Maximum mass based conversion for M5FZ5-1050 showing impact of order of mixing of precursor solutions for the (a) 4th reduction cycles in 5% H_2 and (b) 4th oxidation cycles in air at 1173 K, particle size of 75-250 μm and feed gas flow rate of 20 ml/min for the transition from Fe_2O_3 to Fe and from Mn_3O_4 to MnO.

Appendix B: SEM-EDX Image of Mechanically Mixed Mn/Fe Oxide with ZrO_2 Support

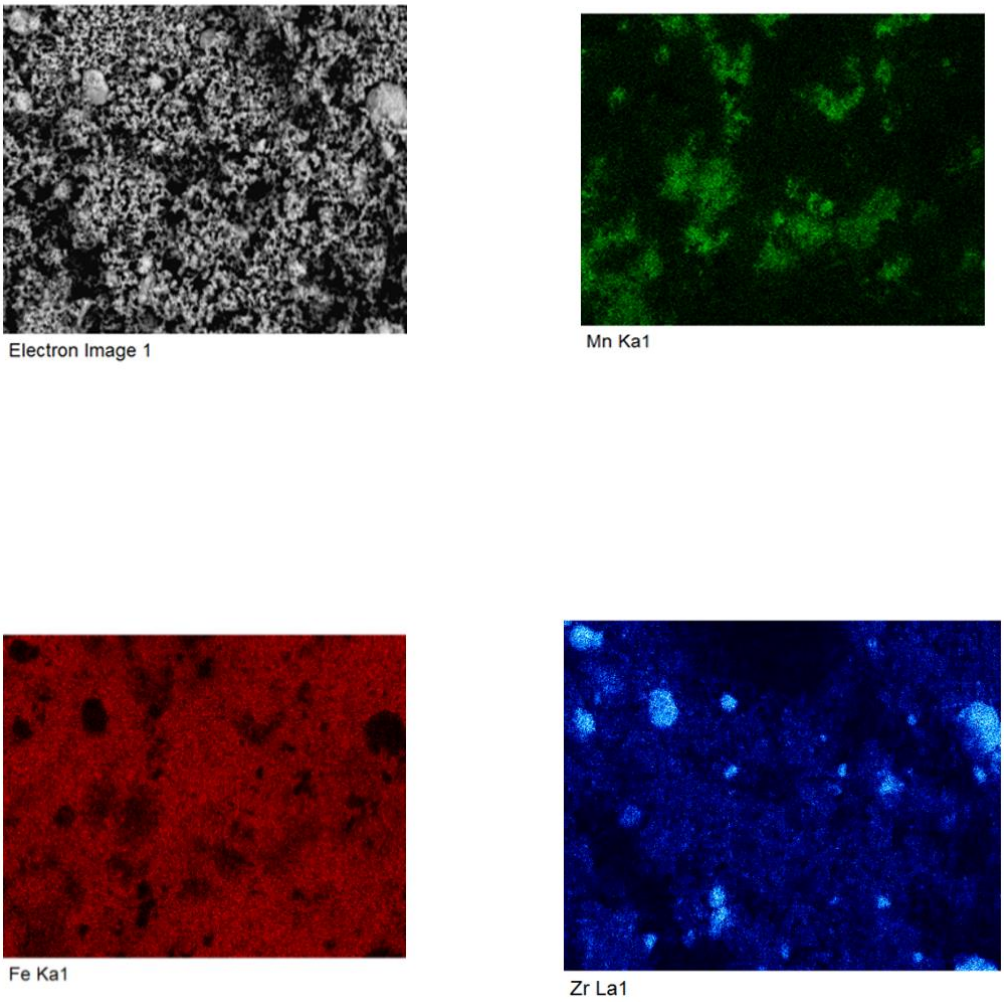

Figure B: SEM-EDX image of mechanically mixed Mn-Fe oxide with ZrO_2 support, magnification (5000X).

Appendix C: Repeatability Runs and Effect of Gas Flows and Mass of Sample on Rate of Reaction

Repeatability Runs

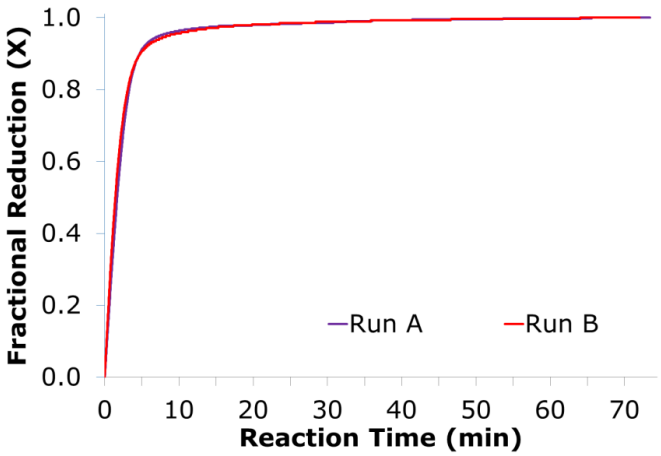

Figure C.1: Repeatability runs for M5Z5-450 for the 4th reduction cycles in 5% H_2 at 1173 K, particle size of 75-250 µm and feed gas flow rate of 20 ml/min for the transition from Mn_3O_4 to MnO. Coefficient of determination (R^2) between the two curves for the assumption that they are equal is 0.998.

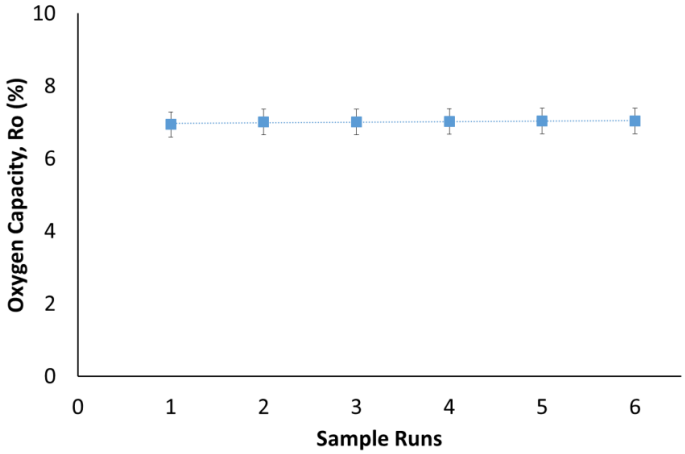

Figure C.2: Repeatability runs for Mn_3O_4 for reduction cycles in 5% H_2 at 1173 K, particle size of 75-250 µm and feed gas flow rate of 20 ml/min for the transition from Mn_3O_4 to MnO. Standard deviation = 0.03598 %. Mean Ro = 7.007 %. Theoretical Ro = 7 %. Percentage Error = 0.51% [Percentage error = standard deviation/mean) x 100%].

Effect of Gas Flows and Mass of Sample on Rate of Reaction

Experiments conducted to check the effect of various gas flows and mass of sample on reaction kinetics (Figures C.3 and C.4) for the oxygen carriers with the highest rates of reaction. Results indicated that similar reaction rates were observed with all gas flows and mass of samples.

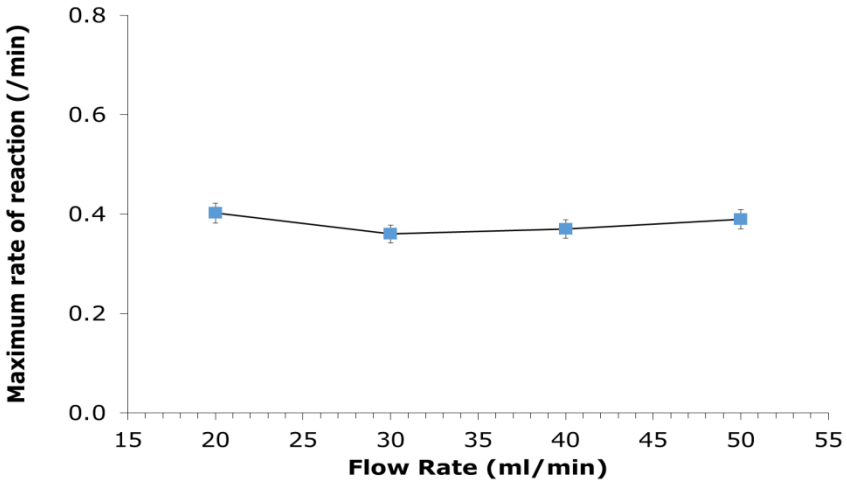

Figure C.3: Varying gas flow rate and maximum rate of reaction of M5Z5-1050 for the 4th reduction cycles in 5% H_2 at 1173 K, particle size of 75-250 µm and feed gas flow rate of 20 ml/min for the transition from Mn_3O_4 to MnO.

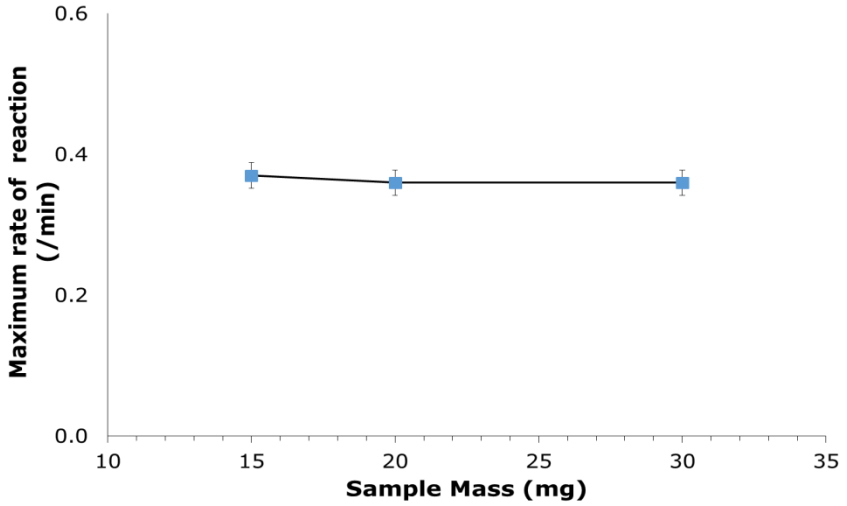

Figure C.4: Varying sample masses and maximum rate of reaction of M5Z5-450 for the 4th reduction cycles in 5% H_2 at 1173 K, particle size of 75-250 µm and feed gas flow rate of 20 ml/min for the transition from Mn_3O_4 to MnO.

Appendix D: Calculation of Reactants Loss and Rate of Conversion of Reactants

Calculations of the quantity of the reactants consumed or loss during the reaction and the rates of conversion of reactants are shown in this appendix. Values obtained from these and similar calculations were used in mass transfer estimations and other related calculations. The OC with the highest rates of reaction is used in this example calculation. It was shown that the rates of reaction were not limited by the rate of flow of reacting gases during the experiments.

Reaction of M5Z5-1050 in H_2 gas

The mass of M5Z5-1050 sample used is 20 mg, fraction of Mn_3O_4 in sample is 0.38 and molar mass of Mn_3O_4 is 229 g/mol. This gives the moles of Mn_3O_4 in sample to be 3.319×10^{-5}.

Mn_3O_4 reacts with H_2 in the fuel reactor as follows:

$$Mn_3O_4 + H_2 \rightarrow 3MnO + H_2O \qquad D.1$$

From equation D.1, moles of H_2 gas consumed in the reaction is given to be 3.319×10^{-5}.

The net reaction during the reduction of Mn_3O_4 to MnO in H_2 is as shown in Equation D.2.

$$2H_2 + O_2 \rightarrow 2H_2O \qquad D.2$$

Hence, the quantity of O_2 gas needed to react with H_2 to produce H_2O is

$= 3.319 \times 10^{-5} \times {}^{1}/_{2} = 1.659 \times 10^{-5}$ mol of O_2.

The comparison of the rates of reactants utilized and reactants supplied during the reduction of M5Z5-1050 in H_2 gas is presented below.

Flow rate of H_2 gas supplied = 20 ml/min (or 3.333 x 10^{-7} m^3/s)

Maximum rate of reaction (during conversion of Mn_3O_4 to MnO) = 0.4 min^{-1}

Concentration of H_2 gas supplied during reduction reaction = 5%

Maximum rate of formation (conversion) of O_2 from the reduction of Mn_3O_4 to MnO is given to be

$= 1.659 \times 10^{-5} \times {}^{0.4}/_{60}\,\text{mol/s} = 1.106 \times 10^{-7}\ \text{mol of}\ O_2/\text{s}.$

Also, the maximum rate of consumption (conversion) of H_2 is given to be

$= 3.319 \times 10^{-5} \times {}^{0.4}/_{60}\,\text{mol/s} = 2.212 \times 10^{-7}\ \text{mol of}\ H_2/\text{s}.$

The molar concentration of H_2 gas supplied to the TGA at temperature of ≈ 298 K and pressure of 101.3 KPa is given by:

$$\frac{n}{\text{V}} = \frac{\text{P}}{\text{RT}}$$

(where R is the universal gas constant = 8.314 J K^{-1} mol^{-1}, *n* and V are the number of moles and volume of gas respectively).

Hence, molar concentration of H_2 gas

$$= \frac{101.3 \times 10^3}{8.314 \times 298}\,\text{mol/m}^3 = 40.9\ \text{mol of}\ H_2/\text{m}^3$$

Rate of flow of H_2 gas supplied

= 40.9 x 3.333 x 10^{-7} x 0.05 mol/s =6.817 x 10^{-7} mol of H_2/s.

Comparison of the ratio of the rate of flow/conversion of reactants (H_2) utilised as a percentage of the reactants (H_2) supplied during the reduction of M5Z5-1050 is given to be

$$= \frac{2.212 \times 10^{-7}}{6.817 \times 10^{-7}} = 0.324\ \text{or}\ 32.4\%.$$

Thus, the maximum rate of reaction for the reduction of M5Z5-1050 was not limited by the rate of flow of H_2 during the experiment.

Reaction of M5Z5-1050 in CO

The maximum rate of formation (conversion) of O_2 from the reduction of Mn_3O_4 to MnO and the maximum rates of consumption (conversion) of CO or CH_4 were calculated similar to that of H_2. The flow rate of CO gas supplied = 50 ml/min (or 8.333 x 10^{-7} m^3/s) and concentration during the reduction reaction 10%. The maximum rate of reaction (during conversion of Mn_3O_4 to MnO in CO) = 0.76 min^{-1}.

For the reaction with CO, Mn_3O_4 reacts with CO in the fuel reactor as shown in Equation D.3. Also, the net reaction during the reduction of Mn_3O_4 to MnO in CO is as shown in Equation D.4.

$$Mn_3O_4 + CO \rightarrow 3MnO + CO_2 \qquad D.3$$

$$2CO + O_2 \rightarrow 2CO_2 \qquad D.4$$

Hence, the maximum rate of consumption (conversion) of CO gas to produce CO_2 equals 6.07×10^{-7} mol of CO/s.

Also, the maximum rate of formation (conversion) of O_2 gas from the reduction of Mn_3O_4 to MnO equals 3.04×10^{-7} mol of O_2/s.

In addition, the rate of flow of CO gas supplied is given to be

= 40.9 x 8.333 x 10^{-7} x 0.1 mol/s =3.408 x 10^{-6} mol of CO/s.

Comparison of the ratio of the rate of flow/conversion of reactants (CO) utilised as a percentage of the reactants (CO) supplied during the reduction of M5Z5-1050 is

$$= \frac{6.07 \times 10^{-7}}{3.408 \times 10^{-6}} = 0.178 \text{ or } 17.8\%.$$

Thus, the maximum rate of reaction for the reduction of M5Z5-1050 was not limited by the rate of flow of CO during the experiment.

Reaction of M5Z5-1050 in CH_4

For the reaction with CH4, the flow rate CH_4 gas supplied = 50 ml/min (or 8.333 x 10^{-7} m^3/s) and concentration during the reduction reaction 10% and the maximum rate of reaction (during conversion of Mn_3O_4 to MnO) = 1.55 min^{-1}.

Mn_3O_4 reacts with CH_4 in the fuel reactor as shown in Equation D.5. Also, the net reaction during the reduction of Mn_3O_4 to MnO in CH_4 is as shown in Equation D.6.

$$4Mn_3O_4 + CH_4 \rightarrow 12MnO + 2H_2O + CO_2 \quad \text{D.3}$$

$$CH_4 + 2O_2 \rightarrow 2H_2O + CO_2 \quad \text{D.4}$$

Hence, the maximum rate of consumption (conversion) of CH_4 to produce H_2O and CO_2 $= 2.98 \times 10^{-7}\ \text{mol of } CH_4/\text{s}$ and the maximum rate of formation (conversion) of O_2 gas from the reduction of Mn_3O_4 to MnO equals $5.97 \times 10^{-7}\ \text{mol of } O_2/\text{s}$.

In addition, the rate of flow of CH_4 gas supplied is given to be

= 40.9 x 8.333 x 10^{-7} x 0.1 mol/s =3.408 x 10^{-6} mol of CH_4/s.

Comparison of the ratio of the rate of flow/conversion of reactants (CH_4) utilised as a percentage of the reactants (CH_4) supplied during the reduction of M5Z5-1050 is

$$= \frac{2.98 \times 10^{-7}}{3.408 \times 10^{-6}} = 0.087 \text{ or } 8.7\%.$$

Thus, the maximum rate of reaction for the reduction of M5Z5-1050 was not limited by the rate of flow of CH_4 during the experiment.

Appendix E: Physical Properties of the Reacting Gases

The physical properties of the reacting gas mixtures were estimated as shown in this appendix. The physical properties calculated include: molecular weight, dynamic viscosity, density and diffusivity.

Molecular Weight of the Reacting Gases

The molecular weight of a gas mixture

$$= \sum M_i y_i \qquad \text{E.1}$$

where:

M_i = Molecular weight of *i* components, and

y_i = Mole fraction of *i* components.

Using Equation E.1, the molecular weights of the reacting gases H_2/N_2, $CH_4/CO_2/N_2$ and CO/N_2 were also calculated to be 30.82 and 28.01 respectively.

Dynamic Viscosity of the Reacting Gases

The dynamic viscosity of a gas at a specified temperature is obtained by the relation

$$\mu = \frac{AT^B}{1 + \frac{C}{T} + \frac{D}{T^2}} \qquad \text{E.2}$$

where *A*, *B*, *C* and *D* are correlation coefficients given in Table E.1. *T* is the specified temperature in Kelvin (Daubert and Fitzgerald, 1997).

Substituting for values of temperature and the corresponding correlation coefficients, the dynamic viscosities of the various reacting gases were calculated as shown in Table E.2.

Table E.1: Correlation coefficients for calculating dynamic viscosity of gases [Daubert and Fitzgerald, 1997].

Reacting gases	***A***	***B***	***C***	***D***
H2	1.7964×10^{-7}	6.850×10^{-1}	-5.8889×10^{-1}	1.4×10^{2}
N2	6.5593×10^{-7}	6.081×10^{-1}	5.4711×10^{1}	0
CH_4	5.2553×10^{-7}	5.901×10^{-1}	1.0572×10^{2}	0
CO_2	2.1479×10^{-6}	4.600×10^{-1}	2.9000×10^{2}	0
O_2	1.1010×10^{-6}	5.634×10^{-1}	9.6278×10^{1}	0
CO	1.1131×10^{-6}	5.338×10^{-1}	9.4722×10^{1}	0

Table E.2: Dynamic viscosities of gases at 1173 K and 1 atm.

Gases	**Dynamic viscosity at 1173 K and 1 atm (Kg/m s)**
H_2	2.28×10^{-5}
N_2	4.61×10^{-5}
CH_4	3.12×10^{-5}
CO_2	4.45×10^{-5}
O_2	5.45×10^{-5}
CO	4.48×10^{-5}

The dynamic viscosity of mixture of gases is obtained from Cheremisinoff (2000) as:

$$\mu_m = \frac{\sum y_i \mu_i M_i^{0.5}}{\sum y_i M_i^{0.5}} \quad \text{E.3}$$

where:

μ_i = Dynamic viscosity of *i*th component

y_i = Mole fraction of the *i*th component, and

M_i = Molecular weight of the *i*th component.

The dynamic viscosities for the reacting gas mixtures were calculated from equation E.3 with results shown in Table E.3.

Table E.3: Dynamic viscosities of reacting gas mixtures at 1173 K and 1 atm.

Reacting gases	**Dynamic viscosity at 1173 K and 1 atm (Kg/m s)**
H_2/N_2	4.58 x 10^{-5}
$CH_4/CO_2/N_2$	4.45 x 10^{-5}
O_2/N_2	4.80 x 10^{-5}
CO/N_2	4.59 x 10^{-5}

Reacting Gas Densities

The density of a gas at temperature, *T* and pressure, *P* is given by

$$\rho = \frac{P.M}{R.T} \quad \text{E.4}$$

where:

R = Universal gas constant, 8.314 J/Kg K

M = Molar mass of gas, kg/mol

T = Temperature, K

P = Pressure (atmospheric), 1.013 x 10-5 Pa.

Also, the density of a gas mixture is given by

$$\rho_m = \sum \rho_i y_i \qquad \text{E.5}$$

where:

ρ_i = Density of *i*th component

y_i = Mole fraction of *i*th component.

Using equation E.4 and E.5, the densities of the respective gases and gas mixtures were computed as shown in Table E.4.

Table E.4: Densities of reacting gas mixtures at 1173 K and 1 atm.

Reacting gases	**Density at 1173 K and 1 atm (Kg/m^3)**
H_2/N_2	0.2775
$CH_4/CO_2/N_2$	0.3201
O_2/N_2	0.2997
CO/N_2	0.2909

Gas Diffusivity (Diffusion Coefficient)

The Fuller-Schettler-Giddings equation was used to obtain the binary diffusivities of the reacting gases (Fuller, Schettler and Giddings, 1966).

$$D_{AB} = \frac{10^{-7} T^{1.75} [\frac{1}{M_A} + \frac{1}{M_B}]^{0.5}}{p[(\sum v)_A^{\frac{1}{3}} + (\sum v)_B^{\frac{1}{3}}]^2} \qquad \text{E.6}$$

where:

D_{AB} = Binary gas phase diffusivity of A in B, m^2/s

T = Absolute temperature, K

P = Absolute pressure

M_A, M_B = molecular weight of A and B

$(\sum V)_A$, $(\sum V)_B$ = Molecular diffusion volumes (given in Table E.5).

Using equation E.6, the binary diffusivities of the reacting gases were computed as shown in Table E.6.

Table E.5: Diffusion volumes for the reacting gases (adapted from Perry and Green, 1999).

Gases	**Diffusion volume (cm^3/mol)**
H_2	7.07
N_2	17.9
CH_4	24.42
CO_2	26.9
O_2	16.6
CO	18.9

Table E.6: Binary diffusivity for the reacting gases at 1173 K and 1 atm.

Gases	**Diffusivity (m^2/s)**
H_2/N_2	8.37×10^{-4}
CH_4/CO_2	1.97×10^{-4}
CH_4/N_2	2.42×10^{-4}
O_2/N_2	2.28×10^{-4}
CO/N_2	2.25×10^{-4}

For the case of CH_4 in CO_2 and N_2 (i.e. more than 2 gas mixtures), the diffusivity of CH_4 in the mixture was obtained by the Wilkie (1950) expression.

$$D_{A-mixture} = \frac{1 - y_A}{\sum_{i \neq A}^{N} \frac{y_i}{D_{A-i}}} \quad \text{E.7}$$

where:

y_A = Mole fraction of A in gas mixture

y_i = Mole fraction of ith component in the gas mixture

$D_{A\text{-}i}$ = Binary diffusion coefficient of A in the ith component.

Substituting in equation E.7 using values from Table E.6 gave the diffusivity of CH_4 in CO_2 and N_2 to be 2.28 x 10^{-4} m2/s.

Appendix F: Mass Transfer Calculations

Mass Transfer Coefficient

A valuable method of modelling diffusive transport is to treat the fluid layer next to a solid boundary as a stagnant film of thickness. Additionally, it is taken that all the resistance to mass transfer is located within this hypothetical stagnant film of thickness (δ) and the properties of the fluid at the outer edge of the film are the same as those of the bulk fluid (Fogler, 2013).

The molar flux of A through the stagnant film has been shown to be

$$N_{A_x} = \frac{D_{AB}}{\delta}[C_{AB} - C_{AS}] \qquad \text{F.1}$$

$$= \frac{D_{AB}}{\delta} C_{TO}[y_{AB} - y_{AS}] \qquad \text{F.2}$$

where,

δ = Film thickness

C_{AB} = Concentration at external boundary

y_{AB} = Mole fraction at external boundary

C_{AS} = Concentration at external particle surface

y_{AS} = Mole at external particle surface.

Since the magnitude of δ is usually unknown, the mass transfer coefficient is normally used. The mass transfer coefficient, k_c, is the ratio of the diffusivity, D_{AB} to the film thickness, δ (Davis and Davis, 2002). That is,

$$k_c = \frac{D_{AB}}{\delta} \qquad \text{F.3}$$

Thus, the average molar flux of A, from the bulk fluid to the solid particle surface is given by

$$N_A = k_C(C_{AB} - C_{AS}) \quad \text{F.4}$$

$$= k_C C_{TO}(y_{AB} - y_{AS}) \quad \text{F.5}$$

The maximum rate of external mass transfer of the reacting gas (H_2, CO or CH_4) from the bulk gas to the particle surface could be estimated by the following equation:

$$r_{gas} = \pi d_p^2 k_C(C_{AB} - C_{AS}) = \pi d_p^2 k_C C_{AB} \quad \text{F.6}$$

where C_{AB} is the bulk gas concentration of the reacting gas, mol/m^3, C_{AS} is the concentration of reacting gas on the particle interface, approximate to zero and d_P is a single particle diameter.

Mass transfer correlations have been established to ease the computation of mass transfer coefficient. The Sherwood number, *Sh*, relates the mass transfer coefficient to the particle diameter and its diffusivity.

$$Sh = \frac{k_C d_p}{D_{AB}} \quad \text{F.7}$$

where,

k_C is the mass transfer coefficient, m/s,

D_{AB} = Diffusivity, m^2/s.

d_p = Particle diameter, m.

The Sherwood number has been correlated to the Schmidt number, *Sc*, and the Reynolds number, *Re*, for flow around spherical particles as shown in Equation F.8 (Davis and Davis, 2002; Fogler, 2013; Perry and Green, 1999).

$$sh = 2 + 0.6Re^{\frac{1}{2}}Sc^{\frac{1}{3}} \quad \text{F.8}$$

Equation F.8 is also known as Frössling correlation.

$$Sc = \frac{\mu}{\rho D_{AB}} \quad \text{F.9}$$

$$= \frac{\nu}{D_{AB}} \quad \text{F.10}$$

$$Re = \frac{u\rho d_p}{\mu} \quad \text{F.11}$$

where,

μ = Dynamic viscosity, Kg/m s

ν = kinematic viscosity, m^2/s

u = Free stream velocity, m/s.

ρ = Fluid density, kg/m^3

The mass transfer coefficient and rate of external mass transfer were computed for the M5Z5-1050 sample (having the highest observed rate of reaction for each of the reacting gases) using Equations F.6 to F.11 and data from Appendices D and E. The results obtained are shown in Tables F.1, F.2 and F.3 below. The average particle size, d_P for the 75-250 μm and 300-850 μm sizes are 1.63 X 10^{-4} m and 5.75 X 10^{-4} m respectively. The gas velocities at temperatures of 1173, 1073 and 973 K are 4.64 X 10^{-2}, 4.24 X 10^{-2} and 3.85 X 10^{-2} m/s respectively for reaction in H_2 and 1.16 X 10^{-1}, 1.06 X 10^{-1} and 9.62 X 10^{-2} m/s respectively for reaction in CO and CH_4. Particle densities are shown in Tables 3.1, 3.2 and 3.3 of chapter 3.

Table F.1: Observed maximum rate of consumption (conversion) of H_2 and computed mass transfer coefficient and rate of external mass transfer for M5Z5-1050 at various temperatures and particle sizes.

Oxygen carrier	Reaction temperature (K)	Mass transfer coefficient K_c (m/s)	Rate of external mass transfer r_{H2} (mol/g.s)	Observed maximum rate of consumption (conversion) of H_2 (mol/g.s)
M5Z5-1050 (75-250 μm particle size)	900	10.63	3.85×10^{-2}	1.11×10^{-5}
	800	9.11	3.60×10^{-2}	7.80×10^{-6}
	700	7.69	3.35×10^{-2}	5.37×10^{-6}
M5Z5-1050 (300-850 μm particle size)	900	3.10	3.17×10^{-3}	1.03×10^{-5}

Table F.2: Observed maximum rate of consumption (conversion) of CO and computed mass transfer coefficient and rate of external mass transfer for M5Z5-1050 at various temperatures and particle size of 75-250 μm.

Oxygen carrier	Reaction temperature (K)	Mass transfer coefficient K_c (m/s)	Rate of external mass transfer r_{CO} (mol/g.s)	Observed maximum rate of consumption (conversion) of CO (mol/g.s)
M5Z5-1050	900	3.03	2.19×10^{-2}	2.09×10^{-5}
	800	2.60	2.06×10^{-2}	2.34×10^{-5}
	700	2.20	1.92×10^{-2}	1.40×10^{-5}

Table F.3: Observed maximum rate of consumption (conversion) of CH_4 and computed mass transfer coefficient and rate of external mass transfer for M5Z5-1050 at various temperatures and particle size of 75-250 μm.

Oxygen carrier	Reaction temperature (K)	Mass transfer coefficient K_c (m/s)	Rate of external mass transfer r_{CH4} (mol/g.s)	Observed maximum rate of consumption (conversion) of CH_4 (mol/g.s)
M5Z5-1050	900	3.06	2.22×10^{-2}	1.07×10^{-5}
	800	2.63	2.08×10^{-2}	2.86×10^{-6}
	700	2.22	1.94×10^{-2}	1.33×10^{-6}

From the results shown in Tables F.1, F.2 and F.3, it can be observed that the rates of external mass transfer are significantly higher than the experimental value of the maximum rate of consumption (conversion) of the respective reacting gases. Similar values were obtained for other cases not shown. It could also be noted that increased particle size reduced the mass transfer coefficient proportionally as expected, though not reduced to the extent of imposing external mass transfer limitations. Thus, it can be concluded that the experiments conducted are free of external mass transfer limitations.

Effectiveness Factor

Mass transfer effect on heterogeneous reaction mean that the average reaction rate throughout a particle under isothermal conditions will almost always be less than it would be if there were no mass transfer limitations. The relative importance and relationship between diffusion and reaction limitations is defined by the effectiveness factor which ranges from 0 to 1 (Satterfield, 1970; Klaewkla, Arend and Hoelderich, 2011). Thus, effectiveness factor (η) could be defined as:

$$\eta = \frac{\text{Actual (observed) reaction rate}}{\text{Reaction rate assuming no diffusion}} \qquad \text{F.12}$$

For the first-order irreversible reaction for a spherical particle, the effectiveness factor has been derived to be

$$\eta = \frac{3(\emptyset \coth \emptyset - 1)}{\emptyset^2} \qquad \text{F.13}$$

where, ϕ is the Thiele modulus.

Thiele modulus represents the ratio of reactivity over diffusivity of the reacting species. A plot of effectiveness factor against Thiele modulus for a

spherical particle is shown in Figure F.1. It was shown that as the particle size reduces, the value of Thiele modulus decreases and the effectiveness factor approaches unity resulting in the reaction rate becoming much lower than the diffusion rate. Hence, the surface reaction becomes the rate determining step. Conversely, at high values of Thiele modulus, the reaction rate is fast compared to the diffusion rate and the reaction is diffusion limited (Fogler, 2013; Klaewkla, Arend and Hoelderich, 2011; Satterfield, 1970). A general criterion for mass transfer in heterogeneous reactions is that, diffusional limitations are considered negligible for $\eta \geq 0.95$ (Satterfied, 1996).

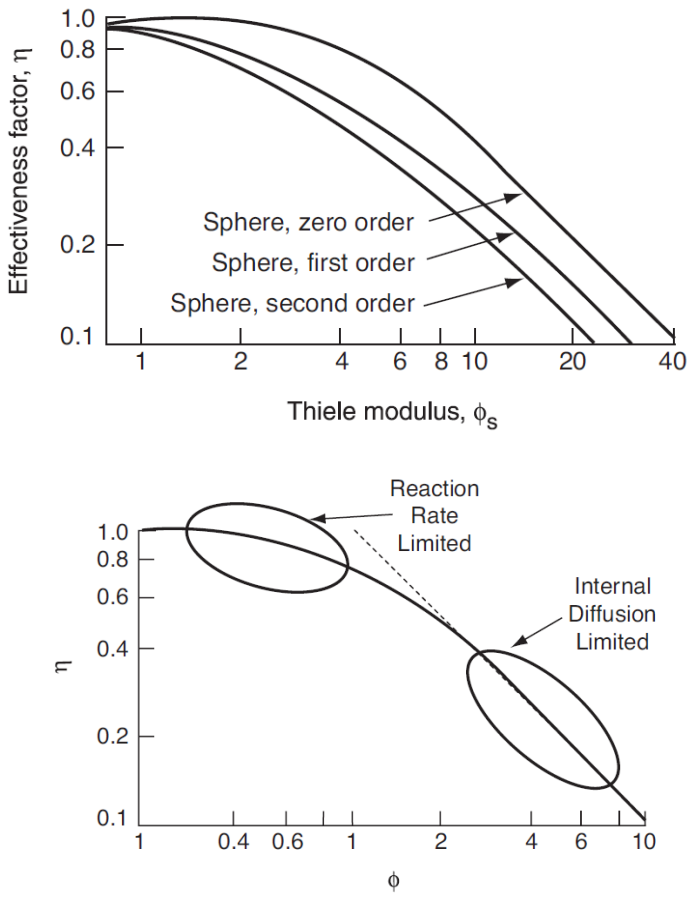

Figure F.1: (a) Effectiveness factor plot for nth-order kinetics on spherical catalyst particles (Satterfield, 1970). (b) First-order reaction indicating reaction rate limited and diffusion rate limited regions of the effectiveness factor against Thiele modulus plot (Aris, 1965).

The effectiveness factor can be readily obtained from the reaction rates of different particle sizes under identical conditions (Satterfield, 1970), (Fogler, 2013). For two particles sizes represented by the subscripts 1 and 2 (large particle size represented by subscript 1 and small size 2), the particle radii are R_{P1} and R_{P2}, Thiele modulus ϕ_1 and ϕ_2, observed rates of reaction r_1 and r_2, and effectiveness factors η_1 and η_2, then,

$$\frac{R_{P1}}{R_{P2}} = \frac{\emptyset_1}{\emptyset_2} \qquad \text{F.14}$$

$$\frac{r_2 R_{P2}}{r_1 R_{P1}} = \frac{\emptyset_2 \coth \emptyset_2 \ - 1}{\emptyset_1 \coth \emptyset_1 \ - 1} \qquad \text{F.15}$$

The values of η_1 and η_2 can then be obtained by solving the simultaneous equations expressing η_1 as a function of ϕ_1 and η_2 as a function of ϕ_2. The Thiele modulus and effectiveness factor for some of the OCs are as shown in Tables F.4 and F.5.

Table F.4: Thiele modulus and effectiveness factor for oxygen carriers with high zirconia content at different particle sizes. Large particle size: 300-850 μm; small particle size: 75-250 μm.

Oxygen carriers	Gas	Thiele modulus (ϕ)		Effectiveness factor (η)	
		Small particle	Large particle	Small particle	Large particle
M5Z5-1050	H_2	0.32	1.13	0.99	0.92
F5Z5-1050	H_2	0.63	2.21	0.97	0.78
M5FZ5-1050	H_2	0.264	0.935	0.99	0.95
M2FZ5-1050	CO	1.52	5.31	0.87	0.45

From the computed results in Table F.4, it can be observed that the single oxides OCs with small particle size have low values of Thiele modulus and effectiveness factors that are close to unity indicating the absence of

internal mass transfer limitations. Similar values were computed for the mixed oxide OC with high zirconia content which shows absence of internal mass transfer limitations in both the small and large particle sizes. This was not the case with M2FZ5-1050 with lower Mn content in the two particle sizes.

Table F.5: Thiele modulus and effectiveness factor for oxygen carriers with low zirconia content at different particle sizes. Large particle size: 300-850 μm; small particle size: 75-250 μm.

Oxygen carriers	Gas	Thiele modulus (ϕ)		Effectiveness factor (η)	
		Small particle	Large particle	Small particle	Large particle
M8FZ2-1050	H_2	0.78	2.75	0.96	0.70
M6FZ2-1050	H_2	2.15	7.60	0.79	0.34
M5FZ2-1050	H_2	1.77	6.26	0.84	0.40
M3FZ2-1050	H_2	3.15	11.14	0.65	0.25
M2FZ2-1050	H_2	1.02	3.61	0.94	0.60
M3FZ2-1050	CO	2.45	8.68	0.74	0.31

On the other hand, from the results in Table F.5, all OCs with low zirconia content show some level of internal mass transfer limited reaction in both particle sizes except M8FZ2-1050 with higher Mn content.

The rate of solid-gas reactions usually decreases with time as a result of deactivation of the active components leading to loss of reactivity. One category of deactivation mechanism is sintering. Deactivation by sintering occurs when there is reduced reactivity as a result of loss of active surface

area. The loss of the active surface area may be as a result of onset of agglomeration leading to closure of internal pores and subsequently limiting the internal mass transfer process from the external surface to the internal pore surface (Klaewkla, Arend and Hoelderich, 2011; Rahaman, 2015 and Fogler, 2006). The result from material characterization (SEM images) after reactivity show that M2FZ5-1050 and the OCs with low zirconia content with exception of M8FZ2-1050 formed agglomerates in CO and H_2 as reacting gases (see section 5.3). The agglomeration of these OCs resulted in the internal mass transfer limited reaction.

Overall, it can be concluded that the single oxide OCs and mixed oxide OCs with high zirconia and Mn contents in the small particle size range are free of internal mass transfer limitations in the experiments.

Appendix G: Brunauer–Emmett–Teller (BET) Surface Area and Isotherms

Table G.1: BET surface area and BET parameters for OCs using Krypton sorption at 77.4 K in a Micrometrics ASAP 2420 Accelerated Surface Area and Porosimetry System.

Samples	BET surface area (m^2/g)	BET parameter (C)	Correlation coefficient
M6FZ5-1050	0.408 ± 0.001	22.52	1.0000
M8FZ5-1050	0.272 ± 0.001	13.99	0.9999
M3FZ5-1050	0.940 ± 0.005	41.37	0.9999
M2FZ5-1050	0.388 ± 0.002	22.40	0.9999
M8FZCe5-1050	0.091 ± 0.002	11.87	0.9985
M6FZCe5-1050	0.189 ± 0.001	53.09	1.0000
M5FZCe5-1050	0.180 ± 0.003	27.32	0.9988
M3FZCe5-1050	0.097 ± 0.001	8.94	0.9996
M5ZCe5-1050	0.237 ± 0.005	19.31	0.9984

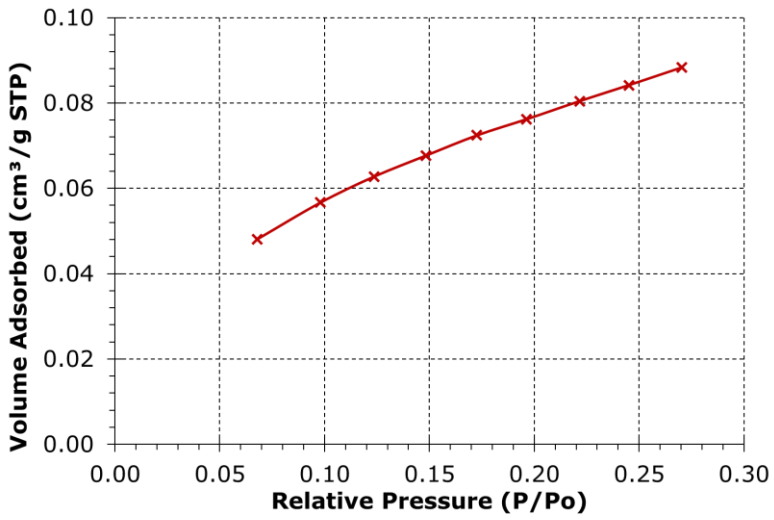

Figure G.1: Krypton adsorption isotherm for M6FZ5-1050.

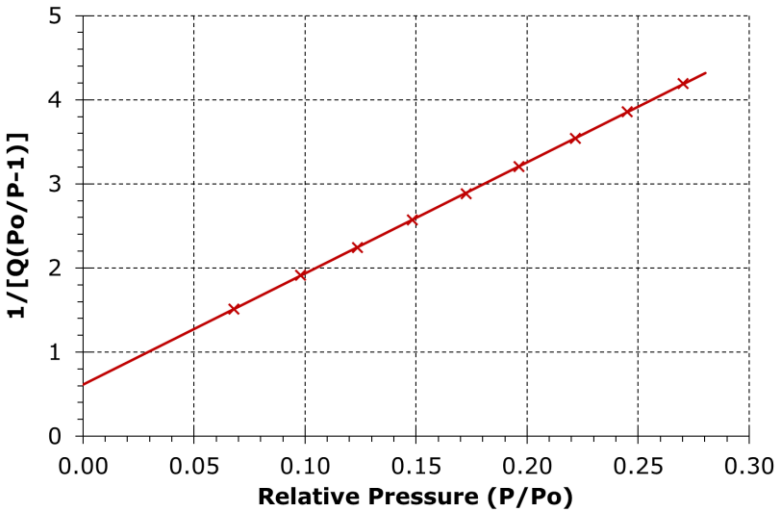

Figure G.2: BET surface area plot for M6FZ5-1050 using a relative pressure (P/Po) between 0.05-0.3 with nine data points.

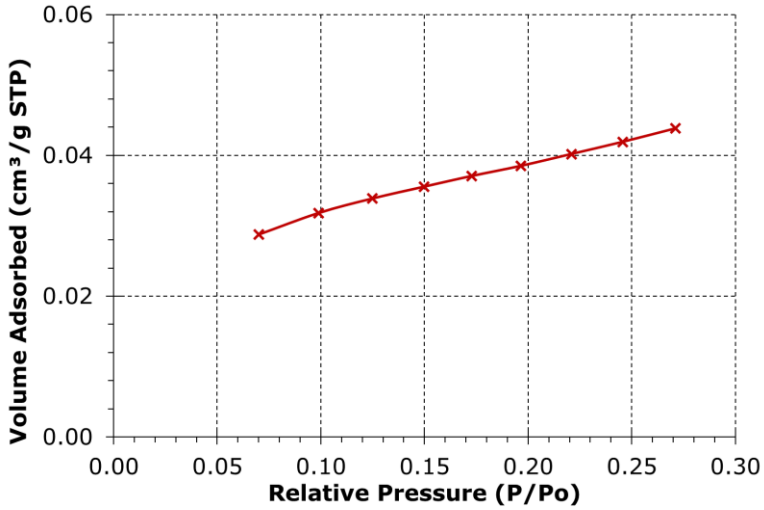

Figure G.3: Krypton adsorption Isotherm for M6FZCe5-1050

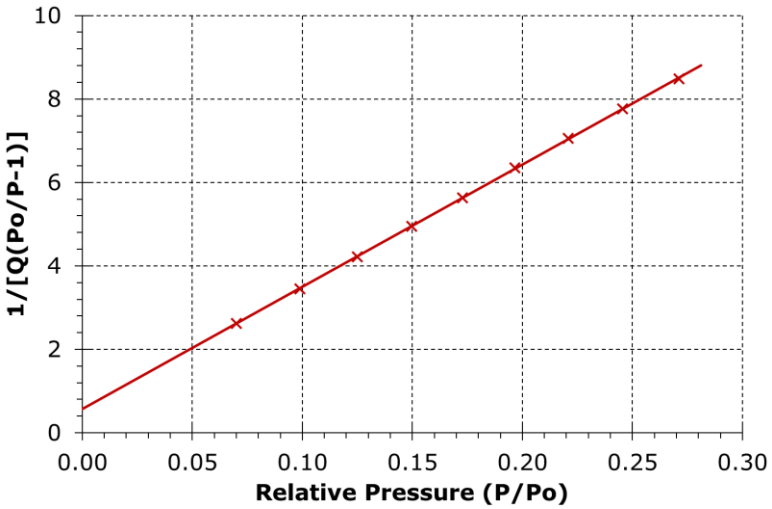

Figure G.4: BET surface area plot for M6FZCe5-1050 using a relative pressure (P/Po) between 0.05-0.3 with nine data points.